Causes for variable hydrothermal vent fluid compositions in intraoceanic arcs

–

Insights from fluid compositions and mineral precipitates of the South Kermadec Arc

Dissertation

zur Erlangung des Grades

-Dr. rer. Nat.-

am Fachbereich für Geowissenschaften

der Universität Bremen

vorgelegt von

Alexander Diehl

Universität Bremen

marum
Zentrum für Marine
Umweltwissenschaften
Universität Bremen

Bremen Januar 2019

Gutachter:

Prof. Dr. Wolfgang Bach

Prof. Dr. Colin Devey

Eingereicht am 08.01.2019
Dissertationskolloquium abgelegt am 06.02.2019

Dieses Dokument wurde hinsichtlich einiger Rechtschreibfehler überarbeitet. Alle Inhalte und Aussagen verbleiben unverändert und entsprechen der original eingereichten Arbeit.
This document was revised for some orthographic mistakes. All contents remain original.

Zusammenfassung

Seit der Entdeckung der ersten hydrothermalquelle am Galapagos Spreizungszentrum im Jahre 1977 haben Forschungsarbeiten an mittelozeanischen Rücken tiefgreifende Einblicke in die Natur und Eigenschaften von ozeanischen Hydrothermalquellen geliefert. Unser Verständnis der chemischen Prozesse und der thermischen Bedeutung von Hydrothermalsystemen, welche magmatische Zentren an Spreizungszonen effektiv kühlen, befindet sich mittlerweile in einem fortgeschrittenen Stadium, wenngleich noch immer Wissenslücken bestehen. Die global weniger vertretenen Inselbögen sind erst zu einem späteren Zeitpunkt in den Fokus der Tiefseeforschung geraten, obwohl deren Bedeutung für die globalen Stoff- und Energieflüsse nicht unbeachtlich sind. Auch wenn Inselbögen mit einer globalen Länge von nur einem Bruchteil der mittelozeanischen Rücken vertreten sind, sind hier besondere Voraussetzungen für Hydrothermalsysteme gegeben. Inselbogen Vulkane werden durch grundlegend andere magmatische Prozesse gebildet als mittelozeanische Rücken. Die Schmelzbildung erfolgt hier oberhalb der subduzierten benachbarten Ozeanplatte, welche unter dem Inselbogen abtaucht. Die dabei gebildeten Schmelzen werden an flüchtigen und fluid mobilen Elementen angereichert. Wenn diese Schmelzen in die verdickte Inselbogenkruste eindringen differenzieren sie zu silikatreichen Schmelzen. Während dieser Prozesse reichern sich flüchtige Bestandteile weiter in den Schmelzen an und können zu magmatischen Entgasungen führen. Hydrothermalsysteme an Inselbögen werden von diesen vulkanischen Gasen stark beeinflusst und somit unterschieden sich manche Hydrothermalfluide an Inselbögen extrem von den klassischen schwarzen Rauchern an mittelozeanischen Rücken. Weiterhin, sind Inselbögen durch ihre höhere Krustenmächtigkeit flacher gelegen als mittelozeanische Rücken. Diese Tatsache führt dazu, dass heiße Lösungen schon bei niedrigeren Temperaturen beginnen zu kochen. Dieser Prozess hat weitreichende Konsequenzen für die Eigenschaften der Lösungen und deren Kapazität Stoffe aus der tiefen Erdkruste in den Ozean zu befördern.

In dieser Arbeit wurden die Einflüsse von vulkanischen Entgasungen, von Prozessen der Phasenseparation und von Wasser-Gesteins Wechselwirkungen auf Hydrothermalsysteme an Inselbögen untersucht. Im Zuge von zwei schiffseitigen Foschungsexpeditionen zum südlichen Kermadec Inselbogen vor der Küste Neuseelands wurden Flüssigkeiten von heißen Quellen und Gesteine in deren Umgebungen an den drei Vulkanen mit den Namen Haungaroa, Macauley und Brothers geborgen.

Es werden detaillierte mineralogische und geochemische Untersuchungen an frischen und stark alterierten vulkanischen Gesteinen von diesen drei Vulkanen vorgestellt. Diese Daten werden genutzt um Reaktionspfadmodellierungen durchzuführen und zu untersuchen, inwieweit sich

die Gesteinszusammensetzung oder der Zusatz von vulkanischen Gasen auf die Zusammensetzung der hydrothermalen Lösungen und die Mineralvergesellschaftungen im Untergrund auswirken. Die Ergebnisse der Arbeit zeigen, dass der Zusatz von magmatischem Schwefeldioxid einen tiefgreifenden Effekt auf die Mineralzusammensetzung im Untergrund hat und hydrothermale Lösungen in besonders saure und aggressive Lösungen verwandelt. Im Gegenzug lassen die Ergebnisse vermuten, dass der Einfluss der Gesteinszusammensetzung weniger bedeutend ist als der Umsatz der hydrothermalen Flüssigkeiten. Die Ergebnisse werden direkt mit den alterierten Gesteinen verglichen, die in der Caldera des Brothers Vulkans und in der Caldera des Macauley Vulkans geborgen wurden. Die Modellierungen wurden weiterhin verwendet, um zu beleuchten wie sich die Alterationsmuster auf die Bildung von Sulfid Erzlagerstätten auswirken, wenn sich heiße Lösungen mit Meerwasser vermischen und aus der Inselbogenkruste austreten. Die Modelle zeigen hier, dass der Fluidumsatz im Untergrund die Vergesellschaftung von Sulfiden maßgeblich beeinflusst, während die Bedeutung der Gesteinszusammensetzung eher in den Hintergrund tritt. Die Ergebnisse werden dann im Zusammenhang mit den sulfidreichen hydrothermalen Schloten vom Brothers Vulkan, sowie vom Haungaroa Vulkan erörtert.

Die Untersuchung der hydrothermalen Lösungen selbst, stellt einen Hauptaspekt der Arbeit dar. Eine Schlüsselrolle in der Untersuchung von gasreichen Lösungen spielt der Einsatz von gasdichten Flüssigkeitsprobenschöpfern (gas-tight isobaric sampler). Diese ermöglichen eine hochpräzise Quantifizierung der volatilen Bestandteile, der damit angereicherten Flüssigkeiten, indem sie das Ausperlen dieser Volatilen bei der Bergung der Proben verhindern. Die Konzentrationen von Bestandteilen wie Kohlenstoffdioxid, Schwefelwasserstoff, Wasserstoff und Methan spielen nicht nur eine wichtige Rolle um den Einfluss magmatischer Entgasungen aufzudecken, sondern haben auch einen intensiven Einfluss auf die Mineralreaktionen im Untergrund. Magmatische Entgasungen von Schwefeldioxid führen durch Disproportionierungsreaktionen des Schwefels im Untergrund zu Säurebildung und beschleunigen so maßgeblich das herauslösen von Metallen und Alkalien aus den Gesteinen. Die dabei von statten gehenden Mineralreaktionen stellen den Haupteinflussfaktor dar, der die Besonderheit von Hydrothermalfluiden an Inselbögen ausmacht. Meine Untersuchungen der heißen Lösungen zeigen eindeutig, dass individuelle Quellen in verschiedenem Maße von den genannten Prozessen beeinflusst sind. So spielen schwefelige Gase in den hydrothermalen Systemen von Brothers und Macauley eine große Rolle, während der Vulkan Haungaroa eher von Phasenseparationen und Kohlenstoffdioxid-reichen Entgasungen geprägt ist.

Zuletzt wird der Umfang von Phasenseparationsprozessen auf austeigende heiße Lösungen beleuchtet. Untersuchungen an Flüssigkeitseinschlüssen liefern Informationen über vergangene Temperaturen in Hydrothermalsystemen und lassen Rekonstruktionen der Salzgehalte dieser

Lösungen zu. Am Beispiel des Brothers Vulkans zeigen diese Untersuchungen, dass aufsteigende Fluide oftmals zu kochen beginnen, bevor diese aus den Quellen austreten. Die Untersuchungen lassen weiterhin vermuten, dass auch in größeren Tiefen Phasenseparation stattfindet. Diese Prozesse haben einen starken Einfluss auf den Transport von Metallen und Alkalien in den hydrothermalen Fluiden.

Die Arbeit verdeutlicht, wie sehr die Zufuhr von vulkanischen Gasen, das Auftreten von Phasenseparationen und der Grad der Flüssigkeits-Gesteins Wechselwirkung in heißen Lösungen an Inselbögen bei der Herstellung deren besonderen Charakters beteiligt sind.

Summary

Since the discovery of the first hydrothermal vent at the Galapagos Spreading Center in 1977, research on mid-ocean ridges has provided profound insights into the nature and properties of oceanic hydrothermal vents. Our understanding of the chemical processes and thermal significance of hydrothermal systems, that effectively cool magmatic centers at mid-ocean ridge environments, today is in an advanced stage, although there are still gaps in our knowledge. The globally less-represented submarine volcanic arcs were given priority in deep-sea research at a later stage, despite their importance/relevance in the global material and energy fluxes is not insignificant. Although volcanic arcs comprise only a fraction of the mid-ocean ridges on a global scale, special conditions for hydrothermal systems that cool active arc volcanoes are given. Arc volcanoes are formed by fundamentally different magmatic processes than mid-ocean ridges. Melt generation occurs above the adjacent subducted oceanic plate, which submerges beneath the island arc. The resulting melts are enriched in volatiles and fluid mobile elements and when these melts intrude into the thicker arc crust, they differentiate to become silicate-rich melts. During these processes, volatiles continue to accumulate in the melts and may favor magmatic degassing. Hydrothermal systems in volcanic arcs are strongly affected by these volcanic gases and additionally, volcanic arcs are shallower than mid-ocean ridges due to their thicker crust. Thus, some hydrothermal fluids at arcs are very different from the classic black smoker fluids at mid-ocean ridges. Hot solutions in the subsurface start to boil at lower temperatures. This process has extensive consequences for the properties of the fluids and their capacity to transport substances from the crust into the ocean.

In this work, the effects of volcanic degassing, phase separation processes and fluid-rock interactions on hydrothermal systems in volcanic arcs were investigated. During two ship expeditions to the southern Kermadec Arc, fluid samples were recovered from hot springs and rocks samples from their surroundings. The three volcanoes named Haungaroa, Macauley and Brothers were investigated/explored.

Detailed mineralogical and geochemical investigations on fresh and pervasively altered volcanic rocks of these three volcanoes are presented. These data are used in thermodynamical reaction paths to investigate the impact of rock composition and addition of volcanic gases during hydrothermal circulation and their effect on the composition of hydrothermal fluids and alteration assemblages in the subsurface. The results show that the addition of magmatic sulfur dioxide largely affects mineral assemblages in the substrate. These model results are compared to altered rocks recovered in both the Brothers and the Macauley Caldera. Furthermore, model runs were performed to understand the influence of subsurface alteration patterns on the

formation of volcanogenic massive sulfide deposits that form when hot fluids mix with seawater and exit volcanic arc crust. The outcome reveals that sulfide assemblages are mainly influenced by the extent of fluid fluxes in the subsurface, whereas the rock composition plays a minor role. The model results are related to the sulfide-rich hydrothermal chimneys from Brothers Caldera and Haungaroa Volcano.

A main focus of this study is the analysis of hydrothermal vent fluids. Essential for the investigation is the deployment of gas-tight fluid samplers (gas-tight isobaric sampler). These samplers allow high precision quantification of dissolved gases in the enriched fluids by avoiding degassing during sample recovery or withdrawal of subsamples. Concentrations of carbon dioxide, hydrogen-sulfide, hydrogen, and methane play an important role in understanding magmatic outgassing. Furthermore, they strongly affect mineral reactions in the subsurface. Magmatic sulfur dioxide, taken up by hydrothermal fluids, leads to disproportion reactions of sulfur in the subsurface and the formation of acids facilitating the release of metals and alkaline elements from the basement rocks. The ongoing mineral reactions lead to the peculiarity of hydrothermal fluids in island arcs. My investigations of vent fluids clearly show that individual vents are affected by volatile addition or phase separation to different extents. Sulfide gases play a major role in hydrothermal systems at Brothers and Macauley Calderas, while phase separation and carbon dioxide outgassing are dominant factors at Haungaroa Volcano.

Finally, I investigated the impact of phase separation processes on upwelling vent fluids. Analyses on fluid inclusions reveal information about past temperatures of hydrothermal systems and allow to reconstruct salinities of the corresponding fluids. These investigations show that upwelling fluids commonly start boiling before exiting orifices in the North West Caldera Wall vent field of Brothers Volcano. Furthermore, these data hint towards supercritical phase separation also occurring at greater depths. These processes have a major effect on the transport of metals and alkalis in hydrothermal fluids.

This study underlines how extensive the supply of volcanic gasses, the appearance of phase separation and the degree of fluid-rock interaction contribute to the peculiar character of hydrothermal vent fluids in volcanic arcs.

For we have crossed many oceans
And we labor in between
In life there are many quotients
And I hope I find the mean

Mark Tremonti / Scott Stapp (Wash away the years)

Versicherung an Eides Statt / *Affirmation in lieu of an oath*

gem. § 5 Abs. 5 der Promotionsordnung vom 18.06.2018 /
according to § 5 (5) of the Doctoral Degree Rules and Regulations of 18 June, 2018

Ich / I, Alexander Diehl / [redacted]

(Vorname / First *Name*, Name / *Name*, Anschrift / *Address*, ggf. Matr.-Nr. / *student ID no., if applicable)*

versichere an Eides Statt durch meine Unterschrift, dass ich die vorliegende Dissertation selbständig und ohne fremde Hilfe angefertigt und alle Stellen, die ich wörtlich dem Sinne nach aus Veröffentlichungen entnommen habe, als solche kenntlich gemacht habe, mich auch keiner anderen als der angegebenen Literatur oder sonstiger Hilfsmittel bedient habe und die zu Prüfungszwecken beigelegte elektronische Version (PDF) der Dissertation mit der abgegebenen gedruckten Version identisch ist. / *With my signature I affirm in lieu of an oath that I prepared the submitted dissertation independently and without illicit assistance from third parties, that I appropriately referenced any text or content from other sources, that I used only literature and resources listed in the dissertation, and that the electronic (PDF) and printed versions of the dissertation are identical.*

Ich versichere an Eides Statt, dass ich die vorgenannten Angaben nach bestem Wissen und Gewissen gemacht habe und dass die Angaben der Wahrheit entsprechen und ich nichts verschwiegen habe*. / I affirm in lieu of an oath that the information provided herein to the best of my knowledge is true and complete.*

Die Strafbarkeit einer falschen eidesstattlichen Versicherung ist mir bekannt, namentlich die Strafandrohung gemäß § 156 StGB bis zu drei Jahren Freiheitsstrafe oder Geldstrafe bei vorsätzlicher Begehung der Tat bzw. gemäß § 161 Abs. 1 StGB bis zu einem Jahr Freiheitsstrafe oder Geldstrafe bei fahrlässiger Begehung. / *I am aware that a false affidavit is a criminal offence which is punishable by law in accordance with § 156 of the German Criminal Code (StGB) with up to three years imprisonment or a fine in case of intention, or in accordance with § 161 (1) of the German Criminal Code with up to one year imprisonment or a fine in case of negligence.*

Bremen, 08.01.2019 [redacted]

Ort / *Place*, Datum / *Date* — Unterschrift / *Signature*

Table of Contents

1 Introduction

1.1 Hydrothermal circulation in oceanic environments

Submarine hydrothermal vents were first discovered in 1977 (Corliss at al., 1979) and still remain one of the most fascinating research objects in modern science. Hydrothermal circulation systems in oceanic environments are the interface in the cycling of energy and mass between the oceans and the earth's interior.

Hydrothermal circulation occurs whenever deep-ocean water masses penetrate the oceanic crust in a volcanically active region. The permeable character of the ocean crust permits fluids to percolate down- or upward moving through the volcanic rock basement or to be laterally recharged by peripheral seawater.

On a global scale, this mainly occurs on divergent plate boundaries, called mid-ocean ridges. Here, hot lithosphere rises from the deep interior of the planet undergoing decompressional melting and continuously forms new ocean crust by intrusion or extrusion of basaltic melts. Hydrothermal circulation is manifested as high-temperature 'black' and 'white' smoker systems or as low-temperature (< 35 °C) diffuse systems gently emanating the crust.

The energy transported in these magmatic processes leads to conductive heating of the seawater-saturated ocean crust. The pore water in the highly porous medium becomes buoyant at high temperatures and rapidly rises to the surface where it is emitted into the ocean (German & Van Damm, 2003). In this way, a convective cell of fluid flow originates in the crust underneath the ocean.

Cooling of the oceanic crust occurs by conduction of heat from the lithosphere to the ocean and by convective circulation of cold seawater within the upper ocean crust - thus through hydrothermal circulation. In fact, the hot rising fluids effectively transport heat originated in the inside of the planet upwards to the shallow lithosphere, and release this heat when exiting the seafloor and mixing with the ocean.

The total heat loss of the planet is estimated to be 46.6 TW from which around 68.5% (31.9 TW) can be attributed to heat loss from the ocean crust (Davies & Davies, 2010). About one-third of the oceanic heat flux (9 TW), or 19.3% of the global heat loss, can be attributed to hydrothermal circulation in oceanic environments (Spinelli & Harris, 2011). The 9 TW partition into 2.7 TW removed on-axis, 0.9 TW removed near-axis and 5.4 TW extracted off-axis, thus 5.8%, 1.9% and 11.6% of the global heat loss. These data clearly exhibit the contribution of oceanic hydrothermal circulation systems to the global cooling of the planet and disclose their importance as energy exchange interface.

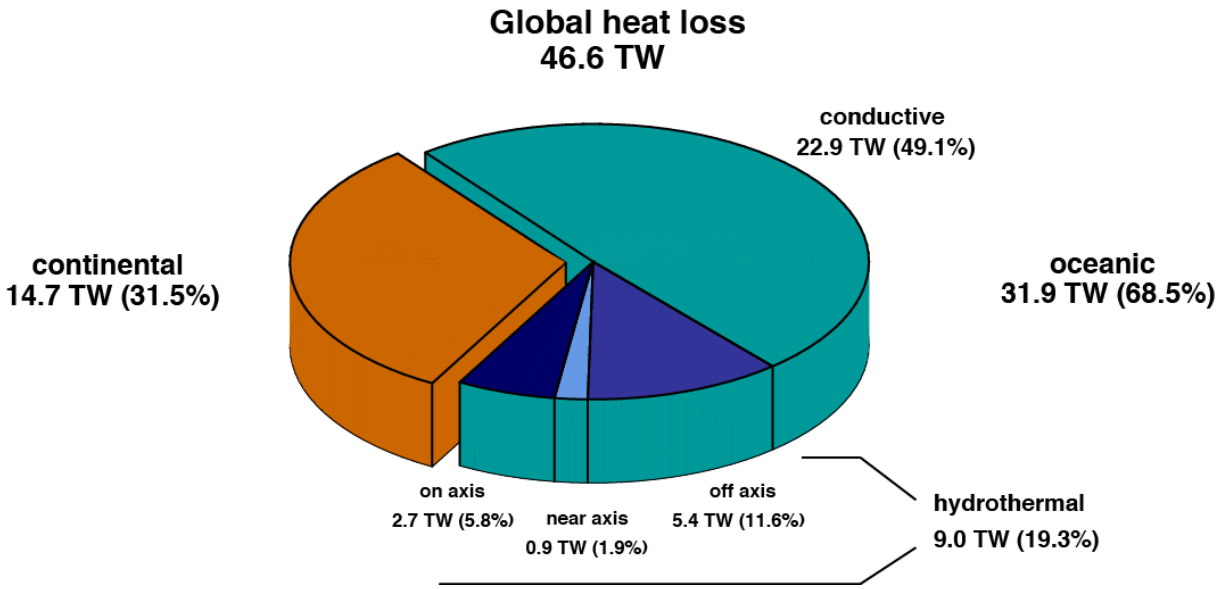

Figure 1: The role of hydrothermal circulation for the global heat loss. Global, continental and oceanic heat loss are derived from global heat flow measurements (Davies & Davies, 2010). Hydrothermal heat loss and partitioning into on-, near- and off-axis is calculated from thermal models in Spinelli and Harris (2011).

While the recharged seawater circulates and is heated up, it interacts with volcanic basement rocks and undergoes chemical reactions changing its own as well as the basement's composition. Ergo, hydrothermal fluids discharge chemically altered seawater, which, in comparison to the original seawater, is in average enriched, inter alia, in alkalis, metals and volatiles (Von Damm, 1985), whereas it is depleted in elements like Mg, SO_4, P, Na (Elderfield & Schultz, 1996). Obviously, hydrothermal circulation systems constitute an interface between the ocean and the solid earth not only in terms of energy but also on the compositional/ geochemical level.

An integrated view on global element fluxes during hydrothermal circulation is achieved when comparing the compositions of hydrothermal fluids with that of seawater, and linking them to the global water mass fluxes (Elderfield & Schultz, 1996). Estimates suggest that the entire volume of the oceans transits through high-temperature hydrothermal systems within a few million years (e.g. Elderfield and Schulz, 1996). This calculation provides an estimate about the chemical impact of hydrothermal fluids on the ocean (Table 1) and puts the contribution of hydrothermal systems to oceanic geochemistry into perspective (c.f. contribution of rivers to the element budget in Table 1). Since hydrothermal fluids exit the ocean crust with variable temperatures as well as variable elemental compositions (focused vs diffuse), this calculation provides a first order approximation only.

Table 1: Contribution of hydrothermal circulation to the chemical budget of the ocean (from Elderfield and Schultz, 1996).

Element	$c_{hydrothermal\ fluid}$ (mol/kg)	$c_{seawater}$ (mol/kg)	$F_{hydrothermal}$ (10^{10} mol/year)	F_{rivers} (10^{10} mol/year)
Li	411 - 1322 µ	2 µ	1.2 - 3.9	1.4
K	17 - 32.9 m	9.8 m	23 - 69	190
Rb	10 - 33 µ	1.3 µ	0.026 - 0.095	0.037
Cs	100 - 202 n	2.0 n	0.00029 - 0.0006	0.00048
Be	10 - 38.5 n	0	0.00003 - 0.00012	0.0037
Mg	0	53 m	-160	530
Ca	10.5 - 55 m	10.2 m	0.90 - 130	1200
Sr	87 µ	87 µ	0	2.2
Ba	> 8 to > 42.6 µ	0.14 µ	> 0.024 - 0.13	1.0
SO_4	0 - 0.6 m	28 m	-84	370
Alk	-0.1 to -1.0 m	2.3 m	-7.2 - 9.9	3000
Si	14.3 - 22.0 m	0.05 m	43 - 66	640
P	0.5 µ	2 µ	-0.0045	3.3
B	451 - 565 µ	416 µ	0.11 - 0.45	5.4
Al	4 - 20 µ	0.02 µ	0.012 - 0.06	6.0
Mn	360 - 1140 µ	0	1.1 - 3.4	0.49
Fe	750 - 6470 µ	0	2.3 - 19	2.3
Co	22 - 227 n	0.03 n	$6.6\text{ -}68 \times 10^{-5}$	0.011
Cu	9.7 - 44 µ	0.007 µ	0.03 - 0.13	0.50
Zn	40 - 106 µ	0.01 µ	0.12 - 0.32	1.4
Ag	26 - 38 n	0.02 n	$7.8 - 11 \times 10^{-5}$	0.0088
Pb	9 - 359 n	0.01 n	$2.7 - 110 \times 10^{-5}$	0.015
As	30 - 452 n	27 n	$0.9 - 140 \times 10^{-5}$	0.072
Se	1 - 72 n	2.5 n	$3.0 - 220 \times 10^{-6}$	0.0079
CO_2	5.7 - 16.7 m	2.3 m	10 - 120	
CH_4	25 - 100 µ	0 µ	0.67 - 2.4	
H_2	0.05 - 1 m	0 m	0.3 - 1.5	
H_2S	2.9 - 12.2 m	0 m	8.5 - 96	

The composition of the basement rocks is changed by metasomatism of the rock when heated seawater percolates in a convection cell (Figure 2). Investigations on hydrothermally altered rocks reveal which types of fluid-rock interactions are responsible for the just mentioned element transfers, estimated in the global element budget.

The drill cores of IODP hole 504B gave insights on the alteration processes which manifest during ingression of seawater into the volcanic basement at mid-ocean ridges under conditions

of increasing temperature and decreasing water-to-rock mass ratio. At low temperatures (< 100 °C), the alteration assemblage created during fluid-rock interaction is composed of Fe-oxyhydroxides, smectites and ferric mica, and leads to oxidation and alkali fixation (eg. K) in the upper volcanic rocks (Alt, 1995). With increasing temperature downwards, the fluids start to lose Mg by precipitation of Mg-bearing smectites (rather low-T), chlorite (rather high-T) and mixtures of both. At the transition between pillow lavas and sheeted-dikes, a large temperature gradient seems to develop and alteration assemblages may shift to greenschist facies conditions (> 200 °C) within only some 10s of meters (Alt, 1995). The alteration assemblage here consists of albite, chlorite quartz, smectite and secondary sulfides. This indicates reducing conditions in the initially seawater-like fluids which start developing their hydrothermal characteristics by loss of OH. OH forms complexes with Mg and decreases the pH value of the fluid. The volcanic basement rocks lose Si, Ca, K, Rb, S and gain Na, H_2O, CO_2. The uptake of Ca in the fluid is balanced by anhydrite precipitation, which coincides with a loss of sulfate, and occurs when seawater is heated, as well as when seawater mixes with hydrothermal fluids (Alt, 1995; Teagle et al. 1998).

From greenschist facies conditions, the fluid enters the reaction zone located above the magmatic source. The permeability decreases and leads to low water-to-rock ratios with high fluid temperatures (300-500 °C). In these conditions, hydrothermal fluids inherit their final chemical signature by interaction with fresh volcanic rocks. Mineralogical investigations in IODP hole 504B reveal actinolite amphibole compositions to be changed to Mg-Hornblende, whilst igneous plagioclase is altered to more calcic plagioclase, and igneous rocks to be strongly depleted in Cu, Zn, S due to breakdown of primary sulfides and Fe-Ti oxides (Alt, 1995).

The depth reached by the fluids depends on the temperature and pressure conditions: fluids at such high temperatures (>> 350 °C) become more and more buoyant or even phase separated (Bischhoff & Rosenbauer, 1985; Humphris & McCollom, 1998; Von Damm, 1995) and start to rise. Jointly, rocks become more and more plastic at high temperatures and do not provide cracks that permit fluids to percolate deeper.

When the high buoyancy hydrothermal fluids rapidly rise to the surface again, they form focused channels (upflow-zone) in which the fluid flow is much higher than in the recharge zone of intruding seawater. Greenschist facies assemblages in the deep subsurface develop and grade into a high sulfidation environment in the shallow subsurface. Polymetallic sulfides may precipitate due to a temperature drop associated with adiabatic cooling or to a temperature drop that is contributed to mixing with downwelling cold and oxidizing seawater (Figure 3). Anhydrite, barite, Fe-sulfides are common minerals that replace the host rocks extensively and

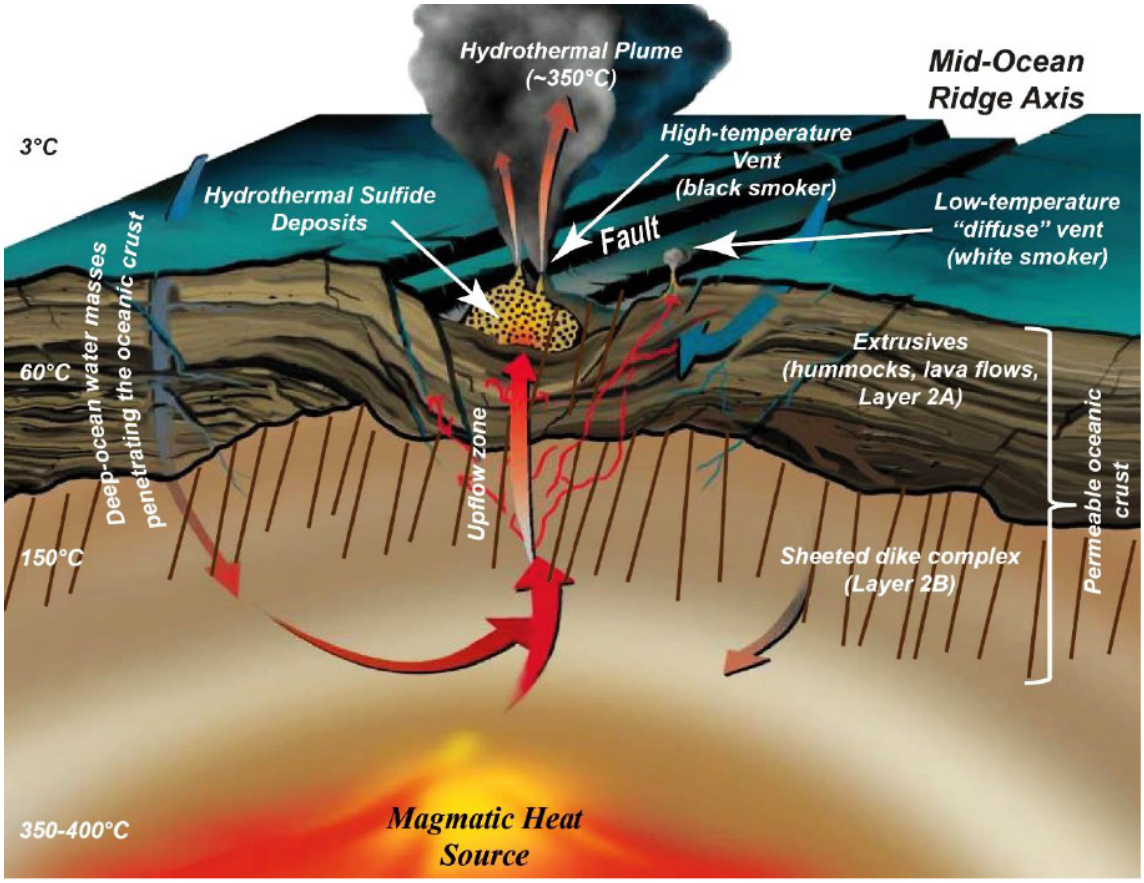

Figure 2: Hydrothermal convection cell driven by a magmatic heat source. Seawater ingresses the volcanic basement, is heated and chemically modified to rapidly rise to the seafloor again and form sulfide deposits (from Palgan, 2017; modified after Humphris and McCollom, 1998).

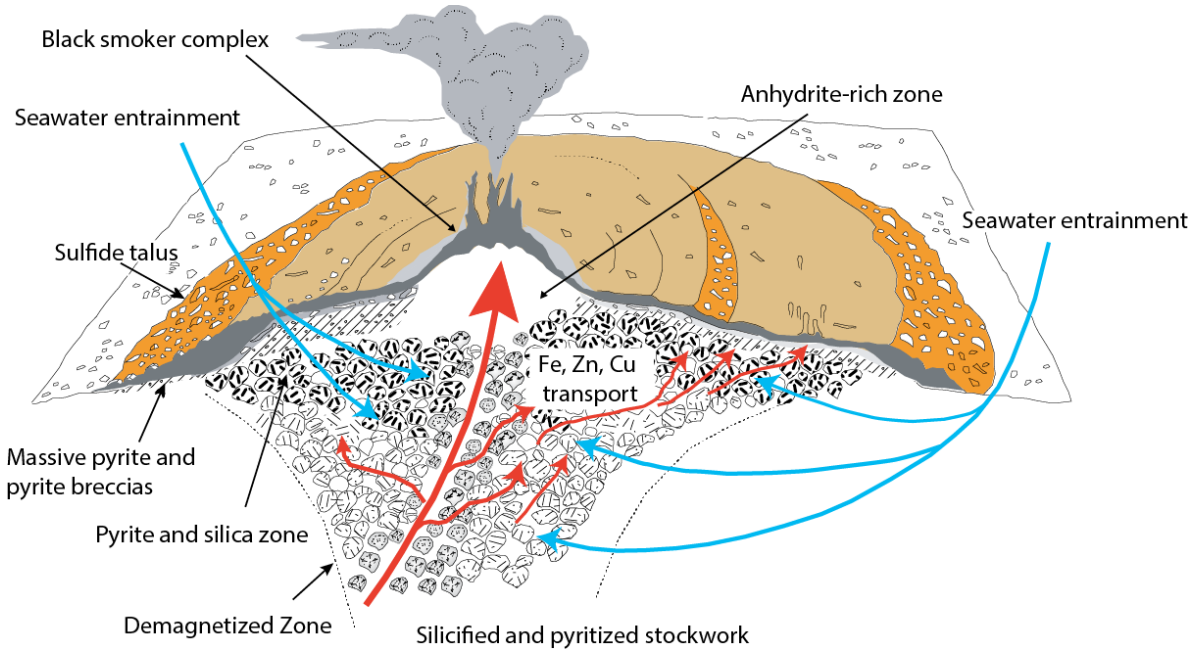

Figure 3: Formation of massive sulfide deposits at hydrothermal vent sites. Hot rising fluids interact with basement rocks and ingression of seawater facilitates subseafloor mineralization before vent fluids exit chimneys. To form buoyant plumes (modified after Tivey, 2007).

form stockwork zones beneath the hydrothermal orifice upon dilution of hydrothermal fluids with seawater. At the vents, freshly precipitated minerals contribute to the growth of chimneys. During prolonged timespans a cycle of growth and collapse events may form accumulations of chimney debris that represent high grade ore deposits.

When the fluids, rich in dissolved chemicals, are emitted from the seafloor, their high buoyancy pushes them hundreds of meters up into the water column. As they mix with cold seawater, vent fluids eventually form non-buoyant plumes of sulfide- and oxide-rich particles or non-metallic particles - named according to their black and white colors: “black smokers” and “white smokers” (German & Van Damm, 2003). Data from the US GEOTRACES Eastern Pacific Zonal Transect report that plumes containing hydrothermal dissolved metals (Fe, Mn, and Al) can be transported several thousand kilometers (more than 4000 km) across the South Pacific Ocean from the southern East Pacific Rise (Resing et al., 2015). This and other studies underline the significant contribution of hydrothermal vents to the oceanic biogeochemistry.

Hydrothermal systems do not only affect inorganic chemistry but also support a dense biomass of a spectrum of various organisms in an ecosystem relying on chemosynthesis. Most of the ocean floor is populated sparsely. In contrast, hydrothermal vents were discovered to host flourishing exotic communities spanning from single-cell organisms that find their habitats in hydrothermal plumes, to small and large invertebrates and vast benthic communities at and around vent orifices. Singular “large” sites are as big as a football field. However, compared to the vast expanse of the seafloor, they are small oasis of life in the vast desert.

Due to the large depth they are situated at, ecosystems at hydrothermal vents are, yet, decoupled from climatic variations and anthropogenic activities and are tightly coupled to geophysical processes. The basaltic seafloor, the reduced compounds carried in hydrothermal fluids and the oxidation state of the deep-sea environment, provide nutrients and sustain life at vents. Depending upon hydrothermal fluids’ chemistry, microbes fix inorganic carbon into organic carbon by chemosynthesis, thus derive energy from sulfur oxidation or methane reduction.

Invertebrate species often host chemosynthetic endosymbiotic bacteria within their tissues. For example, the bacteria in the giant, red-plumed tubeworms (*Riftia pachyptila*) provide nearly all of the nutrition for the host. In turn, the tubeworms offer a chemically-rich and stable environment for growth (Van Dover, 2001). Higher life at hydrothermal vents includes clams, mussels, shrimps and others.

There are major biogeographic differences in vent fauna in the ocean. Some communities are constantly changing, other long-lived sites document essentially no change. Furthermore, it appears that history and evolution of mid-oceanic ridges as well as ocean circulation patterns introduced differences in the communities (Tunnicliffe & Fowler, 1996).

1.2 Magmatic activities and hydrothermal systems in volcanic arcs

The most magmatically active places in the ocean, besides mid-oceanic ridges, are volcanos in volcanic arcs (island arcs and intraoceanic arcs). With a length of 22 000 km (de Ronde et al., 2003) volcanic arcs sum up to a third of the length of mid-oceanic spreading centers (67 000 km; Bird, 2003; de Ronde et al., 2003). Of these 22 000 km about 7000 km of arcs are predominantly submarine intraoceanic arcs such as Tonga-Kermadec and Izu-Bonin-Mariana (Baker et al., 2008). This means that both sides of the arc are bordered by oceanic crust (Baker et al., 2008). Another 4000 km are mainly submarine but volcanoes are mainly subaerial. Consequently, the remaining 11 000 km are island arcs that comprise of a basement of continental crust, in which magmatic activities mainly focus on subaerial volcanos (Figure 4).

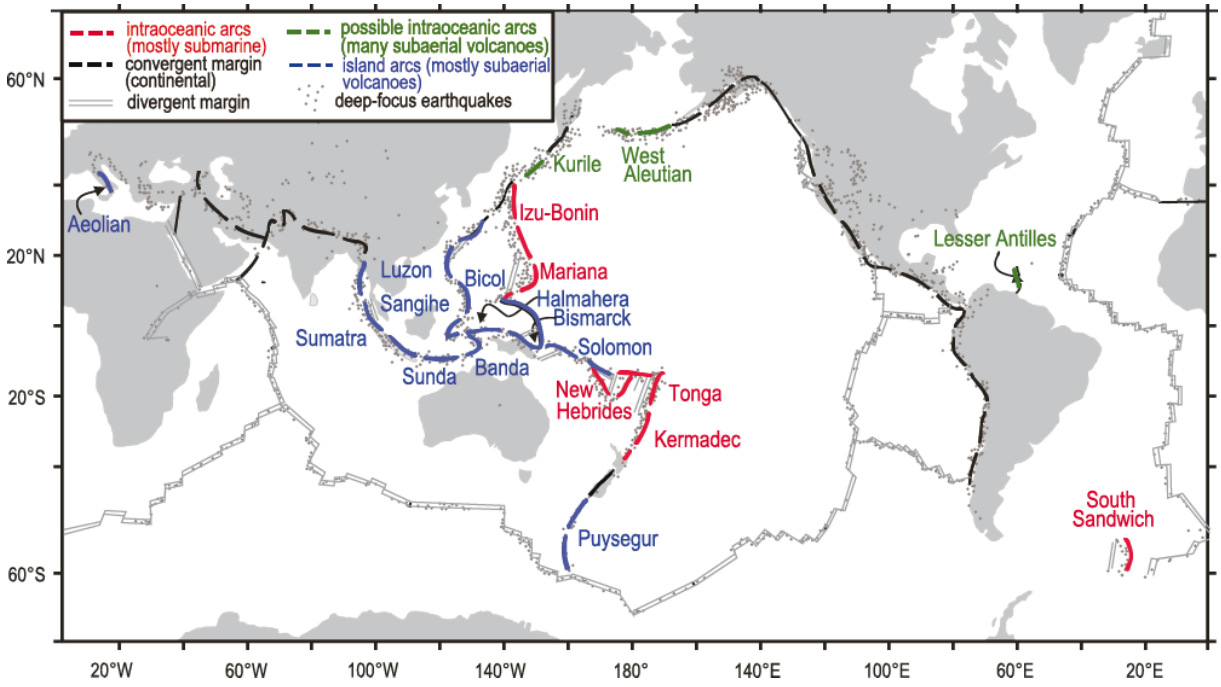

Figure 4: Global distribution of volcanic arcs and oceanic spreading centers. Different types of arcs (intraoceanic and island arcs) are highlighted (from Baker, 2008; modified after Open University 1988).

Magma in island arcs is produced by flux-induced hydrous melting of the mantle (Figure 5) and is enriched in volatiles, as well as fluid-mobile elements derived from the subducting slab (Plank & Langmuir, 1993; Haase et al., 2002; Wysoczanski et al., 2006). The magmas intrude into a thick (up to 35 km) arc crust and are consequently subject to differentiation prior to their eruption (Haase et al., 2006; Smith et al., 2010) and may also be influenced by partial melting and assimilation of lower crust (Smith et al., 2006). The products of these diverse processes of magmatic differentiation range from primitive basalts to highly differentiated rhyolites. Due to

this, island arc crust is built of rocks with highly variable compositions (Graham et al., 2008). Volcanoes in island arcs are formed by eruption mechanisms that are very different from lava flows at mid-ocean ridges. Eruption types of volcanoes differ depending on water depth (Wright et al., 2002; 2006). The majority of arc magmatic systems build caldera volcanoes instead of large volcanic cones.

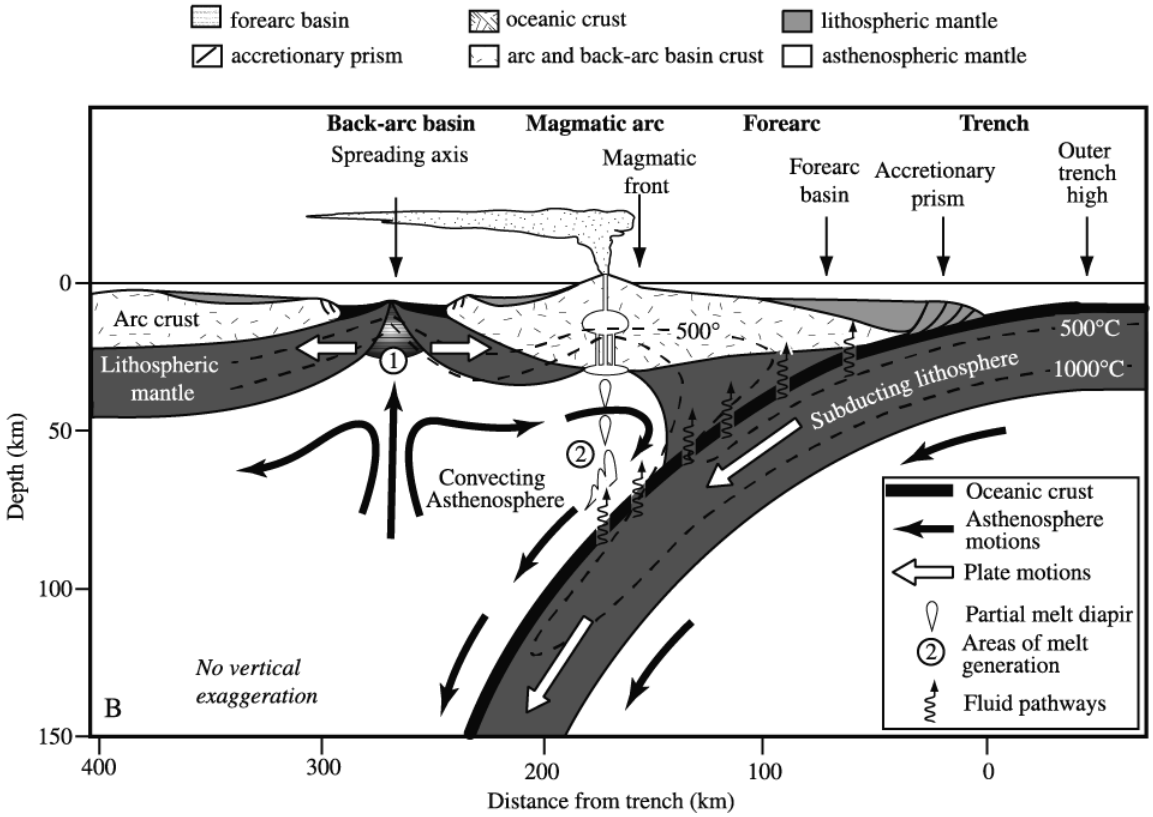

Figure 5: Melt generation in arc environments. Dehydration of the subducting slab initiates hydrous mantle melting and mantle drag leads to mantle corner flow (from Stern 2002).

Formerly, it was believed that the magma production rates in island arcs and intraoceanic arcs were subtle compared to those along oceanic spreading centers (White et al., 2006). Recent studies argue that magma production in volcanic arcs has possibly been underestimated, considering that crustal production in arcs occurs not only by extension but also by crustal thickening (Jicha & Jagoutz, 2015). Furthermore, mantle erosion at the base of the crust may remove parts of newly produced crust and hence mimicking a lower net production rate (Jicha & Jagoutz, 2015; Figure 6).

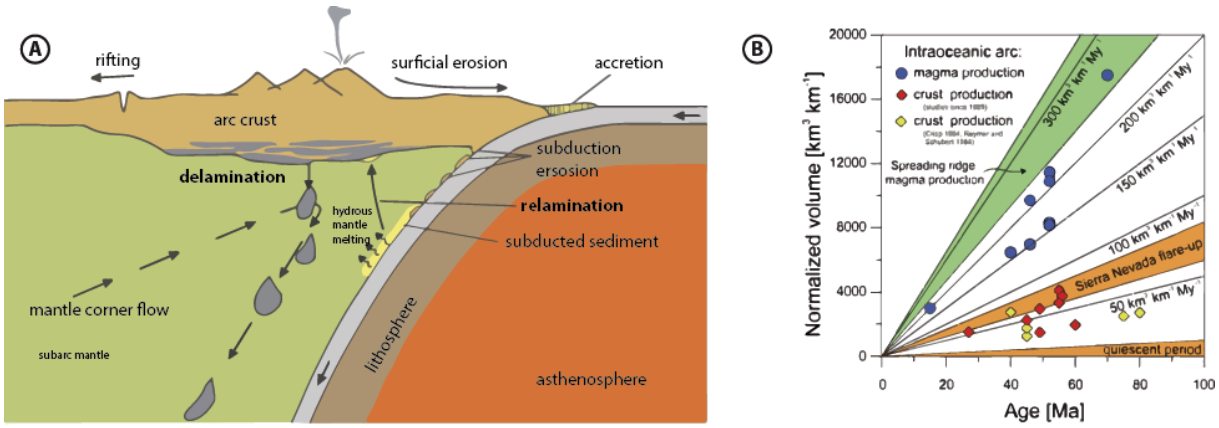

Figure 6: Crustal production in volcanic arcs. A: Schematic showing the balance of lamination and delamination processes exacerbating to estimate magma production (modified from Jicha & Jagoutz, 2015). B: Magma production estimates considering mantle erosion effects (from: Jicha and Jagoutz, 2015).

The incidence of active volcanoes at island arcs compares to the incidence of hydrothermal plumes along mid-oceanic ridges (Baker et al., 2004). Surveys along the Mariana and Kermadec arcs (e.g. de Ronde et al., 2003) indicate that on average two out of three to four volcanoes found along 100 km of island arc are active (Baker, 2017). Hydrothermal circulation systems associated with active volcanism in arcs are estimated to discharge about 10% of the fluids released along mid-oceanic ridges (Baker et al., 2008). These estimates suggest that arc hydrothermal systems may be more important for crust-ocean chemical and energy budgets than previously thought. In addition, these systems are typically shallower than those at mid-ocean ridges and may discharge highly acidic fluids with high metal concentrations, e.g. Fe (Resing et al., 2007; de Ronde et al., 2011; Hawkes et al., 2014), which can influence primary production in the overlying photic zone. This underlines the global importance of island arc hydrothermal systems.

The hydrothermal systems cooling island arcs are influenced by basement composition, phase separation, magmatic fluid influx and systematic permeability variations, which themselves can be attributed to lithological variabilities and structural faulting during caldera formation (e.g. Hedenquist & Lowenstern, 1994; de Ronde et al., 2005; Fouquet et al., 2018). Hydrodynamic models demonstrate that permeability variations at caldera ring faults may be responsible for hydrothermal vent fields at inner caldera walls and that episodic magmatic stages may account for temperature fluctuations and variable stages of phase separation of hydrothermal fluids (Gruen et al., 2012, 2014; Figure 7).

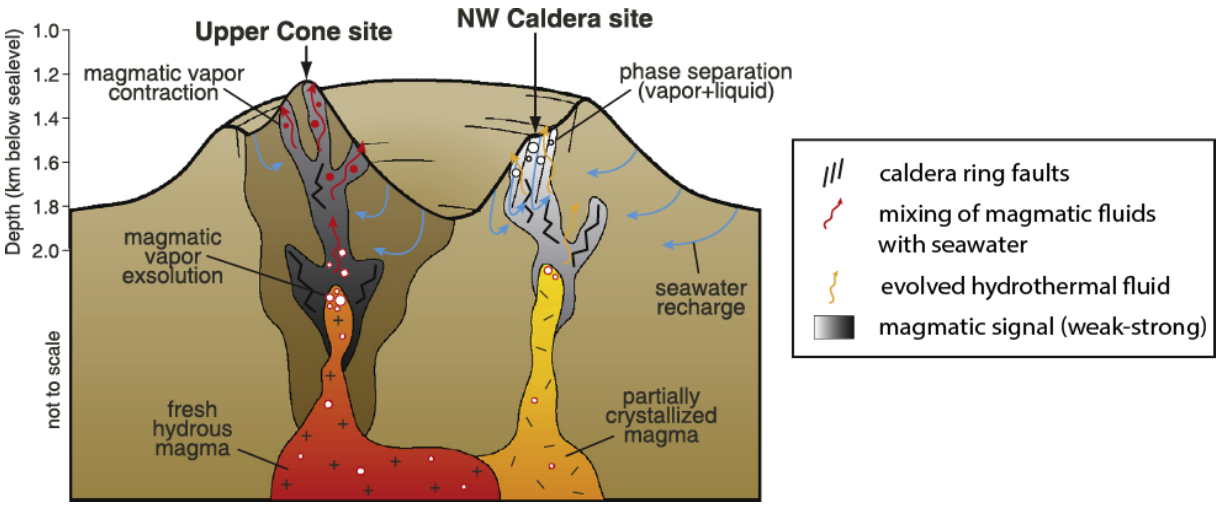

Figure 7: Conceptual model of Brothers Caldera as example for various influences on vent fluid compositions in arc hydrothermal systems (modified from Gruen et al., 2014; after de Ronde et al., 2005).

At shallow depths below the surface of arc volcanoes, the fluids undergo phase separation processes (e.g. de Ronde & Stucker, 2015), which affect salinities and hence the transport of metals from the volcanic basement to the seafloor, where they precipitate to form polymetallic sulfide deposits (e.g. Wright et al., 1998; Berkenbosch et al., 2012, 2015; de Ronde & Stucker, 2015; Fouquet et al., 2018). The fluid compositions are further affected by magma degassing: Magmatic fluids in island arcs are rich in SO_2 and HCl, which form strong mineral acids upon cooling and enhance the leaching of metals from rocks along the flow path of fluids (Gamo et al., 1997; de Ronde et al., 2005; Butterfield et al., 2011; Seewald et al., 2015). These magmatic fluids may also transport metals directly from the magma reservoir to the seafloor (e.g. Yang & Scott, 1996; Keith et al., 2018), very similar to the fumarole gases of White Island just south of our work area (Hedenquist et al., 1993).

1.3 The South Kermadec Arc

The Kermadec Arc is part of the Tonga-Kermadec Arc and is a classic example of an intraoceanic arc (Figure 8). It is situated on the Australian plate under which the about 80 Ma old Pacific plate is subducted with a convergence rate of between 40 mm a^{-1} in the south and 80 mm a^{-1} in the north (DeMets et al., 1994; 2010). The arc runs parallel to the Kermadec Trench at a distance of 150–200 km westwards and is decoupled from the Tonga Arc by a major transform fault at about 24° S, just north of the intersection of the Louisville Seamount Chain and the Kermadec Trench. The arc is the first expression of magmatic activity behind the Kermadec Trench and is separated from the Colville Arc by the Havre Through (e.g. Wright et al., 2006). In the southernmost part of the Kermadec Arc, the Hikurangi Plateau is subducted

and delivers additional sediment- and slab-derived volatiles to the arc magmatic systems (de Ronde et al., 2007, Timm et al., 2014). The South Kermadec Arc is particularly rich in hydrothermal activities. Based on plume surveys, seven active sites in the South Kermadec Arc are known (de Ronde et al., 2005) and at least nineteen active sites are found along the whole Kermadec Arc (de Ronde et al., 2007).

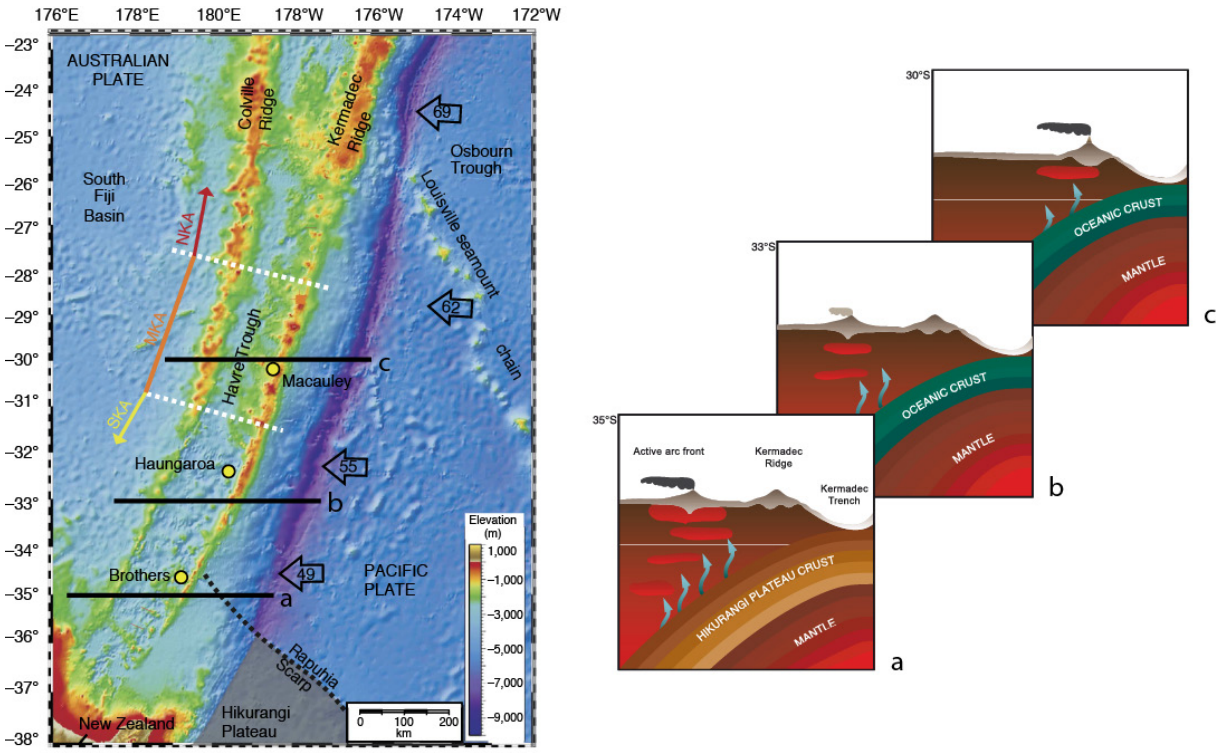

Figure 8: Overview map of the Kermadec Arc (modified after Timm et al., 2014) and conceptual model of variable subduction zone processes occurring from south to north (from de Ronde et al., 2007). The black lines mark the transects shown on the right-hand side. The Macauley, Haungaroa and Brothers volcanos were visited in the course of this study.

1.4 Motivation and Scientific Questions

Investigations on volcanic arc and back-arc high-temperature vent fluids reveal a particular high diversity of hydrothermal fluid types (de Ronde & Stucker, 2015) and several research projects have provided insights on the nature of acid sulfate type fluids (Reeves et al., 2011, Seewald et al., 2015). In spite of everything, the various controls leading to the high diversity of arc fluids, their consequences on subsurface mineralization and their overall impact on the chemical budget of the ocean remain poorly constrained.

The motivation for our fluid sampling program is the further characterization of different hydrothermal vent sites at the South Kermadec Arc. The combined studies of fluid compositions and mineralogical investigations in this thesis lead to an improved understanding about the roles of the different subsurface processes affecting hydrothermal circulation systems in intraoceanic arcs. The main question addressed in the curse of the studies are:

- **Which processes lead to the high diversity of arc hydrothermal fluids?**

- How do basement compositions and the extent of fluid-rock reactions affects the alteration of the heterogeneous island arc basement?
- What are the consequences for the formation of volcanogenic massive sulfides?

- How strong does magmatic degassing effect hydrothermal vent fluids in the south Kermadec?
- Which fluid-rock reactions occur under contribution of magmatically derived dissolved gases and how do they effect the element budget of hydrothermal circulation cells?

- Does the shallow seated arc crust effect the type of hydrothermal circulation systems?
- How strong is the impact of boiling and/or phase separation processes on vent fluid compositions?

2 Material and Methods

In this chapter, the analytical techniques used in the course of this thesis work are described. Section 2.1 provides a brief overview of the various methods used. In the following sections I provide some more detailed insights into the sampling procedure of hydrothermal vent fluids using isobaric gas-tight samplers (Section 2.2) and the quantification of volatile species in vent fluid samples by gas chromatography (Section 2.3). In Section 2.4 the preparational work and the analytical procedure to determine $^{87}Sr/^{86}Sr$ by thermal ionization mass spectrometry is given in more details. Finally, (in Section 2.5) the reconstruction of salinities and formation temperatures of hydrothermal fluids by microthermometric studies of fluid inclusions is outlined.

2.1 Overview of methods

In terms of hydrothermal vent fluid analyses, knowledge about the basic chemical composition is needed for all considerations about fluids. The major composition of fluids is typically measured by inductively coupled plasma-optical emission spectrometry (ICP-OES) analyses (cations) and by ion chromatography (IC) (anions).

During cruise SO253, a cooperation was established between the University of Bremen, the Jacobs University of Bremen and the GNS Science New Zealand. Analyses of cations were performed by the group of the Jacobs University in the Department of Physics and Earth Sciences and anion analyses were conducted by the GNS group in the New Zealand Geothermal Analytical Laboratory. The cooperation resulted in a submitted manuscript which is repeatedly referred to in the manuscripts of this thesis (Chapter 4-6) and included in the technical report of manuscripts (Chapter 3). Also, here is referred to this manuscript for details of the analyses.

During cruise TN350, I conducted analyses of major element concentrations. This requires preparatory work off-shore to get aliquots ready for later home-based analyses. In specific, fluid samples are filtered to prevent clogging of the ICP-OES nebulizer and are subsequently acidified with supra-pure HNO_3 to suppress the precipitation of oversaturated metals. For IC analytics samples remained untreated and all samples were stored in a refrigerator. The major compositional analyses for cruise TN350 were passed on to our experienced colleagues of the Department of Chemistry of the University of Bremen. The devices used for measurements were a Varian Vista Pro ICP-OES and a Metrohm Compact ion chromatograph.

The rock analyses I conducted comprised of detailed microscopic investigations of incipient volcanic rocks, pervasively altered rocks and sulfide-rich chimneys. Thin sections were prepared from a selection of samples recovered during expedition SO253. I prepared the

specimen in the rock preparation laboratories of the Department of Geosciences at the University of Bremen. During this time, I produced slices for thin section preparation and bulk rock powders of material adjacent to the thin section slices.

The powders were investigated in a cooperation with the Institute for Chemistry and Biology of the Marine Environment, ICBM at the University of Oldenburg by X-ray fluorescence analyses. For different sample types containing variable amounts of S, Ba, Cu and Zn, different preparatory techniques were applied to improve the fusion process of glass beads. First, 700 mg of all samples were mixed with 4.2 g of $Li_2B_4O_7$ and 1.0 g of $(NH_4)_2NO_3$ as oxidizing agent. After pre-oxidation at 500 °C, the samples were fused to borate glass beads at 1350 °C in platinum crucibles. For chimney samples in which considerable concentrations of Ba, Cu or Zn were expected the sample weight was adjusted to a tenth of the 700 mg, to maintain measured values inside the calibration range. For a subset of samples this dilution was not sufficient. These samples were mixed with 630 mg grinded and pre-combusted quartz. The measurements were performed on a wavelength-dispersive XRF spectrometer (Panalytical Axios Plus), calibrated with a total of n = 66 samples. Here, quality control was assured by repeated measurements of the international standard NOD-A-1 (U.S. Geological Survey, Flanagan & Gottfried, 1980), as well as two in-house standards (basalt and black shale). The precision of the measurements for major and trace elements exceeded 5% and 15%, respectively. Matrix effects and possible line overlaps were checked with artificial samples with high Ba or Zn content (pure $BaSO_4$, $ZnCl_2$, $C_4H_6O_4Zn$) and corrected when necessary. Sulfur was determined as total S via combustion analysis using an ELTRA CS Analyzer.

The thin sections were used for electron microprobe analyses (EMPA) of sub-microcrystalline groundmasses of altered rocks that could not be identified by microscopic investigations and further reliably identified sulfide minerals in chimneys. These analyses were performed in the laboratories of the Department of Geosciences of the University of Bremen. A CAMECA SX 100 microprobe was used to identify sulfide and sulfate minerals as well as fine-grained groundmasses of pervasively altered volcanics. Silicic groundmasses were microprobed with 15 nA beam current and an acceleration voltage of 15 kV. Sulfide assemblages were analyzed with 20 nA beam current and 20 kV acceleration voltage. The microprobe was calibrated using the standard material NMNH-111356 Hornblende Arenal. The reference materials chalcopyrite/sphalerite/arsenopyrite were measured in a daily fashion prior to sulfide measurements and reference materials olivine/plagioclase/microcline were measured prior to silicate measurements to provide a quality control of the results.

2.2 Work at sea: IGT sampling and gas chromatography of dissolved gases

My main tasks during the research expeditions were to deploy isobaric gas-tight samplers (IGT) (Seewald et al., 2002) and to analyze the volatile concentrations with gas chromatography aboard. Every expedition in which gas analytics at sea are planned, is a logistical challenge. The full equipment for the IGT sampling procedure and the spare parts and accessories necessary for aboard determination of volatiles are manifold and include gas flasks, with their corresponding pressure reducer to operate the gas chromatograph (GC), laboratory equipment for processing and storing high quality vent fluid samples, and electronic devices to evaluate and process temperature and gas chromatograph raw data.

Being responsible for the IGT samplers, the working day begins prior to any ROV dive planned to recover fluid samples. First, the samplers have to be assembled by positioning the pistons in their corresponding chambers. The assembler chambers are pre-charged with pressurized N_2 according to 10% of the seafloor pressure at which fluid samples will be recovered (Figure 9B). The temperature probes are attached to the sample inlet and tested for functionality. The main valve is electronically closed. Second, the internal communication line between the ROV container, over the ROV to the IGT's has to be assured. Now, the dive can start with the IGT's ready to be deployed.

During a ROV dive, IGT samplers are worth their weight in gold, making them first choice fluid sampling devices compared to other conventional samplers. The samplers are equipped with temperature probes that enable real time temperature readings during sampling of hydrothermal vent fluids and enable to execute the sampling in the optimal position, when the snorkel-inlets reach the most undiluted and high-temperature fluid. The temperature reading also improves the sampling when visibility is diminished due to black-smoke or dust clouds. Advantageous is the wireless communication system to start the sampling procedure. No extra handling with the manipulator arm is necessary. When the sampling procedure is initiated the sample valve opens and the sample chamber is filled by passive inflow of fluid due to the higher ambient pressure at the seafloor. Both pistons now move from the side of the sample inlet towards the side of the pre-charge valve and the sample chamber is filled with the vent fluid sample (Figure 9A). The flow is damped by the pre-charged pressure in the accumulator chamber and by the Visco Jet®. The Visco Jet® guarantees a constant inflow of fluid during the sampling interval and hence minimizes entrainment of ambient seawater. The sample valve closes automatically after 90 seconds of sampling interval, during which the temperature of the inflowing fluid is recorded alongside.

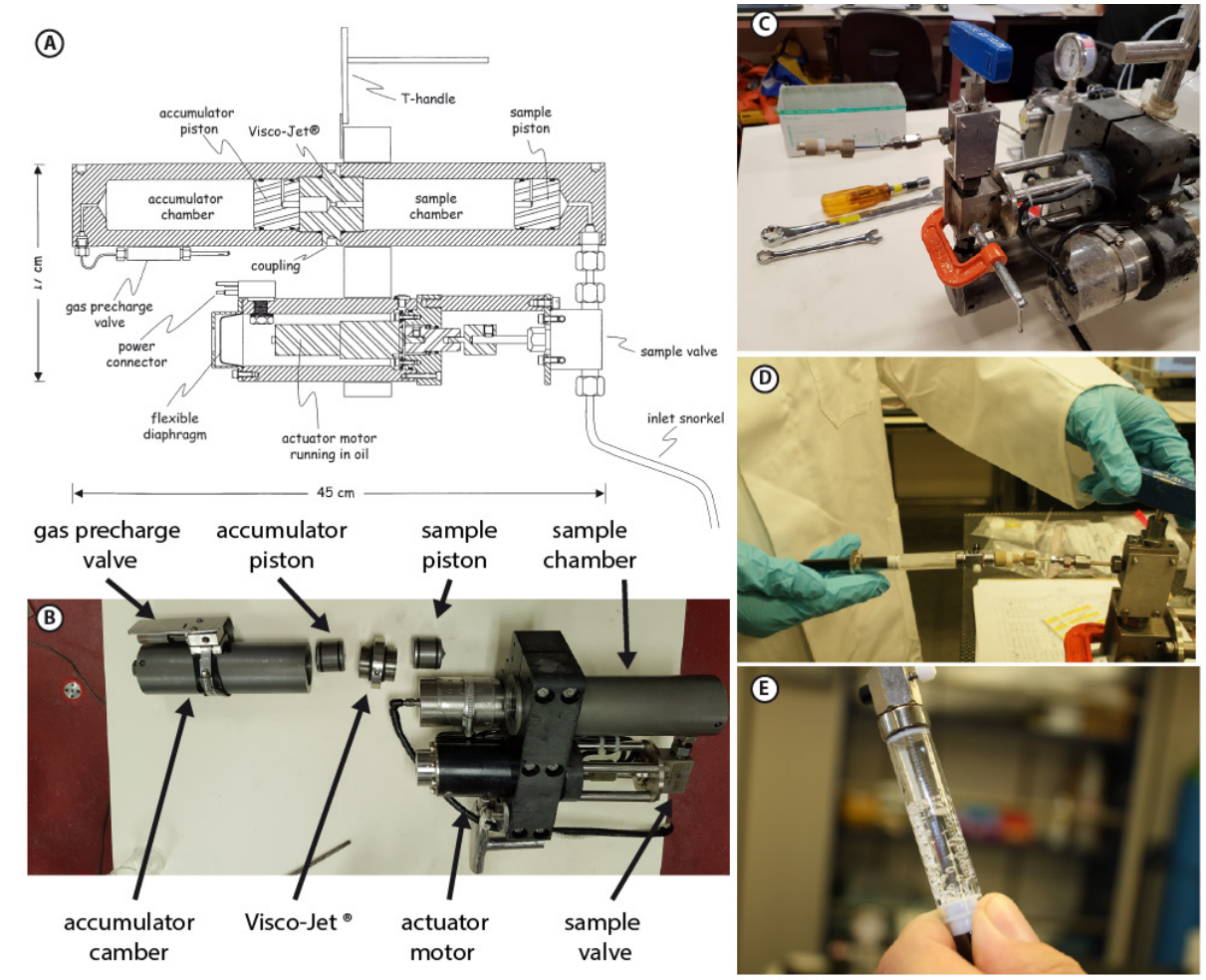

Figure 9: Sampling of hydrothermal fluids using IGT samplers. A: Schematic illustration of the sampler (from Seewald et al., 2002). B: Image of IGT sampler with its components highlighted. C: Setup of the sample-draw procedure. D: gas tight syringe connected to the sample-draw valve. E: Fizzing sample upon application of underinflation.

When the ROV dive comes to an end, the samplers can be picked up at the vehicle. In the laboratory the samples are now extracted. The specialty of the IGT sampler is that during the sample withdrawal, pressure can be applied to the accumulator chamber by pumping inside deionized water. To the sampler a sample-draw valve (Figure 9C), a Luer lock adapter and a gas tight syringes (Figure 9D) are sequentially connected. Fluid is released from the sampler by opening the sample-draw valve. Due to the pumping of deionized water inside the accumulator chamber the pressure in the sample chamber is even higher than at the seafloor. Therefore, instead of a pressure drop, when the sampled fluid exits the sampler, the pistons move from the accumulator side towards the sample side and the pressure is maintained (Figure 9A). In this way, subsamples are not affected by pressure release and contain the original gas concentration. Next, when passing the sample-draw valve, samples undergo a pressure drop and start to degas in the gas tight syringes (Figure 9D). The first visual analyses

show if the samples are volatile-rich or not. Applying underinflation to the gas tight syringe leads to extensive fizzing in the syringe comparable to a bottle of sparkling water and the sample separates into a gaseous and a liquid phase (Figure 9E).

The volume of the liquid is determined using the volume scale of the syringe. The gas phase is stepwise injected into the gas chromatograph using a 1 ml sample column. This procedure is followed by a headspace extraction method were 1 ml of carrier gas is brought in contact with the remaining liquid. Creating an underinflation by pulling the stamp of the syringe, volatiles are extracted from the liquid into the headspace. The procedure is repeated until the detected signal becomes neglectable compared to the signal of the prior injections. This procedure assures nearly complete removal of dissolved volatiles from the liquid fraction. The cumulative signal is referred to the fluid volume in the syringe, giving a quantitative assessment of the dissolved gases from the sample.

During the two expeditions two different gas chromatographs with the same setup were used (a 7820A Agilent during SO263 and a Thermo Scientific Trace GC Ultra during TN350). The GCs were equipped with a Molsieve 60/80 column (Sigma-Aldrich, St. Louis, MO) and used at 50 °C. A thermal conductivity detector and a flame ionization detector were aligned in a row enabling H_2 and CH_4 analyses. The devices were calibrated with reference gases of either 253 mol-ppm H_2 and 120 mol-ppm CH_4 in a N_2 matrix (during cruise SO253) or with a 1.02 mol% H_2 and a 0.987 mol% CH_4 in a N_2 matrix (during cruise TN350). For each sample multiple measurements (two or more) with different aliquots were conducted. The precision usually is better than 5%. The main error source is believed to be the volumetric estimate of the fluid subsamples.

The chromatographic analyses on board are necessary to determine hydrogen concentrations. Hydrogen molecules are so small that they can diffuse through almost any material. For this reason, hydrogen analyses have to be done immediately after sampling. Hydrogen is a key parameter in determining the redox-state in the subsurface and is the main reason for the on-board analytical procedure.

Generally, He is most convenient as carrier gas due to its viscosity, flow-properties and the fact that the thermal properties are distinct from most other gases. However, the thermal conductivity of H_2 is close to the thermal conductivity of He, which considerably lowers the detection limit and the precision for H_2 measurements. For this reason, N_2 was chosen as carrier gas.

Sample aliquots for determination of CO_2 concentrations were stored for later analyses onshore. The method used was adapted from Reeves et al. (2011). Pre-weighted, helium-filled, evacuated glass serum vials were used to avoid atmospheric CO_2 contamination. Samples were injected from the gas-tight syringes through the septa into the vials and were stored upside

down to seal the septa by the fluid and prevent diffusive gas loss. Prior to measurement 1-2 ml phosphoric acid (25 wt.%) was added to the samples to convert DIC species to CO_2. The gas chromatographs (again the 7820A Agilent for samples of cruise SO263 and the Thermo Scientific Trace GC Ultra for samples of TN350) were equipped with a Haysep 80/100 column (Sigma-Aldrich, St. Louis, MO) and operated with He as carrier gas at 50 °C. The GCs were calibrated with reference gas of pure CO_2 with 99.995 vol%. A control standard was created using $NaHCO_3$ solutions that were produced as samples and acidified in the serum vials. One control standard was measured prior to each sample block (6-8 samples). The accuracy of the measurements was within 10%.

2.3 $^{87}Sr/^{86}Sr$ TIMS analyses

I performed analyses of $^{87}Sr/^{86}Sr$ by thermal ionization mass spectrometry (TIMS) in the Isotope Geochemistry Laboratory at the Center for Marine Environmental Science (MARUM) at Bremen of University. To prepare samples for TIMS analysis of $^{87}Sr/^{86}Sr$ the Sr has to be extracted from the vent fluid aliquots containing various elements in different concentrations. This is done via a chromatographic column extraction procedure using a resin (Figure 10). The vent fluid samples were blend with dissolved 2 M supra-pure sub-boiled HNO_3 and evaporated at 120 °C. The residual solids were dissolved in 2 M HNO_3. This solution was centrifuged and pipetted out of the vials to assure removal of small amounts of solid phases. Meanwhile, a column is prepared by filling it with 70 µl of Sr_{Spec} resin and rinsing it with an amount of Milli-Q equal to four times the reservoir volume (method adapted from Deniel & Pin, 2001). The column then is conditioned by stepwise addition of a total of two reservoir volumes of 2 M HNO_3. The sample is now applied on the column in 200 µl steps. In contact with 2 M HNO_3 Sr_{Spec} holds the Sr in the column, while most other elements pass the column and are washed out. Next, the column is rinsed ten times with 100 µl of 2 M HNO_3 to get rid of most elements. After elution of unwanted matrix elements 200 µl of 0.05 M HNO_3 are added five times on the column to elute Sr (and Ba). The extracted samples are blend with 20 µl of H_3PO_4. When the sample is again evaporated, the H_3PO_4 forms a well visible solid which eases to carry on the loading of the samples on the specific filaments. The filaments are dabbed with 1,45 µl of Ta-emitter and dried using a current of approximately 1 A. The samples are again dissolved in H_3PO_4 and transferred on the filament which again is dried with a higher current of roughly 2 A till it starts glowing. The sample wheel which carries the filaments is now finally inserted into the thermal ionization mass spectrometer and after the vacuum is achieved, samples are ready to be measured. For the measurement I chose to use a static acquisition method and manually tuned the device centering peaks and adjusting the source lenses to control the ion beam.

Measurements were done with filament temperatures of 1350-1400 °C at 8-12 V and with intensities of 50 000 to 100 000 counts per second. One sample analysis comprises of 120 single measurements, which's average gives acceptable values of the internal precision monitored during the measurements. For the purpose of quality control, along with the samples also the NIST SRM 987 was measured, resulting in a value enclosed in the long-term variability of the laboratory and in accordance with literature data (GeoREM data base (Jochum et al., 2005), request September 2017). This indicates that the measurements were conducted successfully.

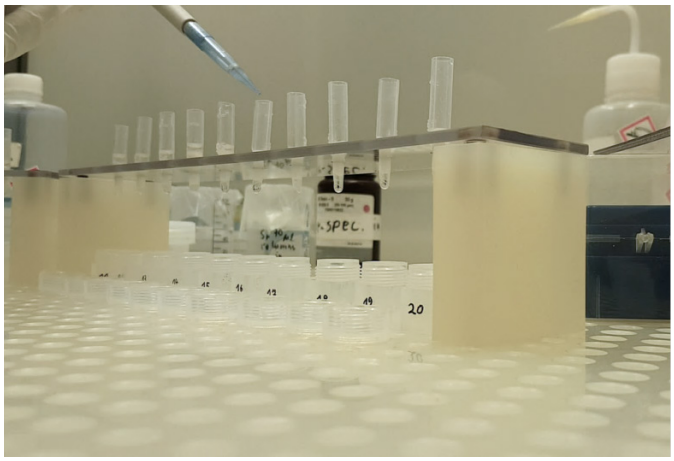

Figure 10:
Column extraction of Sr during TIMS preparation.

Beside the analyses of vent fluid aliquots, $^{87}Sr/^{86}Sr$ were also measured for bulk rock samples of incipient volcanic rocks, pervasively altered rocks, chimney samples and for sulfate crystal separates used in the fluid inclusion study. The procedure for the extraction of solid material is similar to that for fluid aliquots. However, the fact that these samples are solid phased and may contain considerable amounts of Ba requires two additional steps for the column extraction procedure to take place. The bulk-rock (solid) samples were first dissolved in a Matrix of concentrated HNO_3 cooked overnight, subsequently centrifuged to pipette the solution and evaporated, to then start the extraction procedure as mentioned above. An additional separation step of Ba had to be performed: After the sample was added on the column and rinsed with 2M HNO_3 the column was rinsed wit 7M HNO_3 to elute Ba, removing the element from the column before the sample was eluted with 0.05M HNO_3. Subsequent steps of the measurement were executed as mentioned above.

2.4 Microthermometric analyses of fluid inclusion

In the course of this study, I have realized an extensive fluid inclusion study on stockwork and chimney mineralization of Brothers NW Caldera Wall in the laboratories of the working group "Petrology of the Ocean crust" in the Department of Geosciences of the University of Bremen.

Sulfate crystals were extracted from chimney samples (Figure 11: A-B) and used to produce small crystal fragments for microthermometric analyses. The Linkam Stage is attached to a Zeiss Axioskope equipped with an objective providing a magnification of 100x and provides the opportunity to study µm sized fluid inclusions with quite good optical conditions (Figure 11C).

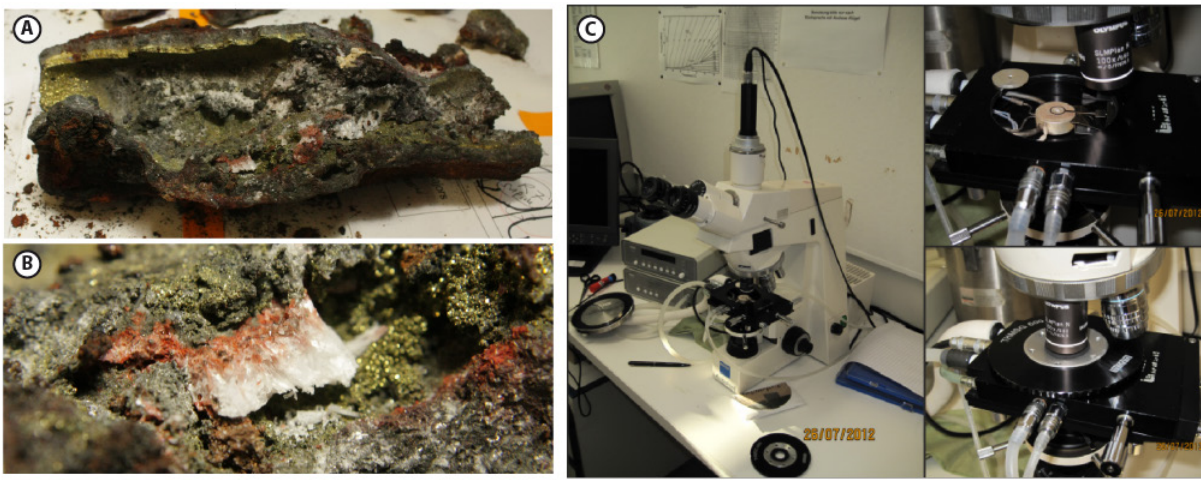

Figure 11: Conducting fluid inclusion analyses. A: Photograph of a chimney sample containing anhydrite; B: close up of coarse crystalline anhydrite crystals; C: photograph of Linkam stage attached to the Zeiss Axioskop with close ups of the opened and closed stage.

The heating and freezing stage is flooded with gaseous nitrogen and provides accurate temperature control to cool or heat fluid inclusions down to -100 °C or up to 500 °C. Sulfate minerals incorporate plenty of aqueous fluid inclusions composed of the hydrothermal fluid from which the minerals have grown. During freezing and heating these fluids undergo phase transitions that enable to reconstruct the salinity and the temperature of formation of this inclusion using thermodynamic constraints (Figure 12A). The freezing interval of an aqueous fluid is dependent on salinity. This knowledge can be used to measure the salinity of fluid inclusions by observing a frozen inclusion and heating it to room temperature. Figure 12B shows a fluid inclusion at room temperature, at low temperature after extensive cooling and during the process of re-heating. At very low temperature the change in appearance of the fluidal phase is subtle due to the formation of a vitreous solid. Approaching the eutectic temperature, the vitreous solid crystallizes to ice and hydrohalite. At the eutectic temperature, hydrohalite melts and euhedral water ice crystals and a saline liquid remain. On further heating, the water ice melts in a melting interval and dilutes the saline liquid until there is no ice left. The melting of the last ice in the inclusion marks the melting temperature with the defined salinity for this temperature. At higher temperatures aqueous fluids are two-phased; dependent

on the density of the inclusion either a gas-bubble in a liquid cavity or a liquid drop in a gassy cavity. Heating the fluid inclusion, at some point, the 2-phased system homogenizes. The homogenization temperature thereby is a function of the density of the system (the density of the systems does not change during the investigation or even after the original fluid has trapped in the inclusion). With this assumption and a known pressure of formation of the inclusion, one can reconstruct the temperature of formation by following the isochore from the point where the system left the 2-phase curve (the homogenization temperature with its corresponding homogenization pressure). This means that the melting- and homogenization temperature of a single inclusion allow to infer the salinity and the temperature of the hydrothermal fluid at a discrete time of crystal growth. Fluid inclusions may not only form during crystal growth but also due to formation of cracks upon applied stress in an already existing crystal. Pressure or temperature changes due to over- or under-pressure can result in the formation of so-called secondary inclusions that do not necessarily reflect the conditions of crystal growth. Fluid inclusion studies have to be accompanied by detailed petrographic investigations to assure that inclusions indeed represent what is intended to be investigated, the initial growth condition. Fluid inclusions may be classified in three groups (Figure 12C). Primary inclusions occur as single inclusions or small groups in a crystal that is free of other inclusions. They usually form as accidental events during crystal growth and are believed to represent crystal growth conditions. Secondary inclusions occur as trails of inclusions that cut crystal boundaries and are either aligned to cleavage directions or do not have a relation to the crystal faces. These inclusions must be handled with care and are believed to form after the original crystal growth (Figure 12B). Pseudosecondary inclusions follow crystal faces and are believed to form during rapid-growth events which result in a phase of skeletal growth. They likely represent the formation conditions of the crystal.

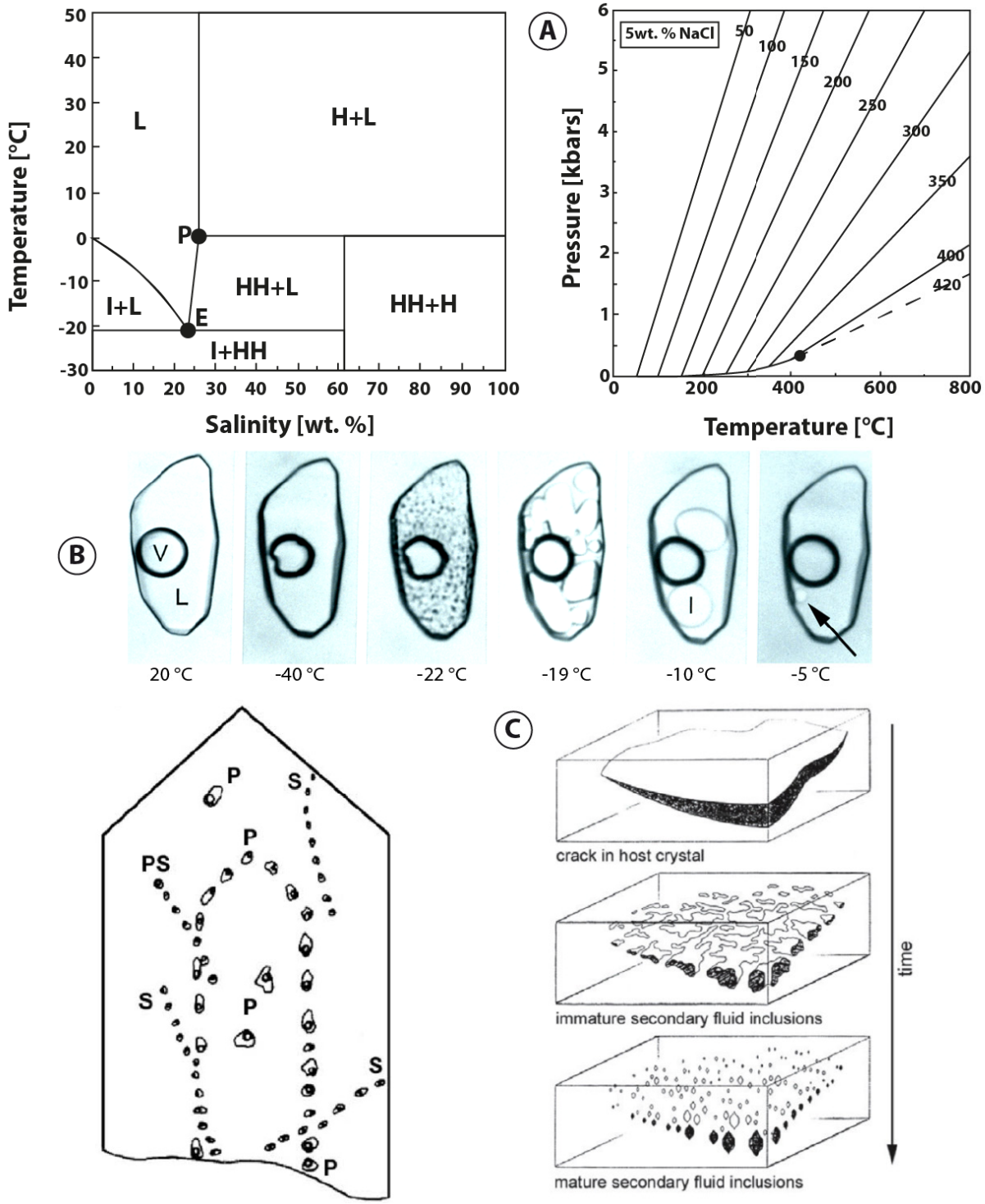

Figure 12: Classification of fluid inclusions and phase relations in the H_2O-NaCl system. A: Formation of secondary inclusions (from Hansteen & Klügel, 2008, after Roedder, 1984); B: petrographic classification of inclusions (from Hansteen & Klügel, 2008, after Shepered et al., 1985); C: heating and subsequent melting of a H_2O-NaCl inclusions (modified after Bodnar, 2003); D: vapor saturated phase relations for the H_2O-NaCl system (from Bodnar & Vityk, 1994).

3 Contribution to Scientific Journals

In this chapter, I summarize the publications and manuscripts I recorded in the scope of this thesis or to which I have contributed significant intellectual input during the PhD period.

3.1 First author manuscripts

I have produced the following three manuscripts in the scope of this thesis work as first author. They are printed in full text in Chapter 4 to 6.

Manuscript 1 (Chapter 4):

High-temperature fluid-rock interactions in the South Kermadec Arc: How volcanic volatiles and host rock compositions influence hydrothermal mineralization

Alexander Diehl[1,2], René Neuholz[3], Bernhard Schnetger[3], Friedrich Lucassen[2], Wolfgang Bach[1,2]

[1] Department of Geosciences, University of Bremen, Bremen, Germany

[2] MARUM Center for Marine Environmental Sciences, Bremen, Germany

[3] Institute for Chemistry and Biology of the Marine Environment, Oldenburg, Germany

Manuscript in preparation

The manuscript presents a comprehensive analysis of incipient and pervasively altered volcanic rocks as well as hydrothermal precipitates recovered during Sonne expedition SO253. I carried out microscopic investigations and electron microprobe analyses in our laboratories in the Department of Geoscience at the University of Bremen. I conducted geochemical analyses of strontium isotopes at MARUM (University of Bremen) with the support of Friedrich Lucassen. In a cooperational project, René Neuholz and Bernhard Schnetger of the University of Oldenburg performed XRF bulk rock analyses. I used the resulting data to run thermodynamical reaction path models to predict subsurface mineral reactions of seawater-dominated and magmatic-volatile dominated hydrothermal fluids. The subsurface reactions are linked to processes of sulfide formation in volcanogenic massive sulfide deposits in volcanic arcs. Further, the data attest the impact of volcanic gases on hydrothermal systems by profoundly changing mineral stability fields during alteration. Besides providing new data for island arc rocks and sulfide deposits, the data provide new insights into the genesis of sulfide deposits in island arcs by evaluating mixing regimes in chimneys and investigating mineral stabilities during mixing of hydrothermal fluids and seawater.

Manuscript 2 (Chapter 5):

Hydrothermal fluids in the South Kermadec Arc indicate various subsurface processes: The role of magmatic volatiles, phase separation processes and subsurface mineral reactions.

Alexander Diehl[1,2], Friedrich Lucassen[2], Charlotte Kleint[2,3], Andrea Koschinski[2,3], Harald Strauss[4], Valerie Stucker[5], Cornel de Ronde[5], Jeffrey Seewald[6], Susan Humphris[6], Wolfgang Bach[1,2]

[1] Department of Geosciences, University of Bremen, Bremen, Germany

[2] MARUM Center for Marine Environmental Sciences, Bremen, Germany

[3] Department of Physics and Earth Sciences, Jacobs University Bremen, Germany

[4] Institut für Geologie und Paläontologie, Universität Münster, Germany

[5] GNS Science, Avalon, New Zealand

[6] Woods Hole Oceanographic Institution, Woods Hole, USA

Manuscript in preparation

The manuscript results from the versatile cooperational work between the University of Bremen, the Jacobs University of Bremen, the University of Münster, the GNS science New Zealand and the Woods Hole Oceanographic Institution. The manuscript introduces a merged dataset of isobaric gas-tight fluid samples from two seagoing expeditions (SO253 and TN350). I analyzed the fluid samples for their volatile compositions and determined Sr isotope analyses for all samples and conducted the major composition analyses of samples from the expedition TN350. These data are merged with the compositional data of Kleint et al. (submitted to GCA, c.f. 3.2) and evaluated together. The hydrothermal systems of the southern Kermadec Arc are influenced by degassing of magmatic volatiles but at the same time phase separation processes are likely to occur. Major elements are influenced by these processes as well as by subsurface mineral reactions. The approach of combining major element data with investigations of dissolved gases was especially useful. REE speciation calculations demonstrate different behavior of REE in seawater-dominated and acid sulfate fluids. The work could shed new light on the extent of magmatic volatile addition and the role of phase separation in the South Kermadec Arc. The manuscript shows that the classical distinction of magmatic-volatile dominated fluids vs. seawater-dominated fluids should be revised, as boundaries between the two do not exist. We found extreme gas contributions for seawater-dominated hydrothermal systems at Haungaroa Volcano and subtle volatile contributions from the acid-sulfate type fluids at Brothers Cones and NW Caldera Wall vent fields.

Manuscript 3 (Chapter 6):

Fluid inclusions in hydrothermal precipitates from the North West Caldera Wall hydrothermal vent field at Brothers volcano indicate subcritical and supercritical phase separation is involved in the formation of chimneys and stockwork zones.

Alexander Diehl[1,2], Wolfgang Bach[1,2]

[1] Department of Geosciences, University of Bremen, Bremen, Germany

[2] MARUM Center for Marine Environmental Sciences, Bremen, Germany

Manuscript in preparation

The third manuscript of this thesis deals with a fluid inclusion investigation in the Brothers NW Caldera vent field. My investigations on fluid inclusions reveals the paleo conditions of hydrothermal systems in terms of temperature and salinity variations. This study clearly demonstrates the importance of phase separation processes in seawater dominated systems of volcanic arcs. The investigation of fluid inclusions was combined with analyses of strontium isotopes, which I performed, as well as state of the art fluid mixing calculations. This manuscript demonstrates that not only boiling accounts for fluid compositions in the North West Caldera Wall vent field, but also that supercritical phase separation may be occurring deep underneath Brothers Caldera.

3.2 Further contributions

During my thesis I have participated on several side projects that lead to successful publications or have been submitted.

Geochemical characterization of highly diverse hydrothermal fluids from volcanic vent systems of the Kermadec intraoceanic arc

Charlotte Kleint *[,1,2], Wolfgang Bach[2,3], Alexander Diehl[2,3], Nico Fröhberg[1], Dieter Garbe-Schönberg[4], Jan F. Hartmann[1,5], Cornel E.J. de Ronde[6], Sylvia G. Sander[7,8], Harald Strauss[9], Valerie K. Stucker[6], Janis Thal[2,3], Rebecca Zitoun[7] and Andrea Koschinsky[1,2]

[1] Department of Physics and Earth Sciences, Jacobs University Bremen, Bremen, Germany

[2] MARUM Center for Marine Environmental Sciences, Bremen, Germany

[3] Department of Geosciences, University of Bremen, Bremen, Germany

[4] Institute of Geosciences, Christian-Albrechts-University Kiel, Kiel, Germany

[5] Institute of Earth Sciences, Heidelberg University, Heidelberg, Germany

[6] Department of Marine Sciences, GNS Science, Lower Hutt, New Zealand

[7] Department of Chemistry, University of Otago, Dunedin, New Zealand

[8] Marine Environmental Studies Laboratory, International Atomic Energy Agency - Nuclear Applications, Monaco, Principality of Monaco

[9] Department for Geology and Palaeontology, University of Münster, Münster, Germany

Submitted in Geochimica et Cosmochimica Acta

The submitted article is product of a similar cooperational project as the one of manuscript 2 presented in Chapter 4. It provides a basis to manuscript 2 and is therefore often referred to. I contributed to this article by using the IGT samplers, thus supplying a part of the samples and by providing temperature data of the vent fluids sampled. In addition, I contributed by editing the manuscript. The article exhibits the vent sites of our study area and presents major and REE element compositions of a comprehensive vent fluid collection of KIPS, major sampler and IGT fluids samples collected during Sonne cruise SO253. The article demonstrates the chemical diversity of vent fluids in the South Kermadec Arc and evaluates the subsurface processes that can be inferred from these vent fluid compositions.

Constraints on Cooling of the Lower Ocean Crust from Epidote Veins in the Wadi Gideah Section, Oman Ophiolite

B. Bieseler[1], A. Diehl[1,2], N. Jöns[1,2,3], F. Lucassen[1,2], and W. Bach[1,2]

[1] Department of Geosciences, University of Bremen, Bremen, Germany

[2] MARUM Center for Marine Environmental Sciences, Bremen, Germany

[3] Now at the Department of Geosciences, Ruhr-University Bochum, Bochum, Germany

Bieseler, B., Diehl, A., Jöns, N., Lucassen, F., and Bach, W. (2018). Constraints on Cooling of the Lower Ocean Crust from Epidote Veins in the Wadi Gideah Section, Oman Ophiolite. Geochemistry, Geophysics, Geosystems, 19(11):4195–4217. doi: 10.1029/2018GC007679.

Published in Geochemistry, Geophysics, Geosystems

The article presents geochemical data and fluid inclusion analyses of epidote vein samples in the lower ocean crust of Wadi Gideah, Oman. I conducted the fluid inclusion study and developed numerical models of conductive heat transport in solids. I have compared the

temperature data of the fluid inclusion study with state-of-the-art thermal models. The findings showed that the epidote veins are formed in the downwelling limb of a hydrothermal circulation systems. The thermal constraints on the epidote veins imply wide consequences for the evaluation of hydrothermal cooling in newly formed ocean crust.

Geothermal heat flux in the Amundsen Sea sector of West Antarctica: new insights from temperature measurements, Depth to the Bottom of the Magnetic Source estimation and thermal modelling

Ricarda Dziadek[1], Karsten Gohl[1], Alexander Diehl[2] and Norbert Kaul[2]

[1] Alfred Wegener Institute - Helmholtz Centre for Polar and Marine Research, Am Alten Hafen 26, 27568 Bremerhaven, Germany

[2] Department of Geosciences, University of Bremen, Bremen, Germany

Dziadek, R., Gohl, K., Diehl, A., and Kaul, N. (2017). Geothermal heat flux in the Amundsen Sea sector of West Antarctica: New insights from temperature measurements, depth to the bottom of the magnetic source estimation, and thermal modeling. Geochemistry, Geophysics, Geosystems, 18(7):2657–2672. doi: 10.1002/2016GC006755.

Published in Geochemistry, Geophysics, Geosystems

In the preparation of this article, I have developed a numerical model that provided the basis to calculate the geothermal heat flux of the Amundsen Sea embayment. Data for the magnetic basement depth were used in a 3-dimensional conductive model to constrain the geothermal heat flux in the area. The data were compared to heat flow measurement and provide insights into processes that potentially lead to the retreat of Antarctic ice sheets and provide an important constraint to ice sheets stability due to basal melting near the coast of the Antarctic continent.

4 High-temperature fluid-rock interactions in the South Kermadec Arc: How volcanic volatiles and host rock compositions influence hydrothermal mineralization

Alexander Diehl[1,2], René Neuholz[3], Bernhard Schnetger[3], Friedrich Lucassen[2], Wolfgang Bach[1,2]

[1] Department of Geosciences, University of Bremen, Bremen, Germany
[2] MARUM Center for Marine Environmental Sciences, Bremen, Germany
[3] Institute for Chemistry and Biology of the Marine Environment, Oldenburg, Germany

Abstract

Volcanic arcs represent an important component of the ocean-lithosphere interface in terms of energetic and chemical exchange between the solid earth and the ocean. The global length of predominantly submarine intraoceanic volcanic arcs comprises about 10% of the length of mid-oceanic ridges. The high incidence of active volcanoes and hydrothermal plumes along intraoceanic arcs suggests that their chemical and energetic turnovers, normalized per length, are comparable to the well-known turnovers of mid-oceanic ridges. Complex magmatic processes within the arcs' volcanic edifices lead to a diversity of hydrothermal systems that cannot be found at mid-oceanic ridges. Hydrothermal circulation systems form the interface between the ocean and the lithosphere and are here influenced by various processes, reaching from phase separation in shallow seated hydrothermal systems, over addition of significant amounts of volatiles from highly differentiated magmas, to fluid-rock interactions in an inhomogeneous basement. Ultimately, these processes form the basis for polymetallic sulfide deposits in the shallow arc crust.

We present chemical data and mineralogical investigations on pristine volcanics, pervasively altered rocks and hydrothermal mineralization from the South Kermadec Arc. Our investigations reveal three types of subsurface alteration assemblages: a quartz + illite + smectite assemblage (argillic alteration); a chlorite + smectite + illite assemblage (propylitic alteration); and a quartz + alunite assemblage (advanced argillic alteration). Reaction path models were developed to recreate subsurface fluid-rock interactions and to assess processes responsible for subsurface alteration patterns that generate hydrothermal fluids. The models suggest that argillic assemblages formed at low degrees of alteration (lower water-to-rock ratios) relative to propylitic assemblages. The modification of host rocks to alunite-quartz

(advanced argillic alteration) occurs when magmatic volatiles (SO_2 and CO_2) are involved in fluid-rock interactions.

We identified three types of hydrothermal mineralization: a Fe-Cu-rich mineralization with abundant chalcopyrite or tennantite; a Zn-Fe-rich mineralization dominated by sphalerite; and a Fe-dominated type with abundant pyrite and pyrrhotite. In a second set of reaction path models, hydrothermal fluids produced in the reaction paths were mixed with seawater to reproduce seafloor mineralization processes. The different hydrothermal fluids created during variable extent of subsurface fluid-rock interaction may account for two of the mineralization types found. Fluids originating from low water-to-rock ratios give rise to extensive sphalerite precipitation, whereas fluids generated at higher water-to-rock ratios produce Cu-bearing sulfide. The models suggest that different mineralization types are coupled to different degrees of subsurface fluid-rock interaction.

4.1 Introduction

4.1.1 Volcanic activities and hydrothermal circulation in volcanic arcs

After mid-oceanic ridges, volcanoes in volcanic arcs (island arcs and intraoceanic arcs) are the most magmatically active places in the ocean. Globally, volcanic arcs stretch over more than 22 000 km, corresponding to roughly one third of the 67 000 km of oceanic spreading ridges (de Ronde et al., 2003; Bird, 2003). About 7000 km are predominantly submarine intraoceanic arcs such as Tonga-Kermadec and Izu-Bonin-Mariana (Baker et al., 2008). Magma production rates in island arcs and intraoceanic arcs were believed to be low compared to those along oceanic spreading centers (White et al., 2006). Recently, Jicha and Jagoutz (2015) argued that magma production in volcanic arcs has possibly been underestimated since crustal production in arcs occurs not only by extension but also by crustal thickening. At the same time, mantle erosion at the base of the crust removes parts of the produced crust. The incidence of active volcanoes at island arcs is similar to that of hydrothermal plumes along mid-oceanic ridges (Baker et al., 2004). Surveys along the Mariana and Kermadec arcs (e.g. de Ronde et al., 2003) indicate that on average two out of three to four volcanoes found along 100 km of island arc are active (Baker, 2017). Hydrothermal circulation systems associated with active volcanism in island arcs are estimated to discharge about 10% of the fluids released along mid-oceanic ridges (Baker et al., 2008). These estimates suggest that island arc hydrothermal systems may be more important for crust-ocean chemical and energy budgets than previously thought. In addition, these systems are typically shallower than those at mid-ocean ridges and may discharge highly acidic fluids with high metal concentrations, e.g. Fe (de Ronde et al., 2011; Hawkes et al., 2014;

Resing et al., 2007), which can influence primary production in the overlying photic zone. This underlines the global importance of island arc hydrothermal systems.

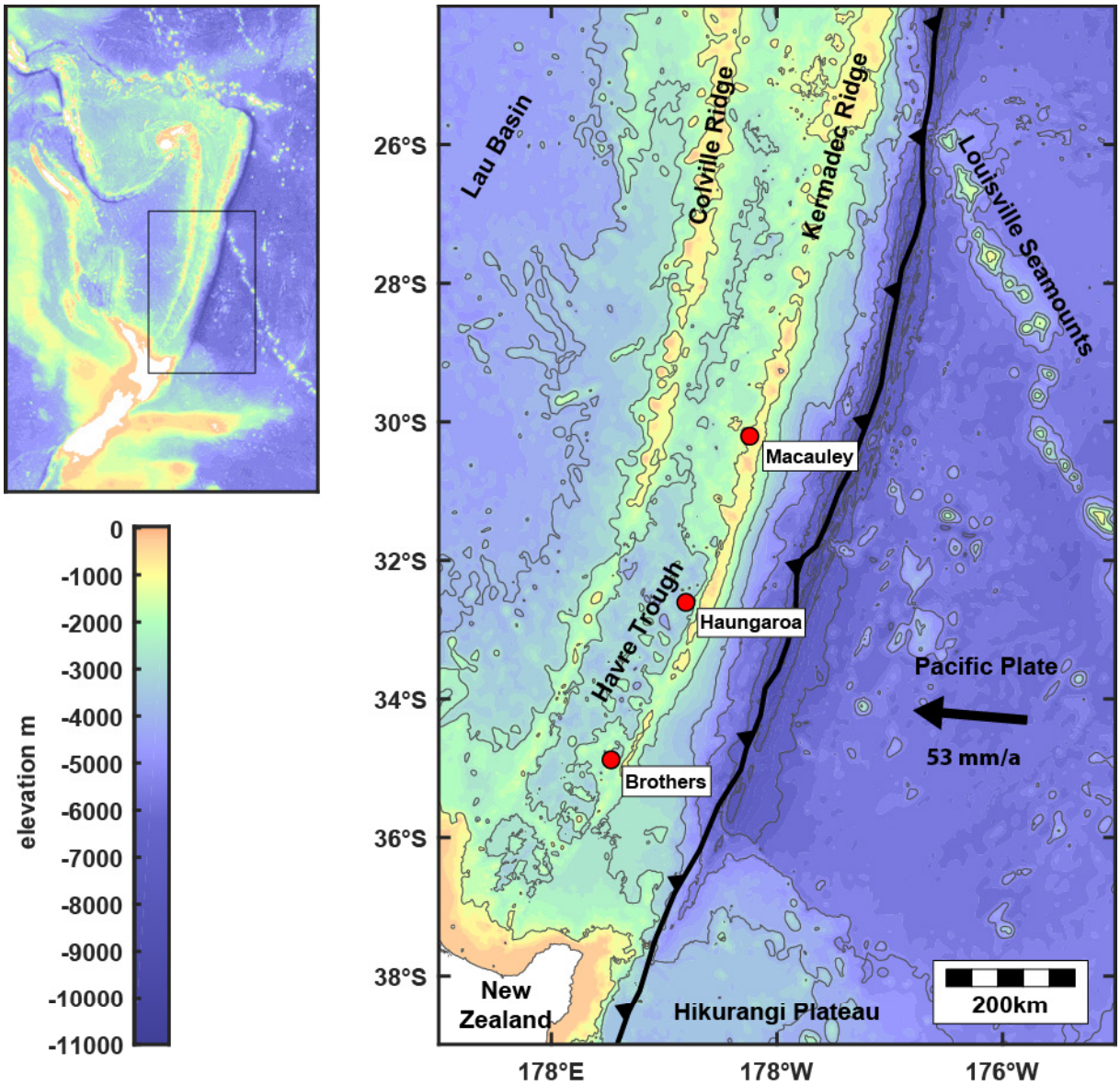

Figure 4.1: Bathymetric Map of the Kermadec Island Arc and volcanos visited during study (Relative plate motion is from DeMets et al., 2010; the plate boundary is from Bird, 2003; bathymetry data: GEBCO 2014).

Magma in volcanic arcs is produced by flux-induced melting of the mantle and is enriched in volatiles, as well as fluid-mobile elements derived from the subducting slab (Planck & Langmuir, 1993; Haase et al., 2002; Wysoczanski et al., 2006). The magmas intrude into thick (up to 35 km) island arc crust and are subject to differentiation prior to eruption (Haase et al., 2006; Smith et al., 2010). Volcanoes in island arcs may also be influenced by partial melting and assimilation of lower crust (Smith et al., 2006). The products of these diverse processes of magmatic differentiation range from primitive basalts to highly differentiated rhyolites. Consequently, island arc crust is built of rocks with highly variable compositions (Graham et

al., 2008). Volcanoes in island arcs are formed by eruption mechanisms that are very different from lava flows at mid-ocean ridges. Eruption types of volcanoes differ depending on water depth (Wright et al., 2002; 2006). The majority of these volcanoes build caldera volcanoes instead of cones and host hydrothermal systems that are influenced by basement composition, phase separation, magmatic fluid influx and systematic permeability variations, which themselves can be attributed to lithological variabilities and structural faulting during caldera formation (e.g. Hedenquist & Lowenstern, 1994; de Ronde et al., 2005). Hydrodynamical models demonstrate that permeability variations at caldera ring faults may be responsible for hydrothermal vent fields at inner caldera walls and that episodic magmatic stages may account for temperature fluctuations and variable stages of phase separation of hydrothermal fluids (Gruen et al., 2012).

At shallow depths below the surface of island arc volcanoes, the fluids undergo phase separation processes (e.g. de Ronde & Stucker, 2015), which affect salinities and hence the transport of metals from the volcanic basement to the seafloor, where they precipitate to form polymetallic sulfide deposits (e.g. Wright et al., 1998; Berkenbosch et al., 2012, 2015; de Ronde & Stucker, 2015; Fouquet et al., 2018). The fluid compositions are further affected by magma degassing. Magmatic fluids in island arcs are rich in SO_2 and HCl, which form strong mineral acids upon cooling and enhance the leaching of metals from rocks along the flow path of fluids (Gamo et al., 1997; de Ronde et al., 2005; Butterfield et al., 2011; Seewald et al., 2015). These magmatic fluids may also transport metals directly from the magma reservoir to the seafloor (e.g. Yang and Scott, 1996; Keith et al., 2018), very similar to the fumarole gases of White Island just south of our work area (Hedenquist et al., 1993).

The South Kermadec Arc is particularly active hydrothermally. Based on plume surveys, seven active sites in the South Kermadec Arc are known (de Ronde et al., 2005). Discrete vent fluid samples were first obtained from the prominent Brothers Volcano (de Ronde et al., 2011) and more recently also Macauley Caldera and Haungaroa Volcano were sampled (Kleint et al., submitted to GCA to GCA).

In this study, we report new geochemical and mineralogical data, as well as Sr isotopes of fresh and altered volcanic rocks and various polymetallic sulfide accumulations from the southern Kermadec Arc. The hydrothermal systems from which these samples were collected have been shown to be geochemically highly diverse, which may reflect different basement compositions as well as variable extents of magmatic volatile influx and phase separation (de Ronde et al., 2011; Kleint et al., submitted to GCA). We have recently shown that phase separation is indeed common in the hydrothermal systems hosted by Brothers Volcano, which is our main study site (Diehl et al., in prep, Chapter 6). We combine compositional data from rocks with geochemical modeling to assess the roles of magmatic volatile influx and subseafloor mixing of vent fluids

with entrained seawater in affecting both the type of basement alteration and the assemblages of polymetallic sulfide accumulations.

4.1.2 The South Kermadec Arc

The South Kermadec Arc is part of the Tonga-Kermadec Arc and a classic example of an intraoceanic arc (Figure 4.1). It is situated on the Australian plate under which the about 80 Ma old Pacific plate is subducted with a convergence rate between 40 mm a^{-1} in the south and 80 mm a^{-1} in the north (DeMets et al., 1994; 2010). The arc runs parallel to the Kermadec Trench at a distance of 150–200 km westwards. The Kermadec Arc is decoupled from the Tonga Arc by a major transform fault at about 24° S, just north of the intersection of the Louisville Seamount Chain and the Kermadec Trench. The arc is the first expression of magmatic activity behind the Kermadec Trench and is separated from the Colville Arc by the Havre Through (e.g. Wright et al., 2006). In the southernmost part of the Kermadec Arc, the Hikurangi Plateau is subducted and delivers additional sediment and slab-derived volatiles to the arc magmatic systems (Timm et al., 2014).

4.1.3 Macauley Caldera

Macauley Caldera is situated at 30° 12' S in the central part of the Kermadec Arc (Figure 4.1- 2). The caldera is part of a large volcanic edifice with a diameter of 35 km, crowned by Macauley Island 5 km south easterly of the caldera. The caldera, with the caldera floor at 850 m water depth, has a size of approximately 10 × 7.5 km and is elongated in east north-easterly, west south-westerly direction. A detailed morphological description is found in Wright et al. (2006). The caldera has formed about 6200 years ago during the Sandy Bay tephra eruption (Lloyd et al., 1996). While the entire volcano is mainly composed of basaltic rocks (Lloyd et al., 1996), the caldera itself consists of rocks with dacitic to rhyolitic compositions. The slope of the southeastern caldera wall is intruded by a young satellite cone that is composed of dacites (cf. Section 4.3, and Wright et al., 2006) and which is probably the youngest eruption product of the volcanic system. The volcanic cone rises 700 m up from the caldera floor up to < 300 m water depth. Its central crater is about 100 m in diameter and features hydrothermal venting from a prominent sulfur mound on the crater floor. The vents exhale low-pH (< 1.5) and intermediate temperature (~110 °C) white smoker acid-sulfate type fluids (Kleint et al., submitted to GCA) that precipitate native sulfur and alter host rocks to alunite-quartz assemblages (cf., Section 4.3). This alteration type is denoted as advanced argillic alteration (Reed, 1997).

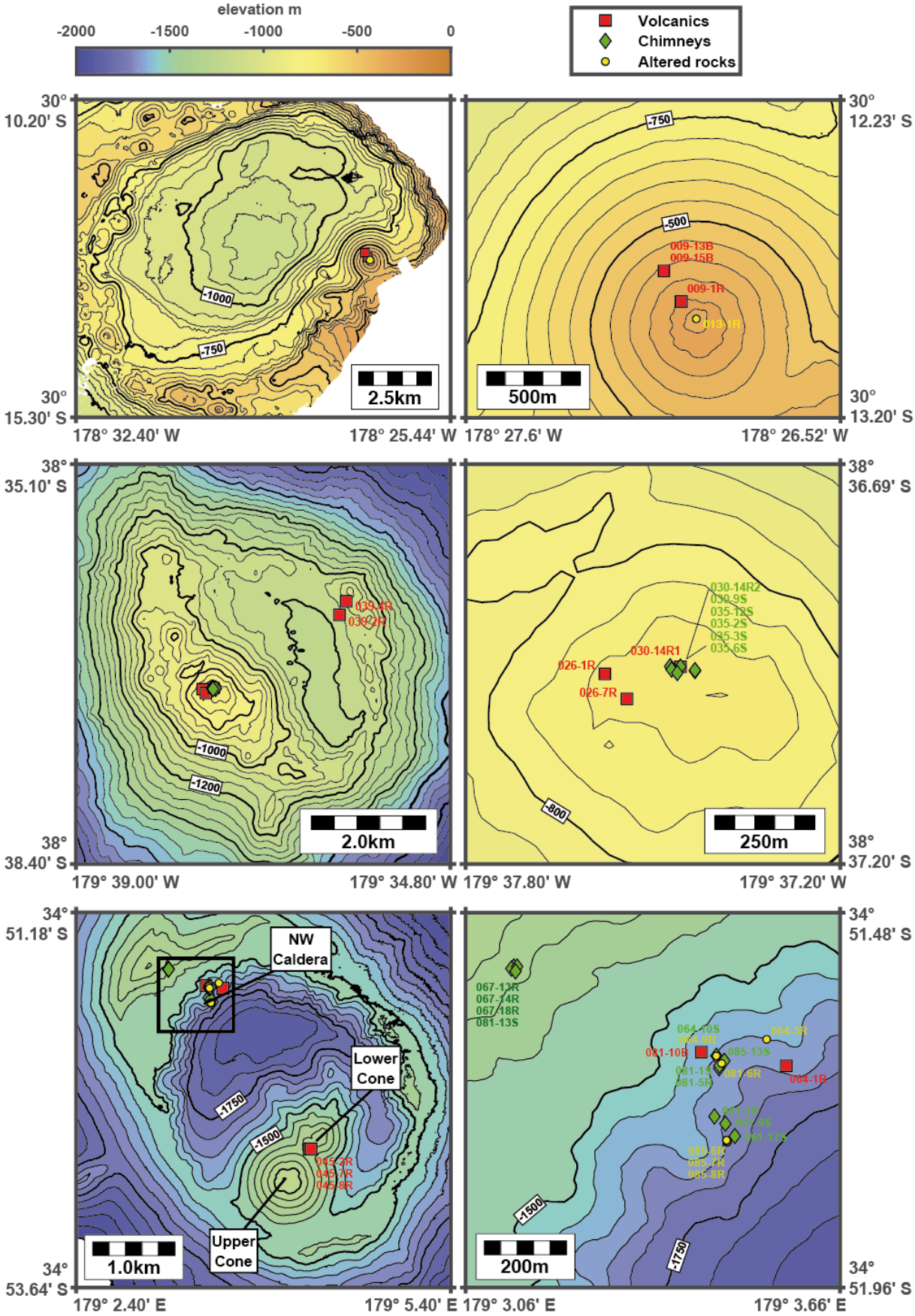

Figure 4.2: Bathymetric maps of working areas and sample locations of this study. Top: Macauley Caldera; Center: Haungaroa Volcano; Bottom: Brothers Caldera (data: Sonne cruise SO253 MBES, Koschinsky et al., 2018).

4.1.4 Haungaroa Volcano

The stratovolcano Haungaroa is situated at 32° 36' S on the Kermadec Arc, about 25 km west of the main ridge (Figure 4.1-2). The edifice has a basal diameter of about 25 km and an elevation that varies between 1900 m in the east and 2600 m in the west (towards the Kermadec Ridge or the Havre Trough, respectively). Analyses of volcanic rocks (Wright et al., 2006; Section 4.3) suggest that the volcano mainly comprises andesitic basalts and was created by a rather juvenile magmatic system lacking intensive differentiation processes. The summit of the volcano is marked by a caldera with a diameter of 3 × 4 km. The southwestern part of the crater wall has probably been subject to the most recent magmatic activities. It is cone shaped suggesting intrusion of melts in an already existing crater wall. Here, the crater wall extends to shallowest water depths (700 m) and hosts a vent site that emanates black smoker type high-temperature fluids with 270 °C (Kleint et al., submitted to GCA; Diehl et al., in prep., Chapter 5). The vent site is characterized by chimneys that comprise Ba-Zn-rich polymetallic sulfides.

4.1.5 Brothers Caldera

Brothers Caldera is situated at 34° 52' S on the Kermadec Arc, about 25 km west the main ridge structure (Figure 4.1-2). The base of the volcano in which the caldera occurs is at about 2300 m water depth and the volcano, with a basal diameter of about 25 km, reaches 1300 m water depth at its shallowest levels. Brothers Caldera is one of several calderas that occur within the volcanic edifice. The northwest-south-east elongated 3.5 × 3 km wide caldera is found in the north eastern part of the edifice. The deepest point in the caldera, 1850 m water depth, is located in the northern part. The central and southern parts are more elevated due to intrusion of two satellite cones, the Upper and Lower Cone. The shallowest parts of Brothers Caldera are the Upper Cone that is shallower than 1250 m, followed by the North West Caldera Wall rim with 1300 m water depth (Dziak et al., 2008; Baker et al., 2012; Embley et al., 2012).

Volcanic rocks at Brothers Caldera comprise dacitic to rhyolitic compositions with high contents of alkalis (especially potassium), so that single bulk rock compositions show almost trachydacitic composition (Berkenbosch et al., 2012, 2015 and Section 4.3). Brothers Caldera is variously hydrothermal active. The NW Caldera Wall is marked by black smoker high-temperature vents (up to 320 °C) that precipitate Cu-rich polymetallic sulfides in chimneys in a large vent field that encompasses at least 0.015 km^2. The vent field sits on top of fault scarps that provide access to the underlying stockwork zone. This stockwork zone is characterized by extensive iron sulfide and sulfate mineralization that occurs in highly altered basement rocks and features illite-smectite-chlorite assemblages (Wright et al., 1998; de Ronde et al., 2011).

The Upper Cone, the larger of the two, features acidic white smoker intermediate-temperature (< 200 °C) hydrothermal vents that precipitate native sulfur. The Lower Cone hosts similar white smoker fluids that emanate diffusely and with lower temperatures of < 80 °C and are not as acidic as the fluid from Upper Cone (Kleint et al., submitted to GCA).

4.2 Methods

4.2.1 Sample material

In this study, we analyzed basement rocks and hydrothermal precipitates recovered by ROV MARUM Quest 4000 during RV Sonne expedition SO253. The selected samples comprise: three unaltered volcanics and one advanced argillic altered rock from Macauley Caldera; five fresh volcanics and six chimney samples from Haungaroa; five pristine volcanics, eleven chimneys and six argillic-altered rocks from Brothers Caldera. Sampling locations are listed in Table 4.1 and shown in Figure 4.2.

4.2.2 Sample preparation

The samples were processed at the laboratories of the Bremen University. A rock saw was used to cut representative chunks of samples, carefully chosen to represent the composition of the large specimens. Samples were used for thin section preparation and for bulk rock compositional analyses. Bulk rock samples were obtained by crushing with an agate mortar. Sample amount for bulk rock analyses were chosen between 10 g for rather homogeneous samples and around 100 g for inhomogeneous samples.

For volcanics rocks, only material from the fresh interior of a hand specimen was used to produce thin sections and bulk rock powders. For chimney specimen, slices that represent the proportions of the different types of mineralization across the chimney wall were cut. Different sections of the chimney walls were not subsampled. We made thin sections to sample the different zones of mineralization along the transects represented by the respective bulk samples. Uniformly altered rock specimen were freed of weathering rinds prior to crushing. For altered rocks that constitute heterogeneities on the scale of hand specimen (eg. varying proportions of thick veins cutting an altered host) we isolated the altered rock from the veins and crushed the altered rock, unless stated otherwise.

4.2.3 Petrography of volcanics, altered rocks and hydrothermal mineralization

We carried out microscopic phase identification and detailed petrographic investigation to examine the genetic relations of phase assemblages in altered rocks and hydrothermal

precipitates. These microscopic studies were complemented by electron microprobe analyses (see Section 4.3.2).

Table 4.1: Locations of specimen collected during cruise SO253 and analyzed for the present study.

Sample Location	Edifice	Latitude	Longitude	Depth [m]
	Volcanics			
SO253-009-1R	Macauley	30° 12.654' S	178° 27.029' W	383
SO253-009-13B	Macauley	30° 12.731' S	178° 26.980' W	290
SO253-009-15B	Macauley	30° 12.730' S	178° 26.979' W	290
SO253-026-1R	Haungaroa	32° 36.955' S	179° 37.577' W	676
SO253-026-7R	Haungaroa	32° 36.988' S	179° 37.542' W	680
SO253-030-14R1	Haungaroa	32° 36.946' S	179° 37.456' W	688
SO253-039-2R	Haungaroa	32° 36.343' S	179° 36.044' W	1169
SO253-039-4R	Haungaroa	32° 36.230' S	179° 35.967' W	1065
SO253-045-2R	Brothers	34° 52.730' S	179° 04.268' E	1318
SO253-045-7R	Brothers	34° 52.730' S	179° 04.266' E	1317
SO253-045-8R	Brothers	34° 52.731' S	179° 04.280' E	1332
SO253-064-1R	Brothers	34° 51.676' S	179° 03.574' E	1634
SO253-081-10B	Brothers	34° 51.659' S	179° 03.438' E	1580
	Chimneys			
SO253-030-9S	Haungaroa	32° 36.946' S	179° 37.472' W	677
SO253-030-14R2	Haungaroa	32° 36.946' S	179° 37.456' W	688
SO253-035-2S	Haungaroa	32° 36.952' S	179° 37.433' W	683
SO253-035-3S	Haungaroa	32° 36.951' S	179° 37.433' W	683
SO253-035-6S	Haungaroa	32° 36.954' S	179° 37.461' W	681
SO253-035-12S	Haungaroa	32° 36.950' S	179° 37.470' W	684
SO253-061-1S	Brothers	34° 51.766' S	179° 03.491' E	1671
SO253-061-9S	Brothers	34° 51.750' S	179° 03.476' E	1658
SO253-061-17S	Brothers	34° 51.741' S	179° 03.459' E	1643
SO253-064-10S	Brothers	34° 51.663' S	179° 03.462' E	1593
SO253-067-13R	Brothers	34° 51.552' S	179° 03.137' E	1374
SO253-067-14R	Brothers	34° 51.552' S	179° 03.136' E	1374
SO253-067-18R	Brothers	34° 51.549' S	179° 03.140' E	1374
SO253-081-1S	Brothers	34° 51.677' S	179° 03.466' E	1619
SO253-081-5R	Brothers	34° 51.676' S	179° 03.467' E	1618
SO253-081-13S	Brothers	34° 51.553' S	179° 03.140' E	1371
SO253-085-13S	Brothers	34° 51.670' S	179° 03.474' E	1616
	Altered Rocks			
SO253-013-1R	Macauley	30° 12.773' S	178° 26.936' W	336
SO253-064-3R	Brothers	34° 51.642' S	179° 03.542' E	1608
SO253-064-9R	Brothers	34° 51.663' S	179° 03.462' E	1593
SO253-081-6R	Brothers	34° 51.675' S	179° 03.467' E	1616
SO253-085-6R	Brothers	34° 51.773' S	179° 03.479' E	1663
SO253-085-7R	Brothers	34° 51.773' S	179° 03.479' E	1664
SO253-085-8R	Brothers	34° 51.771' S	179° 03.478' E	1663

4.2.4 Electron microprobe phase identification

Electron microprobe analyses (EMPA) were performed in the laboratories of the Department of Geosciences of the University of Bremen. A CAMECA SX 100 microprobe was used to identify sulfide and sulfate minerals as well as fine-grained groundmasses of pervasively altered volcanics. Sulfides were analyzed with 20 kV acceleration voltage and 20 nA beam current, while silicic groundmasses were analyzed with 15 kV acceleration voltage and 15 nA beam current. For calibration, the standard material NMNH-111356 Hornblende Arenal was used. In advance to each sulfide measurements sample block, the reference materials (chalcopyrite/sphalerite/arsenopyrite) were measured. In advance to silicate sample blocks reference materials (olivine/plagioclase/microcline) were measured to ensure quality control of results.

4.2.5 X-Ray Fluorescence (XRF) analysis of bulk rock samples

Bulk rock analyses were carried out at the Institute for Chemistry and Biology of the Marine Environment, ICBM in Oldenburg. 700 mg of a dried and ground sample were mixed with 4.2 g of $Li_2B_4O_7$ and 1.0 g of $(NH_4)_2NO_3$ as oxidizing agent. After overnight pre-oxidation at 500 °C, the samples were fused to 30 mm diameter borate glass beads at 1350 °C in platinum crucibles. For samples with high expected concentrations of Ba, Cu or Zn the sample weight was adjusted to 70 mg and 4.83 g of $Li_2B_4O_7$ to maintain measurements within the calibration range. As the fusion was not successful in four cases, we modified the procedure again and used 70 mg of sample mixed with 630 mg of pre-combusted grinded quartz sand with 4.2 g of $Li_2B_4O_7$ for one sample to improve the glass bead stability. The remaining two samples were fused with 70 mg of sample and 4.83 g of 50% $LiBO_2$ + 50% $Li_2B_4O_7$. The different fusion methods are marked in Table 4.3.

Measurements were performed on a wavelength-dispersive XRF spectrometer (Panalytical Axios Plus), calibrated with a total of n=66 samples. The trueness and precision were monitored by repeated measurements of the international standard NOD-A-1 (U.S. Geological Survey, Flanagan & Gottfried, 1980), especially for the quartz dilution, as well as two in-house standards (basalt and black shale). For major elements it was better than 5% and for trace elements better than 15% due to the necessary high dilution. Matrix effects, possible line overlaps and trueness of ore-type samples were checked with separate artificial samples with high Ba or Zn content (pure $BaSO_4$, $ZnCl_2$, $C_4H_6O_4Zn$) and corrected when necessary; trueness and precision were better than 5%. Sulfur was determined as total S via combustion analysis using an ELTRA CS Analyzer. Trueness and precision were monitored with in-house standards and were better than 5%. For each of the bulk samples of altered rocks, we calculated the modal

compositions using mineral compositions established by electron microbe analyses. The Microsoft Excel Solver® was used to conduct these computations.

4.2.6 Sr isotope analyses of volcanics & altered rocks

Thermal ionization mass spectrometry (TIMS) was used to analyze $^{87}Sr/^{86}Sr$ ratios of selected rock samples. The analyzes were performed at the Isotope Geochemistry Laboratory at the Center for Marine Environmental Science MARUM of the University of Bremen. The $^{87}Sr/^{86}Sr$ analyzes were carried out with a Thermo Scientific Triton Plus mass spectrometer. Samples were digested in concentrated nitric acid and dissolved at 130 °C. Strontium was separated from matrix elements using Sr_{Spec} resin (method adapted from Deniel & Pin, 2001). Applied together with Ta-emitter, the samples were analyzed on rhenium filaments in a static acquisition method. Also, the $^{87}Sr/^{86}Sr$ ratio of the reference material NIST SRM 987 was measured as 0.710244 ± 8 (2σ). This value well represents the long-term reproducibility of NIST SRM 987 measurements of the laboratory 0.710249 ± 14 (2σ, n = 263) and compares well to average published data (0.710250 ± 34; 2SD, n = 1245, data < 0.7102 and > 0.7103 are discarded; GeoREM data base (Jochum et al., 2005), request September 2017).

4.2.7 Reaction path models

We used geochemical reaction path models to predict the changes of rock and fluid compositions in the course of interaction of seawater with pristine volcanic rocks. We used Geochemists Workbench (GWB) (Bethke, 2007) and a tailor-made 25 MPa database assembled by SUPCRT92 (Johnson et al., 1992).

Reaction path models were carried out in two steps. First, seawater compositions obtained from analyzes of CTD background samples were used to speciate a "Kermadec seawater" fluid. This seawater was heated to hydrothermal temperatures (according to Mg = 0 end-member temperatures of actual fluid samples; Diehl et al., in prep., Chapter 5), while allowing minerals to precipitate. Second, the resulting fluid (hot seawater) was used in the reaction path models as the initial chemical system to which unaltered volcanic rocks were added until the fluid became rock-buffered. The rock compositions were taken from the XRF results for the unaltered volcanic rocks (see Section 4.3.1). The FeO/Fe_2O_3 ratio was calculated from $Fe_2O_{3(tot)}$ according to the empirical formula developed by El-Hinnawi (2016). All major elements (except for P) were considered in the reaction paths. Ba, Cu, Zn were added to the system as barite, chalcopyrite and sphalerite to the system; As was added as trace component in the rock (As_2O_3). These elements, in addition to sulfur, were included to match concentrations actually measured in samples of fresh rocks. Mean values of the XRF data from several fresh rock

samples from the three work areas were computed and use in respective fluid-rock reaction path model runs.

In a separate set of reaction path calculations, we assessed the consequences of mixing between hydrothermal end-member fluids and cold seawater. We used the hydrothermal fluids generated by the reaction path models at varying temperatures, various water to rock ratios and with different amount of gases added during the subsurface reactions. By varying the temperature during the mixing process, we simulated varying mixing regimes during entrainment of seawater (e.g. conductive cooling or heating). In this way, we compute the comprehensive equilibrium phase relations in T-X sections. We also map mineral stability fields during batch mixing paths, where the temperature of the mixtures is computed from mixing. The results are directly compared to the mineral assemblages found in chimneys and altered rocks and the results are used to assess conditions of the mixing regime during mineral formation.

4.3 Results

4.3.1 Petrographic investigations of different rock types

We investigated unaltered and altered volcanic rocks as well as hydrothermal precipitates. Rock samples from Macauley comprise plagioclase- and to lesser extent pyroxene- and orthoclase-phyric micro- to cryptocrystalline volcanic rocks. The groundmasses show minor amounts of micrometer-sized plagioclase laths in a cryptocrystalline mesostasis. In samples 009-1R and 009-13B, parts of the phenocrystals are arranged aligned and suggest a flow texture. The plagioclase crystals may locally form glomerophyric textures. The vesicularity is high and vesicules are clearly elongated.

Rock sample 030-14R1 from Haungaroa is made of a crystalline groundmass composed mostly of plagioclase with minor pyroxene and mesostasis. The vesicularity is about 30% and vesicules are spherical without elongation.

Both samples from Brothers Volcano show a cryptocrystalline groundmass with small plagioclase laths. The rocks are phyric with larger phenocrysts of mainly plagioclase and pyroxene with lesser amounts of orthoclase, quartz and amphibole. The vesicularity is similar to that of volcanic rocks from the other edifices (about 30 vol%), but the vesicles are extremely elongated, indicating stretching during emplacement of the lava flow.

Altered rocks were sampled at Macauley and Brothers Caldera. The altered rock from Macauley was collected proximal to the vent site. It consists of a whitish to beige groundmass of quartz with small (< 20 µm) euhedral lath-shaped alunite and equant pyrite crystals. The rock is completely recrystallized; no indications of primary textures are preserved.

From Brothers Caldera we investigated four different pervasively altered rocks. Sample 064-3R originated from the northeastern part of the vent field in the NW Caldera Wall. The specimen is an intensively altered aphyric, aphanitic rock. Former plagioclase-microphenocrysts are replaced by illite and roughly equal proportions of smectite and quartz. In brecciated domains, clasts were replaced by similar clay assemblages that occur together with pyrite and show coatings of quartz.

Sample 064-9R has an intensively altered white groundmass that is cut by mm- to cm-sized massive anhydrite veins. In these veins, high-birefringence anhydrite is accompanied by low-birefringence material (presumably gypsum) filling former irregular pore space. The veins form a network and make up about 50 vol% of the rock. The clay-quartz altered rock clasts are often rimmed by pyrite that is predominantly developed at the interfaces between the veins and the altered groundmass. The groundmass composition seems to reflect intergrowths of illite, smectite and minor chlorite. The groundmass still holds visible vesicles that are partly or completely filled with needle crystals or patches of similar compositions as the groundmass. Former phenocrysts (probably plagioclase) were dissolved and left behind additional porosity.

Sample 081-6R was collected few meters away from the location of sample 064-9R. The groundmass has similar characteristic as the sample described above. Voids are mostly preserved and only partly filled. Former phenocrystals have dissolved and the groundmass consists of a network of more or less dense areas with very different compositions than sample 064-9R, resembling mixtures of mainly chlorite with illite and minor smectite.

Sample 085-5R is from the southern part of the vent field and shows a beige to brownish groundmass that is cut by cm-wide pyrite ± chalcopyrite veins. The brown groundmass is honeycombed due to voids and is composed mostly of euhedral pyrite (about 50%) with a grain size of few µm. The former groundmass minerals dissolved away. Common are larger angular clasts composed of quartz. Other former phenocrysts are replaced by an assemblage with a composition that matches a mixture of illite and smectite.

Chimney samples from Haungaroa and Brothers Volcanoes show two different structural or textural types. Chimney *Type A* features three distinct mineralization zones. (1) An inner conduit, which is monomineralic and shows low porosity, grades sharply to (2) a middle section that is composed of Fe-sulfides intergrown with Zn-sulfides and sulfates. No systematic age relation between the Zn- and Fe-sulfide is apparent from overgrowth textures. The minerals grow as spherical aggregates and there is significant porosity (30% up to over 70%). (3) The outer wall is less porous and shows silicified Fe-oxides and Fe-hydroxides that contain minor amounts of smectites.

The second chimney *Type B* completely lacks a clearly visible inner conduit with densely packed monomineralic sulfide. The mineralization of the central chimney is similar to the

middle wall of chimney *Type A* with loosely packed spherical aggregates of intercalated Fe- and Zn- sulfide. Towards the center of the chimney, the samples have a more massive appearance. The extent of mineralization decreases towards the periphery and porosity increases. The minerals clearly grow along the fluid flow paths and are aligned from the interior to the periphery. Chimneys of *Type B* completely miss a less porous outer layer.

4.3.2 Phase identification in altered rocks and chimneys

The groundmass of sample 013-1R from Macauley Caldera comprises a mixture of quartz and alunite. On the µm scale, the groundmass contains lath shaped alunite crystals patches of quartz and small pyrite crystals. Accessory phases are native sulfur and galena. The assemblage can be classified as advanced argillic alteration, which is typical for acid alteration during interaction of fumarole gases with rocks. This is unsurprising since the sample originates from low temperature and pH = 1.5 acid sulfate type vent from the young cone inside Macauley Caldera.

The groundmasses of four altered rock samples from the Brothers NW Caldera Wall vent field show varying compositions (Figure 4.3). Groundmasses of samples 064-3R and 085-5R are rich in alkaline elements (especially K), whereas samples 064-9R and 081-6R are dominated by Mg and Fe (Figure 4.3A). Compositions of alkali-rich samples may be explained by mineral mixtures of smectite and illite, while the Mg- and Fe-rich samples (064-9R, 081-6R) fall outside the compositional area that is defined by mixtures of smectite, chlorite and illite. The K-Si-Al ratio of the samples (Figure 4.3B) suggests that illite is the dominant K-bearing mineral in all alteration assemblages. Sample 064-3R may be explained by mixtures of illite-smectite-quartz. The Mg-Si-Al and Fe-Si-Al ratios of the samples show that sample 081-6R is not only rich in Mg but also in Fe (Figure 4.3C-3D). This suggests that the groundmass in samples 081-6R contains significant amounts of chlorite next to illite and smectite.

Nine chimney samples were analyzed by EMP to identify sulfide, sulfate and silicate phases. Barite, pyrite, and sphalerite are the dominant phases in all samples. Chalcopyrite is also very abundant and occurs in variable portions, with exception of sample 081-5R where it completely lacks. Anhydrite was found in only one chimney but its abundance might be underrepresented since macroscopic investigations on the chimney samples showed that anhydrite occurs irregularly distributed in some mm to some cm sized pockets, which are not present in the thin sections. Pb-sulfides gratonite or dufrenoysite often occur as accessory minerals in the outer part of the middle wall of the chimneys. In one sample, orpiment and dimorphite were found as accessory phases in the outer part of the middle wall. Some chimneys are encapsulated by silicified oxide/oxyhydroxide crusts, while in other chimneys a prominent seal is missing.

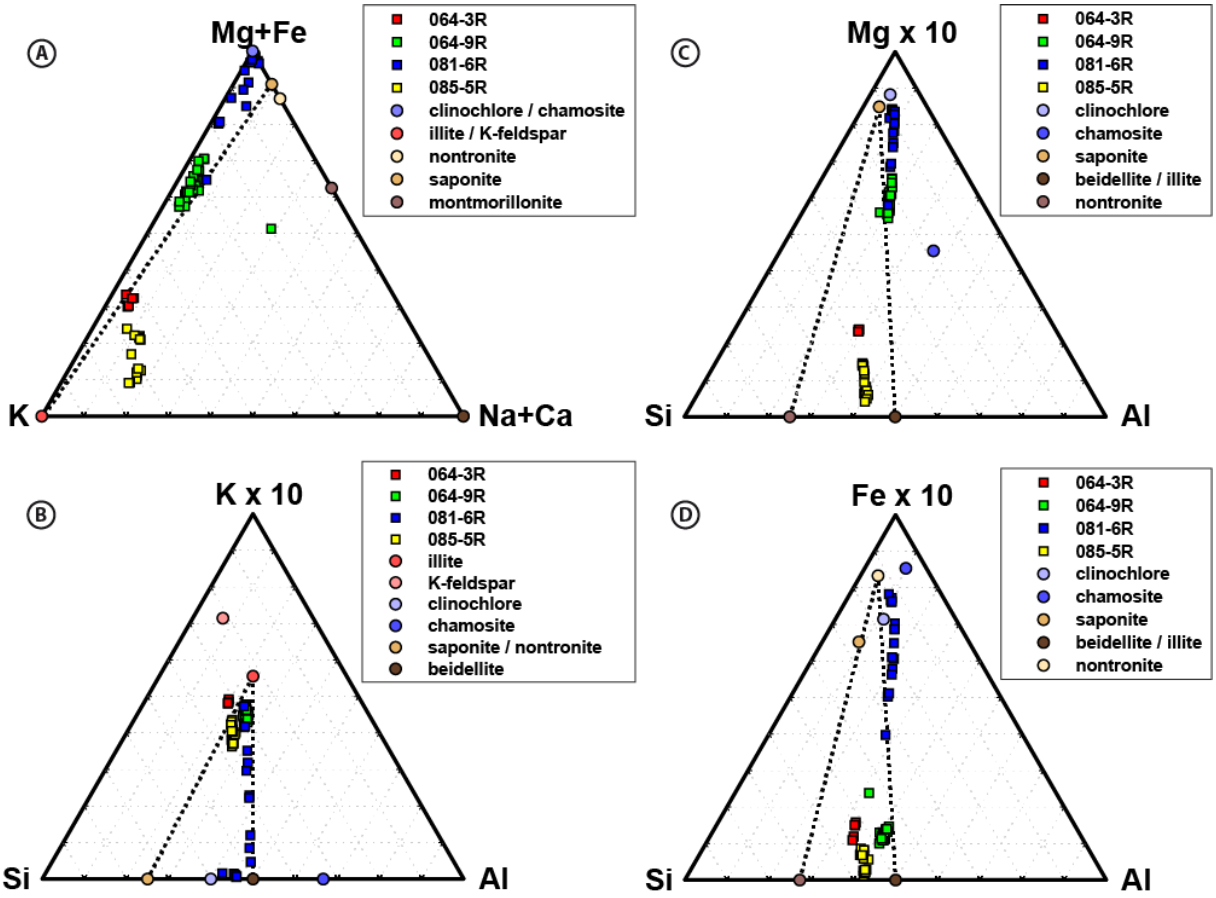

Figure 4.3: EMP analyses of fine-grained groundmass material in altered volcanic rocks plotted along with typical alteration mineral end-members. Note that the alteration minerals occur as solid solutions and actual compositions may lie between the end-member compositions (e.g. chlorite from varying proportions of clinochlore and chamosite). The dotted lines represent the compositional frame of smectite-illite mixtures. Data are plotted in mol%.

Besides the two textural types (cf. Section 4.3.1), from the abundance of minerals the chimney samples can be classified in at least 3 mineralization types (Figure 4.4). Mineralization *Type I* (textural *Type A*) forms an inner wall that is composed of massive chalcopyrite (Figure 4.4A). This inner wall has a sharp transition to the central wall, which shows abundant pyrite and barite with variable amounts of sphalerite. In sample 035-6S, sphalerite is much more abundant than in all other samples. The outermost part of the central wall often contains minor amounts of Pb-bearing sulfides as accessory phases (Figure 4.4B). The outermost wall of the chimney samples is made from silicified oxyhydroxide crusts composed of goethite and opal and with minor amounts of nontronite (Figure 4.4C). Low totals during EMP analyses suggest apparent micro-porosity. Mineralization *Type I* is found in Brothers Caldera as well as in Haungaroa chimney samples (samples 030-14R2, 061-1S, 081-1S, 085-13S).

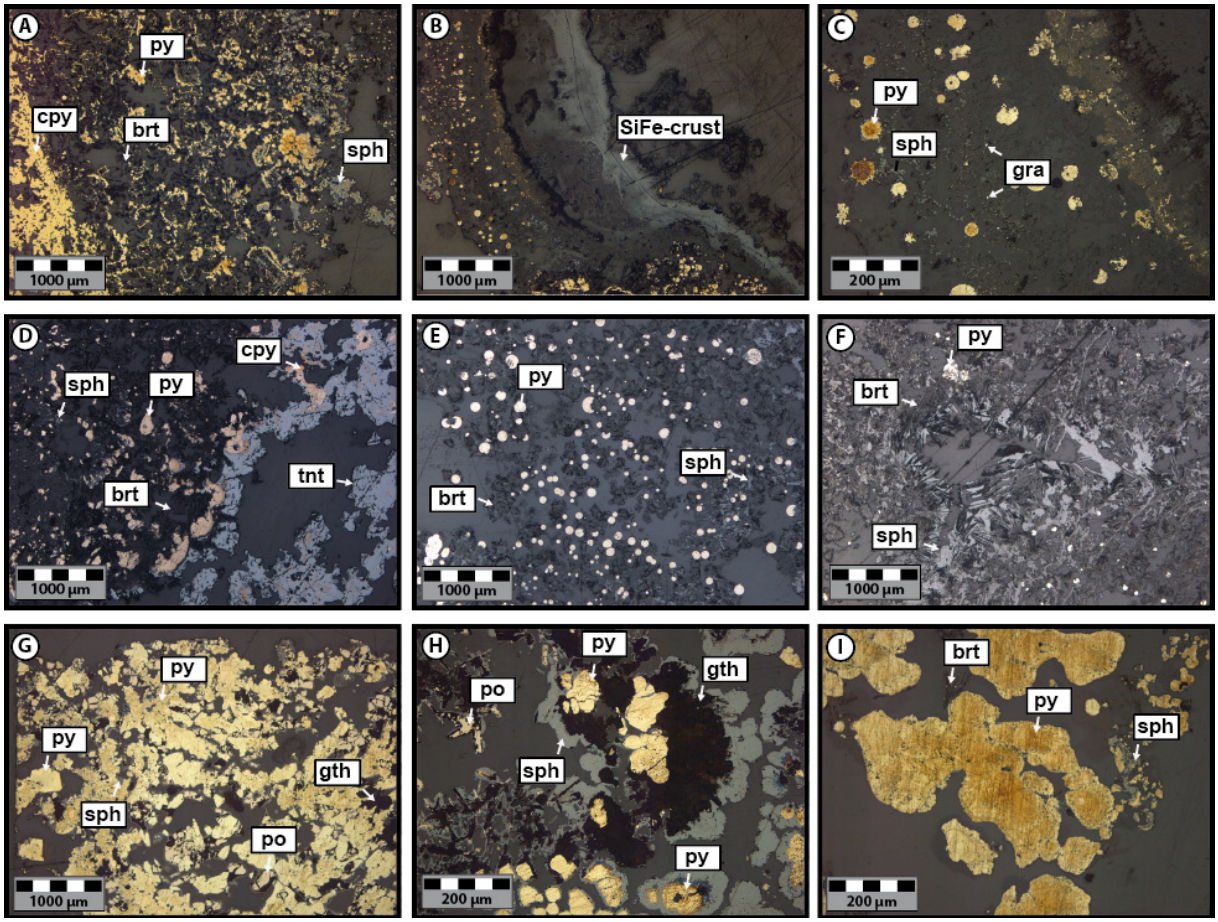

Figure 4.4: Reflected light images of different mineralization types. A-C: sample 061-1S from Brothers Caldera (mineralization *Type I*; structural *Type A*). D-F: Sample 035-2S from Haungaroa Volcano (mineralization *Type II*; structural *Type A*). G-I: Sample 064-10S from Brothers Caldera (mineralization *Type III*; structural *Type B*). Mineral abbreviations: anh: anhydrite; brt: barite; cpy: chalcopyrite; gra: gratonite; gth: goethite; po: pyrrhotite; py: pyrite; sph: sphalerite; tnt: tenanntite.

Mineralization *Type II* (textural *Type A*) has monomineralic tennantite or mixtures of tennantite and chalcopyrite in the inner conduit of the chimneys (Figure 4.4D). The assemblage is followed by a more porous zone of sphalerite and barite with usually minor amounts of pyrite (Figure 4.4E-F). The middle wall has a sharp transition to an outer wall that is compositionally and texturally similar to the outer wall of mineralization *Type I*. Mineralization *Type II* (textural *Type A*) is apparent only at Haungaroa.

Mineralization *Type III* (textural *Type B*) lacks chalcopyrite/tennantite buildup in the central conduit. From the center to the outer wall, the mineral assemblages gradually change so that sharp transitions in composition or texture are missing. Pyrite is the most abundant sulfide mineral and is associated with pyrrhotite or intergrowths of Fe-oxide (presumably goethite or mixtures of goethite/hematite/magnetite) and quartz (Figure 4.4H). This assemblage seems to replace pyrrhotite (Figure 4.4G-H). In the middle part of the chimney wall sphalerite becomes

abundant and seems intergrown with Fe-oxide/quartz, which indicate that it formed late. The outermost part of the chimney consists mainly of pyrite (Figure 4.4I).

Table 4.2 summarizes phase identification and lists all identified minerals in different samples.

Table 4.2: Phase assemblages in chimney samples and hydrothermally altered rocks. Note bracketed minerals are calculated from the composition of submicroscopic intergrowths. Mineral abbreviations: alu: alunite; anh: anhydrite; brt: barite; chl: chlorite; cpy: chalcopyrite; cv: covvelite; dim: dimorphite; duf: dufrenoysite; gn: galena; gra: gratonite; gth: goethite; ilt: illite; orp: oripiment; po: pyrrhotite; py: pyrite; qz: quartz; rt: rutile; sme: smectite; sph: sphalerite; tnt: tenanntite.

Sample	Sulfates			Fe-Sulfide		Cu-Zn Sulfide				Pb-Sulfide			As- Sulfide		Clay minerals/ sheet silicates			Oxides / Hydroxides		
	brt	anh	alu	py	po	cpy	tnt	cv	sph	duf	gra	gn	orp	dim	sme	ilt	chl	gth	qz	rt
Chimneys																				
030-9S	x	x		x		x	x		x											
030-14R2	x			x		x			x	x								(x)	(x)	
035-2S	x			x		x	x		x	x										
035-6S	x			x		x	x		x				x	x						
061-1S	x			x		x			x		x				(x)			(x)	(x)	
061-9S	x			x		x			x									(x)	(x)	
064-10S	x			x	x	x			x									(x)	(x)	
081-5R	x			x	x				x		x							(x)	(x)	
085-13S	x			x		x			x									(x)	(x)	
Altered rocks																				
013-1R			x	x								x							x	x
064-3R				x											(x)	(x)			x	
064-9R		x		x											(x)	(x)	(x)			
081-6R				x											(x)	(x)	(x)			
085-5R	x			x		x									(x)	(x)			x	
085-6R	x			x				x	x											

4.3.3 Bulk rock compositions

We present data of 13 bulk rock samples of unaltered volcanics, 17 analyses of bulk chimneys and 12 analyses of bulk altered rocks deduced from XRF analyses (Table 4.3).

Table 4.3: XRF analyses results. The concentrations are given in their elemental form, as oxides may not be the prevailing form in all samples. Also note that some elements assigned as trace elements are in fact major elements (e.g. Ba, Cu). For samples marked with ◊, 70 mg sample were used for the measurement; * indicates samples to which quartz sand was added for the fusion process (the elemental composition of quartz sand was already subtracted from the results shown here); Δ indicates samples fused with a mixture of lithium tetraborate and lithium metaborate. All samples without a symbol suffix were fused as 700 mg glass beads.

Major elements [wt. %]												
Sample	**Edifice**	**Si**	**Ti**	**Al**	**Fe**	**Mn**	**Mg**	**Ca**	**Na**	**K**	**P**	**ges. S**
Fresh Volcanics												
009-13B	Macauley	31.35	0.496	7.27	4.504	0.148	0.764	3.110	3.2	1.130	0.1174	0.11
009-15B	Macauley	31.36	0.496	7.26	4.434	0.135	0.729	3.040	3.3	1.160	0.1056	0.24
009-1R	Macauley	31.38	0.501	7.22	4.613	0.139	0.765	3.048	3.2	1.140	0.1144	0.01
026-1R	Haungaroa	26.03	0.567	8.04	7.79	0.149	2.449	6.20	2.5	0.3991	0.0482	0.03
026-7R	Haungaroa	26.10	0.575	8.06	8.10	0.174	2.432	6.16	2.1	0.3843	0.0512	0.01
030-14R1 ◊	Haungaroa	26.34	0.562	8.16	7.57	0.133	2.232	6.00	2.2	<1.25	<0.13	0.30
039-2R	Haungaroa	25.61	0.506	9.38	7.13	0.126	1.939	7.04	1.91	0.354	0.0413	0.01
039-4R	Haungaroa	25.26	0.703	7.54	9.60	0.178	2.095	6.72	2.1	0.477	0.0480	0.02
045-2R	Brothers	31.04	0.563	7.91	3.506	0.0950	0.821	2.749	3.5	1.807	0.0945	0.13
045-7R ◊	Brothers	30.61	0.539	7.80	3.600	0.0791	0.813	3.58	3.3	1.846	<0.13	0.13
045-8R	Brothers	30.75	0.564	7.86	3.685	0.0980	0.881	3.125	3.4	1.777	0.1060	0.04
064-1R	Brothers	30.54	0.590	7.90	4.006	0.110	0.886	3.104	3.2	1.850	0.1273	0.01
081-10B	Brothers	30.58	0.593	7.74	4.079	0.104	0.840	2.909	3.4	1.795	0.1174	0.32
Chimneys												
030-14R2 Δ	Haungaroa	<0.94	0.2874	<0.53	17.01	<0.04	<0.6	<0.72	1.09	<1.25	<0.13	28.17
030-9S ◊	Haungaroa	<0.94	0.384	<0.53	5.94	<0.04	<0.6	0.920	<1.04	<1.25	<0.13	28.5
035-12S ◊	Haungaroa	4.601	0.2045	<0.53	5.10	<0.04	<0.6	0.734	<1.04	<1.25	<0.13	27.7
035-2S ★	Haungaroa	0.472	0.461	8.16	3.862			0.884	0.55			21.9
035-3S ◊	Haungaroa	<0.94	0.588	<0.53	4.875	<0.04	<0.6	5.17	<1.04	<1.25	<0.13	24.1
035-6S ◊	Haungaroa	<0.94	0.1254	<0.53	11.92	<0.04		<0.72	<1.04	<1.25	<0.13	32.0
061-17S ◊	Brothers	2.302	0.749	<0.53	5.92	<0.04	<0.6	1.233	<1.04	<1.25	<0.13	21.0
061-1S ◊	Brothers	1.417	0.346	<0.53	14.8	<0.04	<0.6	1.426	<1.04	<1.25	<0.13	27.1
061-9S Δ	Brothers	<0.94	0.410	<0.53	16.8	<0.04	<0.6	<0.72	2.8	<1.25	<0.13	26.1
064-10S ◊	Brothers	0.140	<0.06	<0.53	36.4	<0.04	<0.6	1.724	<1.04	<1.25	<0.13	41.6
067-13R ◊	Brothers	<0.94	0.552		6.17			<0.72	<1.04		<0.13	25.0
067-14R ◊	Brothers	1.127	<0.06	<0.53	5.48	<0.04	<0.6	34.4	<1.04	<1.25	<0.13	31.5
067-18R ◊	Brothers	<0.94	0.700	<0.53	7.3	<0.04	<0.6	<0.72	<1.04	<1.25	<0.13	22.6
081-13S ◊	Brothers	<0.94	0.726	<0.53	1.192	<0.04	<0.6	1.181	<1.04	<1.25	<0.13	19.1
081-1S ◊	Brothers	<0.94	0.0762	<0.53	24.12	<0.04	<0.6	10.61	<1.04	<1.25	<0.13	40.3
081-5R ◊	Brothers	1.181	0.443	<0.53	15.30	<0.04	<0.6	1.001	<1.04	<1.25	<0.13	30.0
085-13S Δ	Brothers	<0.94	0.1580	<0.53	25.62	<0.04	<0.6	<0.72	3.85	<1.25	<0.13	31.1
Altered Rocks and stockwork mineralization												
013-1R	Macauley	40.74	0.818	2.401	0.197	<0.004	0.1154	0.2011	0.99	0.4765	0.0329	4.1
064-3R	Brothers	30.22	0.410	5.59	7.05	<0.004	0.363	0.2280	0.50	1.711	0.0942	9.2
064-9R1	Brothers	3.276	0.2411	3.146	18.83	<0.004	0.813	15.41	<0.1	0.803	<0.01	35.4
064-9R2 ◊	Brothers	7.67	0.613	7.21	15.60	<0.04	0.628	8.90	<1.04	2.129	<0.13	29.8
081-6R ◊	Brothers	14.07	1.007	12.52	14.48	<0.04	6.96	0.623	<1.04	2.005	0.0805	8.0
085-6Ra	Brothers	30.43	0.596	7.80	5.44	<0.004	<0.06	0.531	0.76	0.860	0.0673	6.7
085-6Rb ◊	Brothers	5.74	0.2532	1.723	26.62	<0.04	<0.6	<0.72	<1.04	<1.25	<0.13	31.8
085-6Rc ◊	Brothers	30.38	0.588	7.88	6.04	<0.04	<0.6	<0.72	<1.04	<1.25	<0.13	7.0
085-7R1 ◊	Brothers	22.82	<0.06	7.85	18.57	<0.04	<0.6	<0.72	<1.04	<1.25	<0.13	8.1
085-7R2 ◊	Brothers	21.27	<0.06	0.914	19.79	<0.04	<0.6	<0.72	<1.04	<1.25	<0.13	22.9
085-8R1 ◊	Brothers	17.38	0.897	12.17	12.23	<0.04	<0.6	<0.72	<1.04	3.73	<0.13	13.8
085-8R2 ◊	Brothers			<0.53	35.11	<0.04	<0.6	1.88	<1.04	<1.25	<0.13	46.8
LOQ	undiluted	0.09	0.006	0.05	0.01	0.00	0.06	0.07	0.10	0.12	0.01	
LOQ	diluted	0.93	0.06	0.53	0.07	0.04	0.60	0.715	1.04	1.25	0.13	

Table 4.3: continued.

Trace elements [mg/kg]														
As	**Ba**	**Co**	**Cr**	**Cu**	**Ga**	**Mo**	**Nb**	**Pb**	**Rb**	**Sr**	**V**	**Y**	**Zn**	**Zr**
Fresh Volcanics														
3.12	370	6.2	<2.5	15.6	14.5	3.12	<4	4.2	22.9	211	34.3	45.7	108	142
4.2	350	8.3	<2.5	15.6	15.6	5.2	<4	4.2	21.9	218	31.3	44.8	111	146
4.2	560	7.3	<2.5	60	16.6	3.12	<4	6.2	23.9	216	35.4	45.8	119	143
7.2	180	32.0	<2.5	115	15.3	2.05	7.16	2.0	7.16	158.6	384	24.6	96.2	56
10.3	330	33.0	<2.5	210	15.4	3.09	10.3	4.1	8.23	155.3	394	25.7	134	59
32.3	<300	40	<25	<120	<50	<20	<40	<40	<50	<150	395	26.2	<100	<100
4.2	187	26	<2.5	104	17.7	2.08	6.24	5.2	6.24	165.4	360	21.9	113	50
7.5	230	36	<2.5	111	16.2	<2	6.25	<4	8.75	176.2	505	30.0	131	65
4.1	1020	7.2	<2.5	30	16.5	5.2	<4	9.3	43.3	222	76.3	40.2	91.8	182
<2	1250	<30	<25		<50	<20	<40	<40	66.4	232	<150	36.8	<100	111
4.1	1000	8.2	<2.5	25	16.5	3.09	<4	8.2	42.2	246	83.3	41.2	95.7	178
7.3	1000	6.2	<2.5	8.3	17.7	3.12	<4	9.4	42.7	242	86.4	42.7	98.9	178
9.5	1440	9.5	<2.5	94	16.9	6.3	<4	21	41.1	229	91.8	41.1	124	178
Chimneys														
6900	270000	280		11700	170	120	<40	3300	79.0	5570			35900	150
11900	270000	<30		49000		<20	<40	6500	65.4	5540			252000	
1560	135000	<30		12500		130	<40	3200	<50	2120		<20	366000	
11400	360000			21000	590			8300		7220			131000	
5600	430000	<30		14200		<20	<40	5400	72.1	8070			117000	
4500	98000	43		82000		210	<40	7000	80.8	1210			304000	140
4400	550000	<30		9500	300	<20	<40	5000	66.6	6120		<20	40200	
1520	300000	88		73000	260	90	<40	6900	96.0	6420			55900	<100
1130	300000	104		104000	74	334	<40	2900	89.6	4390			9160	
1830	8000	610		2300	114	17	<40	1600	<50	396	<150	<20	18800	
2220	420000	<30		2100			<40	9200	92.5	6800			196000	
104	53000			23000	<50	<20	<40	1100	50.5	4930			3200	116
670	530000	<30		41000	<50	<20	<40	2200	<50	7530		<20	39500	
4500	550000	<30		220		<20	<40	13100	115	5910		<20	172000	
2380	32000	1860		58000	<50	600	<40	630	<50	1839		<20	3600	
5200	320000	1020		1130	<50	<20	<40	7900	98.5	5640		<20	87300	
2170	133000	154		108000	69	88	<40	2200	69.5	2730			4820	115
Altered Rocks and stockwork mineralization														
3.4	320	<3	<2.5	<12	<5	4.5	<4	<4	<5	465	<15	7.9	36.0	181
226	8100	7.4	3.7	230	11.0	2.45	<4	55	45.4	396	78.5	27.0	22.1	106
174	490	78	<2.5	41	7.2	45	<4	16	15.5	1760	63.3	14.3	13.1	70
96	1230	125		173	<50	<20	<40	<40	77.3	1060	210	36.3		<100
54	930	129		<120	16.8	<20	<40	<40	61.5	168.8		61	36.9	179
174	4000	7.9	15.8	510	32	5.6	8	200	20.3	78.8	131	38.3	3260	170
1730	120000			7900		96	<40	160	<50	843			1140	193
140	2180	<30	270	480	<50	<20	<40	180	<50	<150	<150	38.4	1760	160
980	1390		<25	1030		80	62	70	44.4	<150	<150	<20	<100	110
1050	890	<30	<25	630	<50	85	66	74	<50	<150	<150	<20	<100	<100
228	5900						<40	150	86.1	182.0			765	165
89	850	<30	<25	220	<50	<20	<40		<50	<150	<150	<20	2200	<100
2	30	3	2.50	12	5	2	4	4	5.0	15.0	15	2	10	10
20	300	30	25.00	120	50	20	40	40	50	150	150	20	100	100

4.3.3.1 Bulk rock composition of unaltered volcanics

Data for unaltered volcanics are plotted in Figure 4.5. In the AFM diagram (Figure 4.5A), the compositional data for rocks from the different volcanos are plotted along a tholeiitic differentiation path typical of intraoceanic island arcs. Samples from Haungaroa are enriched in Fe and Mg compared to alkaline elements and plot in the section of intermediate differentiated tholeiitic rocks. Volcanics from Macauley are more enriched in alkaline elements compared to Fe and Mg and plot in the high differentiation section of the tholeiitic differentiation trend. Volcanics of Brothers are slightly more enriched in Mg and alkalis compared to Fe and plot at the boundary between the calc-alkaline and tholeiitic differentiation trends. The data correspond well to existing literature data from the sampled volcanoes (Gamble et al., 1990, 1993, 1996; Wright & Gamble, 1999; Smith et al., 2003; Haase et al., 2006; Barker et al., 2013). In the total alkalis vs. silica (TAS) diagram (Figure 4.5B), Haungaroa samples plot in the basaltic andesite section. In contrast, volcanics from Macauley and Brothers plot in the dacite field. Brothers samples are rich in alkalis and plot near the boundary to trachydacitic compositions. The difference between Brothers and Macauley rocks becomes most obvious in the potassium concentrations (Figure 4.5C), which are considerable higher at Brothers.

4.3.3.2 Bulk rock composition of chimneys and altered rocks

Figure 4.6 shows the compositions of chimney samples and altered rocks with respect to major elements. Figure 4.6A gives an overview of the mineralization type: The top apex (Ca+Ba) represents sulfate minerals, the bottom left apex (Fe+Zn+Cu) represents sulfides and the bottom right apex (Si+Al+Na+K) represents silicates. Bulk chimney samples are mostly dominated by sulfide and sulfate minerals. In only four out of 17 samples the molar fraction of elements representing silicates exceeds 20%. In contrast, all altered rock samples, except for one, are dominated by silicates.

Figure 4.6B shows the composition of sulfates: There are two distinct groups of chimneys. In most chimneys, barite is the dominant sulfate phase with only minor fractions of anhydrite. However, in three chimney samples from Brothers NW Caldera Wall sulfates are dominated by anhydrite. This is in contrast to the mineralogical observations, where significant amounts of anhydrite were found in only one chimney sample at Haungaroa. In altered rocks anhydrite is the dominant sulfate phase.

Figures 4.6C-D show the compositional variety of sulfides. Figure 4.6C shows that one mineralization type is Zn-Fe dominated and the other type represents a Fe-Cu mineralization.

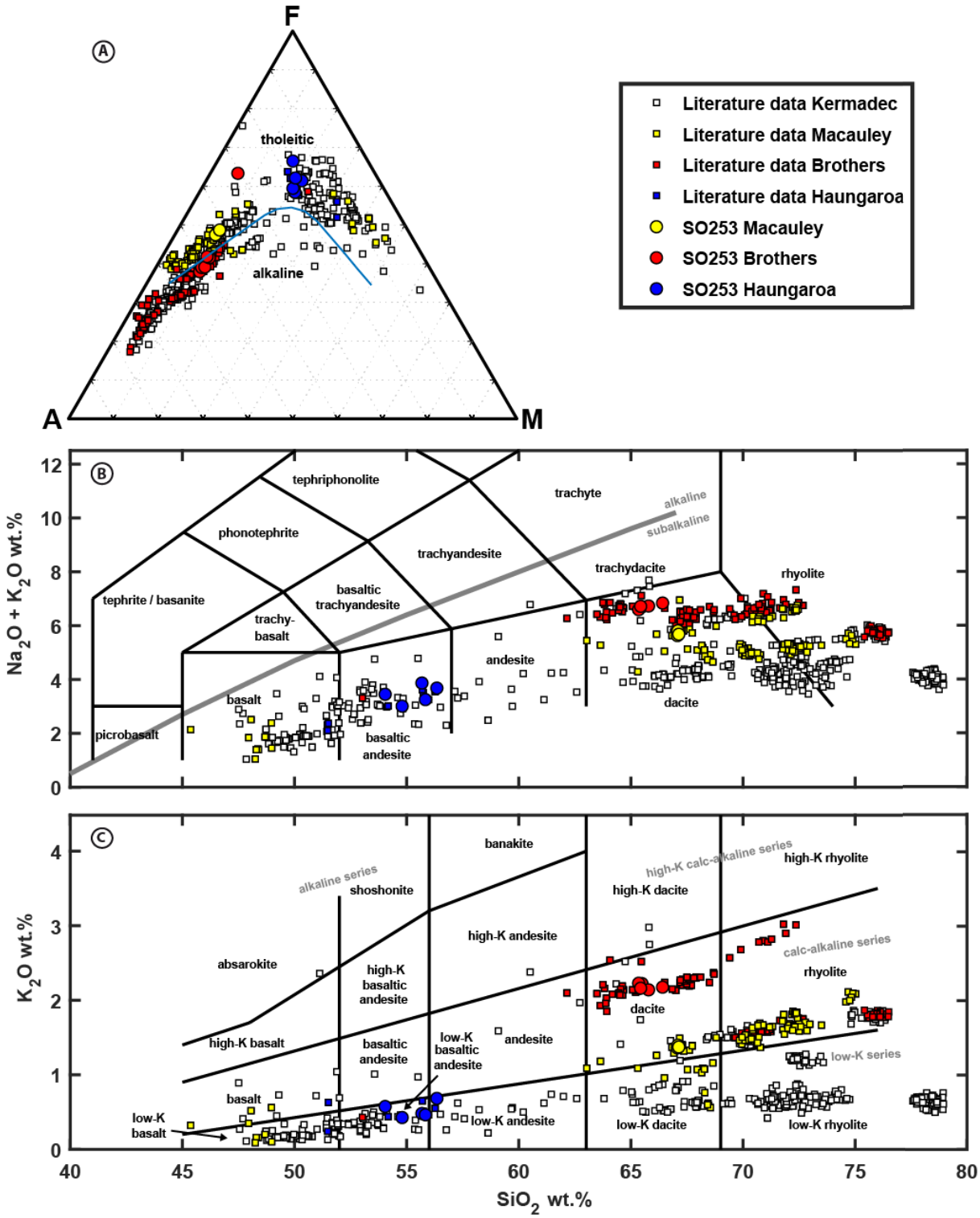

Figure 4.5: Data of unaltered volcanic bulk rock samples in the AFM, TAS and Potassium diagram plotted along with literature data of the Kermadec Island Arc (Gamble et al. 1990, 1993, 1996; Wright & Gamble 1999; Smith et al., 2003; Haase et al., 2006; Barker et al., 2013). The blue curve in the AFM diagram discriminates between tholeiitic and alkaline differentiation trends.

Altered rocks plot near the top apex (Fe) and indicate that pure Fe-sulfide is the predominant sulfide type and Cu-Zn sulfides are scarce. Figure 4.6D shows that Pb-bearing sulfides are of minor importance and the mineralization is clearly dominated by Cu- and Zn-sulfides. This

compositional variety is conform with the mineralogical investigations, which reveal that Pb-sulfides (gratonite, dufrenoysite and galenite) occur only as accessory phases in the outer periphery of chimney samples. In contrast, Zn-sulfide (sphalerite) usually built a significant proportion of the central wall and Cu-Fe-sulfide (chalcopyrite) or Cu-As-Fe sulfide (tennantite) built the inner wall that lines the inner conduit, if persistent. Chimneys and altered rock samples plot in two distinct groups. One group of samples is particularly Cu-rich, the other group is particularly rich in Zn. Also for altered rocks there is one type where polymetallic sulfides are composed of chalcopyrite, whereas other samples contain sphalerite as minor component next to abundant pyrite.

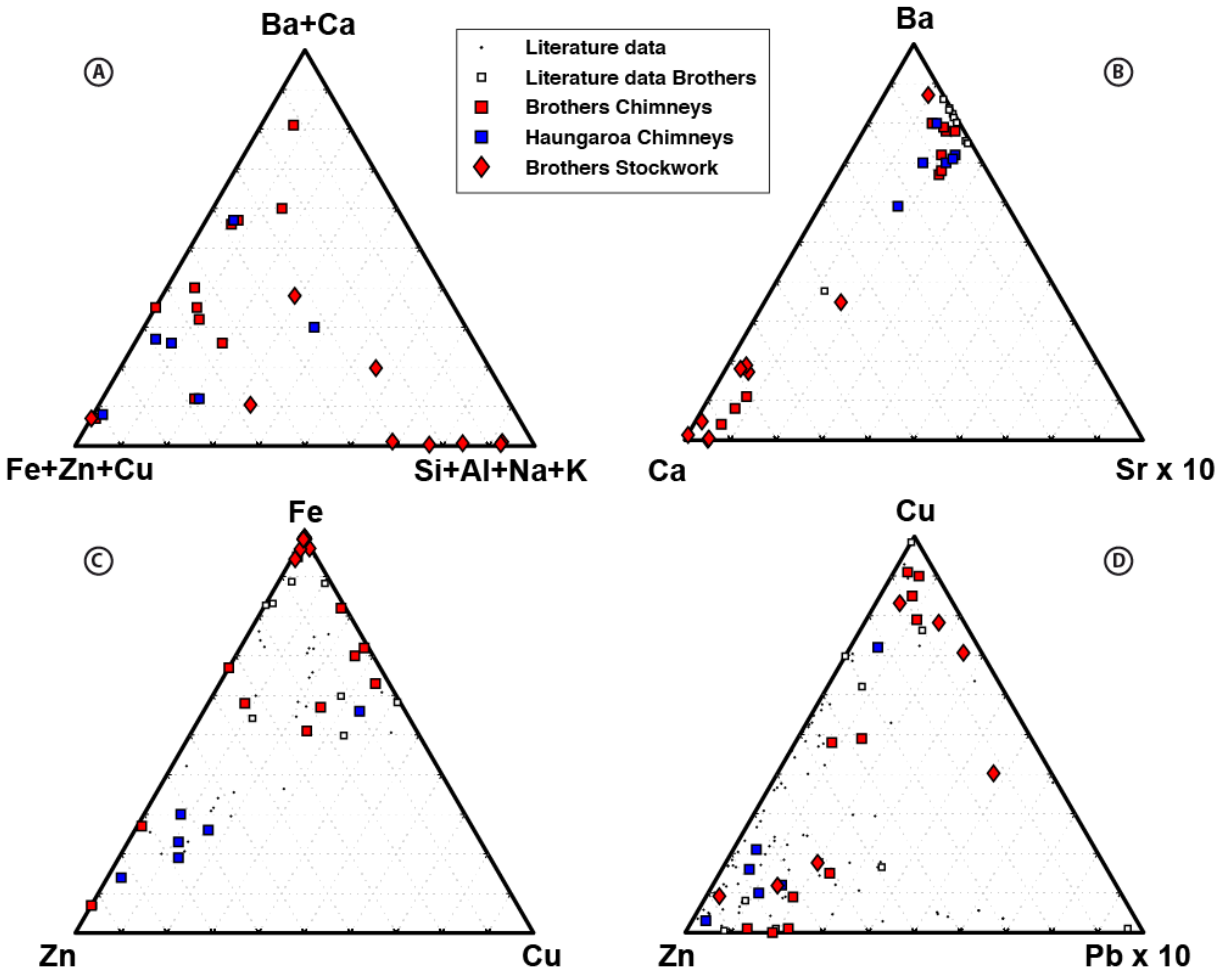

Figure 4.6: Ternary diagrams showing the compositional variety in chimneys and altered rocks for Brothers Caldera and Haungaroa in mol%. Literature data are averaged ore grades of oceanic massive sulfide deposits worldwide (data from Hannington et al., 2011 and Fouquet et al., 2018 and references therein). "Literature data Brothers" is a dataset of dredged samples from Brothers Caldera (Wright et al., 1998).

4.3.4 Calculation of mineral modes

We combined the XRF bulk-rock data with the EMP analyses to identify the minerals in the samples and to calculate mineral modes for individual samples. A least square calculation was performed with Microsoft Excel Solver® including all major elements in the calculation. The results of these calculations (Figure 4.7) show varying mineral proportions for different chimneys and altered rocks.

The different mineralization types in the chimney samples can be recognized in the calculated mineral composition. Samples 030-9S and 035-2S are examples for mineralization *Type I*. Tennantite is the main constituent of the inner wall, while barite and sphalerite are the most abundant minerals in the central wall. Samples 061-1S and 081-1S are examples for mineralization *Type II*. Chalcopyrite is more abundant (with 20 to 35 mol%) than in *Type I*. Pyrite abundances are higher while sphalerite rarely occurs. Mineralization *Type III* is represented in sample 064-10S. Pyrite is clearly the dominating phase and pyrrhotite is abundant next to minor amounts of sphalerite and anhydrite. Generally, calculated mineral modes (in agreement with bulk rock compositions) confirm the impression that anhydrite is more abundant than suggested during the microscopic investigation.

The mineral modes of altered rocks show that pyrite is the abundant sulfide mineral and that the groundmasses of the rocks are composed of mixtures of chlorite, illite and smectite, with different proportions of these minerals. Sample 064-9R2 is composed of a large fraction of pyrite and anhydrite, aside from a groundmass made to large extent of illite, with minor chlorite and smectite. The abundant anhydrite suggests, that the rock sample is not only cut by the mm to cm sized anhydrite veins, but that the groundmass itself contains significant portions of anhydrite. Sample 081-6R holds the most chlorite among all altered rocks sampled (50 mol%). Sample 085-6RA is dominated by quartz and pyrite, embedded in a groundmass of smectite and illite. The advanced argillic rock of Macauley largely consists of quartz with alunite and minor pyrite.

4.3.5 $^{87}Sr/^{86}Sr$ of bulk rock samples and water-to-rock ratios

The results of TIMS analyzes are presented in Table 4.4. Strontium isotope ratios of unaltered volcanic rocks were detected between 0.703519 ± 6 and 0.704269 ± 6 (± 2σ; refers to the last digit). Strontium isotopic values of altered rocks comprise a broad range from 0.704889 ± 8 to 0.708572 ± 5. The mean value for all altered rocks is 0.706728 ± 0.001098 (n = 10). The high standard deviation shows that the variability of altered rocks is considerably higher than the variability of pristine rocks. This is likely a consequence of hydrothermal alteration. Using $^{87}Sr/^{86}Sr$, the degree of alteration can be estimated. Samples with non-radiogenic Sr isotope

signatures close to the pristine rock are presumably less altered than rocks with Sr isotope compositions close to seawater (0.709183 ± 8; Diehl et al., in prep., Chapter 5).

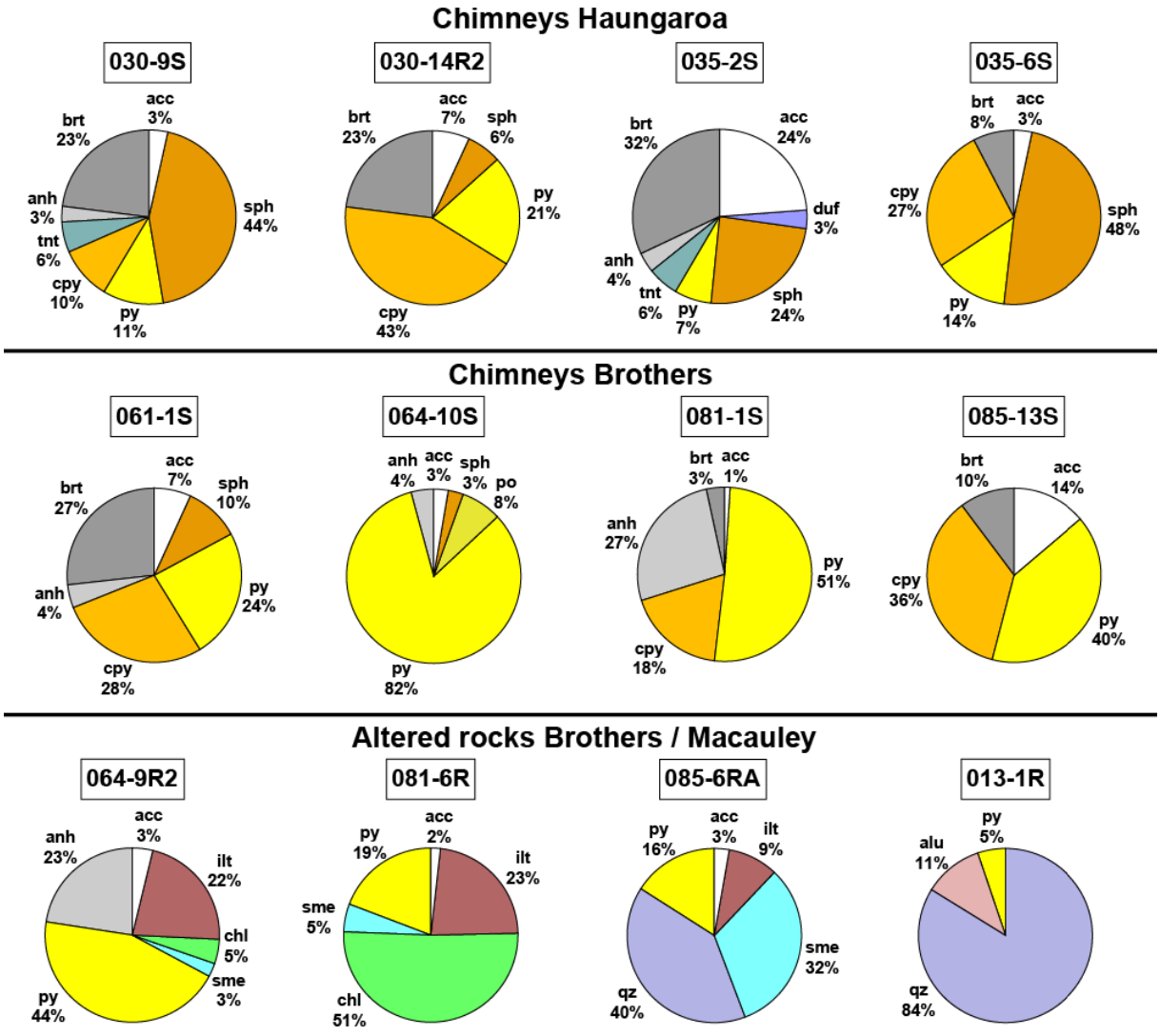

Figure 4.7: Mineral modes for assorted chimneys and altered rocks derived from least squares calculations using XRF bulk-rock analyzes and actual minerals identified during EMP analyses. Proportions are given in mol%. Acc denotes the sum of accessories (minerals smaller 2 mol% and oxihydroxides for chimneys). Mineral abbreviations: alu: alunite; anh: anhydrite; brt: barite; chl: chlorite; cpy: chalcopyrite; duf: dufrenoysite; ilt: illite; po: pyrrhotite; py: pyrite; qz: quartz; sme: smectite; sph: sphalerite; tnt: tenanntite.

Sample 064-3R is closest to the range of pristine volcanics and seems to be less intensively altered as recorded by Sr isotopes. This is in line with the petrographic results indicating the preservation of the original textures of this rock. Sample 081-6R is altered to an $^{87}Sr/^{86}Sr$ intermediate value between pristine volcanics and seawater. Samples 085-6R to 085-8R resemble the same rock type with different degrees of alteration reflected by different degrees of pyrite mineralization (groundmass composition of sample 085-5R was described in

Section 4.3.2). The mean value of this rock type is 0.706464 ± 0.000533 (n = 4), indicating increased alteration compared to the samples mentioned before. Sample 064-9R is closest to seawater Sr signatures and hence reflects the rock that has been altered to the highest degree. Sample 064-9R2 is the isolated groundmass, while 064-9R1 reflects a bulk sample of groundmass and vein material.

Table 4.4: Results of $^{87}Sr/^{86}Sr$ TIMS analyzes. Note: The value 2σ marks the internal precision and refers to the last digit of the measured value.

Sample name	Edifice	$^{87}Sr/^{86}Sr$	2σ
Pristine volcanics			
009-1R	Macauley	0.703519	6
009-15B	Macauley	0.703568	6
026-1R	Haungaroa	0.704269	6
030-14R1	Haungaroa	0.703959	7
039-2R	Haungaroa	0.703913	8
045-2R	Brothers	0.703947	6
064-1R	Brothers	0.704023	9
081-10B	Brothers	0.704109	6
Altered rocks			
013-1R	Macauley	0.707558	6
064-3R	Brothers	0.704889	8
064-9R-1	Brothers	0.708572	5
064-9R-2	Brothers	0.707551	5
081-6R	Brothers	0.706130	6
085-6Ra	Brothers	0.706894	6
085-6Rc	Brothers	0.706848	8
085-7R1	Brothers	0.705749	7
085-8R1	Brothers	0.706365	6

We used the Sr isotope compositions to compute the water-to-rock ratios (w/r) during rock alteration from mass balance constraints. According to Taylor (1977), the w/r for open and closed systems can be calculated using the Sr concentrations of the initial fluid and rock together with the isotopic compositions of both, fluid and rock before and after the fluid-rock interaction (Equations 1-2). We used mean values of the strontium concentration (c_{Sr}) and $^{87}Sr/^{86}Sr$ of unaltered host-rocks and individual values of $^{87}Sr/^{86}Sr$ for the intensively altered rocks. To calculate the w/r of the latter in Equation 1, we applied the calculated end-member Sr isotope compositions derived from hydrothermal fluids samples (Diehl et al., in prep., Chapter 5) and seawater values. The w/r range between 5.5 and 29.2 for closed systems and between 0.8 and 1.5 for open systems. For sample 064-3R, the Sr isotope mass balances indicate

smallest w/r. Sample 081-6R and sample 085-6R are suggested to have formed during intermediate extent of water flux and sample 064-6R has most extensively been percolated by hydrothermal solutions.

Equation 1:
$$\frac{\mathrm{w}}{\mathrm{r}_{\,\mathrm{closed}}} = \frac{\left(\frac{^{87}Sr}{^{86}Sr}_{\mathrm{rock,init}} - \frac{^{87}Sr}{^{86}Sr}_{\mathrm{rock,final}}\right) * c_{Sr,rock}}{\left(\frac{^{87}Sr}{^{86}Sr}_{\mathrm{fluid,final}} - \frac{^{87}Sr}{^{86}Sr}_{\mathrm{fluid,init}}\right) * c_{Sr,fluid}}$$

Equation 2:
$$\frac{\mathrm{w}}{\mathrm{r}_{\,\mathrm{open}}} = \ln\left(\frac{\mathrm{w}}{\mathrm{r}_{\,\mathrm{closed}}} + 1\right)$$

Table 4.5: Results and parameter of w/r calculations (Equation 1 and 2) from strontium mass balance equation. cSr_{fluid} and cSr_{rock} denote the Sr of seawater and the initial rocks; $^{87}Sr/^{86}Sr_{fluid,init}$ and $^{87}Sr/^{86}Sr_{fluid,final}$ denote the Sr isotope ratios of seawater and the final hydrothermal fluid; $^{87}Sr/^{86}Sr_{rock,init}$ and $^{87}Sr/^{86}Sr_{rock,final}$ denote the Sr isotope ratios of pristine volcanics and the altered rocks; w/r_{closed} and w/r_{open} are the results for the calculation of open and closed systems.

Sample	Edifice	cSr fluid	cSr rock	$^{87}Sr/^{86}Sr$ fluid,init	$^{87}Sr/^{86}Sr$ fluid,final	$^{87}Sr/^{86}Sr$ rock,init	$^{87}Sr/^{86}Sr$ rock,final	w/r closed	w/r open
013-1R	Macauley	7.5	217	0.709183	0.704000	0.703544	0.707558	**22.4**	**1.4**
064-3R	Brothers	7.5	231	0.709183	0.704400	0.704026	0.704889	**5.5**	**0.8**
064-9R-1							0.708572	**29.2**	**1.5**
064-9R-2							0.707551	**22.7**	**1.4**
081-6R							0.706130	**13.5**	**1.2**
085-6Ra							0.706894	**18.4**	**1.3**
085-6Rc							0.706848	**18.1**	**1.3**
085-7R1							0.705749	**11.1**	**1.1**
085-8R1							0.706365	**15.0**	**1.2**

4.3.6 Reaction path models

In reaction path models, we investigated how temperatures, host-rock compositions and input of volcanic volatiles influence mineralization processes during reaction with seawater at elevated temperatures. The model rock compositions used for the computations were calculated from average values of XRF bulk rock analyses (according to the procedure mentioned in Section 4.2.5) and are given in Table 4.6.

Table 4.6: Composition of model rocks used in the reaction path calculation. Abbreviations: Mac: Macauley; Haun: Haungaroa; Bro: Brothers; brt: barite; cpy: chalcopyrite; sph: sphalerite. Major components are given as wt.%. As_2O_3, brt, cpy, sph are given in ppm.

Location	Rock	SiO_2	Al_2O_3	FeO	Fe_2O_3	MnO	MgO	CaO	Na_2O	K_2O	As_2O_3	brt	cpy	sph
Mac	high-K dacite	68.1	13.9	3.5	2.8	0.2	1.3	4.4	4.4	1.4	5.0	630	38	165
Haun	basaltic andesite	58.0	15.4	8.1	3.1	0.2	3.3	8.0	3.2	0.7	15.3	520	265	155
Bro	high-K dacite	65.5	15.2	2.6	2.7	0.1	1.9	5.6	4.3	1.9	7.1	1630	107	136

With increasing extent of alteration, three alteration stages can be distinguished (e.g. Figure 4.8, 330 °C): The alteration assemblage predicted for low water-to-rock ratios (w/r < 30) consists of albite, epidote/prehnite, quartz and minor proportions of K-feldspar, saponite and phyllosilicates (muscovite and annite). The assemblage grades into a second alteration type at intermediate water-to-rock ratios (w/r ≈ 30-300). This second assemblage consists mainly of quartz, smectite, diaspore and anhydrite. The alteration is marked by the vanishing of albite and epidote, the onset of diaspore and an increase of quartz abundance. At w/r > 300, quartz is predicted to disappear and the amount of smectite increases. At extremely high fluid flow conditions, chlorite with minor hematite, diaspore and anhydrite are predicted to occur.

We investigated the influence of temperature on alteration of the K-rich dacite from Brothers Caldera in four reaction path models at temperatures of 100 °C, 200 °C, 280 °C and 330 °C (Figure 4.8, note: the model run with 280 °C is included in Figure 4.9). Both the mineral assemblages and their transitions are influenced by the temperature of the fluid. The transitions of intermediate to fluid dominated alteration is considerably shifted to lower water-to-rock ratios with increasing temperature (w/r ≈ 8000 at 100 °C, w/r ≈ 500 at 330 °C). The mineral assemblages are changed in a way that, in the incipient alteration stage, at low temperatures, prehnite occurs at the cost of epidote and at high temperatures biotite (annite) is predicted to form. At low temperatures the intermediate stage consists of nontronite, whereas at high temperature nontronite is not stable but Na-alunite is predicted to form. In the fluid-dominated regime, low-temperature reactions produce smectite, hematite and diaspore. At higher temperatures chlorite is predicted to substitute smectite/diaspore and occurs together with minor hematite.

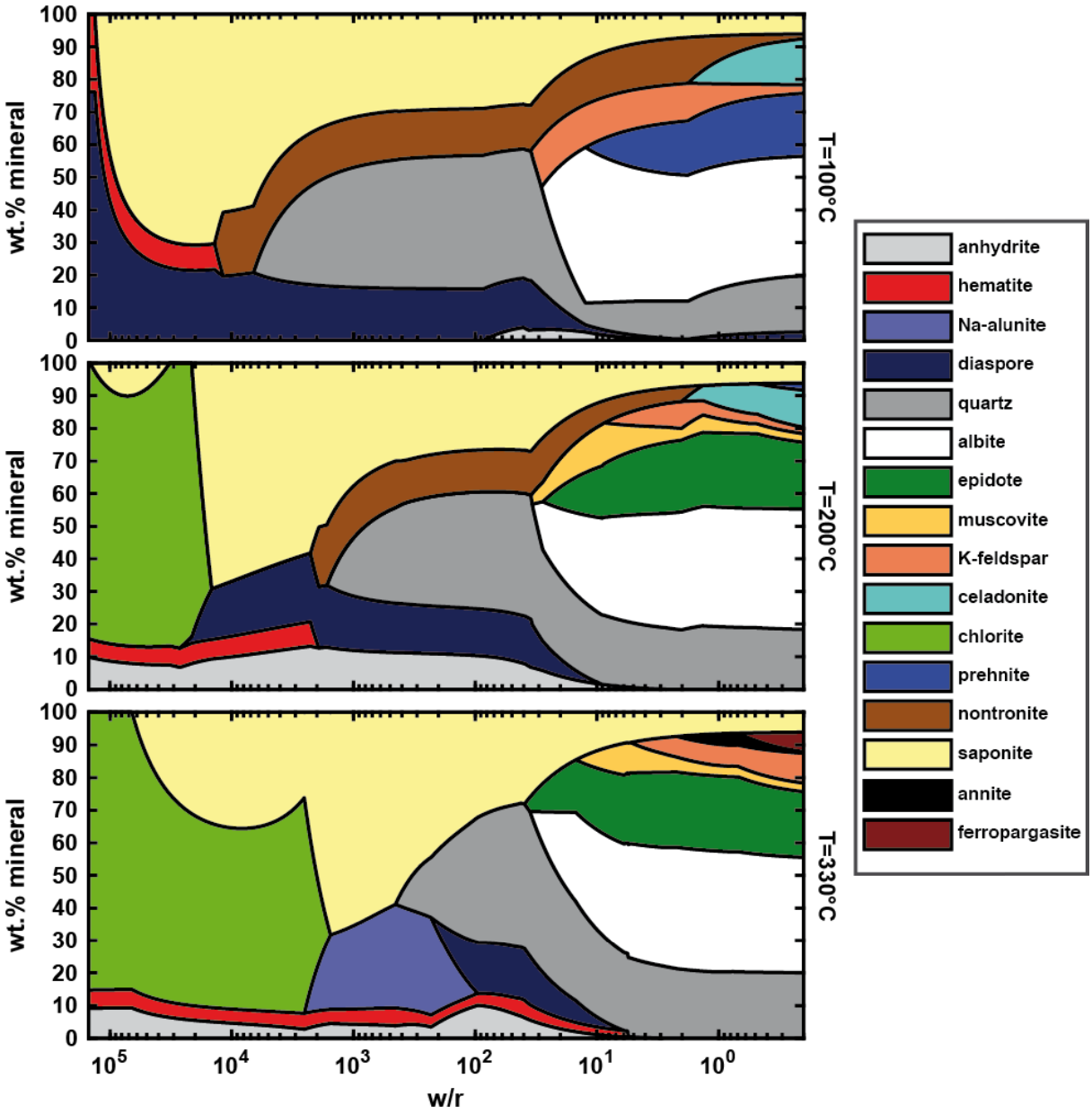

Figure 4.8: Secondary mineral assemblages predicted by reaction path models for hydrothermal fluids in equilibrium with Brothers' high-K dacite at varying temperatures.

We also investigated how host-rock compositions influence the mineralogy of alteration products. We performed reaction path models in which seawater reacted with the three different host-rock types (Haungaroa's basaltic andesite, Brothers' high-K dacite and Macauley's low-K dacite) at 280 °C (Figure 4.9). Secondary assemblages are generally very similar, but differences occur at low w/r for Brothers, where K-Feldspar is predicted. Minor amounts of magnetite appear in the reaction paths, with exception of Brothers. For basaltic andesite from Haungaroa, K-feldspar and muscovite are missing at low w/r and are substituted by prehnite and minnesotaite. At intermediate w/r all three rocks result into the same alteration assemblage consisting of smectite, quartz, diaspore, hematite and anhydrite. Hematite is more abundant at

Haungaroa compared to the other reaction paths. Also, at high w/r, the three volcanic rocks result in the same alteration mineralogy and all compose of chlorite, hematite and minor smectite. At Haungaroa significantly more hematite is predicted to precipitate and at Brothers, when the rocks are intensively altered, additionally anhydrite is predicted to precipitate.

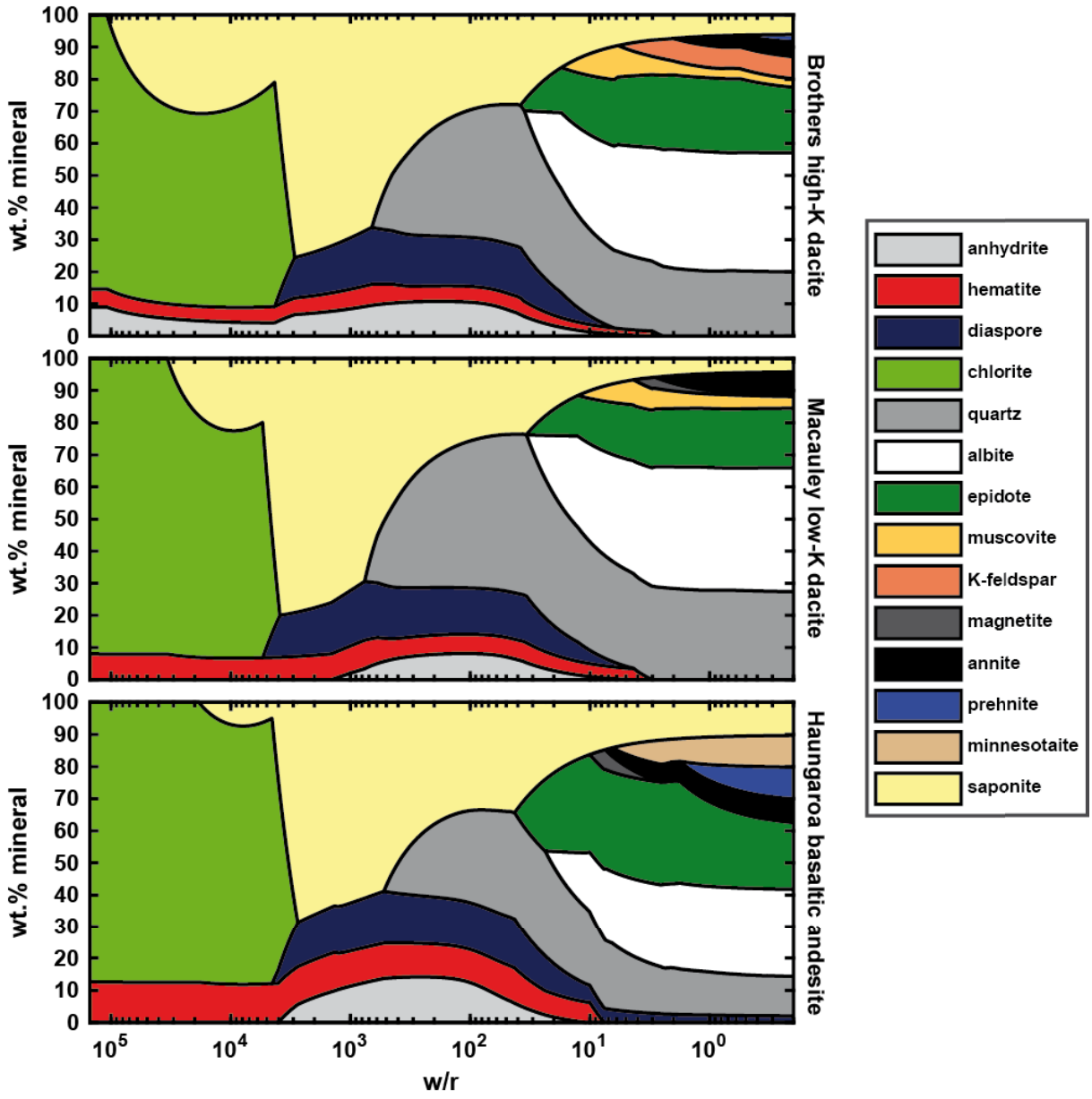

Figure 4.9: Secondary mineral assemblages predicted by reaction path models for seawater in equilibrium with varying rock types at 280 °C.

Additionally, we investigated the role of magmatic volatile input during hydrothermal alteration of host rocks. We used two scenarios: (1) Brothers Caldera high-K dacite reacted with seawater at 200 °C while SO_2 and CO_2 were added in a molar ratio of 3:1; (2) Low-K dacite from Macauley Caldera reacted with seawater at 150 °C while SO_2 and CO_2 were added in a molar

ratio of 8:1. The fluids produced by using these molar ratios resemble actual fluid compositions of the two vent sites (Diehl et al., in prep., Chapter 5). The predicted alteration assemblages are markedly different from the scenarios without volatile input (Figure 4.10). Alteration assemblages consist of quartz, Na-alunite, anhydrite and pyrite over a wide range of w/r. At very high w/r, large proportions of anhydrite with diaspore and minor amounts of hematite, smectite or chlorite are predicted to form.

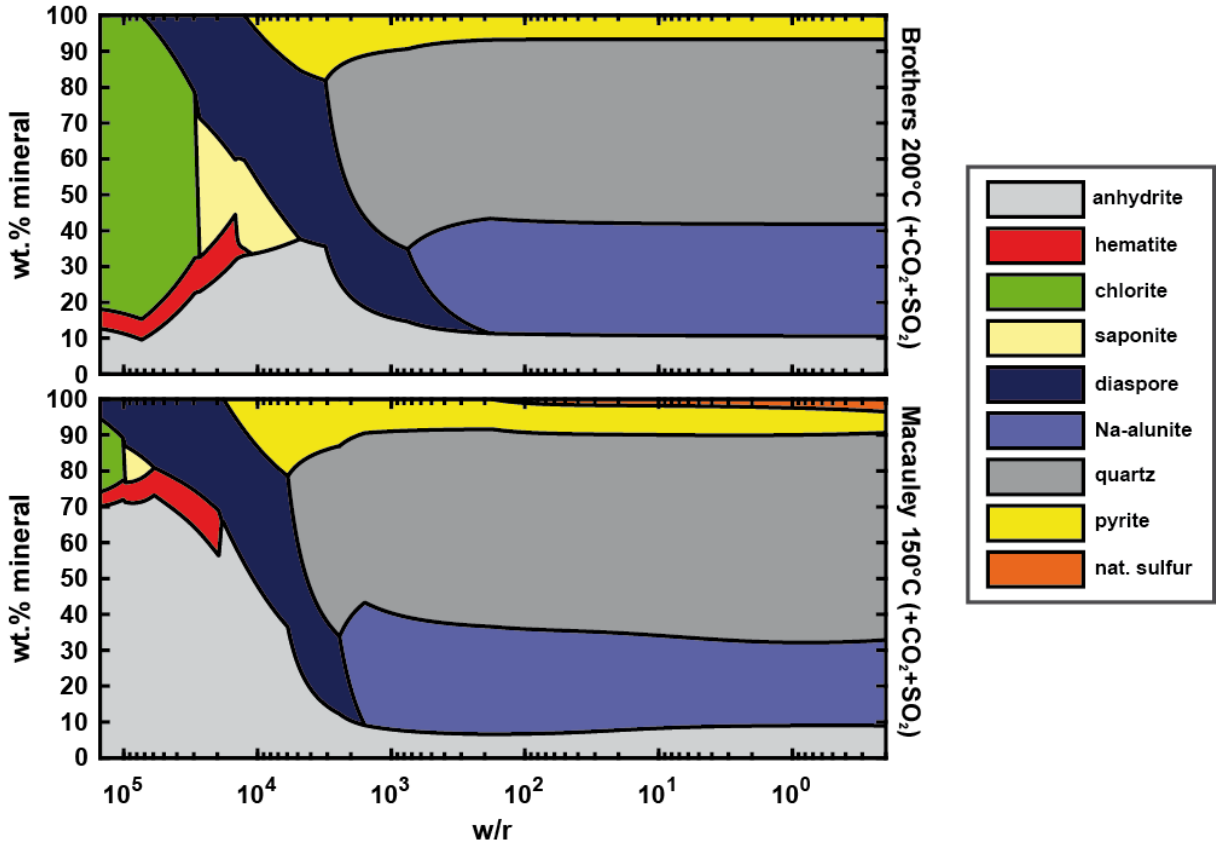

Figure 4.10: Secondary mineral assemblages predicted by reaction paths models for seawater and magmatic volatiles in equilibrium with dacitic rocks from Brothers and Macauley.

4.3.7 Mineral precipitation during seawater entrainment

We calculated mixing models between seawater and hydrothermal vent fluids deduced in Section 4.3.6 with Geochemists Workbench (the compositions of the vent fluids are plotted along with the corresponding reaction paths in Appendix 4.A1-A5). These calculations allow the investigation of potential mineralization processes during seawater entrainment and mixing with ascending hydrothermal fluids in the subseafloor and in chimneys. The modeled fluids were generated by subsurface fluid-rock interactions at w/r = 100 and w/r = 10 and their composition comprises major element (and volatile) concentrations similar to those measured

in vent fluid samples collected from the respective hydrothermal sites at the three volcanoes (cf. Diehl et al., in prep, Chapter 5).

We can investigate the phase relations during mixing between seawater and hydrothermal vent fluids in T-X sections in which temperature and mixing ratios (F_{Sw}, the mass fraction of seawater in the fluid mixture) of the hydrothermal fluids are varied (Figure 4.11-12). The hydrothermal endmember is situated in the lower right corner of the diagrams ($T = T_{endmember}$, $F_{Sw} = 0$; i.e. a pure hydrothermal fluid with its end-member temperature). Seawater is situated in the upper left corner ($T = T_{seawater}$, $F_{Sw} = 1$; pure seawater with T = 5 °C). The diagonal line represents a batch mixing process, where mixing of a hot hydrothermal fluid with cold seawater solely controls the temperature. Below the diagonal line the mixing process is accompanied by conductive cooling, whereas above the mixing line conductive heating occurs (Figure 4.11-A1). The colored lines, with corresponding mineral abbreviations, represent predicted mineral precipitation (phase stabilities) during the mixing process with variable temperatures and fluid mixing conditions. A colored frame encompassing the plane indicates the mineral is stable throughout the T-X range of the entire plane (Figure 4.11-A2).

The mixing models for Haungaroa show that fluids generated with different w/r ratios lead to remarkably different sulfide mineral assemblages (Figure 4.11-B1-C2). A fluid generated by reacting Haungaroa basaltic andesite and seawater with a w/r = 100 is predicted to precipitate pyrite over the entire range of the T-X conditions. Following a batch mixing path, the formed mineral assemblages would be chalcopyrite, followed by chalcopyrite + tennantite, followed by bornite + tennantite, then covellite + tennantite and, finally, covellite (Figure 4.11-B1). Orpiment and sphalerite are only stable under conditions of extreme conductive cooling with minor entrainment of seawater. The predicted sulfates and oxides are barite (over the entire range of T-X), anhydrite (at T > 150 °C and preferably at high seawater fractions) and chalcedony (at T < 250 °C and preferably under conductive cooling conditions) (Figure 4.11-B2). Furthermore, hematite/goethite is predicted to form over a large range of T-X conditions except for those that come with excessive conductive cooling. For sulfate and oxide minerals, the second model run for Haungaroa fluids with a w/r < 10 results in similar mineral parageneses, except that goethite and hematite are not predicted to form (Figure 4.11-C2). For the sulfide parageneses, however, drastic changes occur: Cu-bearing minerals are not predicted to be stable, except for covellite which, together with pyrite, is stable in the entire T-X plane (Figure 4.11-B2). Sphalerite stability increased to a large extend and is now predicted to precipitate at all mixing ratios and temperatures ≤ 200 °C. Additionally, realgar appears at temperatures below 100 °C.

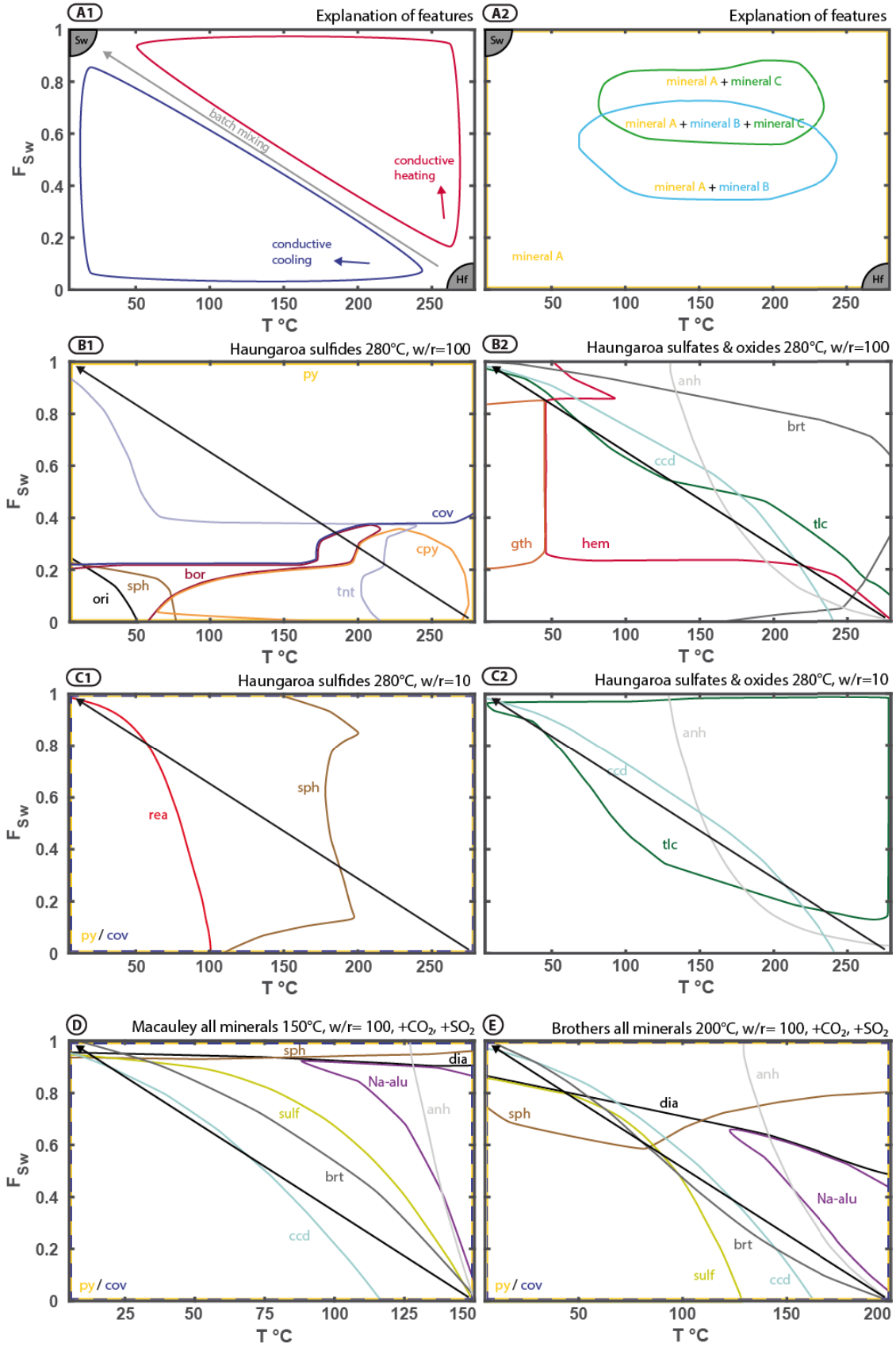

Figure 4.11: Explanatory figure (A1-A2), mixing models for Haungaroa (B1-C2) and gassy fluids at Macauley (D) and Brothers (E). Mineral abbreviations: anh: anhydrite; bor: bornite; brt: barite; ccd: chalcedony; cov: covellite; cpy: chalcopyrite; dia: diaspore; gth: goethite; hem: hematite; Na-alu: natroalunite; ori: orpiment; py: pyrite; rea: realgar; sph: sphalerite; sulf: native sulfur; tlc: talcum; tnt: tenanntite.

Four mixing model runs were conducted for Brothers high-K dacite (Figure 4.12-A1-D2). We tested mixing of hydrothermal fluids equilibrated at 280 °C and 330 °C (two typical temperatures of fluids at the North West Caldera Wall vent site) each at w/r = 10 and w/r = 100. The predicted mineral precipitation in the first model for Brothers at 280 °C and w/r = 100 (Figure 4.12-A1-A2), is similar to the model for Haungaroa. Hydrothermal fluids that undergo batch mixing with seawater first precipitate chalcopyrite + pyrite then tennantite + pyrite and finally covellite + pyrite. The bornite stability field has retreated from the line of batch mixing and bornite is only expected to precipitate where massive conductive cooling takes place. Sphalerite and orpiment, identical to Haungaroa, will only precipitate where extreme conductive cooling dominates. The predicted oxide and sulfate assemblages also are very similar to the assemblages predicted for Haungaroa. During batch mixing at high temperatures, barite and anhydrite are predicted together with hematite. At lower temperatures and higher seawater dilutions chalcedony forms together with hematite and barite. When conductive heating takes place, talcum may form.

The second model for a fluid that re-equilibrated with Brothers rocks in the subsurface with a w/r = 10 at 330 °C (Figure 4.12-B1-B2), predicts similar phase relations as at 280 °C. Under these conditions, sulfide precipitation is not expected from mixtures with < 30% seawater. Only oxides and sulfates, in particular hematite + anhydrite + barite, are predicted to form. Upon further dilution during batch mixing the sequence of sulfide assemblages is chalcopyrite, followed by chalcopyrite + pyrite, tennantite + pyrite and finally covellite + pyrite. With extreme conductive cooling bornite might form and sphalerite is completely missing. Talcum + magnetite + barite + anhydrite may form with conductive heating or mixing with heated seawater.

The last set of mixing models addresses the formation of moderate-temperature (150-200 °C) hydrothermal fluids that originate when hydrothermal fluids in equilibrium with rock (here: high-K dacite from Brothers and the low-K dacite from Macauley) interact with inflowing magmatic fluids rich in CO_2 and SO_2 (Figure 4.11-D-E). The phase assemblages created during mixing with seawater are considerably different from the previous mixing models. Since less minerals are predicted to form, here all minerals are plotted along one T-X section. Predicted phase assemblages during batch mixing are pyrite + covellite, which are overall stable in variable temperature and mixing stages, together with barite and native sulfur. At high dilutions with seawater chalcedony accompanies the mentioned assemblage. Conductive cooling results in the same mineral paragenesis, whereas conductive heating would suppress the formation of native sulfur and chalcedony and lead to precipitation of anhydrite and Na-alunite. At high dilution with seawater sphalerite is predicted to form.

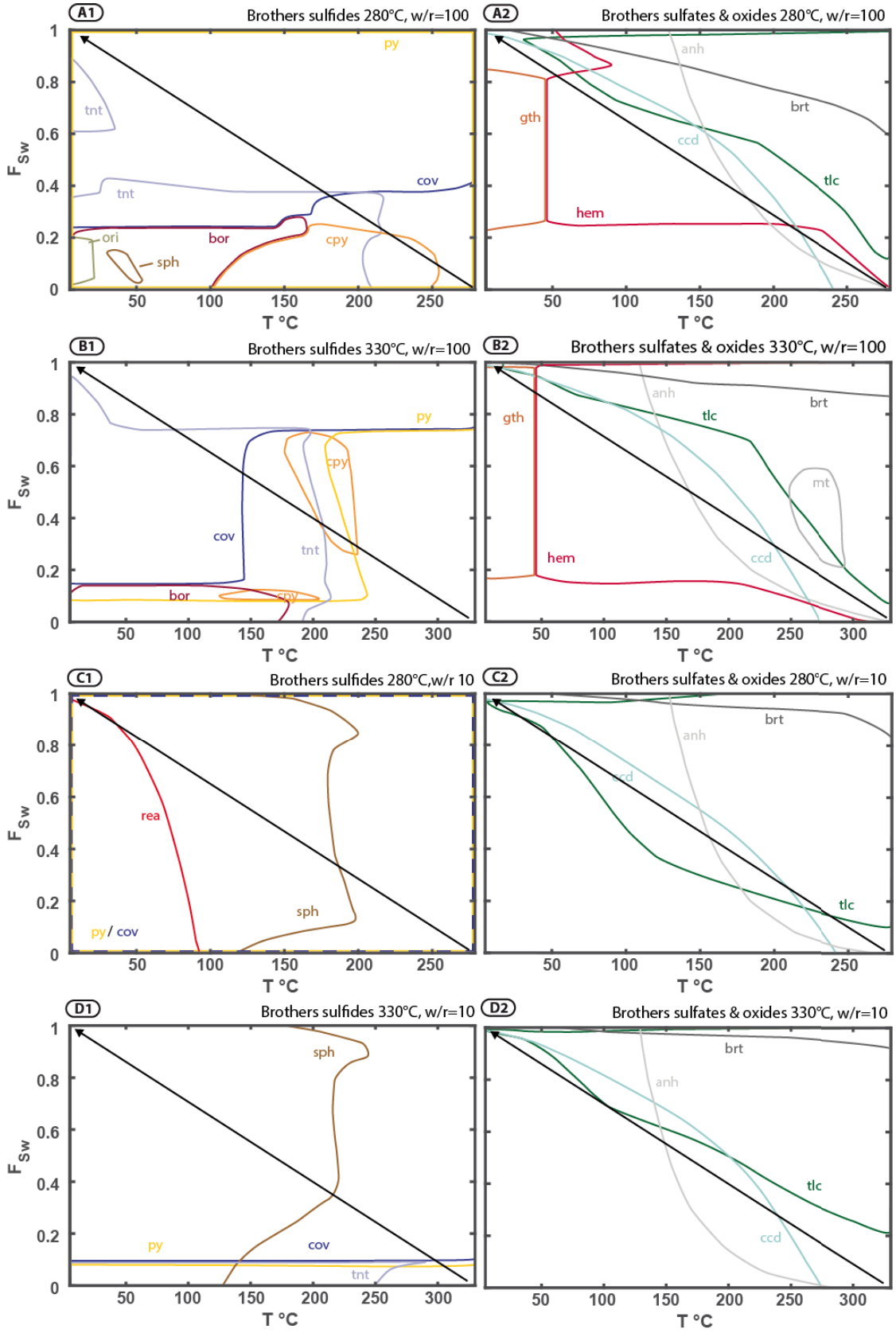

Figure 4.12: Mixing models for the Brothers NW Caldera wall vent field. Mineral abbreviations: anh: anhydrite; bor: bornite; brt: barite; ccd: chalcedony; cov: covellite; cpy: chalcopyrite; dia: diaspore; gth: goethite; hem: hematite; mt: magnetit; Na-alu: natroalunite; ori: orpiment; py: pyrite; rea: realgar; sph: sphalerite; sulf: native sulfur; tlc: talcum; tnt: tenanntite.

4.4 Discussion

4.4.1 The role of volcanic basement composition on fluid-rock reactions and mass balance

Our investigations reveal that both bulk compositions and primary mineralogy from pristine volcanics from Macauley Caldera (low-K dacite), Brothers Caldera (high-K dacite) and Haungaroa Volcano (andesitic basalt), are typical examples for the respective rock types. The rocks are hence appropriate reactants to be used in our reaction path models.

Of particular interest is the high-K nature of Brothers dacite rocks, which might be due to magma differentiation in a thick arc crust (Best, 2003). However, seismic and gravimetric structural analyses of the South Kermadec Arc reveal a rather thin crust in the area where Brothers Caldera is situated (Basset et al., 2016).

$^{87}Sr/^{86}Sr$ isotopes of unaltered volcanics for Brothers Caldera and Haungaroa Volcano are considerably more radiogenic (0.704037 ± 0.000133; n = 6) than compositions from Macauley Caldera (0.703544 ± 0.000035; n = 2). These values span a typical range for island arc igneous rocks (cf. Gamble et al., 1993, 1996; Ewart et al., 1998; Haase et al., 2002, 2006; Timm et al., 2014). The different signatures are probably a consequence of element recycling processes during the subduction process of the Hikurangi Plateau that has formerly extended about 250 km further northwards (Timm et al., 2014) and hence influences Brothers and Haungaroa volcanics but not Macauley rocks. The different isotope signatures in pristine volcanics from the three working areas come to bear in determining the effect of fluid-rock reactions. Our study shows that the pronounced differences in volcanic basement compositions (e.g. basaltic andesite versus dacite) have little effect on the results of the reaction path models, both in terms of rock mineralogy and fluid composition. Both dacitic volcanoes (Brothers and Macauley) degas SO_2, as expected for differentiated magmas of arc volcanoes (e.g. Wallace, 2001). The less differentiated magma of basaltic andesite composition at Haungaroa does not degas SO_2, and hence, advanced argillic alteration and native sulfur deposits are not developed in these hydrothermal systems. The non-reactive nature of CO_2 in hydrothermal fluids at high temperatures (Bischoff & Rosenbauer, 1996) comes with a very minor effect of magma degassing at Haungaroa. Thus, whereas the substrate compositions have a negligible effect on vent fluid compositions, the degassing fluxes that reflect different magma compositions do notably influence fluid-rock reactions in the South Kermadec Arc hydrothermal systems.

Assessing the local variability of Sr isotope composition allows the comparison of the Sr isotope signature of hydrothermal fluids with those of the fresh volcanic rock for all three working areas. We used the Sr isotope compositions of the altered rocks to compute integrated

water-to-rock ratios for fluid-rock reactions in a range between 5 and 30 for closed system behavior. Lower values (0.8 to 1.5) are computed for open systems (i.e. $^{87}Sr/^{86}Sr$ of fluid is indistinguishable from recharging seawater). Because in seafloor hydrothermal systems recharging seawater does exchange Sr with the basement, the estimates for closed systems are probably more reasonable. Water-to-rock ratios from this type of geochemical mass balance refer to simple Sr exchange between host-rocks and fluids. Such mass balance calculations do not consider precipitation or dissolution of Sr-bearing phases. The occurrence of anhydrite in chimneys and some altered host-rocks, as well as Sr concentrations of hydrothermal fluids that considerably deviate from seawater Sr concentrations, demonstrate that these assumptions are not satisfied in the investigated hydrothermal environments. When a fluid loses or gains Sr during the process of alteration, the result of the mass balance is considerably shifted towards higher or lower values, respectively. Strontium concentrations in most altered rocks are considerably higher than Sr concentrations of pristine volcanics, suggesting that Sr is lost from the fluid during alteration. This would lead to an underestimation of the water-to-rock ratio by isotope mass balances. Also, in these rock alteration systems, the inflowing fluids are less radiogenic than seawater. In consequence, by assuming seawater Sr isotopic composition of the fluids, the calculated water-to-rock ratios are likewise minimum values. In the stockwork zone at NW Caldera, for instance, the interacting fluids are mixtures of seawater and upwelling hydrothermal fluids. The true time-integrated water-to-rock ratios are hence likely much higher than the values obtained from the simple mass balance approach. Likewise, chemical mass balance arguments provide non-unique solutions that are different for each element considered. We therefore argue, that results from isotopic and chemical mass balance computations are problematic and therefore a better approach is to use the overall phase relations of fluid-rock reactions as a guide to fluid fluxes.

4.4.2 Reaction path models and conditions of formation of intensely altered volcanics

Our reaction path models demonstrate that changing water-to-rock ratios during alteration may be a dominant factor in determining the alteration mineralogy. The models further suggest that host-rock composition variations (andesitic basalt to dacite) do not have a strong control on different mineralization types in the subsurface. The major difference occurs at low water-to-rock ratios (w/r < 10) at which Brothers and Macauley rocks are predicted to form assemblages of potassic alteration (fluids in equilibrium with those rocks are predicted to form K-feldspar and muscovite). Fluids in thermodynamic equilibrium with the basaltic andesite at Haungaroa are predicted to produce an assemblage of minnesotaite + prehnite instead of the K-bearing

phases. All rock types develop the same mineral assemblages for higher water-to-rock ratios (w/r > 30). At water-to-rock ratio of roughly 30-3000, assemblages of quartz + diaspore + smectite and minor hematite and anhydrite are predicted. The composition shifts into a quartz-free assemblage of chlorite + smectite + hematite at even higher water-to-rock ratio. The results suggest that the host rock types do not play a major role in determining the subsurface mineral assemblages. This is in accordance with experimental studies on fluid-rock interactions suggesting broadly similar results for interaction of seawater with more silicic rocks and basalt, respectively (Hajash & Chandler, 1982; Shiraki et al., 1987). In turn, when variable starting composition of rocks all grade into nearly the same alteration assemblage, this means that the net element flux may be considerably variable for interaction of hydrothermal fluids with different host rocks types.

Using the high-K dacite from Brothers Caldera, we investigated how the alteration temperature affects potential subsurface mineralization. Temperature controls the extent of rock alteration (related to w/r) and timing when one assemblage grades into another. High-temperature fluids turn host-rocks faster into a fluid-dominated alteration assemblage compared to intermediate- and low-temperature fluids. Overall, temperature, like host-rock compositions, seems to barely affect the mineral assemblages in the subsurface.

The addition of magmatic volatiles in the form of large amounts of SO_2 and CO_2 has a profound impact on mineral assemblages, as well as fluid compositions. When acid-sulfate-type fluids equilibrate with dacitic host-rocks, the predicted mineral assemblages consist of quartz + alunite + pyrite for a wide range of water-to-rock ratios. This is exactly the assemblage we observed in the advanced argillic alteration sample from Macauley. Bulk rock compositions suggest that fluids have been effectively leached of alkaline elements and metals from the original pristine rock. K, Ca, Cu, Fe and Al concentrations are considerably lower than for altered rocks at Brothers NW Caldera Wall, although the rock is composed of alunite and pyrite. This shows how effective low-pH, volatile-driven hydrothermal fluids leach host-rocks and also how fluid immobile elements as Al may be mobilized during alteration under low-pH conditions (Inoue, 1995; Gamo et al., 1997; Resing et al., 2007; Butterfield et al., 2011; Seewald et al., 2015). Mineralogy and compositions of the assemblage as well as the sampling location suggest that the sample originated in the upflow zone of the volatile-rich white-smoker vents at Macauley. This alteration type is common in other areas of acid-sulfate-type venting, e.g. the eastern Manus Basin (Gena et al., 1997; Seewald et al., 2015).

At Brothers NW Caldera Wall, faulting has exposed altered basement from underneath active vent fields, which allows to examine processes in the hydrothermal upflow zone. Four alteration types can be distinguished and are interpreted to represent different parts of the upflow zone. Alteration *Type I* (sample 064-3R) shows an assemblage dominated by quartz + illite. The

primary texture of the brecciated rock is preserved but former phenocrysts are turned into the similar assemblages of illite + smectite + quartz that may be termed argillic or intermediate argillic. The altered clasts are cemented by a matrix of pure quartz. Reaction path models suggest that quartz abundance is high for low-intermediate extents of fluid-rock interactions. Furthermore, sample 064-3R has the most non-radiogenic Sr isotope signature and may hence represent the lowest water-to-rock ratio of all samples. The lack of anhydrite and chlorite suggests that the rock has not been exposed to entrainment and heating of seawater. The rock has high amounts of K, Al and Si; Mg, Cu and Zn are not enriched. The rock is also not mineralized, as Cu and Zn concentrations are low. This alteration type may represent less intense fluid-rock interaction in a part of the system where fluid flow was subdued, but temperatures were still elevated due to vent fluid discharge nearby.

The second alteration assemblage (sample 081-6R) consists of large amounts of chlorite + illite (propylitic alteration). The completely altered groundmass is very rich in Mg and Fe and depleted in alkalis. Pyrite is the only abundant sulfide phase; the rock is not enriched in Cu or Zn. High Mg concentrations reflect abundant chlorite and suggest that the rock forms in a place, where interacting fluids effectively loose Mg. At the same time, the Si concentration of the rock is considerably lower than in pristine volcanics, which suggest that the same fluids that precipitated Mg were able to effectively mobilize Si. We propose, that this rock has formed in the vicinity of the hydrothermal upflow zones, where seawater is heated before it enters the upflow zone to mix with the rising hydrothermal fluid.

A third type of alteration (sample 064-9R) is an anhydrite-cemented breccia. The clasts are altered to an assemblage of illite + chlorite + anhydrite + smectite (propylitic alteration). A network of anhydrite veins invaded and partially replaced the rock, making up > 50 vol% of the rock. High Ca concentrations of the clasts are further testament for replacive anhydrite. Abundant pyrite mineralization occurs mostly at the contacts between the clasts and the anhydrite veins; neither Cu nor Zn are enriched. The abundant anhydrite veins and the occurrence of chlorite may result from entrainment (and rapid heating) of high proportions of seawater in the hydrothermal upflow zone. The Sr isotopic composition of this sample is most radiogenic, which is also indicative of high extent of seawater entrainment. We conclude that alteration *Type II* and *Type III* both represent part of the discharge zone that are influenced by seawater entrainment. The high abundance of anhydrite in *Type III* indicates that the entrained seawater was heated to temperatures > 150 °C.

A fourth alteration type is represented by samples 085-5R to 085-8R from an outcrop of the stockwork zone underneath an active hydrothermal vent. The clasts of former volcanic rock are completely replaced by quartz + illite + smectite + pyrite (argillic alteration). They are embedded in a dense network of massive pyrite veins. The pyrite mineralization extends into

the clasts to a point where the rocks are completely replaced by pyrite (sample 085-8R2). Pyrite veins sometimes contain small amounts of chalcopyrite or sphalerite and the rocks are significantly enriched in Cu and Zn compared to the unaltered host-rocks. Concentration of Cu and Zn do not exceed 1 wt.% in the seven subsamples analyzed. Single barite veins or single larger barite crystals are also apparent. The rock type is believed to form directly within the upflow zone of the hydrothermal fluids but at a shallow level where entrainment of seawater is accompanied by considerable cooling.

4.4.3 Mixing model results and implications for chimney mineralization

Sulfide-sulfate chimneys form where high-temperature hydrothermal fluids discharge and mix with cold seawater. Within the walls on an active chimney, strong gradients in temperature and fluid composition may develop, which are governed by complex permeability structures and tortuous fluid flow (e.g. Tivey, 1995; Berkenbosch et al., 2012, 2015). The equilibrium phase relations across the entire range of temperatures and fluid compositions can be assessed by T-X sections. Also, reaction path models can be computed to predict the sequence and abundance of precipitating phases along specific paths of mixing between hydrothermal fluids and seawater.

Phase assemblages found in chimneys at Brothers NW Caldera Wall and Haungaroa may be classified in three mineralization types and two textural types of chimneys. Textural chimney *Type A* has an inner conduit that is lined by a mm- to cm-thick inner wall composed of massive sulfide at its center. This inner conduit wall is either composed of chalcopyrite (*Type I*) or tennantite ± chalcopyrite (*Type II*). The middle part of the chimney wall shows variable mineral proportions that can be dominated by pyrite (*Type I*) or by sphalerite and barite (*Type II*). The outer wall is composed of silicified oxyhydroxide crusts. Textural *Type B* lacks an inner conduit. The entire chimney wall texturally and compositionally resembles the middle part of the chimney wall of *Type A*. This structure implies a particular flow regime, since the massive inner conduit and the outer wall are zones of low permeabilities compared to the porous middle part of wall. The inner conduit does not come into contact with large amounts of seawater and fluids may hence flow through these parts without being diluted by seawater. Our models correctly predict that chalcopyrite (at Brothers NW Caldera) and tennantite (at Haungaroa) are precipitates that form at high temperatures upon little cooling and mixing with seawater.

The central wall is a place where the input of undiluted hydrothermal fluid is diminished by the inner wall, whereas the input of seawater is diminished by the outer wall. In the central wall the permeability is extremely high because minerals grow as spherical aggregates with large cavities between them. In this zone, the mixing regime may be extremely variable and various mixtures between hydrothermal fluids and seawater may occur and conductive cooling as well

as conductive heating may take place to different extents. Our models predict that the main precipitates in the central part of the T-X planes should be pyrite, sphalerite and barite; these phases are indeed observed in the samples. For the Brothers NW Caldera site and the vent field at Haungaroa our mixing models predict similar results. Mixing between endmember fluids with different temperatures tested for Brothers results in shifts of the predicted minerals according to temperature and mixing ratios, but does not affect the overall phase relations to a large degree.

In contrast, different water-to-rock ratios for the hydrothermal fluids seem to have a strong impact on the predicted minerals. Fluids at w/r = 10 are predicted to form mainly pyrite, covellite and sphalerite during a batch mixing without conductive heat transfer. At high dilution factors also realgar is predicted. Fluids that have equilibrated at w/r = 100 are predicted to form a different sulfide parageneses than fluids equilibrated at w/r = 10. When these fluids mix with seawater, sphalerite is not expected to precipitate upon batch mixing. Instead, sphalerite is stable only in a very narrow range for considerably cooled and seawater-dominated mixtures. The high water-to-rock ratios endmember fluids predict a precipitate succession of chalcopyrite over tennantite to covellite upon increasing dilution factors. Another difference is that these fluids predict the precipitation of hematite over wide ranges of temperatures and mixing-regimes, as well as goethite for seawater-dominated mixtures.

The reaction path and mixing models suggest that two types of hydrothermal fluids are involved in the mineralization of high-temperature black smoker type chimneys. Fluids generated at high water-to-rock ratios that subsequently mix with seawater are responsible for the formation of structural *Type I* chimneys, which contain valuable polymetallic sulfides (tennantite and chalcopyrite). These polymetallic sulfides seem to form from relatively undiluted high-temperature hydrothermal fluids that traverse the inner conduit of the structure. A key role in creating a chimney structure, which permits ascending fluids not to entrain large proportions of seawater, plays the formation of silicified oxyhydroxide crusts; these are also predicted for this mineralization type at high water-to-rock ratios.

The second mineralization type predicted by the reaction path and mixing models originates when fluids generated at a lower water-to-rock ratios of 10 mix with seawater. The mixing models predict extensive sphalerite precipitation to occur whereas polymetallic sulfides are completely absent. Also, hematite and goethite are absent and thus, this type of mineralization will not lead to structural *Type I* chimneys. The analogy between the two fluids is that pyrite and barite are stable for all mixing regimes. Some chimneys expose characteristics of both mineralization types and suggest that the type emanating single chimneys may temporally and spatially be variable.

Our general findings are in excellent agreement to previous mineralogical investigations on precipitates from the NW Caldera Wall vent field (Berkenbosch et al., 2012) which also classified the three mentioned zones of mineralization in single chimneys as well as four different chimney types that are proposed to form simultaneously along the vent field from different types of hydrothermal fluids. The fourth type composing of an impermeable layer of chalcopyrite + covellite + bornite was not represented in our sample collection but the assemblage is predicted by our reaction paths.

In our chimney *Type III* polymetallic sulfides are missing and the mineralization type is clearly dominated by pyrite and pyrrhotite. Our mixing models were unable to reproduce the formation of pyrrhotite at varying temperatures and water-to-rock ratios. For the formation of pyrrhotite high activities of H_2 and low fugacities fO_2 and fS_2 are required (Kawasumi & Chiba, 2017). For instance, abundant pyrrhotite mineralization are found at chimneys in the Kulo Lasi Caldera where H_2 concentrations exceed 1 mmol (Fouquet et al., 2018). This suggests that hydrogen concentrations in hydrothermal fluids at Brothers Volcano also have exceeded values measured during expedition SO253 (> 20 µmol; Diehl et al., in prep, Chapter 5).

For the Macauley and Brothers Cone sites, we implemented additional runs with gassy fluids at lower temperatures (150 °C and 200 °C, respectively). The mixing model results well explain the different mineralization types.

When gassy endmember fluids mix with seawater, pyrite and covellite are predicted as stable phases. Further, anhydrite, barite and Na-alunite are predicted to precipitate under conductive heating conditions. Most important is that native sulfur is predicted to form when the mixing occurs as batch mixing process without conductive heat transfers or when considerable conductive cooling is involved. We have collected monomineralic specimen of native sulfur at the white-smoker vents at Brothers Cone site as well as at Macauleys venting site. These rock samples contain mm-sized accessory phases of blackish minerals that likely represent the predicted sulfides; the samples were, however, not yet investigated in greater detail.

This result, together with the reaction path models, suggests that our approach with gassy fluids is predictive for the subsurface processes occurring below white-smoker vents. The reaction path model predicts the right alteration assemblages (sample 013-1R) in the subsurface and our mixing models predict native sulfur to form when the hydrothermal end-member fluids mix with seawater. The depletion of alkalis and metals in the advanced argillic altered rock is typical for acid-alteration fluids that consequently form metal-rich brines.

4.5 Summary and Conclusions

Our study demonstrates that variable extents of subsurface fluid-rock reactions are responsible for different mineralization types found at the hydrothermal systems of Brothers NW Caldera Wall and Haungaroa. Altered rocks, which seem to have formed in the seawater dominated region close to hydrothermal upflow zones, represent either argillic assemblages of quartz + illite + smectite or comprise extensive amounts of chlorite (propylitic alteration). Reaction path models predict quartz-rich alteration assemblages for fluids in equilibrium with rocks at low-intermediate water-to-rock ratios and quartz-free but chlorite-rich assemblages for fluids in equilibrium with rocks at high water-to-rock ratios. Where hydrothermal fluids in the subsurface equilibrate at low water-to-rock ratios, ascend and subsequently mix with seawater, sphalerite-rich mineralization occur in chimneys and the underlying stockwork zone. Where fluids equilibrate at high water-to-rock ratios they tend to form valuable polymetallic sulfide deposits in chimneys and the underlying substrate. Varying temperatures and extents of subsurface alteration lack to explain a third mineralization type that includes the formation of pyrrhotite bearing chimneys. The mineralization type might indicate that hydrothermal fluids at the North West Caldera Wall temporally contained higher hydrogen concentrations favoring reducing conditions. The regular occurrence of polymetallic sulfides and sphalerite in the same chimney suggest that fluids with varying water-to-rock ratios temporally and spatially emanate to variable extents. This might point to variable stages of magmatic input in the subsurface that is reflected by the mineralization type.

The subordinate occurrence of sphalerite at Brothers Volcano suggests that the hydrothermal vent field is rather mature and that the extent of subsurface fluid-rock interaction is in an advanced stadium of hydrothermal alteration. Haungaroa vents represent a rather juvenile vent field where polymetallic sulfides indicating high extents of subsurface alteration but abundant sphalerite mineralizations, mirroring less extents of subsurface fluid-rock interactions.

When gassy fluids react with dacite (Brothers or Macauley) an assemblage of quartz + alunite + pyrite ± native sulfur is predicted. This assemblage matches well observations of an advanced argillic altered sample from Macauley Caldera. When fluids that equilibrate with rocks (and magmatic volatiles) at Brothers Cone sites or at Macauley Caldera rise to the seafloor, they precipitate native sulfur amongst silicates and sulfate, mainly. The models demonstrate, that addition of magmatic volatiles is a favorable scenario for the formation of Brothers Cone site fluids and Macauleys white-smoker vents.

Acknowledgements

We thank Captain Mallon and the crew of the research vessel Sonne on the cruise SO253 for their valuable work at sea. Further the crew of the MARUM Quest team is thanked for many successful dives and the recovery of unique samples. The Bundesministerium für Bildung und Forschung (BMBF) provided financial resources for the project Hydrothermadec (cruise SO253) and this work with grant no. 03G0253B. AD was also partly supported by the MARUM Center for Marine Environmental Science.

References

Baker, E. T., Edmonds, H. N., Michael, P. J., Bach, W., Dick, H. J. B., Snow, J. E., Walker, S. L., Banerjee, N. R., and Langmuir, C. H. (2004). Hydrothermal venting in magma deserts: The ultraslow-spreading Gakkel and Southwest Indian Ridges. Geochemistry, Geophysics, Geosystems, 5(8). doi: 10.1029/2004GC000712.

Baker, E. T., Embley, R. W., Walker, S. L., Resing, J. A., Lupton, J. E., Nakamura, K., de Ronde, C. E. J., and Massoth, G. J. (2008). Hydrothermal activity and volcano distribution along the Mariana arc. Journal of Geophysical Research: Solid Earth, 113(B8). doi: 10.1029/2007JB005423.

Baker, E. T., Walker, S. L., Embley, R. W., and de Ronde, C. E. (2012). High-Resolution Hydrothermal Mapping of Brothers Caldera, Kermadec Arc. Economic Geology. doi: 10.2113/econgeo.107.8.1583.

Baker, E. T. (2017). Exploring the ocean for hydrothermal venting: New techniques, new discoveries, new insights. Ore Geology Reviews, 86:55 – 69. doi: https://doi.org/10.1016/j.oregeorev.2017.02.006.

Barker, S. J., Wilson, C. J. N., Baker, J. A., Millet, M.-A., Rotella, M. D., Wright, I. C., and Wysoczanski, R. J. (2013). Geochemistry and Petrogenesis of Silicic Magmas in the Intra-Oceanic Kermadec Arc. Journal of Petrology, 54(2):351–391. doi: 10.1093/petrology/egs071.

Bassett, D., Kopp, H., Sutherland, R., Henrys, S., Watts, A. B., Timm, C., Scherwath, M., Grevemeyer, I., and de Ronde, C. E. J. (2016). Crustal structure of the Kermadec arc from MANGO seismic refraction profiles. Journal of Geophysical Research: Solid Earth, 121(10):7514–7546. doi: 10.1002/2016JB013194.

Berkenbosch, H. A., de Ronde, C., Gemmell, J. B., McNeill, A. W., and Goemann, K. (2012). Mineralogy and Formation of Black Smoker Chimneys from Brothers Submarine Volcano, Kermadec Arc. Economic Geology, 107(8):1613. doi: 10.2113/econ- geo.107.8.1613.

Berkenbosch, H. A., de Ronde, C. E. J., Paul, B. T., and Gemmell, J. B. (2015). Characteristics of Cu isotopes from chalcopyrite-rich black smoker chimneys at Brothers volcano, Kermadec arc, and Niuatahi volcano, Lau basin. Mineralium Deposita, 50(7):811–824. doi: 10.1007/s00126-014-0571-y.

Best, M. G. (2003). Igneous and Metamorphic Petrology. Blackwell Science Ltd, Second edition.

Bethke, C. M. (2007). Geochemical and Biogeochemical Reaction Modeling. Cambridge University Press, Second edition. doi: 10.1017/CBO9780511619670.

Bird, P. (2003). An updated digital model of plate boundaries. Geochemistry, Geophysics, Geosystems, 4(3). doi: 10.1029/2001GC000252.

Bischoff, J. and Rosenbauer, R. (1996). The alteration of rhyolite in CO_2 charged water at 200 and 350 ˚C: The unreactivity of CO_2 at higher temperature. Geochimica et Cosmochimica Acta, 60(20):3859 – 3867. doi: https://doi.org/10.1016/0016- 7037(96)00208-6.

Butterfield, D. A., Nakamura, K., Takano, B., Lilley, M. D., Lupton, J. E., Resing, J. A., and Roe, K. K. (2011). High SO_2 flux, sulfur accumulation, and gas fractionation at an erupting submarine volcano. Geology, 39(9):803. doi: 10.1130/G31901.1.

de Ronde, C. E., Faure, K., Bray, C. J., Chappell, D. A., and Wright, I. C. (2003). Hydrothermal fluids associated with seafloor mineralization at two southern Kermadec arc volcanoes, offshore New Zealand. Mineralium Deposita. doi: 10.1007/s00126-002- 0305-4.

de Ronde, C. E. J., Hannington, M. D., Stoffers, P., Wright, I. C., Ditchburn, R. G., Reyes, A. G., Baker, E. T., Massoth, G. J., Lupton, J. E., Walker, S. L., Greene, R. R., Soong, C. W. R., Ishibashi, J., Lebon, G. T., Bray, C. J., and Resing, J. A. (2005). Evolution of a Submarine Magmatic-Hydrothermal System: Brothers Volcano, Southern Kermadec Arc, New Zealand. Economic Geology. doi: 10.2113/gsecongeo.100.6.1097.

de Ronde, C. E. J., Massoth, G. J., Butterfield, D. A., Christenson, B. W., Ishibashi, J., Ditchburn, R. G., Hannington, M. D., Brathwaite, R. L., Lupton, J. E., Kamenetsky, V. S., Graham, I. J., Zellmer, G. F., Dziak, R. P., Embley, R. W., Dekov, V. M., Munnik, F., Lahr, J., Evans, L. J., and Takai, K. (2011). Submarine hydrothermal activity and gold-rich mineralization at Brothers Volcano, Kermadec Arc, New Zealand. Mineralium Deposita. doi: 10.1007/s00126-011-0345-8.

de Ronde, C. E. J. and Stucker, V. K. (2015). Chapter 47 - Seafloor Hydrothermal Venting at Volcanic Arcs and Backarcs. In Sigurdsson, H., editor, The Encyclopedia of Volcanoes, pages 823 – 849. Academic Press, Amsterdam, Second edition.
doi: https://doi.org/10.1016/B978-0-12-385938-9.00047-X.

DeMets, C., Gordon, R. G., and Argus, D. F. (2010). Geologically current plate motions. Geophysical Journal International, 181(1):1–80. doi: 10.1111/j.1365- 246X.2009.04491.x.

DeMets, C., Gordon, R. G., Argus, D. F., and Stein, S. (1994). Effect of recent revisions to the geomagnetic reversal time scale on estimates of current plate motions. Geophysical Research Letters, 21(20):2191–2194. doi: 10.1029/94GL02118.

Deniel, C. and Pin, C. (2001). Single-stage method for the simultaneous isolation of lead and strontium from silicate samples for isotopic measurements. Analytica Chimica Acta.
doi: https://doi.org/10.1016/S0003-2670(00)01185-5.

Dziak, R. P., Haxel, J. H., Matsumoto, H., Lau, T. K., Merle, S. G., de Ronde, C. E. J., Embley, R. W., and Mellinger, D. K. (2008). Observations of regional seismicity and local harmonic tremor at Brothers volcano, south Kermadec arc, using an ocean bottom hydrophone array. Journal of Geophysical Research: Solid Earth. doi: 10.1029/2007JB005533.

El-Hinnawi, E. (2016). A new method for the adjustment of Fe_2O_3/FeO ratio in volcanic rocks for the calculation of CIPW norm. Neues Jahrbuch für Mineralogie - Abhandlungen: Journal of Mineralogy and Geochemistry, 193(1):87–93. doi: doi:10.1127/njma/2015/0295.

Embley, R. W., de Ronde, C. E. J., Merle, S. G., Davy, B., and Tontini, F. C. (2012). Detailed Morphology and Structure of an Active Submarine Arc Caldera: Brothers Volcano, Kermadec Arc. Economic Geology. doi: 10.2113/econgeo.107.8.1557.

Ewart, A., Collerson, K. D., Regelous, M., Wendt, J. I., and Niu, Y. (1998). Geochemical Evolution within the Tonga-Kermadec-Lau Arc-Back-arc Systems: the Role of Varying Mantle Wedge Composition in Space and Time. Journal of Petrology, 39(3):331–368.
doi: 10.1093/petroj/39.3.331.

Flanagan, F. and Gottfried, D. (1980). USGS rock standards; III, Manganese-nodule reference samples USGS-Nod-A-1 and USGS-Nod-P-1. USGS Publications Warehouse. doi: 10.3133/pp1155.

Fouquet, Y., Pelleter, E., Konn, C., Chazot, G., Dupré, S., Alix, A., Chéron, S., Donval, J. P., Guyader, V., Etoubleau, J., Charlou, J. L., Labanieh, S., and Scalabrin, C. (2018). Volcanic and hydrothermal processes in submarine calderas: The Kulo Lasi example (SW Pacific). Ore Geology Reviews, 99:314 – 343. doi: https://doi.org/10.1016/j.oregeorev.2018.06.006.

Gamble, J. A., Smith, I. E. M., Graham, I. J., Kokelaar, B. P., Cole, J. W., Houghton, B. F., and Wilson, C. J. N. (1990). The petrology, phase relations and tectonic setting of basalts from the taupo volcanic zone, New Zealand and the Kermadec Island arc - Havre Trough, SW Pacific. Journal of Volcanology and Geothermal Research. doi: https://doi.org/10.1016/0377-0273(90)90055-K.

Gamble, J. A., Smith, I. E. M., McCulloch, M. T., Graham, I. J., and Kokelaar, B. P. (1993). The geochemistry and petrogenesis of basalts from the Taupo Volcanic Zone and Kermadec Island Arc, S.W. Pacific. Journal of Volcanology and Geothermal Research.
doi: https://doi.org/10.1016/0377-0273(93)90067-2.

Gamble, J. A., Woodhead, J., Wright, I., and Smith, I. (1996). Basalt and Sediment Geochemistry and Magma Petrogenesis in a Transect from Oceanic Island Arc to Rifted Continental Margin Arc: the Kermadec-Hikurangi Margin, SW Pacific. Journal of Petrology. doi: 10.1093/petrology/37.6.1523.

Gamo, T., Okamura, K., Charlou, J., Urabe, T., Auzende, J., Ishibashi, J., Shitashima, K., and Chiba, H. (1997). Acidic and sulfate-rich hydrothermal fluids from the Manus back-arc basin, Papua New Guinea. Geology, 25(2):139. doi: 10.1130/0091- 7613(1997)025<0139:AASRHF>2.3.CO;2.

GEBCO (2014). Intergovernmental Oceanographic Commission, IHO, and BODC. Centenary edition of the GEBCO digital Atlas, published on CD-ROM on behalf of the Intergovernmental Oceanographic Commission and the International Hydrographic Organization as part of the General Bathymetric Chart of the Oceans, British Oceanographic Data Centre, Liverpool, U. K.

Gena, K. (1997). Geochemical characteristics of altered basaltic andesite by sulphuric-acid rich solution from the Demos caldera, Manus Basin, Papua New Guinea. JAMSTEC Deep Sea Research, 13:269–285. doi: https://ci.nii.ac.jp/naid/80010064021/en/.

Graham, I. J., Reyes, A. G., Wright, I. C., Peckett, K. M., Smith, I. E. M., and Arculus, R. J. (2008). Structure and petrology of newly discovered volcanic centers in the northern Kermadec southern Tofua arc, South Pacific Ocean. Journal of Geophysical Research: Solid Earth, 113(B8).
doi: 10.1029/2007JB005453.

Gruen, G., Weis, P., Driesner, T., de Ronde, C. E. J., and Heinrich, C. A. (2012). Fluid-Flow Patterns at Brothers Volcano, Southern Kermadec Arc: Insights from Geologically Constrained Numerical Simulations. Economic Geology. doi: 10.2113/econ- geo.107.8.1595.

Haase, K. M., Stroncik, N., Garbe-Schönberg, D., and Stoffers, P. (2006). Formation of island arc dacite magmas by extreme crystal fractionation: An example from Brothers Seamount, Kermadec island arc (SW Pacific). Journal of Volcanology and Geothermal Research.
doi: https://doi.org/10.1016/j.jvolgeores.2005.10.010.

Haase, K. M., Worthington, T. J., Stoffers, P., Garbe-Schönberg, D., and Wright, I. (2002). Mantle dynamics, element recycling, and magma genesis beneath the Kermadec Arc-Havre Trough. Geochemistry, Geophysics, Geosystems. doi: 10.1029/2002GC000335.

Hajash, A. and Chandler, G. W. (1982). An experimental investigation of high-temperature interactions between seawater and rhyolite, andesite, basalt and peridotite. Contributions to Mineralogy and Petrology, 78(3):240–254. doi: 10.1007/BF00398919.

Hannington, M., Jamieson, J., Monecke, T., Petersen, S., and Beaulieu, S. (2011). The abundance of seafloor massive sulfide deposits. Geology, 39(12):1155. doi: 10.1130/G32468.1.

Hawkes, J. A., Connelly, D. P., Rijkenberg, M. J. A., and Achterberg, E. P. (2014). The importance of shallow hydrothermal island arc systems in ocean biogeochemistry. Geophysical Research Letters.
doi: 10.1002/2013GL058817.

Hedenquist, J. W. and Lowenstern, J. B. (1994). The role of magmas in the formation of hydrothermal ore deposits. Nature, 370. doi: https://doi.org/10.1038/370519a0.

Hedenquist, J. W., Simmons, S. F., Giggenbach, W. F., and Eldridge, C. S. (1993). White Island, New Zealand, volcanic-hydrothermal system represents the geochemical environment of high-sulfidation Cu and Au ore deposition. Geology, 21(8):731.

doi: https://doi.org/10.1130/0091-7613(1993)021<0731:WINZVH>2.3.CO;2.

Inoue, A. (1995). Formation of Clay Minerals in Hydrothermal Environments, pages 268–329. Springer Berlin Heidelberg. doi: 10.1007/978-3-662-12648-6-7.

Jicha, B. R. and Jagoutz, O. (2015). Magma Production Rates for Intraoceanic Arcs. Elements, 11(2):105. doi: 10.2113/gselements.11.2.105.

Jochum, K. P., Nohl, U., Herwig, K., Lammel, E., Stoll, B., and Hofmann, A. W. (2005). Georem: A new geochemical database for reference materials and isotopic standards. Geostandards and Geoanalytical Research, 29(3):333–338.

Johnson, J., Oelkers, E., and Helgeson, H. (1992). SUPCRT92: A software package for calculating the standard molal thermodynamic properties of minerals, gases, aqueous species, and reactions from 1 to 5000 bar and 0 to 1000°C. Computers and Geosciences, 18(7):899 – 947.
doi: https://doi.org/10.1016/0098-3004(92)90029-Q.

Kawasumi, S. and Chiba, H. (2017). Redox state of seafloor hydrothermal fluids and its effect on sulfide mineralization. Chemical Geology, 451:25 – 37.
doi: https://doi.org/10.1016/j.chemgeo.2017.01.001.

Keith, M., Haase, K. M., Klemd, R., Smith, D. J., Schwarz-Schampera, U., and Bach, W. (2018). Constraints on the source of Cu in a submarine magmatic-hydrothermal system, Brothers volcano, Kermadec island arc. Contributions to Mineralogy and Petrology.
doi: 10.1007/s00410-018-1470-5.

Koschinsky, A., Thal, J., and Wölfl, A.-C. (2018). Raw multibeam EM122 data: transits of SONNE cruise SO253 (South Pacific). doi: 10.1594/PANGAEA.892787.

Lloyd, E. F., Nathan, S., Smith, I. E. M., and Stewart, R. B. (1996). Volcanic history of Macauley Island, Kermadec Ridge, New Zealand. New Zealand Journal of Geology and Geophysics, 39(2):295–308. doi: 10.1080/00288306.1996.9514713.

Plank, T. and Langmuir, C. H. (1993). Tracing trace elements from sediment input to volcanic output at subduction zones. Nature, 362. doi: https://doi.org/10.1038/362739a0.

Reed, M. H. (1997). Hydrothermal alteration and its relationship to ore fluid composition. In Barnes, H. L., editor, Geochemistry of hydrothermal ore deposits, Third edition.

Resing, J. A., Lebon, G., Baker, E. T., Lupton, J. E., Embley, R. W., Massoth, G. J., Chadwick, Jr., W. W., and de Ronde, C. E. J. (2007). Venting of Acid-Sulfate Fluids in a High-Sulfidation Setting at NW Rota-1 Submarine Volcano on the Mariana Arc. Economic Geology.
doi: 10.2113/gsecongeo.102.6.1047.

Seewald, J., Reeves, E., Bach, W., Saccocia, P., Craddock, P., Shanks, W., Sylva, S., Pichler, T., Rosner, M., and Walsh, E. (2015). Submarine venting of magmatic volatiles in the Eastern Manus Basin, Papua New Guinea. Geochimica et Cosmochimica Acta, 163:178 – 199.
doi: https://doi.org/10.1016/j.gca.2015.04.023.

Shiraki, R., Sakai, H., Endoh, M., and Kishima, N. (1987). Experimental studies on rhyolite- and andesite-seawater interactions at 300°C and 1000 bars. Geochemical Journal, 21(4):139–148.
doi: 10.2343/geochemj.21.139.

Smith, I., Worthington, T., Stewart, R., Price, R. C., and Gamble, J. (2003). Felsic volcanism in the Kermadec arc, SW Pacific: crustal recycling in an oceanic setting. Geological Society, London, Special Publications, 219(1):99–118. doi: 10.1144/GSL.SP.2003.219.01.05.

Smith, I. E., Worthington, T. J., Price, R. C., Stewart, R. B., and Maas, R. (2006). Petrogenesis of dacite in an oceanic subduction environment: Raoul Island, Kermadec arc. Journal of Volcanology and Geothermal Research, 156(3):252 – 265. doi: https://doi.org/10.1016/j.jvolgeores.2006.03.003.

Smith, I. E., Stewart, R. B., Price, R. C., and Worthington, T. J. (2010). Are arc-type rocks the products of magma crystallisation? Observations from a simple oceanic arc volcano: Raoul Island, Kermadec Arc, SW Pacific. Journal of Volcanology and Geothermal Research, 190(1):219 – 234. doi: https://doi.org/10.1016/j.jvolgeores.2009.05.006.

Taylor, H. P. (1977). Water/rock interactions and the origin of H_2O in granitic batholiths. Journal of the Geological Society, 133(6):509–558.

Timm, C., Davy, B., Haase, K., Hoernle, K. A., Graham, I. J., de Ronde, C. E. J., Woodhead, J., Bassett, D., Hauff, F., Mortimer, N., Seebeck, H. C., Wysoczanski, R. J., Caratori-Tontini, F., and Gamble, J. A. (2014). Subduction of the oceanic Hikurangi Plateau and its impact on the Kermadec arc. Nature Communications. doi: https://doi.org/10.1038/ncomms5923.

Tivey, M. (1995). The influence of hydrothermal fluid composition and advection rates on black smoker chimney mineralogy: Insights from modeling tranport and reaction. Geochimica et Cosmochimica Acta, 59(10):1933 – 1949. doi: https://doi.org/10.1016/0016-7037(95)00118-2.

Wallace, P. (2001). Volcanic SO_2 emissions and the abundance and distribution of exsolved gas in magma bodies. Journal of Volcanology and Geothermal Research, 108(1):85 – 106. doi: https://doi.org/10.1016/S0377-0273(00)00279-1.

White, S. M., Crisp, J. A., and Spera, F. J. (2006). Long-term volumetric eruption rates and magma budgets. Geochemistry, Geophysics, Geosystems, 7(3). doi: 10.1029/2005GC001002.

Wright, I., Stoffers, P., Hannington, M., de Ronde, C., Herzig, P., Smith, I., and Browne, P. (2002). Towed-camera investigations of shallow-intermediate water-depth submarine stratovolcanoes of the southern Kermadec arc, New Zealand. Marine Geology, 185(3):207 – 218. doi: https://doi.org/10.1016/S0025-3227(01)00285-7.

Wright, I., Worthington, T., and Gamble, J. (2006). New multibeam mapping and geochemistry of the 30° - 35°S sector, and overview, of southern Kermadec arc volcanism. Journal of Volcanology and Geothermal Research, 149(3):263 – 296. doi: https://doi.org/10.1016/j.jvolgeores.2005.03.021.

Wright, I. C., de Ronde, C. E. J., Faure, K., and Gamble, J. A. (1998). Discovery of hydrothermal sulfide mineralization from southern Kermadec arc volcanoes (SW Pacific). Earth and Planetary Science Letters. doi: https://doi.org/10.1016/S0012- 821X(98)00225-8.

Wright, I. C. and Gamble, J. A. (1999). Southern Kermadec submarine caldera arc volcanoes (SW Pacific): caldera formation by effusive and pyroclastic eruption. Marine Geology. doi: https://doi.org/10.1016/S0025-3227(99)00040-7.

Wysoczanski, R., Wright, I., Gamble, J., E.H. Hauri, E., Luhr, J., Eggins, S., and Handler, M. (2006). Volatile contents of Kermadec Arc-Havre Trough pillow glasses: Fingerprinting slab-derived aqueous fluids in the mantle sources of arc and back-arc lavas. Journal of Volcanology and Geothermal Research, 152(1):51 – 73. doi: https://doi.org/10.1016/j.jvolgeores.2005.04.021.

Yang, K. and Scott, S. D. (1996). Possible contribution of a metal-rich magmatic fluid to a sea-floor hydrothermal system. Nature. doi: https://doi.org/10.1038/383420a0.

Appendix

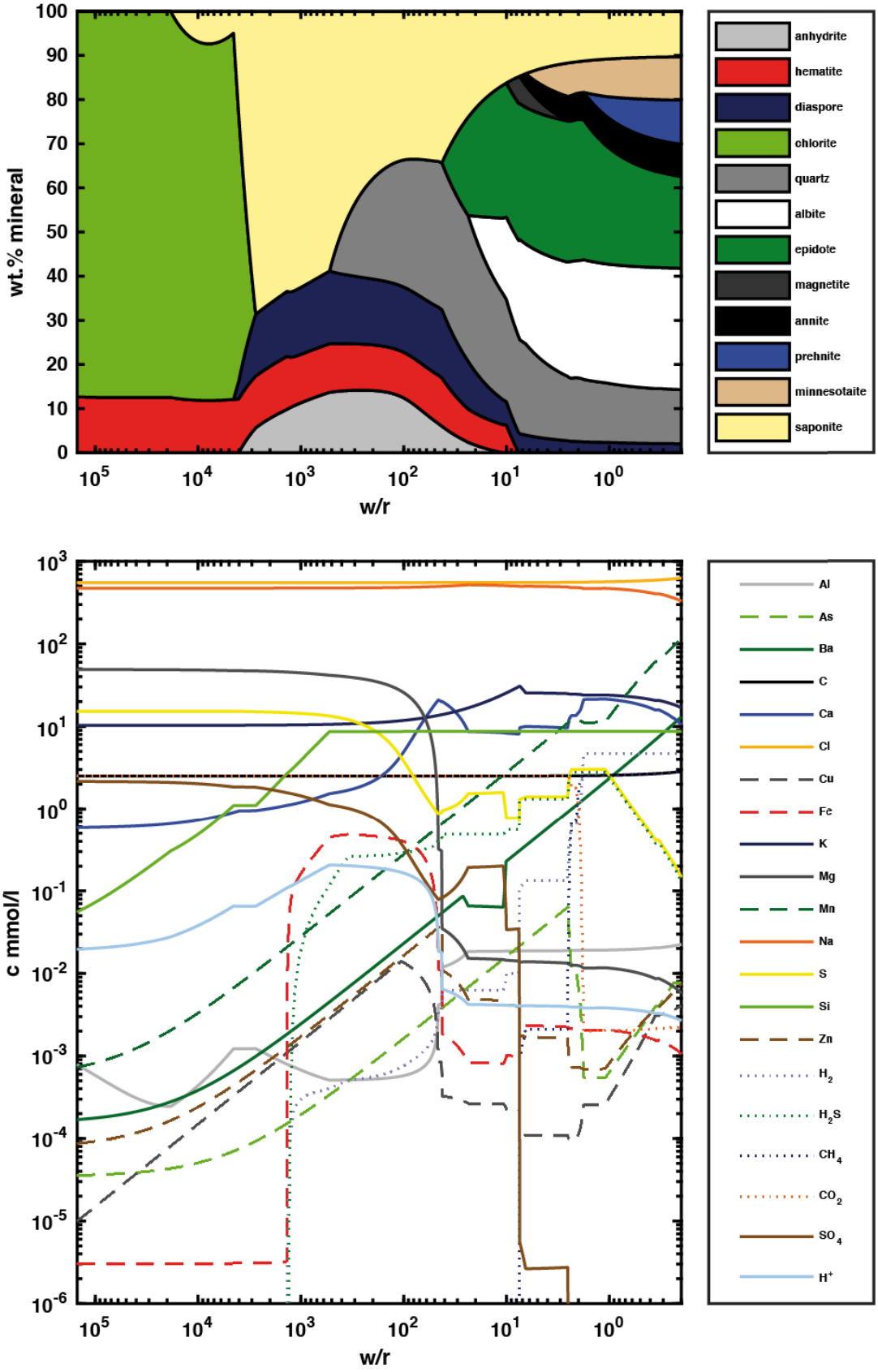

Appendix 4.A1: Evolution of fluid composition during subsurface fluid-rock alteration (Haungaroa; basaltic andesite; 280 °C).

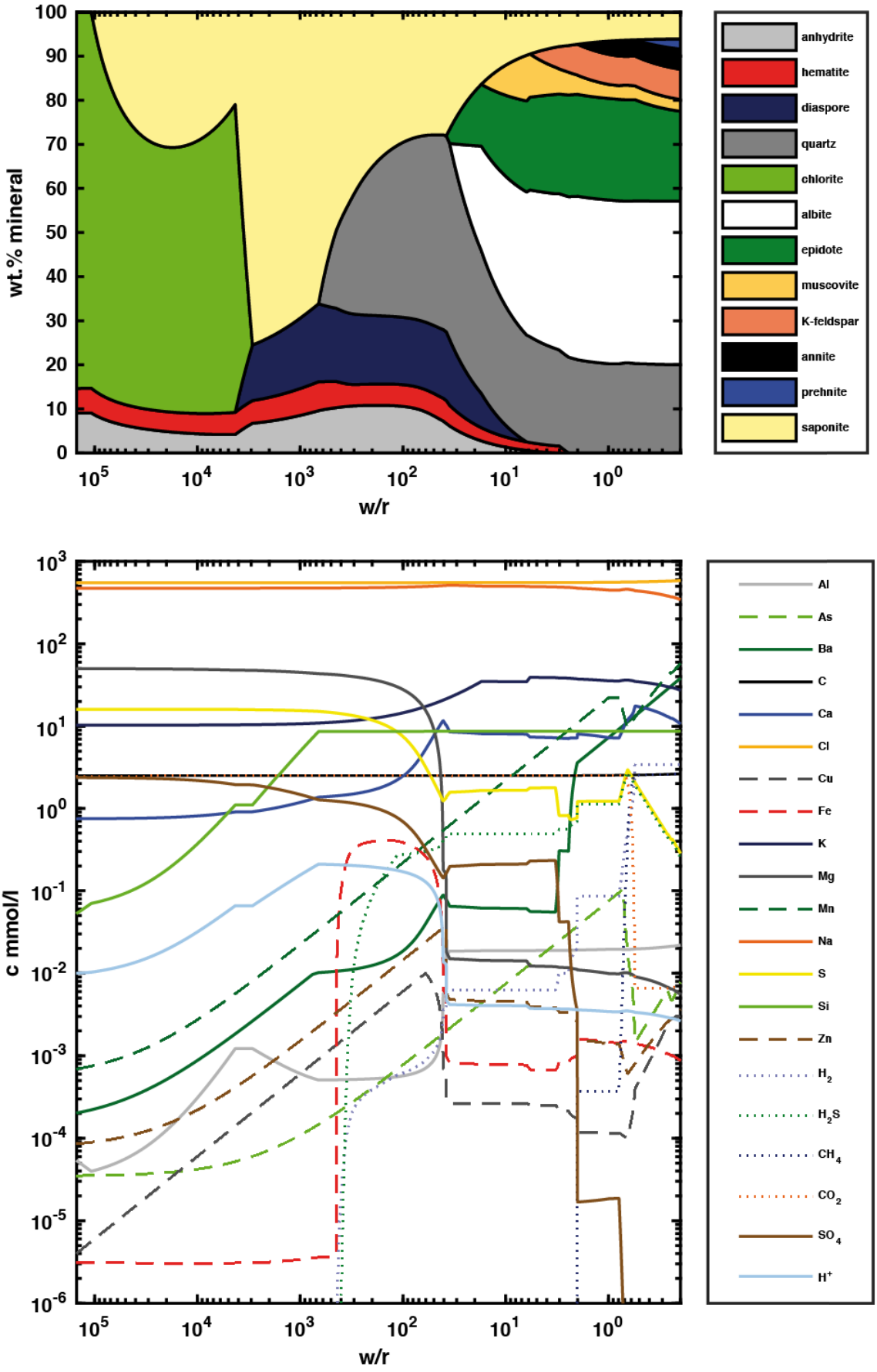

Appendix 4.A2: Evolution of fluid composition during subsurface fluid-rock alteration (Brothers; high-K dacite; 280 °C).

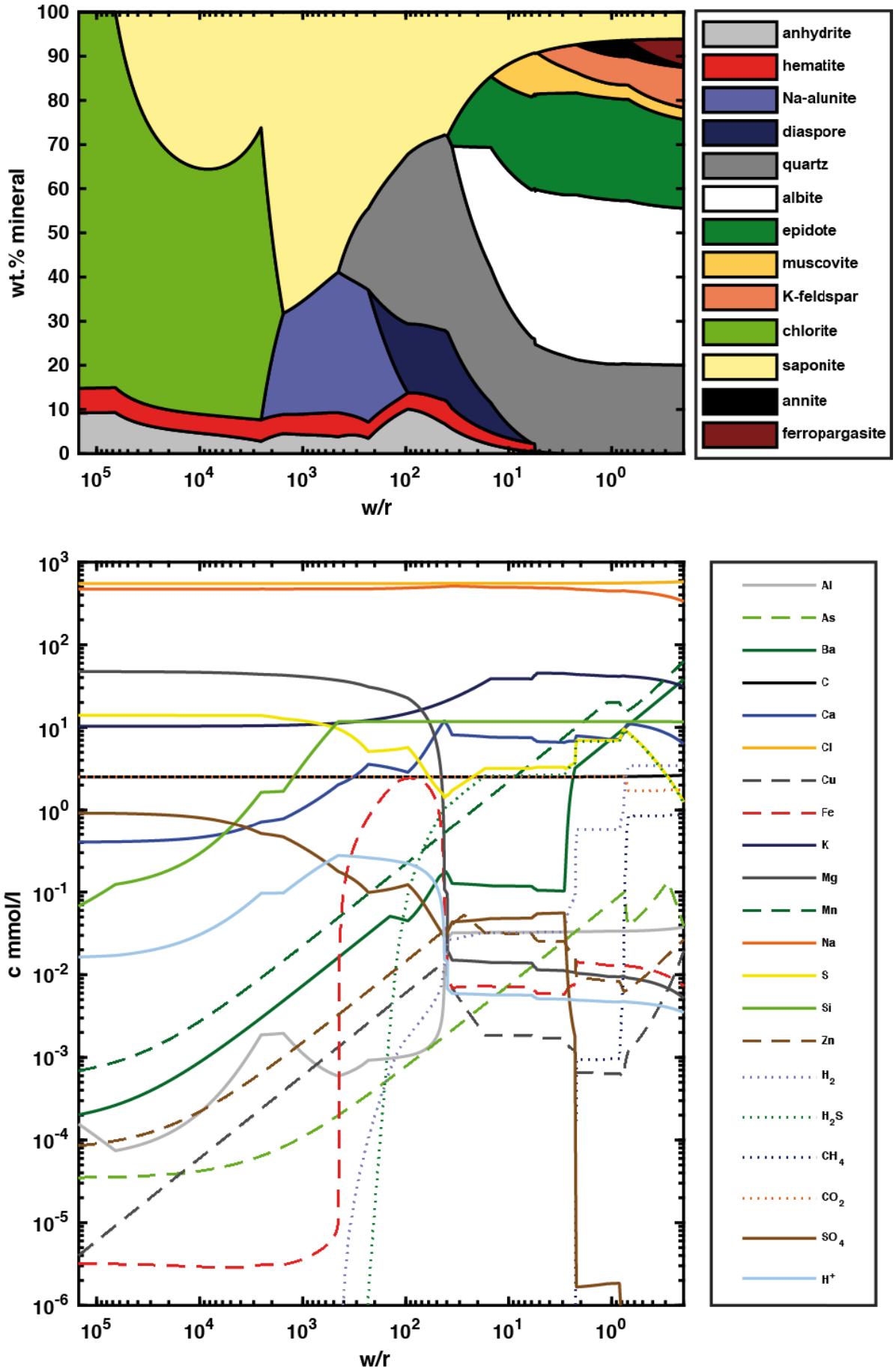

Appendix 4.A3: Evolution of fluid composition during subsurface fluid-rock alteration (Brothers; high-K dacite; 330 °C).

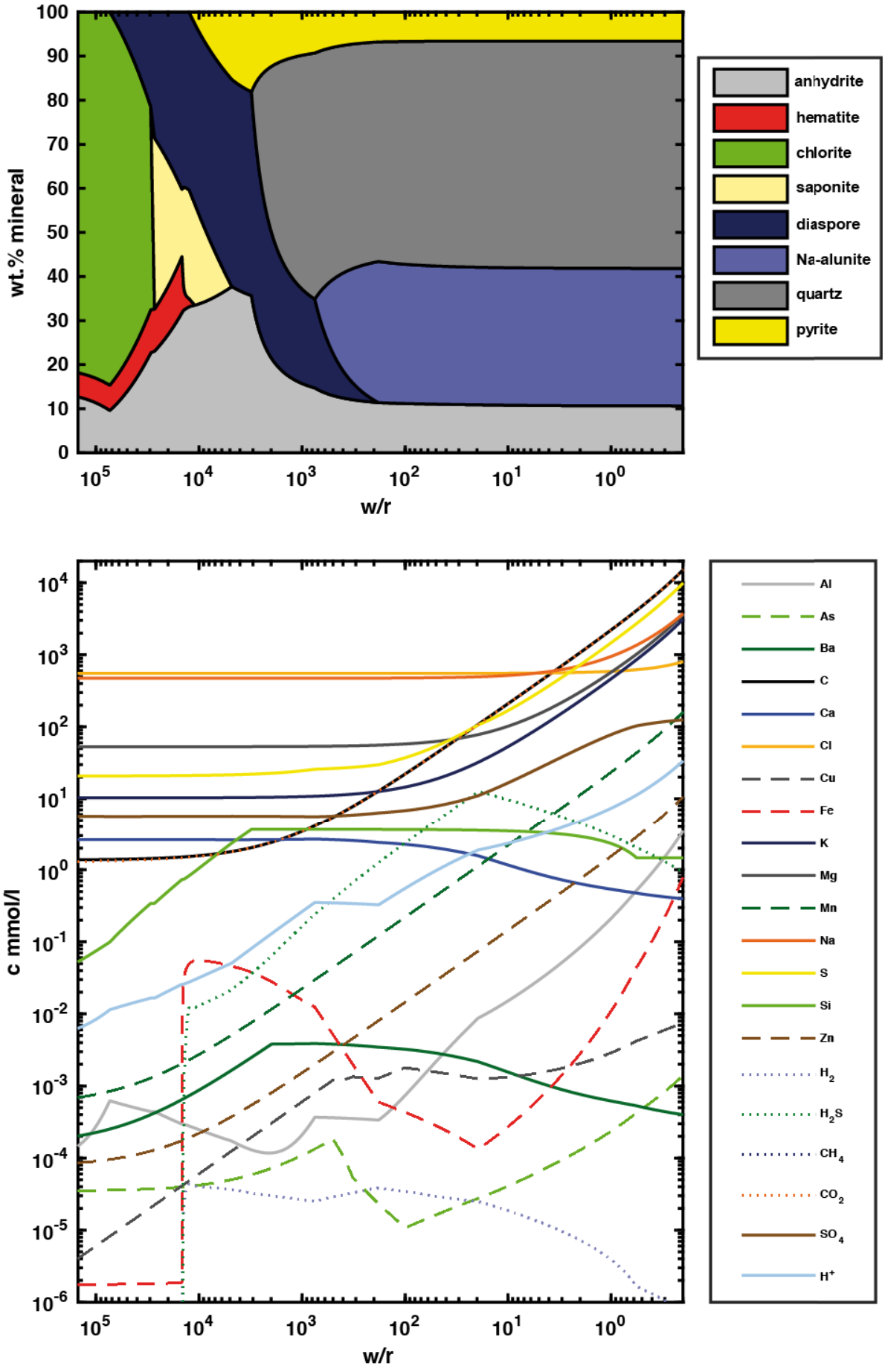

Appendix 4.A4: Evolution of fluid composition during subsurface fluid-rock alteration (Brothers; high-K dacite; 200 °C; +CO_2 + SO_2).

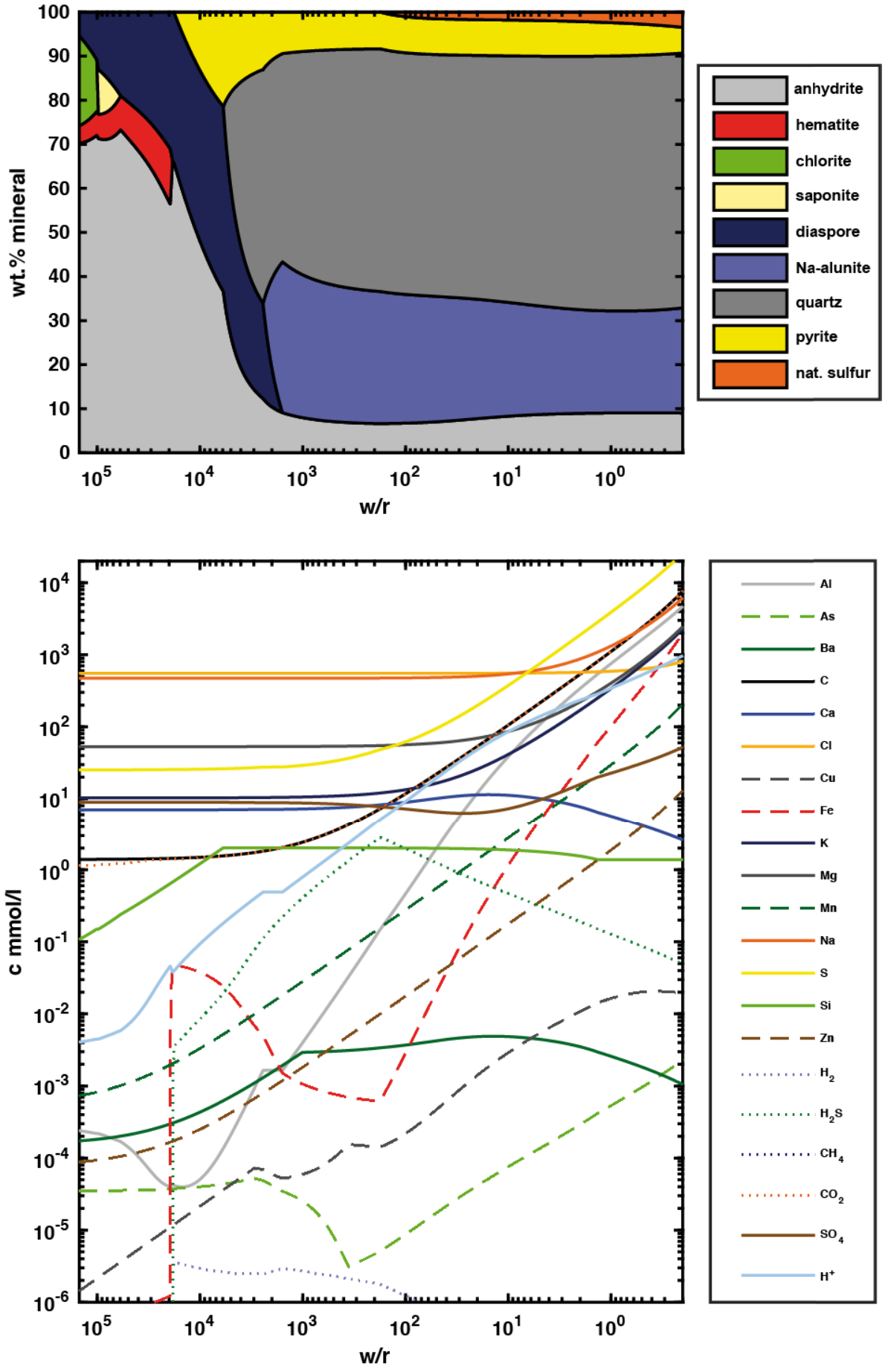

Appendix 4.A5: Evolution of fluid composition during subsurface fluid-rock alteration (Macauley; low-K dacite; 200 °C; +CO_2 + SO_2).

5 Hydrothermal fluids in the South Kermadec Arc indicate various subsurface processes: The role of magmatic volatiles, phase separation processes and subsurface mineral reactions.

Alexander Diehl[1,2], Friedrich Lucassen[2], Charlotte Kleint[2,3], Andrea Koschinski[2,3], Harald Strauss[4], Valerie Stucker[5], Cornel de Ronde[5], Jeffrey Seewald[6], Susan Humphris[6], Wolfgang Bach[1,2]

[1] Department of Geosciences, University of Bremen, Bremen, Germany
[2] MARUM Center for Marine Environmental Sciences, Bremen, Germany
[3] Department of Physics and Earth Sciences, Jacobs University Bremen, Germany
[4] Institut für Geologie und Paläontologie, Universität Münster, Germany
[5] GNS Science, Avalon, New Zealand
[6] Woods Hole Oceanographic Institution, Woods Hole, USA

Abstract

We present major element concentrations, volatile compositions (H_2, CH_4, CO_2, H_2S), $^{87}Sr/^{86}Sr$ ratios and temperatures of different hydrothermal vent fluid types that were sampled with isobaric gas-tight samplers in the South Kermadec Arc. The samples were recovered at Brothers Caldera, Brothers Upper and Lower Cone sites, Macauley Caldera and Haungaroa Volcano. Their characteristics vary from magmatic volatile-dominated acid-sulfate type white smoker fluids to seawater-dominated black smoker fluids.

We present zero-Mg end-member compositions and Sr isotope values for the black smoker-type fluids, as well as end-member temperatures, which were calculated in isenthalpic mixing models. The acid-sulfate fluids have elevated Mg contents and end-member compositions could not be computed. We discuss the characteristics in terms of gas contents in both fluid types and present results of REE speciation and solubility calculations for both types of fluids under in-situ conditions. We evaluate these parameters and discuss their potential use to identify magmatic fluid input to venting hydrothermal fluids. The relationship between major element concentrations and gas concentrations is used to investigate the effects of phase separation and

some subsurface mineral reactions. Our results point to the overall importance of magmatic fluid addition in the formation of the hydrothermal fluids in the South Kermadec Arc. This input is highly variable: At Haungaroa volcano fluids are particular rich in CO_2 with an estimated CO_2:SO_2 of 24:1. Although extremely enriched in CO_2 other properties of fluids and precipitates from Haungaroa are very common for black smoker-type fluids that are of seawater origin. We suggest that Haungaroa is affected by degassing of CO_2, and that degassive fluxes of HCl and SO_2 are minor. Our data confirms that CO_2 is unreactive at high-temperatures and CO_2 degassing does not influence water-rock reactions in the system to a noticeable extent. The acid-sulfate vents at Macauley caldera are enriched in CO_2 as well, but also show very high influx of SO_2, which disproportionates to sulfuric acid and either sulfur or sulfide. Macauley fluids have high gas contents combined with high contents of salt, which makes them unique in the spectrum of arc-hosted vents sampled thus far. These compositions indicate a strong decoupling of phase separation and magma degassing. At both Brothers Cone sites, dissolved gas concentrations of fluids are highly variable. According to CO_2, H_2S, SO_4 concentrations the range of CO_2:SO_2 of the volatile source for eight samples is estimated between 2:1 and 1:2 for both sites. At Brothers North West Caldera Wall, seawater-derived fluids show clear evidence for water-rock reactions (albilitization) and phase separation. There is also evidence for minor degassive influx, indicated by excess SO_4 concentrations and deviations from a phase separation trend in a subset of the samples. All fluids are fairly oxidized with H_2 contents < 200 µmol/l. The redox potential of the fluids seems to be controlled by fluid-rock reactions and SO_2 influx. Our results suggest that magma degassing also controls REE systematics of the fluids: SO_2 influx leads to flat patterns and overall high concentrations of REE in the fluids. Overall, the fluid-rock reactions in these arc-hosted hydrothermal systems are very strongly controlled by the composition of influxing magmatic fluids.

5.1 Introduction

Volcanic arc hydrothermal fluids are extremely variable in their chemical and physical properties (de Ronde et al., 2001; Baker et al., 2012; de Ronde & Stucker, 2015). A coarse distinction can be made between traditional black-smoker type and island arc typical acid-sulfate type fluids. The black-smoker type fluids are believed to form in a seawater dominated realm whereas acid-sulfate type fluids are generated under involvement of magmatic volatiles (Resing et al., 2007; Craddock et al., 2010; Reeves et al., 2011; Seewald et al., 2015). The acid sulfate type fluids are highly acidic and carry high metal concentrations (de Ronde et al., 2011; Hawkes et al., 2014; Resing et al., 2007). In the subsurface acidity is created by addition of SO_2 and HCl-rich magmatic vapors that mix with the hydrothermal fluids and lead to

disproportionation reactions of SO_2 (Gamo et al., 1997; de Ronde et al., 2005; Butterfield et al., 2011; Seewald et al., 2015). Acid sulfate type fluids typically contain large amount of magnesium and sulfate besides higher amounts of metals (e.g. Al) which makes one of the main differences between them and seawater dominated fluids (de Ronde & Stucker al., 2015). The hydrothermal systems are usually of intermediate temperature (around 120 °C) because the heat source driving the circulation is probably the heat transported by the ascending magmatic volatiles themselves. These systems have a rather small thermal impact but the chemical budget due to high acidity and the special mineral reactions is still relevant.

In contrast to this are rather permeability-controlled seawater-dominated systems. They predominantly form along commonly developed ring-faults of caldera volcanoes (Gruen et al., 2012, 2014; Berkenbosch et al., 2012; Fouquet et al., 2018) and are driven by heat from the host rock they percolate trough. Seawater dominated systems are comparable to mid-ocean-ridge hydrothermal systems with depletions in Mg and SO_4 (Mottl & Holland, 1978; Von Damm, 1990) and form massive sulfide deposits when exiting the seafloor (de Ronde et al. 2005; Gemmel et al. 2004; Berkenbosch et al., 2012, 2015; Fouquet et al., 2018). A clear distinction between those extreme types of circulation systems cannot entirely be made since some seawater dominated systems show contributions of magmatic volatiles as well or vice versa (Gemmel et al. 2004; Stucker et al., 2017).

We present a comprehensive dataset of 31 fluid samples from acid-sulfate and black-smoker type-fluids from different volcanoes along the South Kermadec Arc (Figure 5.1). The dataset includes major element compositional data, temperatures, pH values, volatile concentrations and $^{87}Sr/^{86}Sr$ values. We evaluate the specific roles of subsurface fluid-rock interaction, phase separation processes and magmatic gassing in setting the compositions of the hydrothermal vent fluids. Speciation and solubility calculations are used to assess REE distribution and provide insights into the contrasting behavior of REE in fluid-rock systems with variable magmatic fluid input.

5.1.2 Vents inside Macauley Caldera

Hydrothermal venting in Macauley Caldera occurs in a young dacitic satellite cone that was emplaced in the southeastern part of the Caldera (Figure 5.2 Top). During expedition SO253 the vigorously venting site discharged 112 °C, particle-rich, extreme low pH (< 1.5) and high saline (salinity up to 5 wt.%) acid-sulfate type fluids. Additionally, the fluids are enriched in H_2S (Kleint et al., submitted to GCA.), in alkalis, metals and Al, which is considered as a fluid immobile element. The overall chemical composition suggests that the fluids are derived by subsurface fluid-rock interactions involving magmatic SO_2. Macauley is a typical example for the consequences of SO_2 disproportionation reactions producing sulfuric acid and extreme low

pH values (Gamo et al., 1997; Resing et al., 2007; Butterfield et al., 2011; Seewald et al., 2015). The extreme acidic environment enables fluids to break down alteration minerals like kaolinite and pyrophyllite and hence mobilize Al (Inoue, 1995). The dacitic host rock beneath the venting site are altered to quartz-alunite-pyrite, an assemblage called advanced called argillic alteration (cf. Reed, 1997), and are strongly depleted in alkalis, metals and even Al (Diehl et al., in prep., Chapter 4). We sampled this vent site three times during two separate dives of expedition SO253.

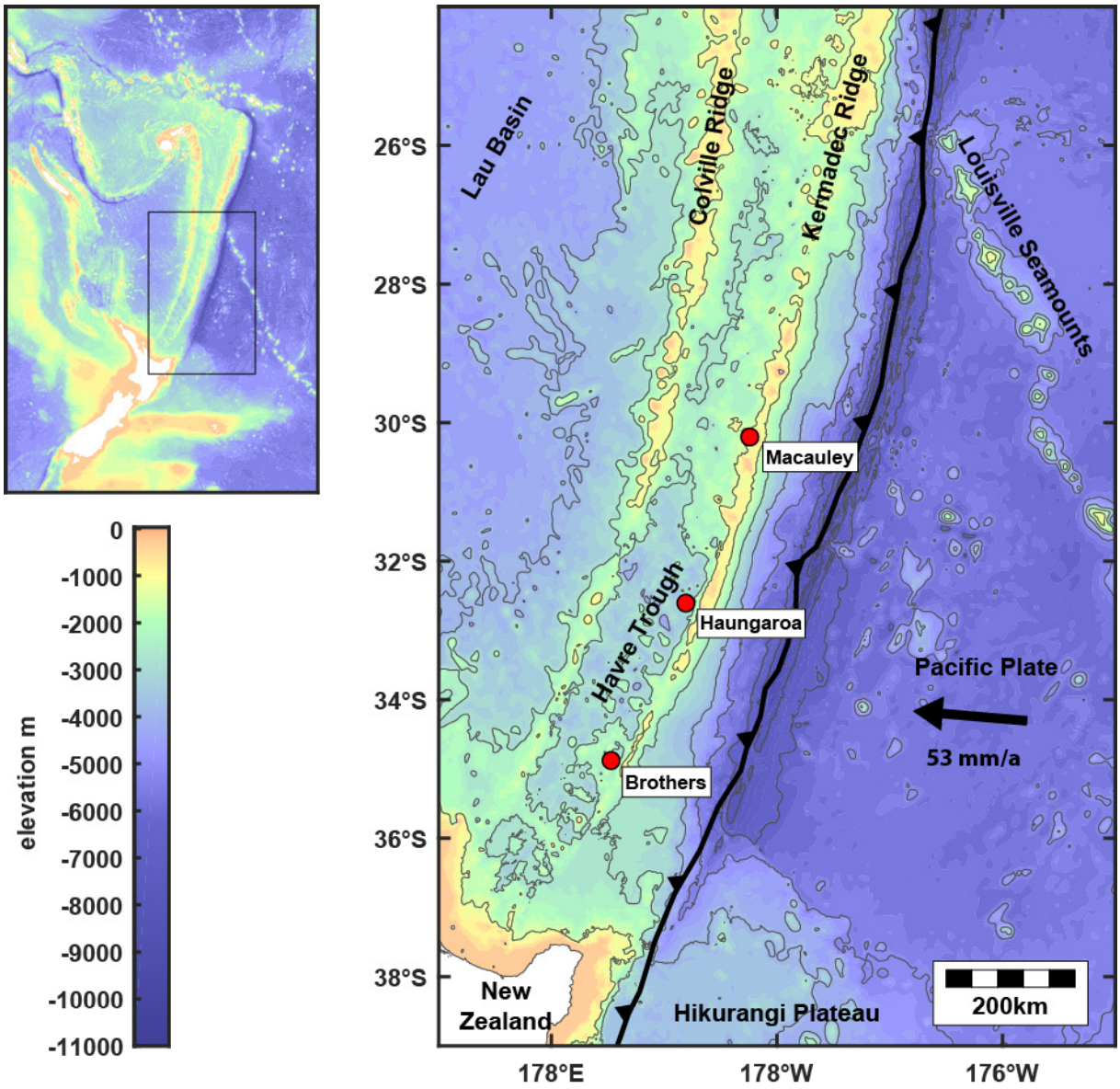

Figure 5.1: Bathymetric overview map of the South Kermadec Arc with the volcanos sampled for hydrothermal fluids (Relative plate motion is from DeMets et al., 2010; the plate boundary is from Bird, 2003; bathymetry data: GEBCO 2014).

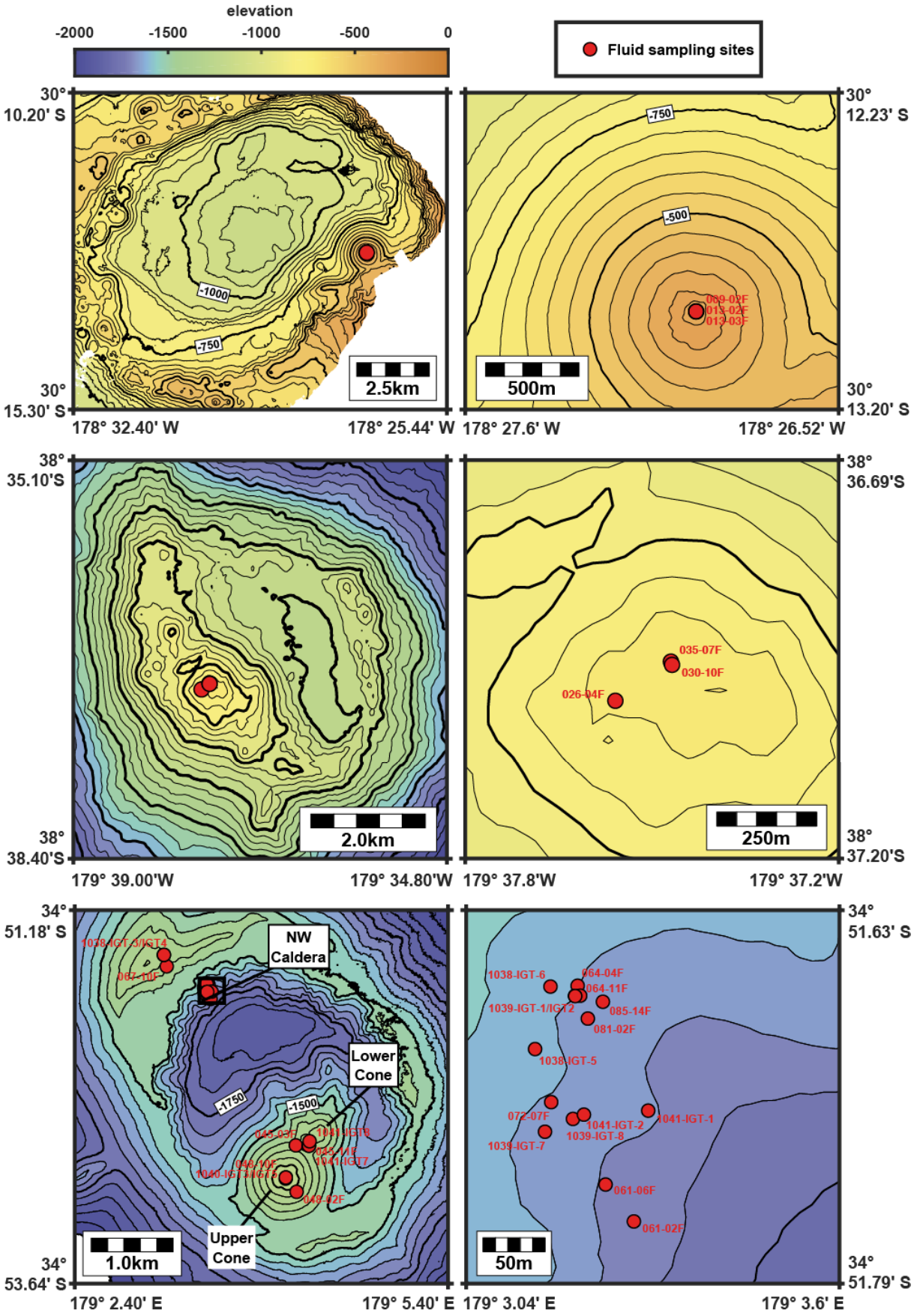

Figure 5.2: Fluid sampling sites at Macauley Caldera (Top), Haungaroa Volcano (Center) and Brothers Caldera (Bottom; elevation data: Sonne cruise SO253 MBES, Koschinsky et al., 2018).

5.1.3 Hydrothermal fluids at Haungaroa Volcano

Haungaroa volcano features a wide crater rim in the southwestern part (Figure 5.2 Center). The crater rim has a conical shape and constitutes the peak of the volcanic edifice. Fresh pillow lavas indicate recent magmatic activity in the area. The hydrothermal vent field is hosted at the northwestern part of the cone where basaltic andesites (Diehl et al. in prep, Chapter 4) are exposed. This rock type appears to make up the bulk of the volcano (Wright et al., 2006). Hydrothermal chimneys are dominated by sphalerite-barite-rich chimneys in which tennantite and chalcopyrite precipitate (Diehl et al., in prep, Chapter 4). The fluids venting at temperatures up to 280 °C are particle-poor. Bubbles of liquid CO_2 could be observed to discharge from some of the chimneys along with venting aqueous fluids. Diffuse discharge of hydrothermal fluids as shimmering water is common. Owing to widespread diffuse venting, the site is characterized by abundant vent fauna over a larger area of about 170 × 60 m.

5.1.4 Fluid discharge at Brothers Caldera

Brothers Caldera is the main working area of this study and was visited twice during expeditions (SO253 and TN350). On both cruises the hydrothermal systems situated at the NW Caldera Wall and the two cone sites were sampled (Figure 5.2 Bottom).

The NW Caldera Wall vent field occurs over an area of at least 0.015 km^2 and features the most vigorous fluid discharge. Hydrothermal vents generally are seawater-dominated and represent classical black-smoker type fluids (Kleint et al., submitted to GCA). Vent types are variable in composition, temperatures and may emanate either gas-rich, particle-poor fluids or high-temperature, particle-rich fluids. Rocks in the subsurface of the NW Caldera Wall underwent extensive reaction with fluids and were altered to chlorite-rich rocks or quartz-illite assemblages (Diehl et al., in prep., Chapter 4). The stockwork zone below the vent field is exposed in the headwalls due to faulting or slope failure. The stockwork vein network comprises extensive Fe-sulfide and Ca-sulfate (Diehl et al., in prep., Chapter 4). The extent of hydrothermal alteration reaches deep as indicated by a magnetic anomaly reaching from the seafloor down to 1 km depth (Caratori Tontini et al., 2012a, 2012b). This suggests that primary Ti-magnetite in the dacitic host-rock has been destructed to great depths and may indicate that the vent field has been active for a prolonged period of time. In the NW Caldera Wall sulfide is extensively mineralized forming Cu-rich and Zn-rich chimneys (de Ronde et al., 2003, 2005, 2011; Berkenbosch et al., 2012, 2015; Diehl et al., in prep., Chapter 4).

The Upper Cone is place of vigorous acid-sulfate type venting with temperatures of up to 200 °C. The Upper Cone vent sites are located within a small central crater at the summit of the cone and on the southeastern slope just below the summit area. They represent the most acidic

fluids at Brothers with pH values < 2.1 (Kleint et al., submitted to GCA). Vents at Brothers Upper Cone and Macauley Caldera are both particle-rich acidic; however, Macauley vents represent highly saline brines, whereas Upper Cone fluids at Brothers have salinities slightly below seawater (Kleint et al., submitted to GCA).

At the Lower Cone exit temperatures are significant lower (< 80 °C) and fluid discharge occurs in a rather diffuse fashion. The fluids are particle-poor and emanate as shimmering water out of small mounds mineralized by native sulfur. These fluids found during both cruises have highest Mg enrichments and are only mild acidic (pH values of 4-4.5).

5.2 Methods

5.2.1 Fluid sampling

During expeditions SO253 and TN350 we collected a total of 32 fluid samples with isobaric gas-tight fluid samplers (IGT). The samplers are equipped with a temperature sensor, which enables to measure temperatures prior to and during sampling. The autoclave system allows to retrieve samples without degassing during recovery or withdrawal of subsamples by maintaining the pressure in the sampler (Seewald et al., 2002). Moreover, it facilitates the measurement of gas concentrations in aliquots drawn from the sampler without affecting the composition of the fluid inside the sampler.

Our sample collection comprises 26 fluid samples from Brothers Caldera. Eighteen of those samples originate from high-temperature black-smoker type vents at the NW Caldera Wall. Here vent fluids are variable in temperatures and gas concentrations and span a range from particle-poor lower-temperature (150 °C), gas-rich fluids (Figure 5.3A) to vigorously venting high-temperature (320 °C) and particle-rich fluids (Figure 5.3B).

Eight samples originate from the acid-sulfate type vents at the Cone sites. Of these, four samples originate from the Upper Cone where fluids have elevated temperatures up to 200 °C and form abundant white-smoke particles when mixing with seawater (Figure 5.3E). The remaining four samples were recovered from the Lower Cone, where similar (acid-sulfate) but less acidic fluids, which emanated diffusely as clear fluids were sampled (Figure 5.3F).

At the crater wall of Haungaroa Volcano high-temperature, CO_2-rich particle-poor fluids emanate from small chimneys (Figure 5.3B). The fluids are oversaturated with respect to CO_2 and form liquid droplets of CO_2 that can be seen at the samplers housing (Figure 5.3B). Three samples were retrieved at the summit of Haungaroa Volcano.

Finally, three samples originated from the young cone inside Macauley Caldera. Similar to the fluids at Brothers Upper Cone, these fluids are particle-rich, of acid-sulfate type but with high salinities and with somewhat lower temperature of 110 °C.

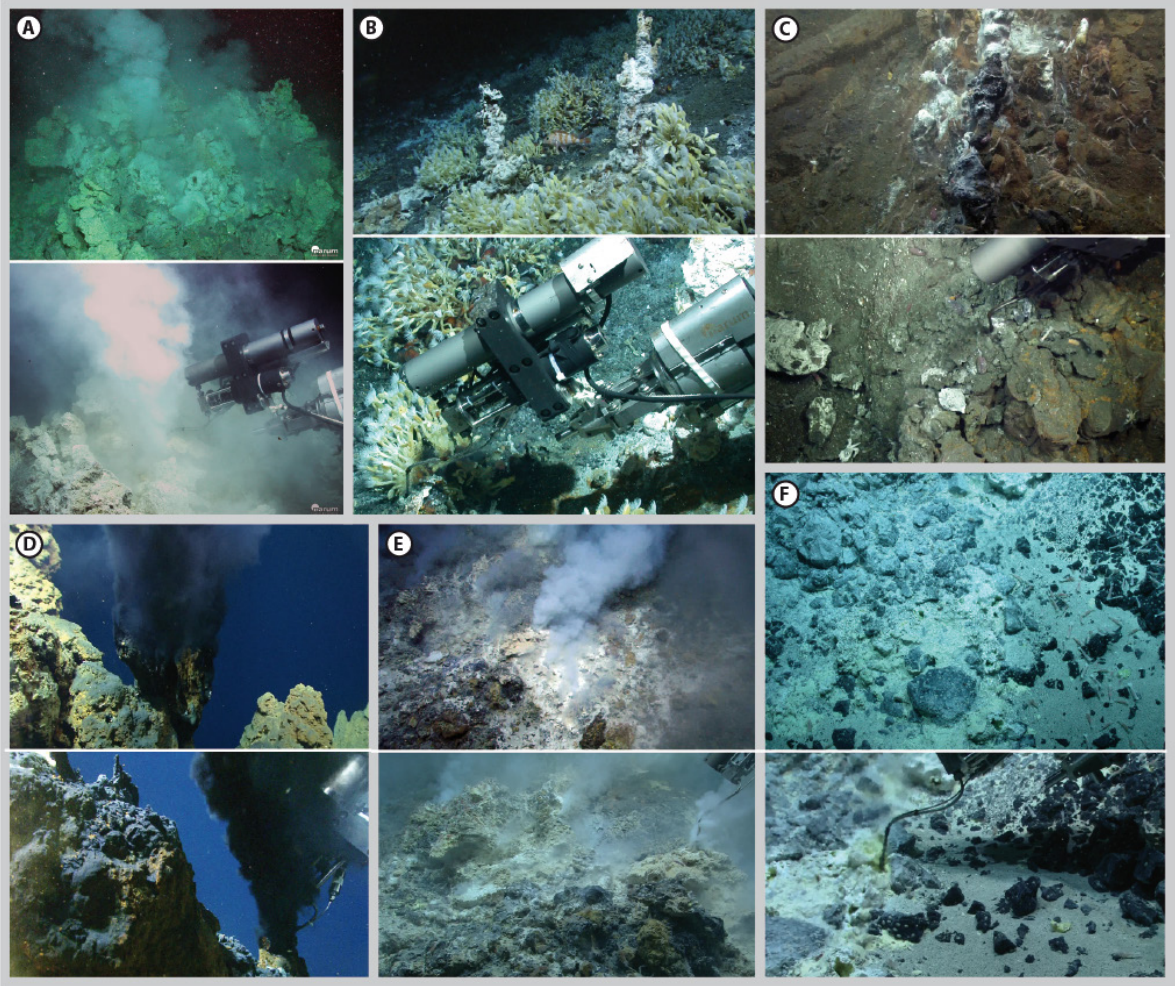

Figure 5.3: Photographs of variable types of hydrothermal orifices prior to and during IGT fluid sampling at different volcanoes: (A) acid-sulfate type fluids at Macauley; (B) small chimneys near the summit of Haungaroa (note the droplets of liquid CO_2 sticking at the samplers casing); (C) the most gassy vent sampled at Brothers NW Caldera; (D) high-temperature particle-rich vent at the NW Caldera; (E) acid-sulfate type vent of Brothers Upper Cone; (F) rather diffuse acid-sulfate type vent at Brothers Lower Cone. (Photographs: MARUM QUEST 4000)

5.2.1 Major element composition

Major element compositions were determined by inductively coupled plasma optical emission spectrometry (ICP-OES) and ion chromatography (IC). The methods and corresponding accuracies are presented in Kleint et al. (submitted). The remaining samples were measured at the University of Bremen with a Varian Vista Pro spectrometer and a Metrohm Compact ion chromatograph. Control measurements of the NASS-5 reference material suggest that the trueness and precision of the measurements for most elements lie in the usual range for these methods (± 5%).

5.2.2 Volatile concentrations

Concentrations of H_2 and CH_4 were determined by gas chromatography during shipboard measurements directly after dives. A defined sample volume was transferred from the samplers into gas-tight syringes. The gas phase was stepwise injected into the gas chromatograph (GC) using a 1 mL sample column. This procedure was followed by a headspace extraction method. 1 mL of pure nitrogen was brought in contact with the remaining liquid. Creating an underpressure by pulling the stamp of the syringe, volatiles are extracted from the liquid into the headspace. The nitrogen gas is subsequently injected into the gas chromatograph. The procedure was repeated until the detector signal becomes neglectable compared to the signal of the prior injections. This procedure assures nearly complete removal of dissolved volatiles from the liquid fraction.

The gas chromatographs used during the two expeditions were an 7820A Agilent (SO263) and a Thermo Scientific Trace GC Ultra (TN350). The GCs were equipped with a packed Molsieve 60/80 column (Sigma-Aldrich, St. Louis, MO) and were operated with N_2 as carrier gas at 50 °C. H_2 was quantified with a thermal conductivity detector and CH_4 was quantified using a flame ionization detector. The devices were calibrated with reference gases of either 253 mol-ppm H_2 and 120 mol-ppm CH_4 (during cruise SO253) or with a 1.02 mol% H_2 and a 0.987 mol% CH_4 in a N_2 matrix (during cruise TN350). For each sample multiple measurements (two or more) with different aliquots were conducted, usually a with precision significantly better than 5%. Samples for CO_2 analyses were stored in pre-weighted He-filled and subsequently evacuated glass serum vials to avoid atmospheric CO_2 contamination. Samples were injected from gas-tight syringes through the septa, and vials were stored upside down to seal the septa by the fluid and prevent diffusive gas loss.

Measurements of CO_2 concentrations were determined post-cruise with a different device setup. The method used was adapted from Reeves et al. (2011). Prior to measurements 1-2 mL phosphoric acid (25 wt.%) were added to the samples to convert DIC species to CO_2. The gas chromatographs (again the 7820A Agilent for samples of cruise SO263 and the Thermo Scientific Trace GC Ultra for samples of TN350) were equipped with a packed HaySep 80/100 column (Sigma-Aldrich, St. Louis, MO) and operated with helium as carrier gas at 50 °C. The GCs were calibrated with reference gas of pure CO_2 with 99.995 mol%. A control standard was created using $NaHCO_3$ solutions. The control standard was treated as sample and injected into a serum glass vial prior to measurement. One control standard was measured prior to each sample block comprising 6-8 samples. The accuracy of the measurements is within 10%.

2.3 Thermal ionization mass spectrometry

Thermal ionization mass spectrometry (TIMS) was used to measure $^{87}Sr/^{86}Sr$ concentrations of vent fluid samples. A Thermo Scientific Triton Plus mass spectrometer was used in the Isotope Geochemistry Laboratory at the Center for Marine Environmental Science (MARUM) at Bremen University. Concentrated nitric acid was added to 200 µL of sample (a volume calculated to contain more than enough Sr for the following resin extraction procedure). The mixture was completely evaporated and the residual solid was taken up by adding concentrated HNO_3 to subsequently undergo a resin extraction procedure (adapted by Deniel & Pin, 2001). Using a Ta-emitter the samples were measured on rhenium filaments in a static acquisition procedure. The NIST SRM 987 reference material was measured prior the samples and was determined as 0.710245 ± 8. The long-term reproducibility of the NIST reference material in the geochemistry laboratory is 0.710249 ± 14 (2σ; $n = 263$), a value that agrees well with published literature data, 0.710250 ± 34 (2SD, $n = 1245$, data < 0.7102 and > 0.7103 are discarded; GeoREM data base (Jochum et al., 2005), requested in September 2017).

5.2.4 End-member calculation

We present an end-member calculation for the black-smoker type fluids at Haungaroa. We used the approach of Von Damm et al. (1985) extrapolating the chemistry of all elements to Mg = 0 assuming the fluids have lost their Mg during fluid-rock interaction and that Mg behaves as a conservative element during mixing with seawater. The end-member calculation is comprehended by calculation of end-member temperatures in a process of isenthalpic-isobaric mixing, considering a temperature and salinity dependent heat capacity of the fluid mixture. The temperature and salinity dependence is calculated using the correlation scheme of Driesner (2007) that calculates thermodynamic data of H_2O-NaCl fluids according to thermodynamic data of pure water (Haar et al., 1984).

5.2.5 Calculations of REE solubility and speciation

Owing to the use of isobaric gas-tight fluid samplers (Seewald et al., 2002) and onboard analyzes of the H_2 contents dissolved in the fluids, we were able to calculate in situ conditions of pH and redox in the hydrothermal systems. This allowed us to calculate solubilities and speciation of elements in hydrothermal solutions under in situ conditions. This, in turn, enabled us to examine the specific processes that control the abundance of elements in the sampled vent fluids.
We calculated the speciation of rare-earth elements (REE) in hydrothermal vent fluids from the South Kermadec Arc to understand the reasons behind the large variability in pattern types

displayed by fluids from different areas (Kleint et al., submitted to GCA). We used a 50 MPa database and Geochemist's Workbench to conduct the calculations. The REE thermodynamic data are from Haas et al. (1995), except updates for fluoro-, chloro-, and sulfato-complexes advices be Migdisov et al. (2009). Data for REE-phosphates are from Migdisov et al. (2016) and references therein. We conducted speciation calculations for representative fluids from Macauley and Haungaroa as well as both cone sites and the NW Caldera site at Brothers (Section 5.3.6).

5.3 Results

5.3.1 Data compilation

We present a comprehensive dataset of IGT fluid samples from three volcanos of the South Kermadec Arc by supplementing the dataset of Kleint et al. (submitted) with gas concentrations and $^{87}Sr/^{86}Sr$ values of the corresponding samples. Further, we add major compositional data, $^{87}Sr/^{86}Sr$ and gas concentrations of vent fluids recovered at Brothers Volcano during research cruise TN350. This dataset now comprises 32 IGT fluid vent samples containing major element data, gas concentrations and $^{87}Sr/^{86}Sr$ values.

5.3.2 Temperatures

During sampling of hydrothermal fluid vent temperatures were measured. Maximum temperatures of individual vents at Brothers NW Caldera Wall range between 93 °C and 320 °C. A temperature of 320 °C is the so far highest temperature measured for the NW Calderas Wall. Lower temperatures were measured for fluids at the Cone sites. At the Upper Cone fluids emanate with maximum temperatures between 83 °C and 200 °C. The rather diffuse fluids from the Lower Cone emanate with temperatures between 61 °C and 83 °C. At Haungaroa the highest temperatures of two fluids were between 230 °C and 267 °C. One fluid was sampled with a considerably low temperature of 23 °C. At Macauley three fluid samples of the same venting site gave nearly identical temperatures of 111 °C to 112 °C. All fluids are considerably cooler than the boiling temperature of seawater at the corresponding pressures (Figure 5.4). Three samples, one at Haungaroa and two at Brothers NW Caldera Wall vent site, are somewhat hotter than the remaining samples at their respective locations and are still 20- 30 °C below the boiling curve. The temperature data suggest two prominent and narrow temperature ranges at the Brothers NW Caldera, 265 ± 15 °C and 310 ± 10 °C. Calculated end-member temperatures (Section 5.3.3) for zero-Mg end-member fluids reveal more realistic end-member temperatures, since this way cooling due to entrainment of ambient seawater during sampling or the last meters of ascent is considered. End-member temperatures of zero-Mg fluids

at Haungaroa plot on the boiling curve and suggest phase separation is taking place below the vents. The end-member temperature of the 23 °C fluid is calculated to be 280 °C consistent with temperatures of other samples from Haungaroa.

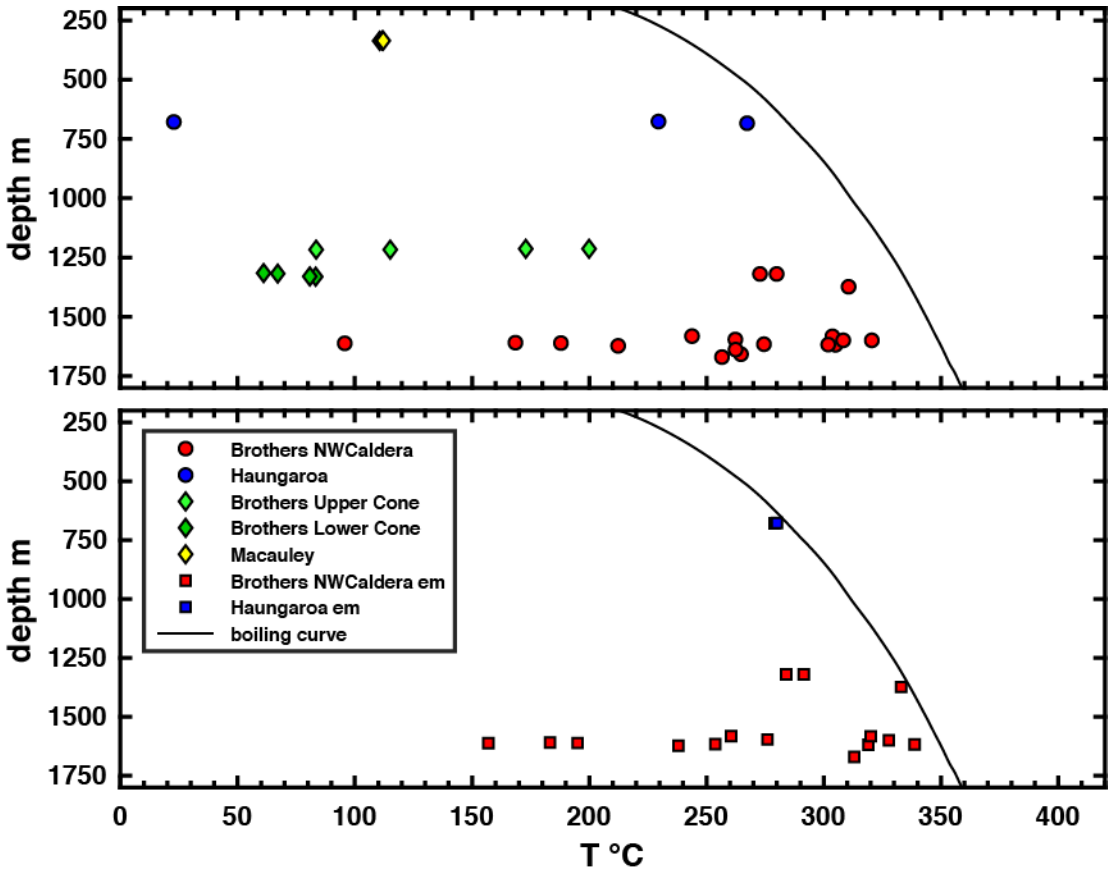

Figure 5.4: Temperatures of hydrothermal fluids. The upper panel shows maximum temperatures measured prior to or during sampling of hydrothermal vent fluids. The lower panel shows calculated end-member temperatures for Mg = 0 end-members for Haungaroa and Brothers NW Caldera Wall (temperatures are recalculated according to isobaric-isenthalpic mixing). The black line shows the boiling curve of seawater (Calculated after Driesner & Heinrich 2007).

5.3.3 $^{87}Sr/^{86}Sr$ of vent fluids

The results of TIMS analysis demonstrate how seawater-dominated black smoker fluids and acid-sulfate fluids fall in two distinct groups (Figure 5.5). The acid-sulfate type fluids are extremely enriched in non-radiogenic Sr isotopes, comparable to seawater. The data plot in a narrow range of 0.709053 ± 0.000099 (n = 11) just below the seawater value of 0.709138 ± 6 (n = 1), which was measured along with the fluid samples. Black smoker type fluids with an average $^{87}Sr/^{86}Sr$ of 0.705054 ± 0.000634 (n = 20) are much closer to the more radiogenic signature of unaltered volcanics from the Kermadec Arc (0.703666 ± 0.000276, n = 100) and give a broader compositional range. $^{87}Sr/^{86}Sr$ ratios of hydrothermal fluids are affected by

subsurface fluid rock interaction. The fluid exchanges Sr with the rocks, in particular during alteration of plagioclase, and Sr is mobilized from the rock and the unradiogenic $^{87}Sr/^{86}Sr$ composition of the unaltered basement is partly imposed onto the fluid. During this process Sr is mildly enriched in the fluid. The Sr concentration of our black smoker fluids lies between seawater and a value twice of seawater. In the acid sulfate type fluids, Sr concentrations are depleted compared to seawater. The $^{87}Sr/^{86}Sr$ of the fluids and their respective Sr concentrations suggest that different chemical processes were involved in setting the compositions of the fluids.

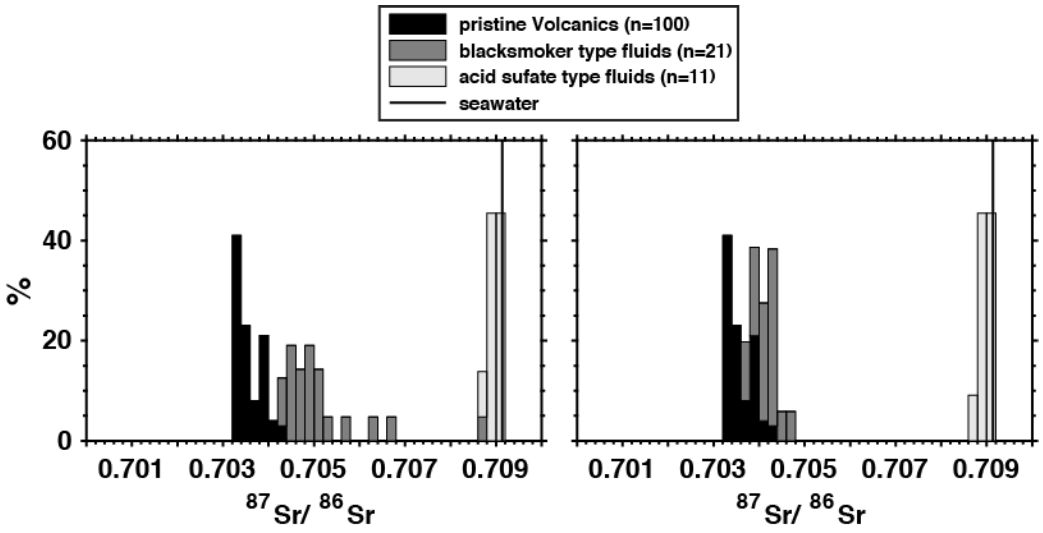

Figure 5.5: $^{87}Sr/^{86}Sr$ of hydrothermal vent fluids and pristine volcanics from the Kermadec Arc. The left panel shows measured $^{87}Sr/^{86}Sr$ of the vent fluids. The right panel shows calculated end-member compositions for black-smoker type fluids.

5.3.4 End-member calculation

The results of calculations of end-member compositions are presented in Figure 5.6. Calculated Sr isotope compositions for Mg = 0 black smoker fluid end-member plot in a narrow range closely above the Sr isotopic composition of unaltered rocks. This pronounces the fact that the black smoker fluids have extensively exchanged Sr with the host rocks during subsurface fluid rock reactions. Four vent fluid end-member Sr compositions plot between 0.7015 and 0.7030. This composition is far below the compositional frame of Kermadec Arc rocks. A likely explanation is precipitation of anhydrite or barite. Due to this the mixing calculation will use a Sr concentration lower than the actual end-member fluid had and provide an overestimation of radiogenic Sr.

The estimation of end-member temperatures yield two dominant temperature windows for NW Caldera fluids. A large proportion of fluid end-members are between 250 and 290 °C another group of end-member rather plot around higher temperatures of 310 and 330 °C. Three fluids

have significant lower end-member temperatures and are likely affected by considerable conductive cooling. The calculated end-member temperatures of three fluids give unreasonably high values of 360 °C and 390 °C that exceed the boiling temperature at that depth. These high temperatures are calculated for three of the four fluids that yield unreasonable low $^{87}Sr/^{86}Sr$ end-member values. This coincidence may demonstrate that these hydrothermal fluids have been affected by subseafloor mixing with conductively heated seawater, which has resulted in sulfate precipitation (and Sr removal). This idea is supported by results of reaction path model calculations, suggesting that conductive heating favors the precipitation of anhydrite (Diehl et al., in prep, Chapter 4).

The acid sulfate type fluids show Mg concentrations similar to or higher than that of seawater. Consequently, zero-Mg end-member calculations are not possible. Because the Sr isotope signature of those fluids is seawater-like, end-member values cannot be computed using a Sr isotope mass balance approach. This is because small errors in the analyses of isotope ratios will lead to large errors in the end-member calculation. Sr contents of the acid-sulfate type fluids is depleted compared to seawater, suggesting that Sr in the hydrothermal endmember must be depleted. Assuming that the Sr isotopic composition of the hydrothermal end-member is similar to that of unaltered rock, we can compute Sr concentrations in the end-member hydrothermal fluids. If we assumed an $^{87}/^{86}Sr$ value of 0.704 we find that the acid sulfate fluid end-members are strongly depleted in Sr with concentrations < 0.2 µmol/l.

5.3.5 Concentrations of dissolved gases

Gas concentrations in the hydrothermal systems of the Kermadec arc are highly variable. Figure 5.7 shows how gas contents co-vary with temperature. For CO_2 concentrations four groups of samples can be identified: Brothers Lower Cone fluids are extremely rich in CO_2 (50- 120 mmol/l) although temperatures are lower than those of other fluids. Vent fluids from Haungaroa are as well rich in CO_2 (80-100 mmol/l) but fluid temperatures are considerably higher than for Brothers Lower Cone.

Samples from Brothers Upper Cone and Macauley Caldera give intermediate concentrations between (17-30 mmol/l). Most fluids from Brothers NW Caldera Wall are particularly poor in CO_2 with values between 3 mmol (barely enriched compared to seawater) and 12 mmol. The three samples with lowest temperatures are exceptional and give values of up to 40 mmol/l CO_2, which is similar to the Upper Cone site.

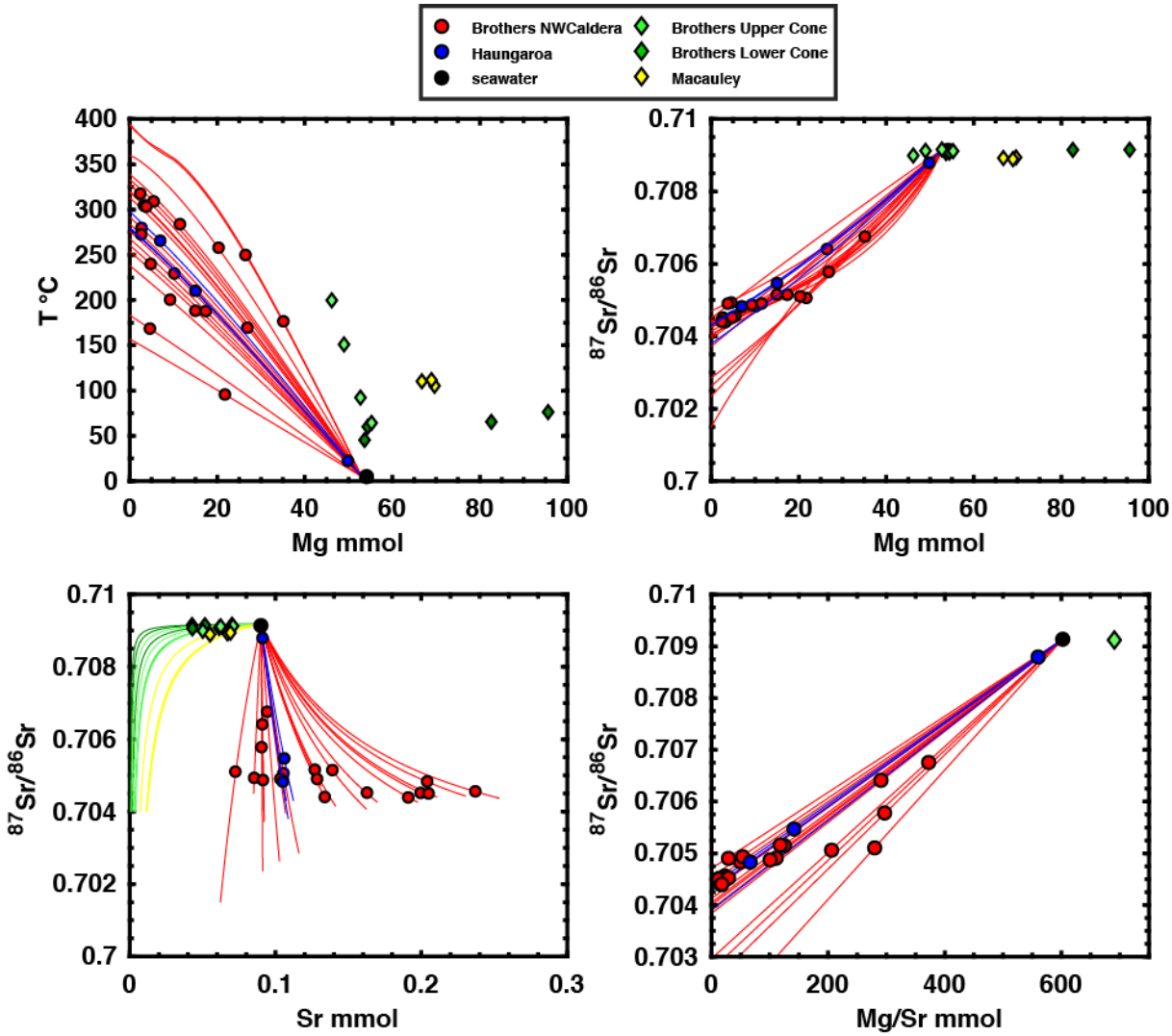

Figure 5.6: Upper-left: End-member calculation for the hydrothermal vent fluids. Isenthalpic temperature calculation for zero-Mg extrapolated fluids. Upper right: Sr mass balance calculation showing $^{87}Sr/^{86}Sr$ composition for zero-Mg fluids. Lower-left: Sr mass balance and calculated end-member Sr concentrations of the fluids. Lower-right: Mg/Sr ratio plotted along with $^{87}Sr/^{86}Sr$. Samples with higher Mg/Sr ratios deviate from the trend most samples follow. Note: Colored lines represent mixing of seawater with the corresponding hydrothermal fluids.

For H_2S there is a clear distinction between the acid-sulfate type vents and the black-smoker type vents. Acid-sulfate type fluids are rich in H_2S (1.5-15 mmol/l) whereas the higher temperature black smoker-type vent fluids are relatively poor in H_2S (0.1-3 mmol/l). The hydrogen concentrations show a clear temperature-dependency with low hydrogen concentrations for the low temperature acid-sulfate type fluids (typically 0.05-1 µmol/l) and higher concentrations for the high-temperature black smoker-type fluids (3-200 µmol/l). CH_4 concentrations can also be discriminated into two groups of fluids: Acid sulfate type vents are depleted in CH_4 (0.1-1 µmol/l) compared to black smoker type fluids (1-10 µmol/l).

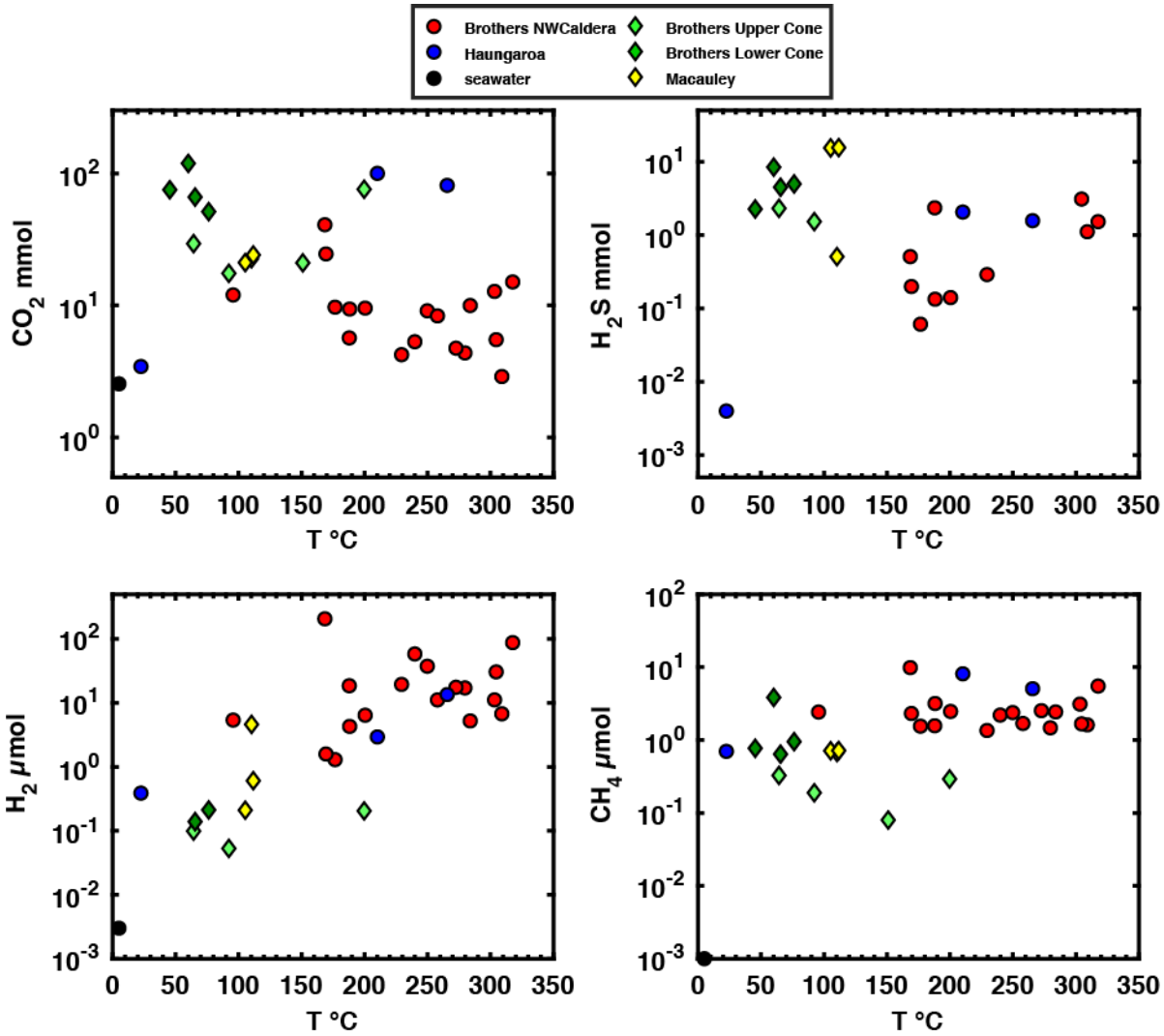

Figure 5.7: Relationship between temperature and volatile compositions (note the logarithmic scale).

We further investigated the relationship between temperature and H_2 concentration. Compositional and temperature dependent H_2 activities were calculated and plotted along with predicted hydrogen equilibrium activities of diverse chemical reactions that potentially buffer the H_2 concentration in the fluids (Figure 5.8). The acid sulfate type fluids plot near the carbonic acid/methane buffer and H_2 concentrations in those fluids might be controlled by the chemical reaction:

$$HCO_3^- + 4H_2 + H^+ = CH_4 + 3\,H_2O$$

A considerable number of the North West Caldera wall vent fluids as well as fluids from Haungaroa plot along the sulfide-sulfate buffer and might be controlled by reaction:

$$H_2S(aq) + 4H_2O = SO_4^{2-} + 4H_2(aq) + 2H^+$$

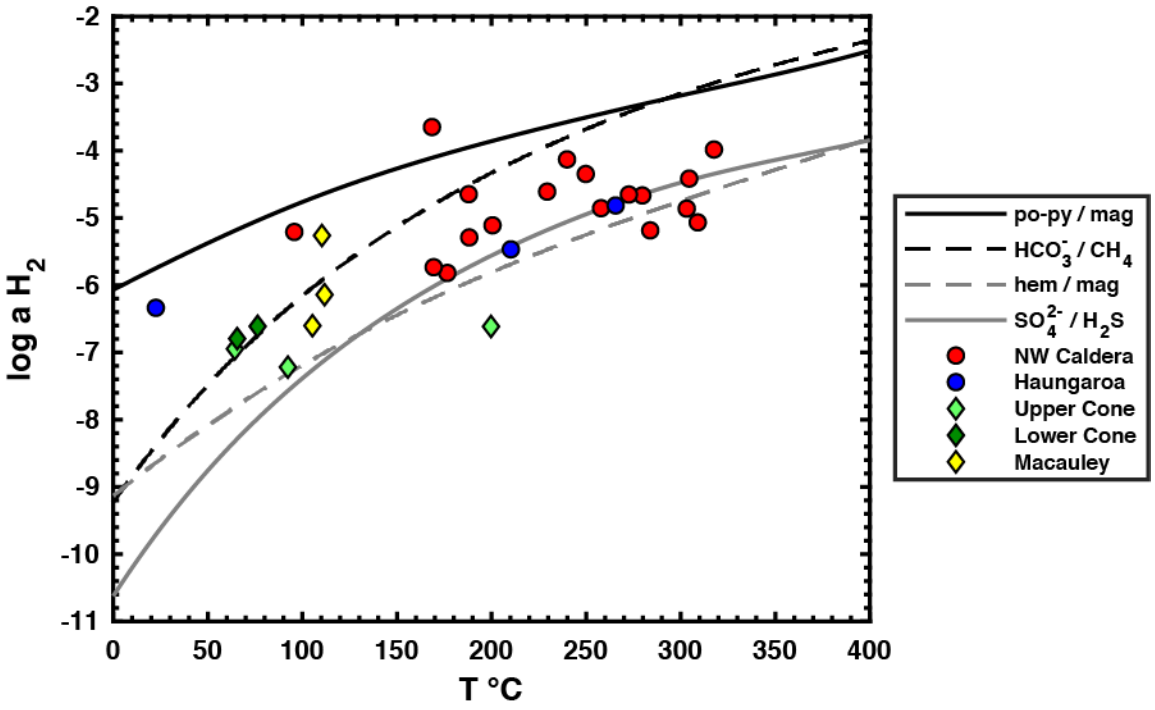

Figure 5.8: H_2 activity in hydrothermal fluids plotted with equilibrium activities of potential subsurface reactions controlling H_2 activities. Vent fluids from Haungaroa and a subset of the fluids from Brothers plot along the equilibrium activity of the sulfate/sulfide reaction. Acid sulfate-type fluids rather scatter around the equilibrium activity of the carbonic acid/methane reaction.

Figure 5.9 shows the compositional relationship between the concentrations of dissolved gases and Mg. Magnesium may provide a means of estimating the purity of black smoker-type fluids and hence increasing contents of some gases associated with decreasing Mg may point to control by subsurface fluid mineral reactions. For CO_2 concentrations, however, this seems not to be the case. For the NW Caldera Wall, most samples with Mg concentrations between 30 mmol and 3 mmol all cluster in the same range of about 3 to 12 mmol/l CO_2 (excluding two samples enriched in CO_2). The particle-poor CO_2-rich black smoker-fluids from Haungaroa also do not show increasing CO_2 with decreasing Mg concentration. Also, for the acid sulfate-type fluids, the CO_2 content is independent of Mg and samples with seawater-like Mg concentrations are enriched in CO_2 as much as samples with Mg contents higher than seawater are.

H_2S concentrations behave in a similar fashion as CO_2. The acid sulfate-type fluids may, independent of Mg, be more or less enriched in H_2S. Most black smoker-type fluids show low concentrations of < 1 mmol/l, whereas some samples show increased H_2S/Mg ratios.

H_2 and CH_4 behave different from H_2S and CO_2: The acid sulfate-type fluids are depleted in these gases and do not exceed a concentration of 1 µmol/l (except for methane in one sample from the upper cone site).

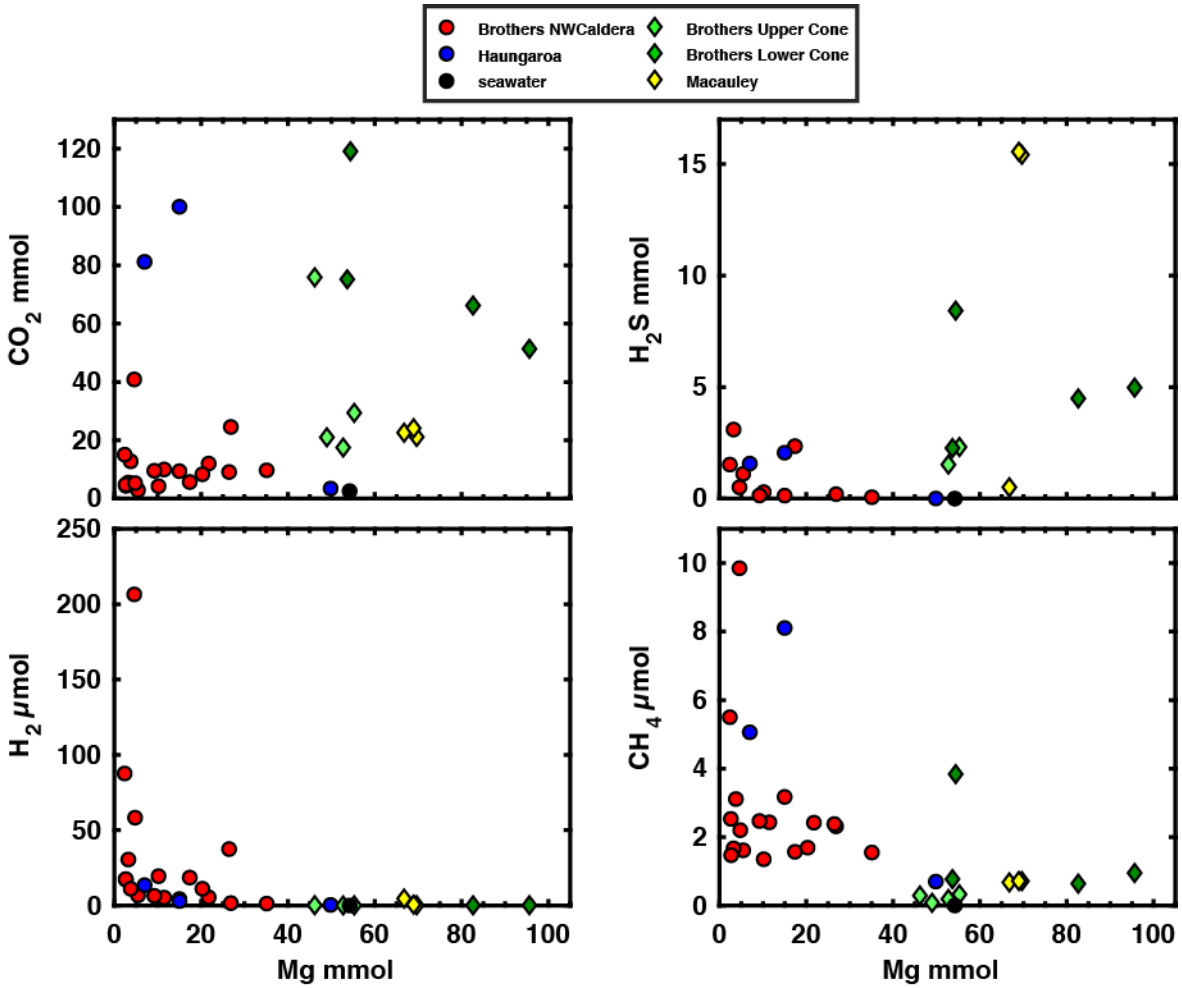

Figure 5.9: Covariation of volatile concentrations and Mg of hydrothermal vent fluids. Anticorrelation of volatile species and Mg might indicate generation due to subsurface mineral reactions.

The black smoker-type fluids from Brothers NW Caldera wall and Haungaroa show a strong anticorrelation of Mg and CH_4 or H_2. This trend suggests that subsurface fluid mineral reactions are most likely responsible for the concentrations of those gases. There are however single samples that have much higher ratios of CH_4 and H_2 over Mg.

Figure 5.10 plots gas concentrations of vent fluids against their Cl concentrations. The relationship between Cl and volatiles may reveal control by phase separation processes since the partitioning of volatiles behaves opposing to the partitioning of salt. Such trends are visible for CO_2 and CH_4 in the vent fluids of the North West Caldera wall. Here, the lowest gas concentrations are associated to highest concentrations in Cl in a large fraction of the samples set. For H_2 contents, however, only some vent fluids follow such a trend whereas most samples show increasing H_2 with increasing Cl contents. H_2S contents do not seem to be controlled by phase separation at the North West Caldera wall. For Haungaroa, CO_2, H_2S and CH_4 are more enriched in the sample with higher chlorinity which suggests that phase separation alone does not explain the compositional range of the fluids. Volatiles in the acid sulfate type fluids of

Brothers Cones are either enriched independently of Cl or there is a slight trend of decreasing Cl with increasing gas contents.

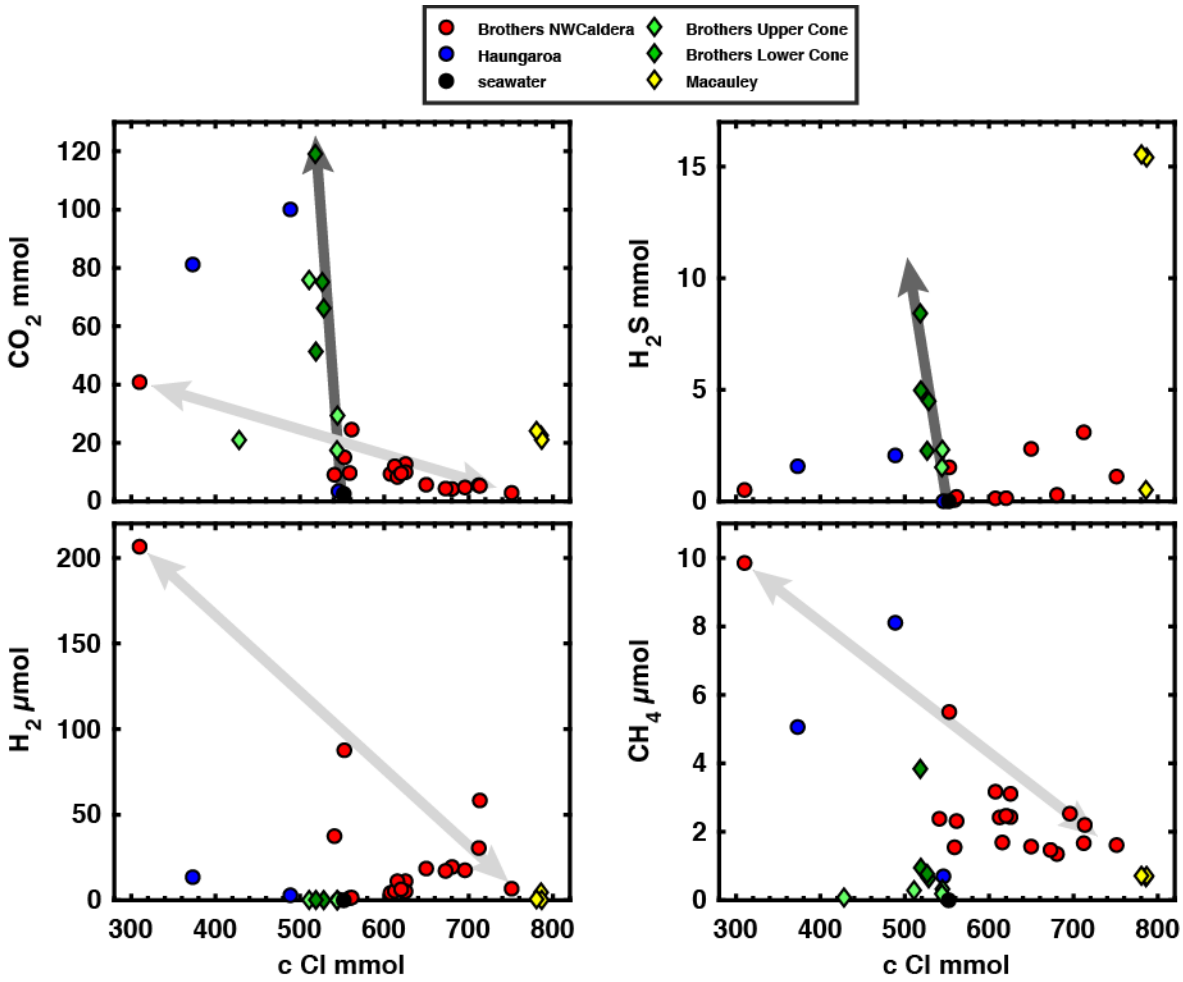

Figure 5.10: Covariation of volatiles and Cl for the vent fluids. Anticorrelation of chloride with volatiles indicates enrichment or depletion due to possible phase separation (indicated by the light grey arrows). The dark grey arrows show the trend for the Cone sites. Major changes in H_2S and CO_2 which barely affect Cl could hint to addition of magmatic volatiles.

Considering phase separation processes, the relationship between individual gases should clearly follow a correlation trend. Figure 5.11 shows the relationship between CO_2, the most abundant volatile in the North West Caldera Wall plotted against sulfate and gases. The rationale for including sulfate in this assessment is that excess sulfate in vent fluids from arc hydrothermal systems may be produced by disproportionation of SO_2 degassing from the magma plumbing system of the volcanoes (e.g. Gamo et al, 1997; Butterfield et al., 2011; Seewald et al., 2015). What this plot shows is that most gaseous species in the majority of samples clearly follow a phase separation trend but there are exceptions. For instance, in vent fluids samples with low sulfate concentrations a tight correlation is found with CO_2. Samples

with high sulfate concentrations, in contrast, clearly deviate from this trend and form an individual cluster where the concentrations of the respective species are decoupled.

For H_2S the impression from the Cl vs H_2S plot is confirmed and phase separation is unlikely to impose a major control on H_2S contents. For instance, the H_2S concentrations for samples that have very high CO_2 contents but are otherwise unaffected by phase separation is very low. But a group of samples gives very high H_2S concentrations of several mmol/l at low to moderate CO_2 contents. For H_2 and CH_4 contents of the North West Caldera fluids, a clear correlation with CO_2 contents exists where H_2 appeared unaffected by phase separation when plotted against Cl contents. Here, magma degassing appears to impose a stronger control than phase separation. Again, a subset of the samples appears unaffected by phase separation and clusters in a region of relatively high CO_2 and low H_2concentrations (Figure 5.11).

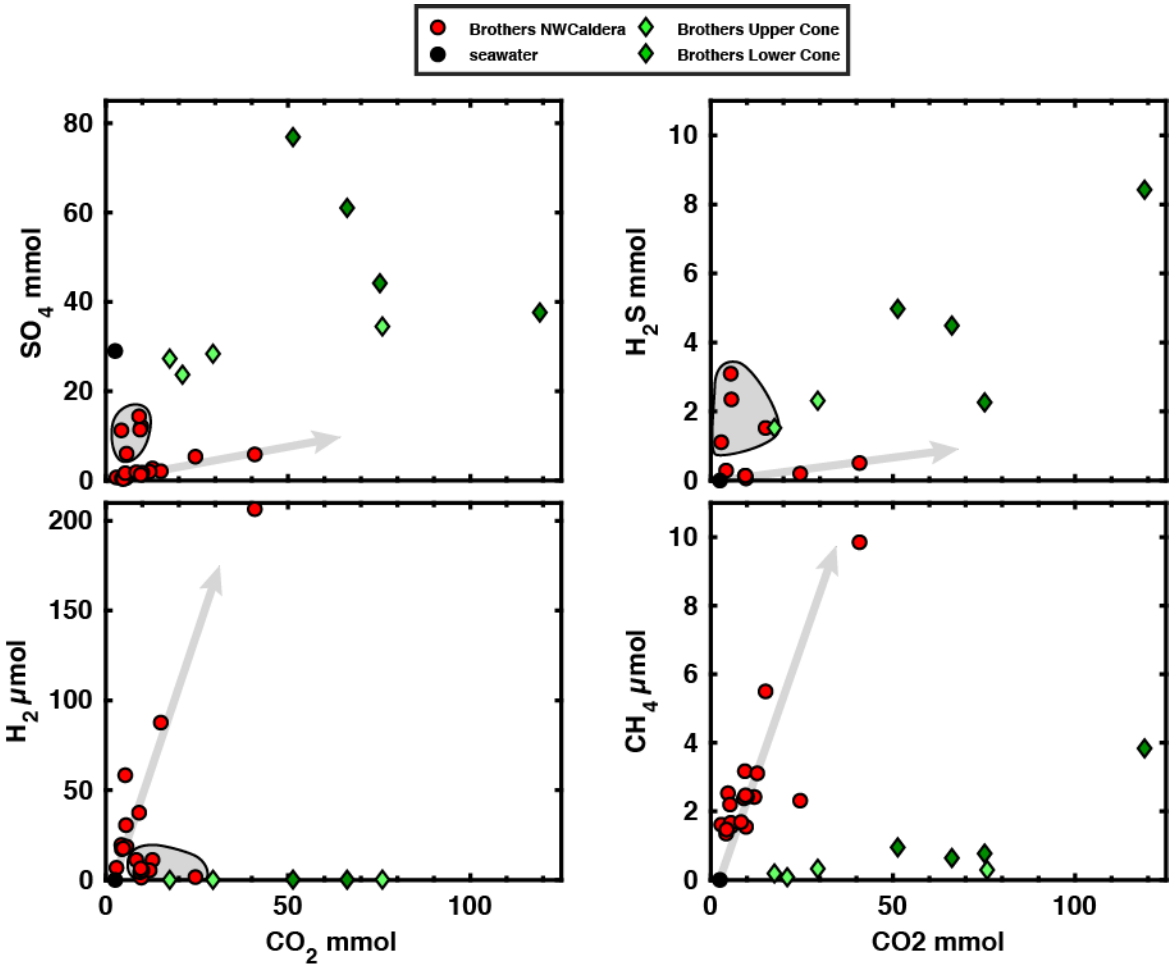

Figure 5.11: Covariation of CO_2 and other volatiles and sulfate for the vent fluids. The light grey arrows indicate the phase separation trend.

Given that the acid sulfate-type fluids (1) are rich in H_2S, SO_4 and CO_2, (2) have gas concentrations that do not correlate with chlorinity and (3) have CO2 concentrations that neither correlate with H2S nor with SO4, we suggest that the gases for the acid sulfate type fluids

originate from magmatic sources that have highly variable relative release fluxes for CO_2 and SO_2

We have calculated the average compositions of the magmatic input regarding the CO_2:SO_2 ratio by simply assuming that all CO_2 and all H_2S from these fluids originated from a magmatic source. For SO_4 we subtracted the seawater value and suggest that all excess SO_4 originates from the magmatic source. This envelope yields a CO_2:SO_2 ratio of 1:1 for the Brothers Lower Cone, a 5:4 ratio for Brothers Upper Cone and a 4:7 ratio for Macauley Caldera. For Haungaroa Volcano this envelope lead to a CO_2:SO_2 ratio of 24:1. Two samples for Haungaroa and three samples for Macauley gave similar results in the envelope whereas for both of Brothers Cone site the results varied with CO_2:SO_2 ratios between 2:1 and 1:2. This suggests that the input of gases is decoupled and that CO_2 and SO_2 are released independently from each other in terms of time and space.

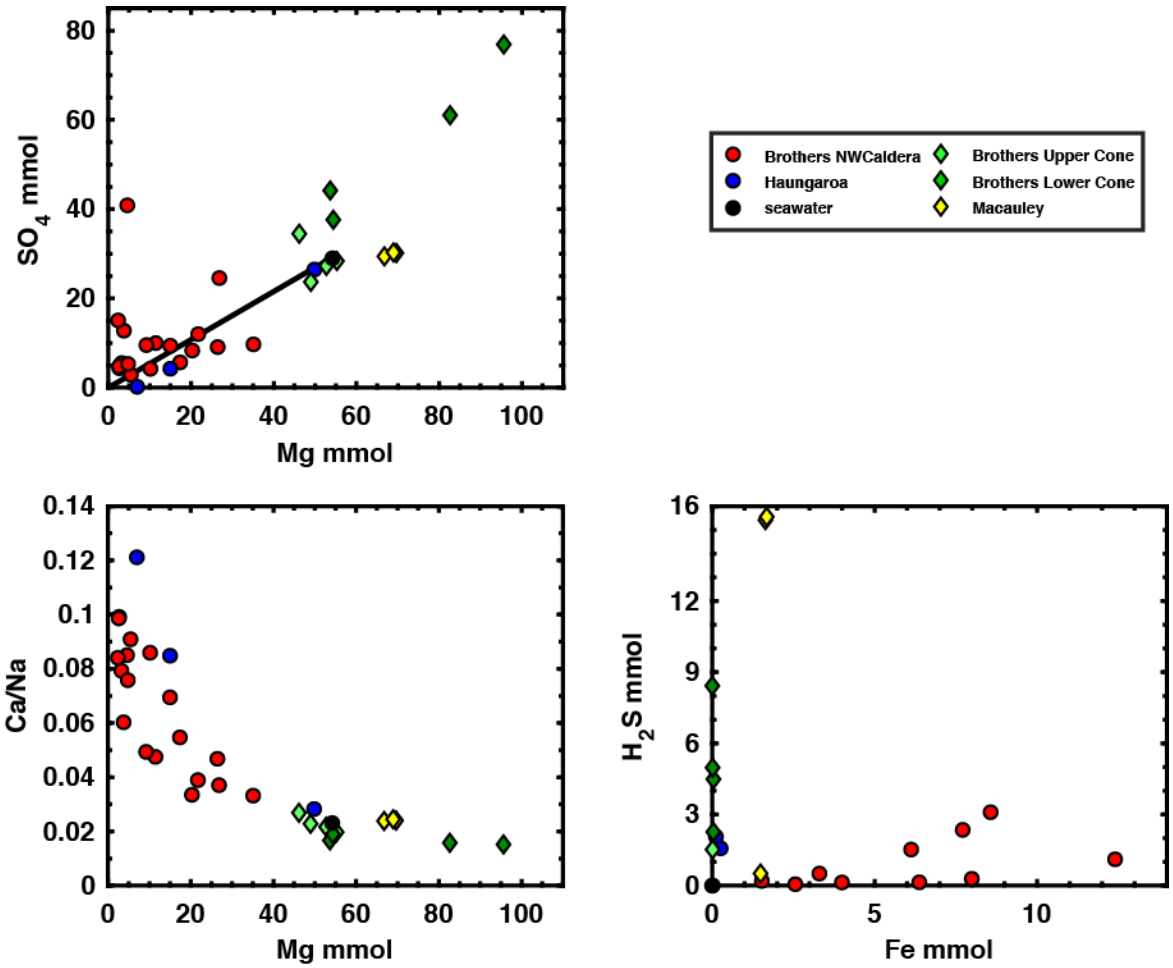

Figure 5.12: Element ratios indicative of subsurface reactions: Apparent scatter of Mg vs SO_4 element ratios points to non-conservative behavior for North West Caldera fluids. Increasing Ca/Na ratios with decreasing Mg reflects albitization processes. Variable H2S:Fe eventually points to magmatic volatiles and advanced argillic alteration in the subsurface.

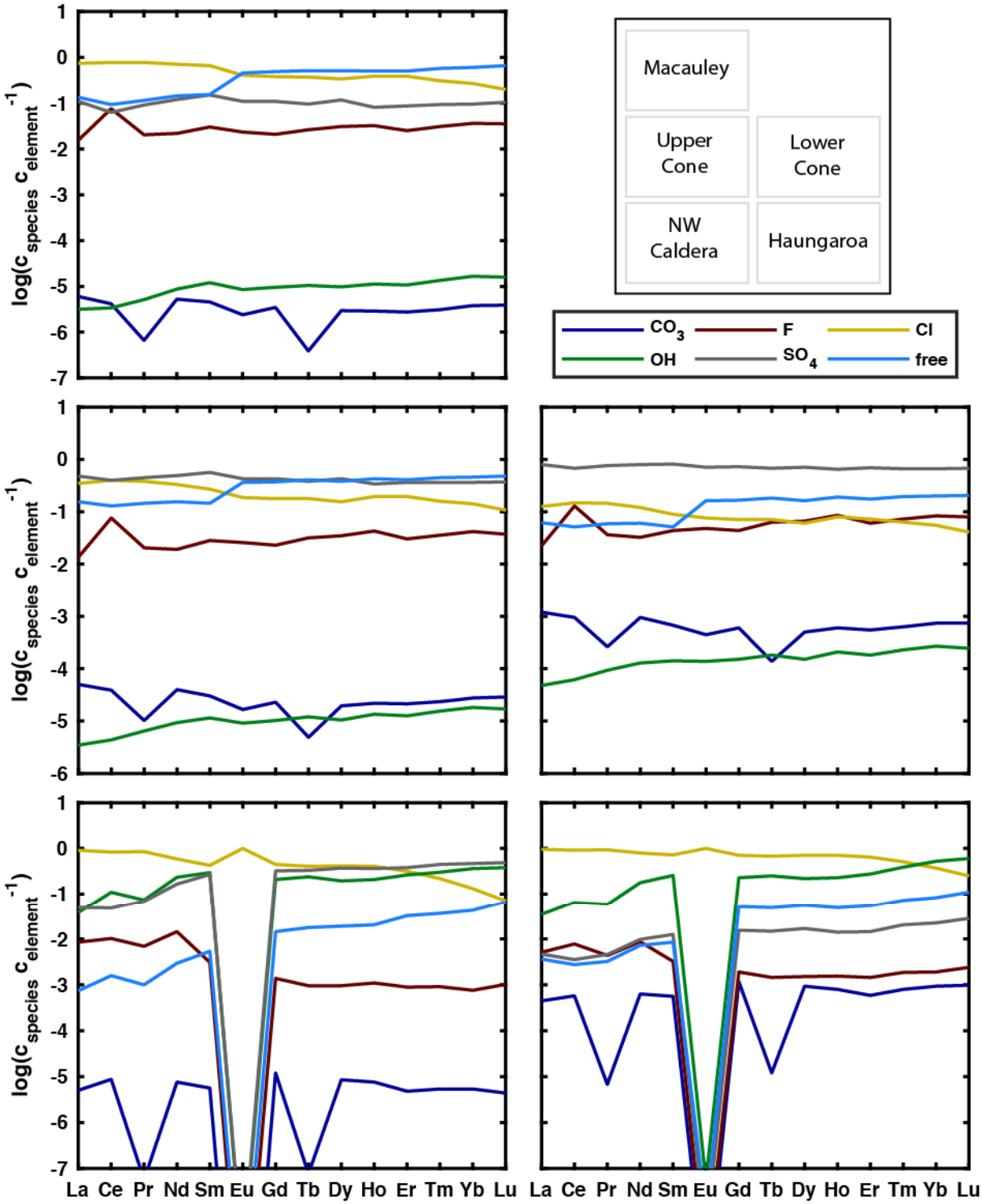

Figure 5.13: Speciation of REE elements in different vent fluid types. Lines denote the relative abundances of REE complexes. In oxidizing conditions Eu is stable in a trivalent oxidation state and hence indistinguishable from neighboring elements in acid sulfate fluids. In seawater dominated fluids Eu is divalent and mostly chloro-complexed which leads to a positive Eu anomaly in the fluid composition. Note the logarithmic scale.

5.3.6 Subsurface mineral reactions indicated by fluid chemistry

The composition of hydrothermal vent fluids provides direct evidence for subsurface mineral reactions (Figure 5.12). The ratio of Mg over SO_4 demonstrates if vent fluids fit the traditional picture of being depleted in Mg and SO_4. For fluids in Brothers NW Caldera the ratio between Mg and SO_4 does not fit that picture. Both, excess of Mg as well as excess SO_4 are apparent. This shows that either SO_4 or Mg do not behave in a conservative fashion. Two reasons are most likely: Sulfate precipitation could decrease SO_4 and lead to an apparent Mg excess, or dissolution of sulfate may add sulfate to the solution can cause an apparent Mg deficit.
An increasing Ca/Na ratio with decreasing Mg shows that albitization is taking place in the subsurface. The relationship of H_2S vs Fe may suggest that Fe-sulfide solubility may play a role in the North West Caldera fluids. High H_2S:Fe values of the acid-sulfate fluids indicate that H_2S is derived from magma degassing and Fe is already leached from the upflow zone in the course of advanced argillic alteration.

5.3.7 REE speciation of in-situ vent fluids

First-order differences in REE speciation can be noted between the acid-sulfate fluids at the Brothers Cone sites and Macauley and the black-smoker type fluids at Brothers NW Caldera and Haungaroa (Figure 5.13). (1) The acid-sulfate fluids are so oxidized that Eu is stable in trivalent oxidation state in the fluids. The speciation of Eu is hence not notably different from the speciation of the neighboring REE. By contrast, Eu is divalent in the black-smoker type fluids, where the speciation of Eu is notably different from that of the neighboring REE. (2) In acid-sulfate fluids, the proportion of free ions in the speciation of the REE is very high in the most acid examples (Macauley and Brothers Upper Cone). Here, sulfate-complexes also play a dominant role in complexation. The REEs in the black-smoker type fluids, in contrast, are dominantly chloro- and hydroxo-complexed. The divalent Eu is almost entirely chloro-complexed, due to the very high stability of the $EuCl_4^{2-}$ complex at high temperatures and under reducing conditions (Haas et al., 1995). The predominance of chloro-complexation is greater for the light REE than for the heavy REE.
In a second set of calculations, we added REE-phosphates (monazite for La through Gd and xenotime for Tb through Lu; cf. Migdisov et al., 2016) to a black-smoker type vent fluid from NW Caldera at Brothers and to an acid-sulfate fluid from Macauley (Figure 5.14). These computations allowed us to assess the solubility of REEs in the different fluid types in the course of increasing extent of fluid-rock reaction. In the black-smoker type fluid, REE contents went up initially, but REE-phosphate saturation was reached quickly and the contents of the trivalent REE were buffered to low concentrations. Due to its divalent oxidation state and thermodynamically

favorable state as aqueous chloro-complex, Eu shows a different behavior and continues to increase in concentration. Among the trivalent REE, the solubility diminishes from La to Yb. The results of these calculations indicate that a hydrothermal solution with the composition of a NW Caldera vent fluid should develop REE concentration patterns characterized by light REE enrichments and positive Eu anomalies. This is exactly how most REE patterns of the NW Caldera fluids look like (Kleint et al., submitted to GCA).

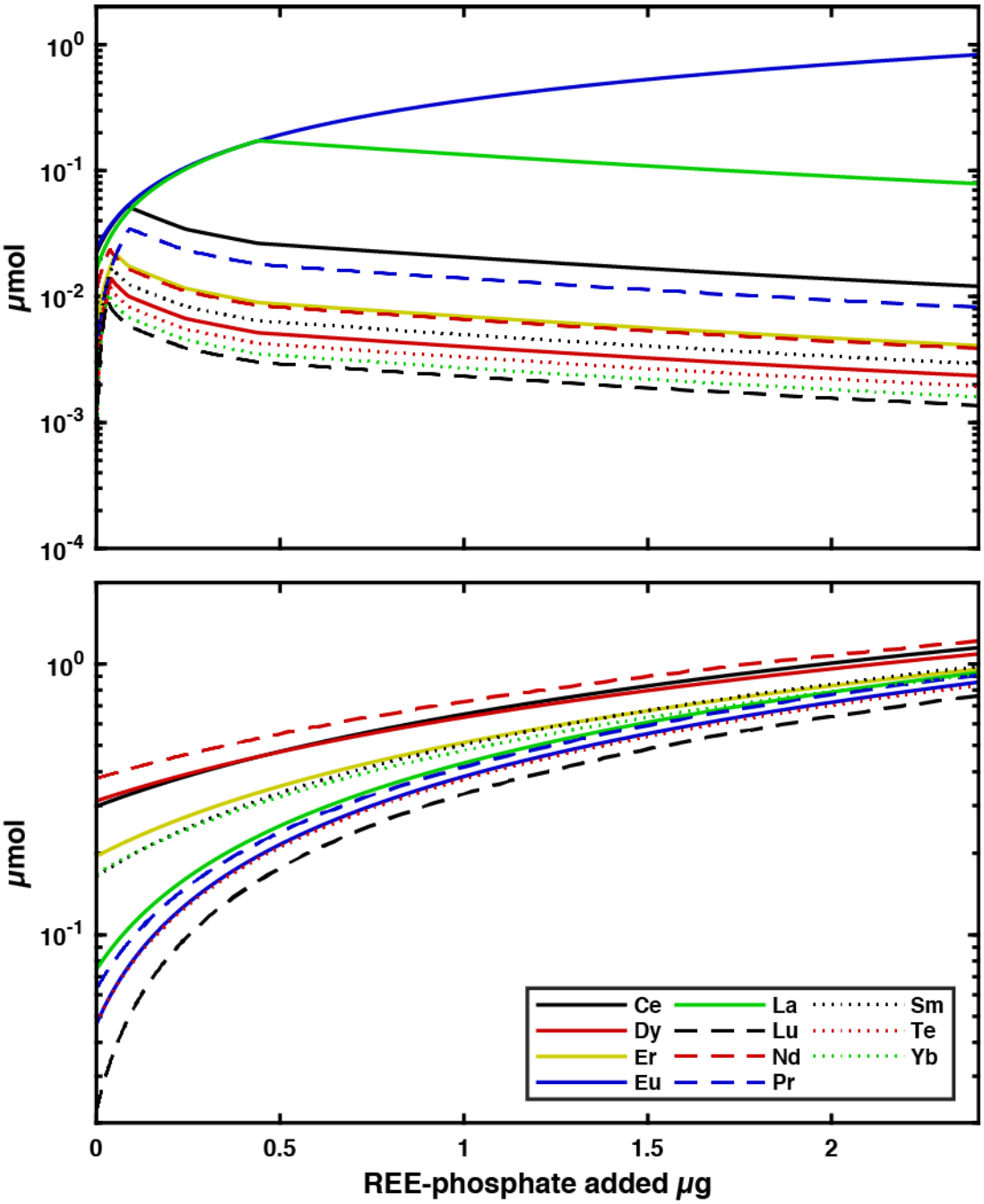

Figure 5.14: Evolution of REE concentration during addition of REE-phosphate. Upper panel: Adding REE-phsophate to a North West Caldera fluid results in an increase of Eu due its divalent state whereas trivalent REEs are decrease. Lower panel: Adding REE-phosphate to an acid-sulfate fluid of Macauley will increase all REE in the same fashion due to the trivalent state.

Adding REE-phosphates to an acid-sulfate fluid from Macauley yields an entirely different development of the REE-characteristics of the fluid. The concentrations of all REE are predicted in increase, and a fractionation amongst the trivalent REE is not expected to take place. These calculation results suggest that the REE patterns of the acid-sulfate hydrothermal fluids should be flat and that REE concentrations should overall be higher than in the black smoker fluids. Again, this is exactly what the REE patterns of the Macauley fluids look like (Kleint et al., submitted to GCA).

In summary, what the results of the speciation and solubility calculations show confirms that the acid-sulfate fluids have flat speciation patterns, and adding rock will increase all REE. The fluids with positive Eu anomalies from NW Caldera at Brothers (and to a lesser extent also the Haungaroa fluids) have a completely different speciation pattern, Eu is predominantly divalent, and adding REE will have enrichments of Eu > light REE > heavy REE.

5.4 Discussion

5.4.1. Variable magma degassing fluxes and subsurface mixing in the South Kermadec

A summary of the vent fluid gas contents indicates how variable first order compositional characteristics are in the different work areas.

At Haungaroa Volcano, vent temperatures close to the boiling curve suggest that the high concentrations could be generated by phase separation processes. Calculated source composition suggests a CO_2:SO_2 ratio of 24:1 if H_2S originates from a magmatic source.

The estimated source composition of Macauley caldera is CO_2:SO_2 of 4:7 and encompasses a close range for more than one subsample. Macauley is the most SO_2 dominated edifice from our working area. The high salinities of the fluids suggest that the fluids are derived by supercritical phase separation and the brine phase ascending. This process is assumed to occur in a late stage of the evolution of a hydrothermal system, as the higher density and more viscous brines are expected to move up to the seafloor much slower than the less salty fluids (Gruen et al., 2014).

At the Brother Cone Sites our estimated source composition of CO_2:SO_2 for the magmatic fluids are 1:1 and 4:5, respectively. Variable CO_2, H_2S and SO_4 ratios for individual samples suggest that the exhalation of volatiles occurs in a temporal and spatial variable fashion. Low Sr concentrations and seawater isotope signatures suggest that the source fluid is extremely depleted in Sr. This could be due to the fact that the magmatic end-member contains no salt (cf. Seewald et al., 2015) or due to extensive anhydrite precipitation in the subsurface (Kleint

et al., submitted to GCA). The trend to slightly lower salinities with increasing gas concentration might also point to supercritical phase separation, if a low salinity, gassy fluid separated and moved up to the seafloor.

In the NW Caldera Wall vent site, the apparent scatter of the Mg/SO_4 ratio shows that fully conservative behavior is not realized in this vent field. Depletions in SO_4 are likely consequences of sulfate precipitation. Sulfates are common in chimneys and stockwork zones. The decreased Mg/Sr values of some vent fluids corroborate the idea of subseafloor sulfate precipitation. Interestingly, the samples that show depleted Mg/Sr ratios are exactly the ones that gave too high extrapolated end-member temperatures, which could be a sign for entrainment and conductive heating of seawater. Indeed, reaction path models (Diehl et al., in prep., Chapter 4) suggest that anhydrite precipitation is favored for samples that are conductively heated during mixing.

The fluid data show that phase separation is common at the NW Caldera wall vent site. Anticorrelation of some volatile species (eg. CO_2) and to lesser amounts H_2 and CH_4 with Cl demonstrate that some samples are affected by phase separation. We found that CO_2 which is the most abundant gas in the North West Caldera Wall vents may serve as a good tracer for phase separation, because there is a strong correlation between CO_2 concentrations and concentrations of other gases. We hence suggest that phase separation is a common process at the North West Caldera Wall vent site.

5.4.2. Evidence for volatile contribution to the NW Caldera vent field

The distribution of CO_2 in relation to both SO_4 and H_2 indicates that processes in addition to phase separation must have taken place. Some samples give high SO_4 and high H_2S values with intermediate CO_2 concentrations and greatly depart from the phase separation trend. Instead, these samples have gas compositions that fall on a different trend that is most likely indicative of magmatic fluid influx. The same samples from dive 064 are the ones that show an SO_4 excess and also are characterized by a flat REE distribution pattern (Kleint et al., submitted to GCA) that is more characteristic of acid-sulfate type fluid. Hence, the NW Caldera wall site is affected by magma degassing to some extent. Finding straightforward chemical indicators for magmatic fluid input is difficult: Fouquet et al, 2019 propose that a clustering of Mg/SO_4 ratios may point toward magmatic contribution. Due to the fact that precipitation or dissolution of sulfates may as well influence the Mg/SO_4 we propose that the element relationship between CO_2 and SO_4 and REE distributions in vent fluids provide the better approach to identify magmatic input to vent fluids. We propose that the Brothers NW Caldera wall is a place where the boundaries of classification become indistinct and where seawater dominated fluids are partly influenced by

magmatic volatiles. The North West Caldera wall hence display a transitional system between seawater-dominated and magmatic-volatile dominated systems. Such transitions are also reported by Stucker et al. (2017) for the vents at the Hinepuia Volcano, which they call a magmatic-hydrothermal system with a water-rock influence.

5.4.3 Consequences for REE speciation and solubility

The fluid compositional difference (magmatically influenced at acid-sulfate springs) versus little or no magma degassing (bar the unreactive CO_2) appears to be the most plausible explanation - and it appears to be robustly supported by the computational results presented here. These results corroborate the idea that magma degassing promoted REE variability first proposed in studies of vent fluids and hydrothermal precipitates from the eastern Manus Basin, in which the vent fluids are also affected by variable magmatic fluid influx (Bach et al., 2003; Craddock & Bach, 2010; Craddock et al., 2010). Our calculations use newer thermodynamic data for speciation calculations and we present solubility computations to conclusively show a causal relation between magmatic volatile influx and REE contents of vent fluids. While the principal findings of flat REE speciation patterns in acid-sulfate fluids is similar to those of earlier studies, our results indicate that the role of fluoro-complexes is much smaller than proposed by Bach et al. (2003). This is due to fact that the Haas et al. (1995) thermodynamic data used in the earlier studies over-predict the stability of fluoro-complexes, while the stabilities of chloro-complexes are underestimated. The Migdisov et al. (2009) thermodynamic data make use of high-temperature experimental studies (Gammons et al., 1996, 2002) and constitute a major improvement over the earlier data that were extrapolated to higher temperatures.

Our new results have wider implications, as they support the idea that the uniform light REE-enriched patterns with positive Eu anomalies of black-smoker type fluids world-wide are not due to exchange with plagioclase (Klinkhammer et al., 1994), but are instead controlled by speciation and solubility of REEs in chloride-dominated, near-neutral pH solutions. Our results, also confirm that degassive influx of magmatic SO_2, which is common in island arc magma-hydrothermal systems, will cause flat REE patterns of hydrothermal fluids and will generally enhance the solubility of REEs in solution. These results hence suggest that REE patterns of hydrothermal precipitates can indeed be used as tracer for magma degassing also in ancient supra-subduction zone settings.

5.5 Conclusions

Compositional data of vent fluid samples along the South Kermadec Arc provide information on subsurface fluid-mineral reactions, phase separation and variable volatile input. Major element compositions demonstrate extensive albitization and dissolution/precipitation reactions of sulfates in the subsurface below the Brothers NW Caldera vent field. Variable dissolved gas contents in the hydrothermal systems are controlled either by phase separation or magmatic input of CO_2 and SO_2. Variable concentrations of H_2S, SO_4 and CO_2 at Brothers Cone sites suggest that the degassing of SO_2 and CO_2 occurs independent in space and time and hence degassing of CO_2 and SO_2 seems to occur decoupled. At Macauley Caldera highly saline fluids with high concentrations of H_2S, SO_4 and CO_2 suggeststst phase separation and magma degassing to occur decoupled. Haungaroa volcano with high concentrations in CO_2 and a lack of H_2S/SO_4 results in a likely scenario of CO_2 and additional phase separation processes. The seawater-dominated hydrothermal vents at Brothers North West Caldera wall are revealed to be mainly influenced by phase separation processes. Some vent fluids depart from phase separation trends and are subtly influenced by magmatic gas influx: CO_2/SO_4 ratios and REE pattern of vent fluids are demonstrated to be convenient to uncover input of volatiles to hydrothermal systems.

Acknowledgements

We thank the captains and crews of the RV Sonne and the RV Thompson for their work aboard the vessels. We acknowledge the teams and engineers of the ROV MARUM Quest and the ROV Jason II. Financial support for cruise TN350 was provided by U.S. National Science Foundation awards OCE-1558356 to Susan Humphris and OCE-1558795 to Anna-Louise Reysenbach. The Bundesministerium für Bildung und Forschung (BMBF) provided financial resources for the project Hydrothermadec (cruise SO253) and this work with grant no. 03G0253B. AD was also partly supported by the MARUM Center for Marine Environmental Science.

References

Bach, W., Peucker-Ehrenbrink, B., Hart, S. R., and Blusztajn, J. S. (2003). Geochemistry of hydrothermally altered oceanic crust: Dsdp/odp hole 504b implications for seawater-crust exchange budgets and sr- and pb-isotopic evolution of the mantle. Geochemistry, Geophysics, Geosystems, 4(3). doi: 10.1029/2002GC000419.

Baker, E. T., Walker, S. L., Embley, R. W., and de Ronde, C. E. J. (2012). High-Resolution Hydrothermal Mapping of Brothers Caldera, Kermadec Arc. Economic Geology. doi: 10.2113/econgeo.107.8.1583.

Berkenbosch, H. A., de Ronde, C., Gemmell, J. B., McNeill, A. W., and Goemann, K. (2012). Mineralogy and Formation of Black Smoker Chimneys from Brothers Submarine Volcano, Kermadec Arc. Economic Geology, 107(8):1613. doi: 10.2113/econ-geo.107.8.1613.

Berkenbosch, H. A., de Ronde, C. E. J., Paul, B. T., and Gemmell, J. B. (2015). Characteristics of Cu isotopes from chalcopyrite-rich black smoker chimneys at Brothers volcano, Kermadec arc, and Niuatahi volcano, Lau basin. Mineralium Deposita, 50(7):811–824. doi: 10.1007/s00126-014-0571-y.

Bird, P. (2003). An updated digital model of plate boundaries. Geochemistry, Geophysics, Geosystems, 4(3). doi: 10.1029/2001GC000252.

Butterfield, D. A., Nakamura, K., Takano, B., Lilley, M. D., Lupton, J. E., Resing, J. A., and Roe, K. K. (2011). High SO_2 flux, sulfur accumulation, and gas fractionation at an erupting submarine volcano. Geology, 39(9):803. doi: 10.1130/G31901.1.

Caratori Tontini, F., Davy, B., de Ronde, C. E. J., Embley, R. W., Leybourne, M., and Tivey, M. A. (2012a). Crustal Magnetization of Brothers Volcano, New Zealand, Measured by Autonomous Underwater Vehicles: Geophysical Expression of a Submarine Hydrothermal System. Economic Geology. doi: 10.2113/econgeo.107.8.1571.

Caratori Tontini, F., de Ronde, C. E. J., Yoerger, D., Kinsey, J., and Tivey, M. (2012b). 3-D focused inversion of near-seafloor magnetic data with application to the Brothers volcano hydrothermal system, Southern Pacific Ocean, New Zealand. Journal of Geophysical Research: Solid Earth. doi: 10.1029/2012JB009349.

Craddock, P. R. and Bach, W. (2010). Insights to magmatic-hydrothermal processes in the Manus back-arc basin as recorded by anhydrite. Geochimica et Cosmochimica Acta. doi: https://doi.org/10.1016/j.gca.2010.07.004.

de Ronde, C. E., Baker, E. T., Massoth, G. J., Lupton, J. E., Wright, I. C., Feely, R. A., and Greene, R. R. (2001). Intra-oceanic subduction-related hydrothermal venting, Kermadec volcanic arc, New Zealand. Earth and Planetary Science Letters, 193(3):359 – 369. doi: https://doi.org/10.1016/S0012-821X(01)00534-9.

de Ronde, C. E., Faure, K., Bray, C. J., Chappell, D. A., and Wright, I. C. (2003). Hydrothermal fluids associated with seafloor mineralization at two southern Kermadec arc volcanoes, offshore New Zealand. Mineralium Deposita. doi: 10.1007/s00126-002- 0305-4.

de Ronde, C. E. J., Hannington, M. D., Stoffers, P., Wright, I. C., Ditchburn, R. G., Reyes, A. G., Baker, E. T., Massoth, G. J., Lupton, J. E., Walker, S. L., Greene, R. R., Soong, C. W. R., Ishibashi, J., Lebon, G. T., Bray, C. J., and Resing, J. A. (2005). Evolution of a Submarine Magmatic-Hydrothermal System: Brothers Volcano, Southern Kermadec Arc, New Zealand. Economic Geology. doi: 10.2113/gsecongeo.100.6.1097.

de Ronde, C. E. J., Massoth, G. J., Butterfield, D. A., Christenson, B. W., Ishibashi, J., Ditchburn, R. G., Hannington, M. D., Brathwaite, R. L., Lupton, J. E., Kamenetsky, V. S., Graham, I. J., Zellmer, G.

F., Dziak, R. P., Embley, R. W., Dekov, V. M., Munnik, F., Lahr, J., Evans, L. J., and Takai, K. (2011). Submarine hydrothermal activity and gold-rich mineralization at Brothers Volcano, Kermadec Arc, New Zealand. Mineralium Deposita. doi: 10.1007/s00126-011-0345-8.

de Ronde, C. E. J. and Stucker, V. K. (2015). Chapter 47 - Seafloor Hydrothermal Venting at Volcanic Arcs and Backarcs. In Sigurdsson, H., editor, The Encyclopedia of Volcanoes, pages 823 – 849. Academic Press, Amsterdam, Second edition.
doi: https://doi.org/10.1016/B978-0-12-385938-9.00047-X.

DeMets, C., Gordon, R. G., and Argus, D. F. (2010). Geologically current plate motions. Geophysical Journal International, 181(1):1–80. doi: 10.1111/j.1365- 246X.2009.04491.x.

Deniel, C. and Pin, C. (2001). Single-stage method for the simultaneous isolation of lead and strontium from silicate samples for isotopic measurements. Analytica Chimica Acta.
doi: https://doi.org/10.1016/S0003-2670(00)01185-5.

Driesner, T. (2007). The system H_2O-NaCl. Part II: Correlations for molar volume, enthalpy, and isobaric heat capacity from 0 to 1000°C, 1 to 5000bar, and 0 to 1 XNaCl. Geochimica et Cosmochimica Acta. doi: https://doi.org/10.1016/j.gca.2007.05.026.

Driesner, T. and Heinrich, C. A. (2007). The system H2O-NaCl. Part I: Correlation formulae for phase relations in temperature-pressure-composition space from 0 to 1000°C, 0 to 5000 bar, and 0 to 1 XNaCl. Geochimica et Cosmochimica Acta. doi: https://doi.org/10.1016/j.gca.2006.01.033.

Fouquet, Y., Pelleter, E., Konn, C., Chazot, G., Dupré, S., Alix, A., Chéron, S., Donval, J. P., Guyader, V., Etoubleau, J., Charlou, J. L., Labanieh, S., and Scalabrin, C. (2018). Volcanic and hydrothermal processes in submarine calderas: The Kulo Lasi example (SW Pacific). Ore Geology Reviews, 99:314 – 343. doi: https://doi.org/10.1016/j.oregeorev.2018.06.006.

Gammons, C. H., Wood, S. A., and Williams-Jones, A. E. (1996). The aqueous geochemistry of the rare earth elements and yttrium: VI. Stability of neodymium chloride complexes from 25 to 300°C. Geochimica et Cosmochimica Acta, 60(23):4615 – 4630.
doi: https://doi.org/10.1016/S0016-7037(96)00262-1.

Gammons, C. H., Woods, S. A., and Li, Y. (2002). Complexation of the rare earth elements with aqueous chloride at 200°C and 300°C and saturated vapor pressure. In Hellmann, R. and Wood, S. A., editors, Water-Rock Interactions, Ore Deposits, and Environmental Geochemistry: A tribute to David A. Crerar, pages 191–207. The Geo- logical Society.

Gamo, T., Okamura, K., Charlou, J., Urabe, T., Auzende, J., Ishibashi, J., Shitashima, K., and Chiba, H. (1997). Acidic and sulfate-rich hydrothermal fluids from the Manus back-arc basin, Papua New Guinea. Geology, 25(2):139. doi: 10.1130/0091- 7613(1997)025<0139:AASRHF>2.3.CO;2.

GEBCO (2014). Intergovernmental Oceanographic Commission, IHO, and BODC. Centenary edition of the GEBCO digital Atlas, published on CD-ROM on behalf of the Intergovernmental Oceanographic Commission and the International Hydrographic Organization as part of the General Bathymetric Chart of the Oceans, British Oceanographic Data Centre, Liverpool, U. K.

Gemmell, J. B., Sharpe, R., Jonasson, I. R., and Herzig, P. M. (2004). Sulfur isotope evidence for magmatic contributions to submarine and subaerial gold mineralization: Conical seamount and the ladolam gold deposit, papua new guinea. Economic Geology, 99(8):1711.
doi: 10.2113/gsecongeo.99.8.1711.

Gruen, G., Weis, P., Driesner, T., de Ronde, C. E. J., and Heinrich, C. A. (2012). Fluid-Flow Patterns at Brothers Volcano, Southern Kermadec Arc: Insights from Geologically Constrained Numerical Simulations. Economic Geology. doi: 10.2113/econ- geo.107.8.1595.

Gruen, G., Weis, P., Driesner, T., Heinrich, C. A., and de Ronde, C. E. J. (2014). Hydrodynamic modeling of magmatic-hydrothermal activity at submarine arc volcanoes, with implications for ore formation. Earth and Planetary Science Letters. doi: https://doi.org/10.1016/j.epsl.2014.07.041.

Haar, L., Gallagher, J. S., and Kell, G. S. (1984). NBS/NRC Steam Tables. Hemisphere Publishing Corporation. NBS/NRC Wasserdampftafeln, Springer Verlag, 1988.

Haas, J. R., Shock, E. L., and Sassani, D. C. (1995). Rare earth elements in hydrothermal systems: Estimates of standard partial molal thermodynamic properties of aqueous complexes of the rare earth elements at high pressures and temperatures. Geochimica et Cosmochimica Acta, 59(21):4329 – 4350. doi: https://doi.org/10.1016/0016- 7037(95)00314-P.

Hawkes, J. A., Connelly, D. P., Rijkenberg, M. J. A., and Achterberg, E. P. (2014). The importance of shallow hydrothermal island arc systems in ocean biogeochemistry. Geophysical Research Letters. doi: 10.1002/2013GL058817.

Inoue, A. (1995). Formation of Clay Minerals in Hydrothermal Environments, pages 268–329. Springer Berlin Heidelberg. doi: 10.1007/978-3-662-12648-6-7.

Jochum, K. P., Nohl, U., Herwig, K., Lammel, E., Stoll, B., and Hofmann, A. W. (2005). Georem: A new geochemical database for reference materials and isotopic standards. Geostandards and Geoanalytical Research, 29(3):333–338.

Klinkhammer, G. P., Elderfield, H., Edmond, J. M., and Mitra, A. (1994). Geochemical implications of rare earth element patterns in hydrothermal fluids from mid-ocean ridges. Geochimica et Cosmochimica Acta, 58(23):5105 – 5113. doi: https://doi.org/10.1016/0016-7037(94)90297-6.

Koschinsky, A., Thal, J., and Wolfl, A.-C. (2018). Raw multibeam EM122 data: transits of SONNE cruise SO253 (South Pacific). doi: 10.1594/PANGAEA.892787.

Migdisov, A., Williams-Jones, A. E., Brugger, J., and Caporuscio, F. A. (2016). Hydrothermal transport, deposition, and fractionation of the REE: Experimental data and thermodynamic calculations. Chemical Geology, 439:13 – 42. doi: https://doi.org/10.1016/j.chemgeo.2016.06.005.

Migdisov, A., Williams-Jones, A. E., and Wagner, T. (2009). An experimental study of the solubility and speciation of the Rare Earth Elements (III) in fluoride- and chloride- bearing aqueous solutions at temperatures up to 300°C. Geochimica et Cosmochimica Acta, 73(23):7087 – 7109. doi: https://doi.org/10.1016/j.gca.2009.08.023.

Mottl, M. J. and Holland, H. D. (1978). Chemical exchange during hydrothermal alteration of basalt by seawater. Experimental results for major and minor components of seawater. Geochimica et Cosmochimica Acta, 42(8):1103 – 1115. doi: https://doi.org/10.1016/0016-7037(78)90107-2.

Reed, M. H. (1997). Hydrothermal alteration and its relationship to ore fluid composition. In Barnes, H. L., editor, Geochemistry of hydrothermal ore deposits. Third edition.

Reeves, E. P., Seewald, J. S., Saccocia, P., Bach, W., Craddock, P. R., Shanks, W. C., Sylva, S. P., Walsh, E., Pichler, T., and Rosner, M. (2011). Geochemistry of hydrothermal fluids from the PACMANUS, Northeast Pual and Vienna Woods hydrothermal fields, Manus Basin, Papua New Guinea. Geochimica et Cosmochimica Acta, 75(4):1088 – 1123. doi: https://doi.org/10.1016/j.gca.2010.11.008.

Resing, J. A., Lebon, G., Baker, E. T., Lupton, J. E., Embley, R. W., Massoth, G. J., Chadwick, Jr., W. W., and de Ronde, C. E. J. (2007). Venting of Acid-Sulfate Fluids in a High-Sulfidation Setting at NW Rota-1 Submarine Volcano on the Mariana Arc. Economic Geology. doi: 10.2113/gsecongeo.102.6.1047.

Seewald, J., Reeves, E., Bach, W., Saccocia, P., Craddock, P., Shanks, W., Sylva, S., Pichler, T., Rosner, M., and Walsh, E. (2015). Submarine venting of magmatic volatiles in the Eastern Manus Basin, Papua New Guinea. Geochimica et Cosmochim- ica Acta, 163:178 – 199.
doi: https://doi.org/10.1016/j.gca.2015.04.023.

Stucker, V. K., Walker, S. L., de Ronde, C. E. J., Caratori Tontini, F., and Tsuchida, S. (2017). Hydrothermal Venting at Hinepuia Submarine Volcano, Kermadec Arc: Understanding Magmatic-Hydrothermal Fluid Chemistry. Geochemistry, Geophysics, Geosystems, 18(10):3646–3661.
doi: 10.1002/2016GC006713.

Von Damm, K. (1985). Chemistry of submarine hydrothermal solutions at 21 N, East Pacific Rise. Geochimica et Cosmochimica Acta. doi: https://doi.org/10.1016/0016- 7037(85)90222-4.

Von Damm, K. L. (1990). Seafloor hydrothermal activity: black smoker chemistry and chimneys. Earth Planet Sci.

Wright, I., Worthington, T., and Gamble, J. (2006). New multibeam mapping and geochemistry of the 30° - 35°S sector, and overview, of southern Kermadec arc volcanism. Journal of Volcanology and Geothermal Research, 149(3):263 – 296. doi: https://doi.org/10.1016/j.jvolgeores.2005.03.021.

Appendix

Appendix 5.A1: Composition of major elements and dissolved gases in vent fluid samples. Note: For samples marked with an asterisk chemical data are published in Kleint et al. (submitted to GCA). These samples are here complemented with concentrations of dissolved gases (CO_2, H_2, CH_4) and $^{87}Sr/^{86}Sr$ values.

Sample	Area	Latitude	Longitude	Depth [m]	T_{mean} [°C]	T_{max} [°C]	pH	CO_2 mM	H_2S mM	H_2 µM	CH_4 µM	Cl mM	SO_4 mM	Br mM	F mM	$^{87}Sr/^{86}Sr$
061-06F *	NWC	34° 51.749'S	179° 03.476'E	1658	177	265	5.0	9.71	0.06	1.3	1.55	559	12.1	0.06	0.04	0.706757±7
061-02F *	NWC	34° 51.765'S	179° 03.491'E	1670	170	257	3.8	24.6	0.20	1.6	2.31	561	5.3	1.00	0.15	0.705780±7
064-04F *	NWC	34° 51.662'S	179° 03.460'E	1596	229	262	3.2	4.24	0.29	20	1.35	680	11.2	1.22	0.21	0.704835±7
064-11F *	NWC	34° 51.667'S	179° 03.461'E	1610	77	169	4.2	40.9	0.51	207	9.85	310	5.8	0.49	0.17	0.704933±7
067-10F *	NWC	34° 51.552'S	179° 03.141'E	1374	309	311	2.9	2.90	1.11	6.8	1.61	751	0.7	0.15	0.06	0.704562±6
072-07F *	NWC	34° 51.713'S	179° 03.446'E	1611	135	188	3.4	5.68	2.35	19	1.57	650	6.0	1.14	0.22	0.705149±6
081-02F *	NWC	34° 51.677'S	179° 03.465'E	1619	305	305	3.3	5.50	3.10	31	1.67	712	0.5	1.25	0.23	0.704393±5
085-14F *	NWC	34° 51.669'S	179° 03.473'E	1616	188	275	3.3	9.40	0.13	4.3	3.17	607	11.4	0.93	0.22	0.705160±6
1038-IGT-3	NWC	34° 51.475'S	179° 03.116'E	1319	280	280	2.9	4.37	n.a.	17	1.47	673	0.5	1.17	0.24	0.704517±6
1038-IGT-4	NWC	34° 51.475'S	179° 03.116'E	1320	273	273	2.9	4.75	n.a.	18	2.53	696	0.3	1.18	0.21	0.704502±8
1038-IGT-5	NWC	34° 51.690'S	179° 03.439'E	1583	303	304	2.8	12.8	n.a.	11	3.11	625	2.7	1.06	0.27	0.704903±7
1038-IGT-6	NWC	34° 51.663'S	179° 03.447'E	1582	240	244	3.2	5.31	n.a.	58	2.2	713	1.6	1.23	0.24	0.704524±7
1039-IGT-1	NWC	34° 51.718'S	179° 03.539'E	1600	318	321	3.3	15.1	1.52	88	5.5	553	2.1	0.94	0.21	0.704405±6
1039-IGT-2	NWC	34° 51.718'S	179° 03.539'E	1599	250	308	4.5	9.11	n.a.	38	2.38	541	14.4	0.90	0.12	0.706411±9
1039-IGT-7	NWC	34° 51.733'S	179° 03.436'E	1612	87	96	3.2	12.0	n.a.	5.4	2.42	612	2.0	0.93	0.25	0.705061±7
1039-IGT-8	NWC	34° 51.757'S	179° 03.473'E	1618	284	302	3.3	9.99	n.a.	5.2	2.43	625	1.8	0.96	0.24	0.704907±6
1041-IGT-1	NWC	34° 51.717'S	179° 03.524'E	1639	258	262	3.0	8.34	n.a.	11	1.69	616	1.9	1.05	0.16	0.705105±8
1041-IGT-2	NWC	34° 51.723'S	179° 03.518'E	1623	201	212	3.2	9.55	0.14	6.4	2.47	620	1.3	1.05	0.19	0.704873±7
045-03F *	LC	34° 52.729'S	179° 04.176'E	1318	66	67	4.6	66.2	4.49	0.1	0.64	528	61.0	0.95	0.15	0.709149±8
045-11F *	LC	34° 52.731'S	179° 04.280'E	1331	76	83	3.5	51.3	4.98	0.2	0.95	519	76.9	0.91	0.19	0.709153±7
1041-IGT-7	LC	34° 54.387'S	179° 02.273'E	1330	45	81	4.5	75.2	2.27	b.d.l.	0.77	527	44.2	0.87	0.10	0.709061±7
1041-IGT8	LC	34° 54.369'S	179° 02.280'E	1316	60	61	5.2	119	8.43	b.d.l.	3.84	518	37.6	0.86	0.10	0.709074±8
048-10F *	UC	34° 52.948'S	179° 04.094'E	1217	64	84	2.0	29.4	2.31	0.1	0.33	545	28.4	0.94	0.36	0.709115±8
048-02F *	UC	34° 53.035'S	179° 04.182'E	1217	92	115	2.2	17.5	1.53	0.1	0.19	544	27.3	n.a.	0.06	0.709160±7
1040-IGT-3	UC	34° 52.943'S	179° 04.093'E	1213	151	173	2.2	21	n.a.	b.d.l.	0.08	428	23.7	0.67	0.16	0.709123±6
1040-IGT5	UC	34° 52.940'S	179° 04.096'E	1213	200	200	1.6	75.9	n.a.	0.2	0.29	511	34.5	0.80	0.36	0.708993±7
009-02F *	Mac	30° 12.775'S	178° 26.939'W	336	110	111	1.6	22.6	0.51	4.6	0.68	786	29.4	1.83	2.57	0.708924±9
013-03F *	Mac	30° 12.775'S	178° 26.938'W	336	105	112	1.1	21.1	15.4	0.2	0.71	787	30.2	1.80	2.48	0.708941±7
013-02F *	Mac	30° 12.775'S	178° 26.938'W	336	112	112	1.5	24.1	15.6	0.6	0.72	780	30.3	1.76	2.72	0.708893±8
026-04F *	Hau	32° 36.997'S	179° 37.558'W	679	23	23	6.4	3.45	0.004	0.4	0.7	546	26.5	0.95	0.11	0.708795±6
030-10F *	Hau	32° 36.946'S	179° 37.473'W	677	210	230	3.7	100	2.06	2.9	8.11	489	4.3	0.83	0.14	0.705470±6
035-07F *	Hau	32° 36.952'S	179° 37.467'W	684	266	267	3.5	81.2	1.57	14	5.06	373	0.2	0.11	0.03	0.704829±6

Sample	Area	Latitude	Longitude	Al mM	Ba µM	B mM	Ca mM	Cu µM	Fe mM	K mM	Li mM	Mg mM	Mn mM	Na mM	P µM	S mM	Si mM	Sr mM	Zn µM
061-06F *	NWC	34° 51.749'S	179° 03.476'E	0.014	4.5	0.68	16.6	n.a	2.6	26.9	0.34	35.1	0.23	500	10	13.9	6.9	0.094	3.8
061-02F *	NWC	34° 51.765'S	179° 03.491'E	0.018	6.0	0.84	18.2	n.a	1.5	33.5	0.44	26.8	0.36	491	n.a	5.4	8.8	0.090	80
064-04F *	NWC	34° 51.662'S	179° 03.460'E	0.039	5.2	1.24	50.1	n.a	8.0	60.9	0.77	10.2	0.59	583	18	11.0	12.4	0.204	2.6
064-11F *	NWC	34° 51.667'S	179° 03.461'E	0.018	3.2	0.73	23.3	n.a	3.3	27.1	0.35	4.6	0.26	274	n.a	5.9	6.0	0.085	2.6
067-10F *	NWC	34° 51.552'S	179° 03.141'E	0.042	32.1	1.16	56.9	n.a	12.4	68.0	0.77	5.4	2.41	626	20	1.0	15.4	0.237	10
072-07F *	NWC	34° 51.713'S	179° 03.446'E	0.014	1.7	0.44	30.9	n.a	7.7	51.2	0.72	17.4	0.49	565	16	6.0	10.4	0.139	11
081-02F *	NWC	34° 51.677'S	179° 03.465'E	0.037	53.6	1.33	48.6	n.a	8.6	69.1	0.88	3.2	0.68	613	16	0.59	14.5	0.191	6.0
085-14F *	NWC	34° 51.669'S	179° 03.473'E	0.018	15.3	2.84	31.8	5.9	4.0	46.8	0.51	15.0	0.40	458	4	6.5	6.6	0.127	46
1038-IGT-3	NWC	34° 51.475'S	179° 03.116'E	0.024	48.6	1.09	47.7	0.6	10.7	60.8	0.71	2.7	2.19	481	1	0.55	12.5	0.199	6.4
1038-IGT-4	NWC	34° 51.475'S	179° 03.116'E	0.024	65.5	1.10	48.5	0.0	11.0	62.4	0.73	2.6	2.22	492	2	0.36	12.9	0.205	4.4
1038-IGT-5	NWC	34° 51.690'S	179° 03.439'E	0.021	14.3	0.89	27.9	0.8	8.6	48.6	0.97	3.8	0.47	464	3	1.8	10.4	0.129	4.3
1038-IGT-6	NWC	34° 51.663'S	179° 03.447'E	0.020	18.6	1.17	40.8	b.d.l	8.0	63.4	0.86	4.8	0.59	539	bdl.	1.6	11.9	0.163	1.4
1039-IGT-1	NWC	34° 51.718'S	179° 03.539'E	0.017	37.4	1.01	34.0	b.d.l	6.1	50.7	0.66	2.4	0.49	404	2	0.70	9.8	0.134	1.2
1039-IGT-2	NWC	34° 51.718'S	179° 03.539'E	0.007	2.4	0.63	19.0	b.d.l	2.3	26.5	0.31	26.4	0.20	406	1	11.0	4.3	0.091	0.5
1039-IGT-7	NWC	34° 51.733'S	179° 03.436'E	0.016	13.9	0.80	21.1	0.3	6.3	42.4	0.67	21.7	0.36	541	4	1.4	10.5	0.105	10
1039-IGT-8	NWC	34° 51.757'S	179° 03.473'E	0.016	13.2	0.85	22.4	b.d.l	7.0	43.8	0.69	11.5	0.38	472	4	1.2	11.2	0.103	2.0
1041-IGT-1	NWC	34° 51.717'S	179° 03.524'E	0.008	21.0	0.70	14.5	0.5	3.2	33.8	0.39	20.3	0.29	432	9	1.0	9.5	0.072	6.4
1041-IGT-2	NWC	34° 51.723'S	179° 03.518'E	0.015	20.1	0.75	20.0	0.2	6.4	38.9	0.58	9.2	0.33	406	2	1.0	9.8	0.091	10
045-03F *	LC	34° 52.729'S	179° 04.176'E	0.010	0.6	0.43	8.1	n.a	0.04	13.2	0.06	82.6	0.84	513	17	62.3	4.8	0.052	2.9
045-11F *	LC	34° 52.731'S	179° 04.280'E	0.009	0.5	0.43	7.3	n.a	0.01	13.7	0.06	95.6	1.04	478	19	76.9	6.0	0.043	1.5
1041-IGT-7	LC	34° 54.387'S	179° 02.273'E	0.016	0.6	0.40	7.0	b.d.l	0.04	11.2	0.06	53.7	0.64	418	39	30.4	3.7	0.043	0.2
1041-IGT8	LC	34° 54.369'S	179° 02.280'E	0.014	0.4	0.42	8.5	b.d.l	0.01	10.9	0.07	54.4	0.44	450	61	28.8	3.3	0.061	0.5
048-10F *	UC	34° 52.948'S	179° 04.094'E	0.013	2.7	0.46	10.2	n.a	n.a	14.5	0.07	55.3	0.36	517	n.a	29.7	4.7	0.062	42
048-02F *	UC	34° 53.035'S	179° 04.182'E	0.010	1.9	0.42	10.2	n.a	0.01	12.4	0.05	52.7	0.21	470	n.a	28.0	2.5	0.070	30
1040-IGT-3	UC	34° 52.943'S	179° 04.093'E	0.049	0.5	0.40	10.0	0.5	0.09	9.2	0.03	49.0	0.06	436	6	22.7	1.3	0.071	53
1040-IGT5	UC	34° 52.940'S	179° 04.096'E	0.173	0.5	0.44	10.9	0.3	0.33	10.7	0.04	46.2	0.19	404	17	26.1	4.1	0.050	53
009-02F *	Mac	30° 12.775'S	178° 26.939'W	0.119	2.6	0.59	16.6	n.a	1.5	15.5	0.10	66.8	0.83	696	12	30.2	7.0	0.067	197
013-03F *	Mac	30° 12.775'S	178° 26.938'W	0.118	2.6	0.60	16.4	n.a	1.6	15.3	0.10	69.6	0.83	683	15	30.4	6.7	0.069	185
013-02F *	Mac	30° 12.775'S	178° 26.938'W	0.122	2.4	0.61	16.4	n.a	1.7	15.4	0.10	68.9	0.84	670	16	30.5	6.9	0.055	243
026-04F *	Hau	32° 36.997'S	179° 37.558'W	0.010	0.5	0.40	13.4	n.a	0.02	11.4	n.a	49.8	0.02	474	n.a	26.7	0.8	0.091	n.a
030-10F *	Hau	32° 36.946'S	179° 37.473'W	0.026	11.3	0.69	36.9	n.a	0.12	24.0	0.30	15.0	0.61	435	n.a	4.2	8.4	0.106	23
035-07F *	Hau	32° 36.952'S	179° 37.467'W	0.030	6.1	0.76	42.4	n.a	0.26	25.6	0.35	7.0	0.74	350	n.a	1.6	6.4	0.105	18

6 Fluid inclusions in hydrothermal precipitates from the North West Caldera Wall hydrothermal vent field at Brothers Volcano indicate subcritical and supercritical phase separation is involved in the formation of chimneys and stockwork zones.

Alexander Diehl[1,2], Wolfgang Bach[1,2]

[1] Department of Geosciences, University of Bremen, Bremen, Germany

[2] MARUM Center for Marine Environmental Sciences, Bremen, Germany

Abstract

The submarine Brothers Volcano as part of the Southern Kermadec Arc hosts four hydrothermal vent areas that represent two important end-member types of hydrothermal circulation in submarine island arcs. The North West Caldera Wall hydrothermal vent field constitutes the most vigorous fluid discharge site at Brothers. Here, seawater-dominated black smoker type hydrothermal springs form a large vent field extending from near the caldera floor (1700 m below sealevel, mbsl) almost up to the crater rim (1300 mbsl). The vent field is linked to several fault scarps along which multiple collapse events exposed the stockwork zone that underlies the active vents. The common occurrence of sulfate mineralization in chimneys and stockwork rocks enabled us to conduct microthermometric investigations on samples collected during two research expeditions (RV Sonne SO253 and RV Thompson TN350). These samples provide insights into growth conditions, mixing regimes and sub-surface phase separation during the formation of hydrothermal vents and underlying stockwork.

We have investigated more than 450 fluid inclusions in 40 crystals of 13 samples in anhydrite, barite and quartz crystals from chimneys, stockwork rocks and a propylitic altered volcanic rock. Our microthermometric investigation included measurements of freezing interval depressions, homogenization temperatures and petrographic classification of the fluid inclusions. From these data, salinities and formation temperatures were calculated. The analysis of fluid inclusions was accompanied by the determination of $^{87}Sr/^{86}Sr$ isotopes in eleven sulfate/bulk rock samples via TIMS analysis.

We found a bimodal distribution of fluid inclusion salinities, three dominant temperature windows for their formation, and a broad range of isotope signatures for sulfate crystals hosting the fluid inclusions.

The variability of fluid inclusion salinities in individual samples suggests phase-separated fluids were involved during the formation of at least 10 of 13 samples. Although no physical evidence for boiling fluids was observed (e.g. temperature or pulsing of fluids) during the fluid sampling program on the two expeditions, formation temperatures suggest that boiling fluids have temporarily exited the seafloor in at least 5 of 13 samples. Moreover, we found increasing ranges of salinities in fluid inclusions with higher formation temperatures asserting evidence for phase separation processes.

We calculated isobaric-isenthalpic mixing trends between co-existing phase-separated vapors and brines with seawater. We found a match for phase separations of rising fluids that proceed to pressures and temperatures of ~350 °C and ~170 bar. These computational results can explain the vast majority of fluid inclusion salinities and formation temperatures, and we conclude that most fluids under the NW Caldera Wall hydrothermal vent field boil up to only some 10s-100 m below seafloor (mbsf) within the caldera rim. Salinities and corresponding temperatures can be best explained by asserting the removal of up to 30 wt.% equilibrium-fractionated vapor.

A small subset of the inclusions, especially those with salinities between 1 and 2 wt.% and formation temperatures of > 280 °C, cannot be explained by shallow boiling. Additionally, inclusions with highest salinities (4.5-8 wt.% NaCl) would require large amounts of fractionated vapor. A mixing model between co-existing supercritically separated fluids and seawater can explain both of these salinity regions of fluid inclusions. $^{87}Sr/^{86}Sr$ isotopes of sulfate crystals consolidate that these inclusions may have been produced by supercritical phase separations that probably occurred transiently in greater depths (between 1200-1700 mbsf).

The results of the study point to the overall common occurrence of phase separation at the NW Caldera Wall vent field and the importance of boiling and seawater mixing processes during the formation of stockwork zones and associated volcanogenic massive sulfide deposits.

6.1 Introduction

6.1.1 Brothers Volcano

The submarine Brothers Volcano as part of the South Kermadec Arc is situated about 350 km north off the northern island of New Zealand and represents a typical island arc caldera volcano. Comprising of mostly dacitic rocks, the 3×3.5 km wide caldera hosts at least four hydrothermal vent areas (Baker et al., 2012, Caratori Tontini et al., 2012a) and is one of the

most well-studied arc volcanoes in the world. Numerous studies on the volcanic structure (Dziak et al., 2008; Baker et al., 2012; Embley et al., 2012) and its magmatic evolution (Wright & Gamble, 1999; Haase et al., 2002, 2006; Keith et al., 2018) have been carried out. Moreover, the nature and extent of hydrothermal circulation (Caratori Tontini et al., 2012b; de Ronde et al., 2005; de Ronde & Stucker, 2015; Gruen et al., 2012, 2014) and mineralization (Wright et al., 1998; de Ronde et al., 2011) have been addressed in many ways. At this time the most recent investigation has been IODP expedition 376 on which five drill sites have penetrated Brothers Volcano to systematically investigate the volcanic history and rock alteration processes in the active hydrothermal systems.

The hydrothermal systems occur on the caldera walls and at the young satellite cones in the southern-central part of the caldera. One venting site is inferred from AUV plume surveys and a low magnetization zone of volcanic rocks (Baker et al., 2012, Caratori Tontini et al., 2012a). The site is situated at the base of the south-west caldera wall. Two young cones (Upper Cone and Lower Cone) emerge from the southern part of the caldera floor and host low-temperature magmatic-volatile-dominated white smoker-type vents. Most vigorous venting, with particle-rich high-temperature, seawater-dominated fluids occurs along the North West Caldera Wall vent field.

During two research expeditions (RV Sonne cruise SO253 and RV Thompson cruise TN350) hydrothermal activities at three of the four active vent sites (the NW Caldera Wall, the Upper and Lower Cone) have been investigated by ROV Quest and ROV Jason II (Figure 6.1A). Besides seafloor observation and heat flow measurements sampling of hydrothermal fluids and precipitates was the main objective of both expeditions. While sulfide/sulfate mineralization is scarce in the two cone sites, the regular occurrence of barite and anhydrite in the mineralization products of the NW Caldera Wall hydrothermal system enabled us to carry out an extensive study of fluid inclusions in thirteen samples and characterize the nature of the hydrothermal fluids that gave rise to the mineralization (Figure 6.1B; Table 6.1).

The most vigorous hydrothermal activities occur at the inner part of the NW Caldera Wall with a large vent field developed over an area of at least 200 × 100 m and extending from 1700 m up to 1300 m water depths (Figure 6.1B). This vent field is characterized by extensive sulfate and sulfide mineralization in chimneys and stockwork rocks and resembles the area with the strongest magnetic anomaly reaching down to 1000 mbsf (Caratori Tontini et al., 2012a). Stockwork zones underlying active vents crop out along fault scarps, which formed during multiple collapse events in the evolution of the caldera volcano. The stockwork composes of argillic-propylitic altered volcanics with disseminated pyrite crystals and are crosscut by either massive vein networks of chalcopyrite/pyrite or massive vein networks of anhydrite/barite veins. This mineralization is a consequence of the vigorous hydrothermal processes occurring

at the NW Caldera Wall vent site and displays an example for the origin of volcanogenic massive sulfides. The accessibility of active chimneys and their underlying stockwork rocks is unique and make the NW Caldera Wall a superb place to study recent processes of ore formation.

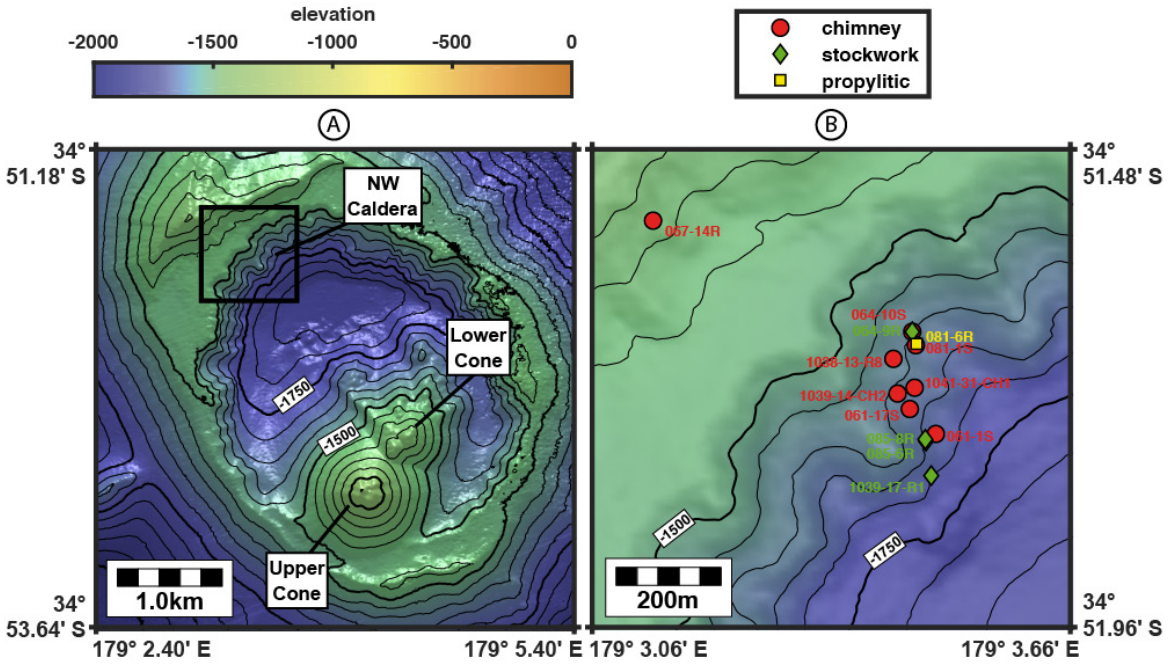

Figure 6.1: Bathymetry of Brothers Caldera and working areas of expeditions SO253 & TN350 (A). Sample sites of hydrothermal precipitates at the NW Caldera Wall hydrothermal vent site (B). (RV Sonne MBES data of cruise SO253).

Table 6.1: Sample types, coordinates, depths and in-situ pressures of investigated samples (pressures were calculated using a seawater density of 1030 kg/m³).

Sample Name	Sample Type	Latitude	Longitude	Depth [m]	Pressure [bar]
SO253-061-1S	Chimney	34° 51.766' S	179° 3.491' E	1671	168.8
SO253-061-17S	Chimney	34° 51.741' S	179° 3.459' E	1643	166.0
SO253-064-9R	Stockwork	34° 51.663' S	179° 3.462' E	1593	161.0
SO253-064-10S	Chimney	34° 51.663' S	179° 3.462' E	1593	161.0
SO253-067-14R	Chimney	34° 51.552' S	179° 3.136' E	1374	138.8
SO253-081-1S	Chimney	34° 51.677' S	179° 3.466' E	1619	163.6
SO253-081-6R	Propylitic	34° 51.676' S	179° 3.467' E	1616	163.3
SO253-085-6R	Stockwork	34° 51.773' S	179° 3.479' E	1663	168.0
SO253-085-8R	Stockwork	34° 51.771' S	179° 3.478' E	1663	168.0
TN350-J2-1038-13-R8	Chimney	34° 51.691' S	179° 3.438' E	1582	159.9
TN350-J2-1039-14-CH2	Chimney	34° 51.725' S	179° 3.443' E	1611	162.8
TN350-J2-1039-17-R1	Stockwork	34° 51.808' S	179° 3.486' E	1698	171.6
TN350-J2-1041-31-CH1	Chimney	34° 51.720' S	179° 3.465' E	1622	163.9

6.1.2 Microthermometric investigations

Microthermometric investigations comprise of petrographic description of fluid inclusions and visual observation of phase transitions in trapped fluids. Measurements of ice-melting temperatures and homogenization temperatures of two-phase liquid-vapor inclusions enabled us to calculate the salinity and the "formation" or "entrapment" temperature of the inclusions (Bodnar & Vityk, 1994; Atkinson, 2002). Under the assumption that a fluid inclusion has not changed in size or composition since it formed in the host crystal, these values represent the state of the hydrothermal fluid from which the crystal was formed. Here, we prefer the term "formation temperature" because the term "entrapment temperature" presumes the fluid inclusion to form during crystal growth in some kind of open void. In fact, in hydrothermal environments during multiple temperature fluctuations inclusions may form during re-equilibration events in already existing crystals. Such inclusions may not represent crystal growth conditions but they still reflect conditions in the hydrothermal system.
Fluid inclusionists use microthermometric data as geothermobarometers to determine the depth of crystal growth in magmatic environments with known temperature (Hansteen & Klügel, 2008; Longpré et al., 2014) or to find the temperature of hydrothermal mineralization with a known pressure (Bodnar et al., 2014, Bieseler et al., 2018). In seafloor hydrothermal systems, fluid inclusion studies reveal information about salinities and temperatures of hydrothermal fluids and yield hints about hydrothermal end-members and mixing regimes during mineral growth (Lécuyer et al., 1999; Vanko et al., 2004, Jamieson et al., 2016). Apart from re-equilibration processes occurring during recovery of the sample or the measurement itself (Bodnar, 2003), one benefit of fluid inclusion data is that fluid inclusions allow not only to gain information about the properties of the recent hydrothermal fluid, but also about the fluid properties at the time of mineralization of their host crystals. Fluid inclusion studies provide a time integrated view on hydrothermal circulation systems.

6.2 Methods

6.2.1 Origin of crystals and sample preparation

Crystal aggregates were extracted from chimneys, stockwork rocks and a propylitic altered volcanic rock that originated proximal to the stockwork. In chimneys the crystals originated either from the central conduit that was lined with barite/anhydrite crystals or from the central wall of the chimney, where mixing of the hot hydrothermal fluids from the inner conduit and peripheral seawater took place. The stockwork rocks comprise propylitic-argillic altered volcanic rocks with disseminated sulfates and sulfides, which are crosscut by either massive

sulfate veins (anhydrite/barite) or massive sulfide veins (pyrite ± chalcopyrite/sphalerite). The vein types occurred in different regions with sulfate veins occurring in the northern outcrop of stockwork mineralization (064-9R). Here, host rocks are altered to a Fe-Mg-rich, mostly chlorite dominated propylitic assemblages (chlorite/illite/ smectite). Sulfide veins are found in the southern outcrop (085-6R, 085-8R, 1039-17-R1) where host rocks are altered to an argillic assemblage of quartz, smectite pyrite and illite. Where sulfate veins were apparent, the crystals originated from the vein material. In the rock type where sulfide veins cut the rock, the sulfate crystals were extracted from the altered groundmass. The propylitic altered volcanic comprised of a mixture of chlorite with minor illite/smectite and finely disseminated quartz. Voids are preserved and in parts lined with larger (up to mm size) quartz crystals. Crystals used in the microthermometric investigation for this sample originated from the lining of the voids.
Of each sample, wherever large and transparent crystals were found (at least a mm in diameter), they were carefully scraped off with a metal pin and subsequently crushed with a hammer to produce crystal fragments with diameters of 100 to 1000 µm. The crushed fragments were then picked under a binocular to find individual crystals with plane cleavage- or crystal-faces providing a good thermal contact to the heating/freezing stage on which the microthermometric investigation is executed.

6.2.2 Microthermometry of fluid inclusions

Microthermometric investigations were carried out in the laboratories of the working group "Petrology of the Ocean crust" in the Department of Geosciences at the University of Bremen. A "Linkam Stage" attached to a "Zeiss Axioskop" microscope was used to investigate the fluid inclusions. Anhydrite and barite were distinguished under the microscope by the difference in birefringence between the two phases (barite: 0.012; anhydrite: 0.044). A Linkam TP92 heat controller provided dynamic temperature control to heat the samples with a defined heating rate between 0.1 and 90 °C/min. An LNP2 flow regulator fed the stage with a constant stream of gaseous nitrogen originating from a Dewar of liquid nitrogen.
The stage-temperature reading of the system was calibrated using "FLINC" synthetic fluid inclusions in quartz. The freezing point of pure water (0.0 °C) and the critical homogenization temperature (374.1 °C) were used to determine if a sample's temperature complies with the temperature of the stage's sensor. In the course of the study, the calibration procedure was repeated 14 times and the freezing point was determined as 0.04 ± 0.07 °C. The critical temperature was determined as 373.6 ± 0.75 °C (Table 6.2). This indicates the stage's sensor provides accurate temperature values (0 ± 0.1 °C; 374 ± 1 °C), but also that a sample's temperature may stronger deviate from the sensor's temperature, the higher the actual

temperature is. Since, samples for this investigation were not polished, the sample temperature may deviate from the stage's temperature due to surface roughness of the stage-contacting crystal- or cleavage-face. Such kind of surface roughness could lead to a limited contact and thus to a poor thermal link between sample and stage. This effect would lead to different phase transition temperatures when using different heating rates and lead to higher temperature differences between sample and stage, the higher the heating rate was set. To avoid this kind of temperature differences in every sample one inclusion was measured repeatedly with significantly different heating rates. For the ice melting temperature rates of 0.5 °C/min, 1 °C/min, 2 °C/min were evaluated. The phase transition temperature never deviated more than 0.1 °C at heating rates between 0.5 and 2 °C/min, leading to the conclusion that surface roughness does not play a role for the samples at these heating rates. For the homogenization temperature the same procedure was carried out with 5, 10 and 20 °C/min giving the same result for heating rates at or below 10 °C/min. During the measurements freezing point depressions were measured with a heating rate of 1 °C/min whereas homogenization temperatures were determined between 5 and 10 °C/min.

The microthermometric investigation comprised of: a detailed petrographic description and photo documentation of the fluid inclusions; cooling the inclusions to about -60 °C and subsequent heating till the melting point was detected; and heating to high temperatures until the homogenization of the two-phase inclusions was observed. We classified the inclusions in primary, pseudosecondary and secondary inclusions. Primary inclusions occur as single inclusions or as small groups of inclusions, pseudosecondary inclusions occur as trails that follow crystal faces and secondary inclusions occur in trails aligned parallel to cleavage faces or with no visible relation to crystal faces. In each sample several inclusions were cooled to -100 °C to detect the presence of mixtures others than H_2O-NaCl. Since no phase transitions except for the ones expected in the H_2O-NaCl could be determined, the H_2O-NaCl system was used to interpret phase transitions. The microthermometric technique was described by Bodnar and Vityk (1994). Since the minerals anhydrite and barite have a low hardness and are prone to stretching and re-equilibrations during the measurement procedure, the technique introduced by Vanko and Bach (2005) was applied. Their heating and freezing experiments on anhydrite hosted fluid inclusions show that hydration of anhydrite hosts may form gypsum in the low temperature region during microthermometric measurements. In subsequent measurements the salinity of a fluid inclusion may be increased. This process seems to occur reversibly, and heating to 130 °C converts the newly formed gypsum back to anhydrite. Furthermore, Vanko and Bach (2005) found that overheating only some 10 °C over the homogenization temperature in anhydrite easily leads to stretching or re-equilibration and significantly changes the homogenization temperature.

Using the procedure proposed by Vanko and Bach (2005), not one inclusion after another was measured, but in a first step all ice-melting temperatures were detected. Thereby it was considered that no crystals were formed in the inclusions or at their walls, nor their shapes have considerably changed. Afterwards, for the homogenization temperature, the temperature of the sample was subsequently increased and all inclusions were observed in 5 °C intervals, so that no inclusion was significantly over-heated before detecting the homogenization temperature.

Table 6.2: Calibration of the Linkam Stage temperature sensor with synthetic fluid inclusions. Temperatures are given in °C.

Observation	Melting point	Critical Homogenization
Number of obs.	14	16
Mean	0.04	373.6
Std	0.07	0.75
Min	-0.1	372.4
Max	0.1	374.8

2.3 Analysis of $^{87}Sr/^{86}Sr$

The $^{87}Sr/^{86}Sr$ isotope ratios of sulfates and bulk rocks were analyzed by Thermal Ionization Mass Spectrometry (TIMS) using a Thermo Scientific Triton Plus mass spectrometer at the Isotope Geochemistry Laboratory at the Center for Marine Environmental Science MARUM of the University of Bremen. In total, eleven analyses (eight stockwork, two chimney, one propylitic altered rock) were carried out to determine $^{87}Sr/^{86}Sr$ ratios in six sulfate samples. The samples include five hand-picked mineral separates of barite and anhydrite and seven bulk sample powders from the corresponding bulk rock specimen (data are introduced in Section 6.3.5).

The samples were digested in concentrated HNO_3 at 130 °C. Strontium was isolated from the matrix elements, including Ba, using Sr_{Spec} resin (adapted from Deniel & Pin, 2001). Samples were analyzed with a Ta-emitter on rhenium filaments in the static acquisition method. Two analyses of the NIST SRM 987 reference material run with the samples yielded $^{87}Sr/^{86}Sr$ of 0.710244 ± 8 and 0.710239 ± 9 that plot well within long-term reproducibility of NIST SRM 987 0.710249 ± 14 (2σ, $n = 263$) of the laboratory, which in turn compares well to average published data (0.710250 ± 34; 2σ, $n = 1245$, data < 0.7102 and > 0.7103 are discarded; GeoREM data base (Jochum et al., 2005), request September 2017).

6.2.4 Isenthalpic-isobaric mixing models

Fluid inclusion data were used to develop mixing models between seawater and hydrothermal end-member pairs formed by phase separation. Potential end-member pairs are determined by the phase relations in the H_2O-NaCl system introduced by Driesner and Heinrich (2007). Isobaric LV (liquid-vapor) curves were calculated via the program "SOWAT" from which pressure and temperature dependent co-existing vapor and brine pairs were derived.
For simulation of isenthalpic mixing we calculated the heat capacity as a function of T-P-X. Driesner (2007) used the IAPWS-84 method (Haar et al., 1984) to calculate the thermodynamic properties of pure water and developed a correlation method to calculate heat capacities of binary H_2O-NaCl solutions. We used the program PROST (implemented by Olaf Bauer & Ole Engel at the Technische Universität Hamburg-Harburg, 1998) to calculate the thermodynamic properties of pure water according to the IAPWS-84 method (Haar et al., 1984). From this data, we used the method of Driesner (2007) to calculate the compositional dependency of the heat capacity of salty solutions. For individual mixing paths of our different end-member vent fluids and seawater, we simultaneously calculated heat capacities and temperatures of those mixtures. These isenthalpic mixing trends are then plotted in T-X diagrams along with the fluid inclusion data. We also used this method to calculate temperatures of precipitation for anhydrite and barite based on mixing ratios deduced from Sr isotope mass balance.

6.3 Results

6.3.1 Petrography of inclusions

Five types of fluid inclusions were found which decrease in abundance in the following order. *Type 1* inclusions with salinities greater or lower than seawater are two-phase, liquid-rich and homogenize into the liquid phase. *Type 2* inclusions mostly have salinities lower than seawater; they are vapor-rich and homogenize into the liquid phase as well. *Type 3* inclusions are similar to *Type 2*, but give no ice melting temperatures and the homogenization temperatures of 380 °C and 440 °C is much higher than that of all other inclusions. *Type 3* inclusions often decrepitated upon heating before the inclusions homogenized (see below). *Type 4* inclusions contain daughter minerals with no dissolution up to 500 °C but give ice melting temperatures similar to inclusions of *Type 1* and *2*, which indicates that halite cannot be the daughter mineral. One inclusion was classified as *Type 5*. It gave no ice melting temperature for the H_2O-NaCl system but showed reproducible ice melting/dissolution of a phase at +2 °C signifying the presence of a chemically different fluid or additional components in this inclusion.

A total of 464 fluid inclusions were subject to documentation and microthermometric measurements. In 424 inclusions, ice-melting temperatures could be detected, for 423 inclusions salinities could be calculated and for 345 inclusions the homogenization temperature was detected. This results in 326 inclusions for which both the ice melting temperature and the homogenization temperature were determined and the formation temperature could be calculated (note that one inclusion with an extraordinary high salinity of 17 wt.% is excluded in the following Tables and Figures). The failure of detecting ice-melting temperatures in 40 inclusions often occurred due to optical limitations. However, some inclusions of *Type 2* were clearly visible and still ice melting was not observed. These inclusions are interpreted to be vapor-rich and contain only small amounts of liquid, which makes it hard to observe melting of ice. Some of the 98 inclusions in which the homogenization temperature could not be determined were simply missed during heating and hence were excluded to avoid measurements of stretched inclusions. In fact, most of those inclusions could not be measured as a consequence of audible decrepitating events, which occurred in barite as well as anhydrite crystals during measurement of homogenization temperatures. Post-decrepitation inspection revealed that the crystals were considerably damaged and it seemed to be that all inclusions suffered from these decrepitation events and could not be measured anymore. Such events occurred regularly at a temperature of about 300 °C and sometimes at slightly higher ones (330- 350 °C). This problem commonly occurred when heating *Type 3* inclusions, which are therefore heavily underrepresented in the statistical treatment of the fluid inclusion data.

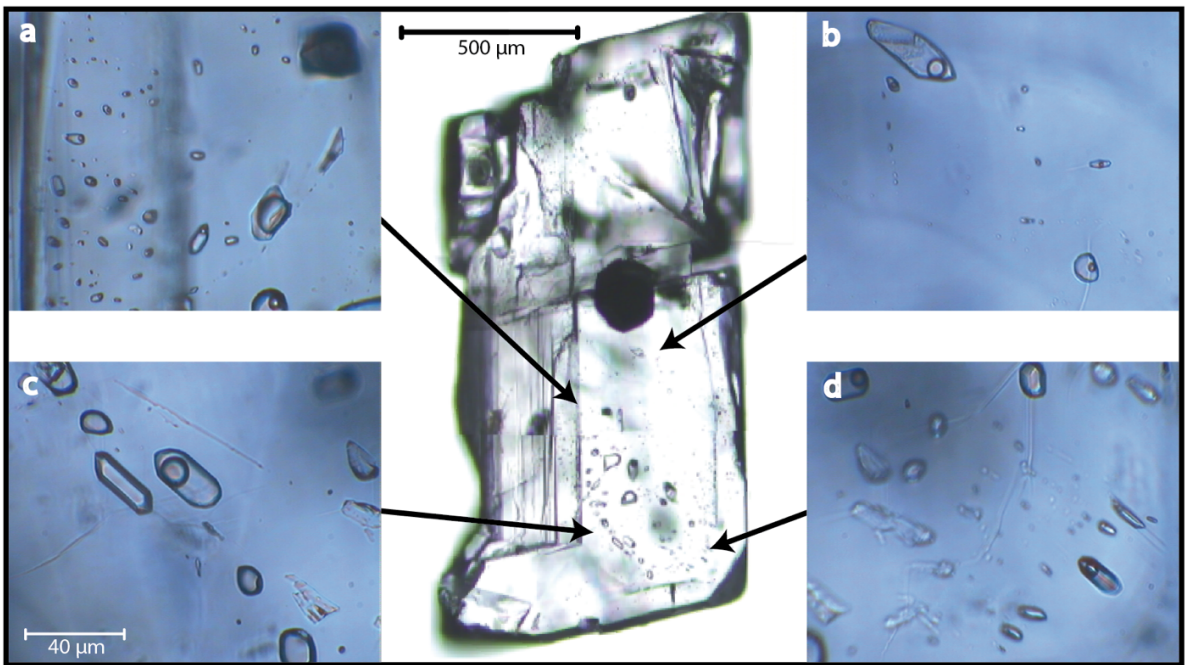

Figure 6.2: Petrographic relation of fluid inclusions in sample SO253-085-6R. a: Inclusions with varying L-V ratios; b: Small group of primary inclusions; c and d: Two photographs of a prominent pseudosecondary trail (also with varying L-V ratios)

The successfully analyzed fluid inclusions are hosted in barite (172 inclusions), anhydrite (136 inclusions) and quartz (17 inclusions) crystals. The minerals were extracted from chimneys (181 inclusions), stockwork rocks (127 inclusions) and a propylitic altered rock (17 inclusions). Barite and anhydrite crystals were separated from chimneys and stockwork zones and quartz crystals exclusively originated as vug coating in the altered rock specimen. Most inclusions (153) occurred as pseudosecondary trails following crystal faces and changing their orientation at crystal edges. A significant fraction of all inclusions (124) occurred as single inclusions or small groups and are hence classified as primary inclusions. The smallest fraction of analyzed inclusions (48) was considered secondary, since they occurred in trails parallel to cleavage faces or without visible relations to crystal faces. Figure 6.2 gives an example for the petrographic relations in sample SO253-085-6R. Table 6.3 summarizes the microthermometric results.

Table 6.3: Summarized results of the microthermometric study. (note: one inclusion of sample 061-1S (salinity 17 wt. % NaCl) was excluded. This results in one inclusion less for the sum of T_{melt}, S_{eq} and T_{form} than mentioned in the text above).

Sample/ Group	N				S_{eq} [wt.% NaCl]					T_{form} [°C]				
	T_{melt}	S_{eq}	T_{hom}	T_{form}	Mean	Std	Min	Max	Median	Mean	Std	Min	Max	Median
061-17S	22	22	15	14	3.0	1.3	0.1	4.2	3.4	216	62	149	352	183
061-1S	33	33	33	30	3.6	0.9	0.2	5.2	3.8	243	35	135	310	243
064-10S	34	34	34	31	1.8	1.6	0.2	5.3	0.8	289	32	251	344	269
064-9R	44	44	25	25	2.9	0.9	1.5	4.1	3.0	284	44	184	345	290
067-14R	15	15	16	13	3.6	0.6	2.1	5.0	3.4	301	15	277	344	302
081-1S	37	36	34	32	3.6	0.4	3.0	4.4	3.6	246	33	185	303	234
081-6R	17	17	17	17	3.5	1.1	1.1	5.0	3.6	329	9	306	346	329
085-6R	61	61	42	41	1.9	0.5	0.1	3.9	1.8	241	27	155	295	251
085-8R	33	33	29	25	3.3	1.5	0.9	8.9	3.3	208	28	168	265	198
1038-13-R8	39	39	35	35	3.7	1.0	3.3	7.9	3.4	295	4	288	306	296
1039-14-CH2	21	21	19	18	3.6	0.3	3.3	4.4	3.4	226	42	144	298	225
1039-17-R1	57	57	38	36	3.6	1.4	0.1	8.1	3.4	237	40	155	318	241
1041-31-CH1	10	10	8	8	3.3	0.5	2.3	3.9	3.4	214	36	169	270	222
Barite	243	243	185	172	3.1	1.3	0.1	8.9	3.4	235	43	135	352	239
Anhydrite	163	162	143	136	3.0	1.2	0.2	7.9	3.3	275	37	169	344	289
Quarz	17	17	17	17	3.5	1.1	1.1	5.0	3.6	329	9	306	346	329
Chimneys	211	210	194	181	3.3	1.2	0.1	7.9	3.4	261	45	135	352	268
Stockwork	195	195	134	127	2.9	1.3	0.1	8.9	2.6	242	42	155	345	246
Propylitic	17	17	17	17	3.5	1.1	1.1	5.0	3.6	329	9	306	346	329
Primary	165	164	129	124	2.9	1.2	0.2	8.9	3.3	249	48	144	344	251
Secondary	60	60	56	48	3.3	1.4	0.1	7.1	3.4	294	36	197	352	294
Pseudosecondary	198	198	160	153	3.2	1.2	0.1	8.1	3.4	252	43	135	345	250
All	423	422	345	325	3.1	1.3	0.1	8.9	3.4	257	47	135	352	255

6.3.2 Salinities

Salinities of the 423 measured fluid inclusions range from 0.1 to almost 9 wt.% NaCl. The mean value of all inclusions is 3.1 ± 1.3 with a median of 3.4 wt.% NaCl. Mean values in single samples range from 1.8 ± 1.6 wt.% NaCl (sample 064-10S) to 3.7 ± 1.0 wt.% NaCl (sample 1038-R8), with medians of 0.9 and 3.4 wt.% NaCl, respectively.

In the overall dataset two pronounced distributional highs are apparent. The first group with about 45 inclusions is found in a narrow range between 1.5 and 1.7 wt.% NaCl. The second and more prominent group with about 220 inclusions is found between 3.2 and 4.0 wt.% NaCl. There is no relation between fluid inclusion salinity and the identity of the host phase (Figure 6.3A) as all phases show inclusions covering virtually the entire range of salinities. There does seem to be a relation between fluid inclusion salinity and mineralization type (Figure 6.3B). Extremely low salinities (< 0.7 wt.% NaCl) were measured almost exclusively in chimney samples, while salinities in the range of 0.7-3.0 wt.% NaCl are exclusively found in stockwork rock samples. Inclusions with salinities similar to or greater than seawater are found in both stockwork and chimney samples, but these inclusions occur much more frequently in the chimney samples. Hence, fluid inclusion salinities seem not to be dependent on the host phase, but rather on the host rock type. Different fluid inclusion types (classified after petrography) are represented broadly over the entire spectrum of salinities (Figure 6.3C) and cannot be assigned to a certain salinity range.

6.3.3 Formation temperatures

Formation temperatures of the entire set of fluid inclusion data fall in the range between 135 and 352 °C. The overall mean is 257 ± 47 °C with a median of 255 °C. Mean formation temperatures of single samples range from 208 ± 28 °C (sample 085-8R) to 329 ± 9 °C (sample 081-6R). Median values are 198 °C and 329 °C, respectively.

Like the distribution of salinities, the distribution of formation temperatures shows several modes, two of which are most pronounced. The first pronounced mode is at around 250 °C and is primarily made up by inclusions hosted in barite (Figure 6.3D). These inclusions were predominantly formed in the stockwork zone, which is the most abundant mineralization type within this mode. A second marked mode occurs at around 290 °C and is strongly dominated by anhydrite-hosted fluid inclusions in chimneys (Figure 6.3E). Only very few inclusions hosted in barite or occurring in stockwork rocks fall within that mode. A third, less pronounced mode is at 330 °C. Anhydrite, barite and quartz hosted inclusions from stockwork rocks, chimneys and the propylitic altered rock contribute equally to this population. Most of the quartz-hosted inclusions representing the propylitic mineralization type fall in this group of

highest formation temperatures (Figure 6.3E). As for different inclusion types, secondary inclusions are predominantly found in the temperature-window between 250 and 350 °C (Figure 6.3F) and suggest that re-equilibration processes play an important role in the formation of some of these inclusions.

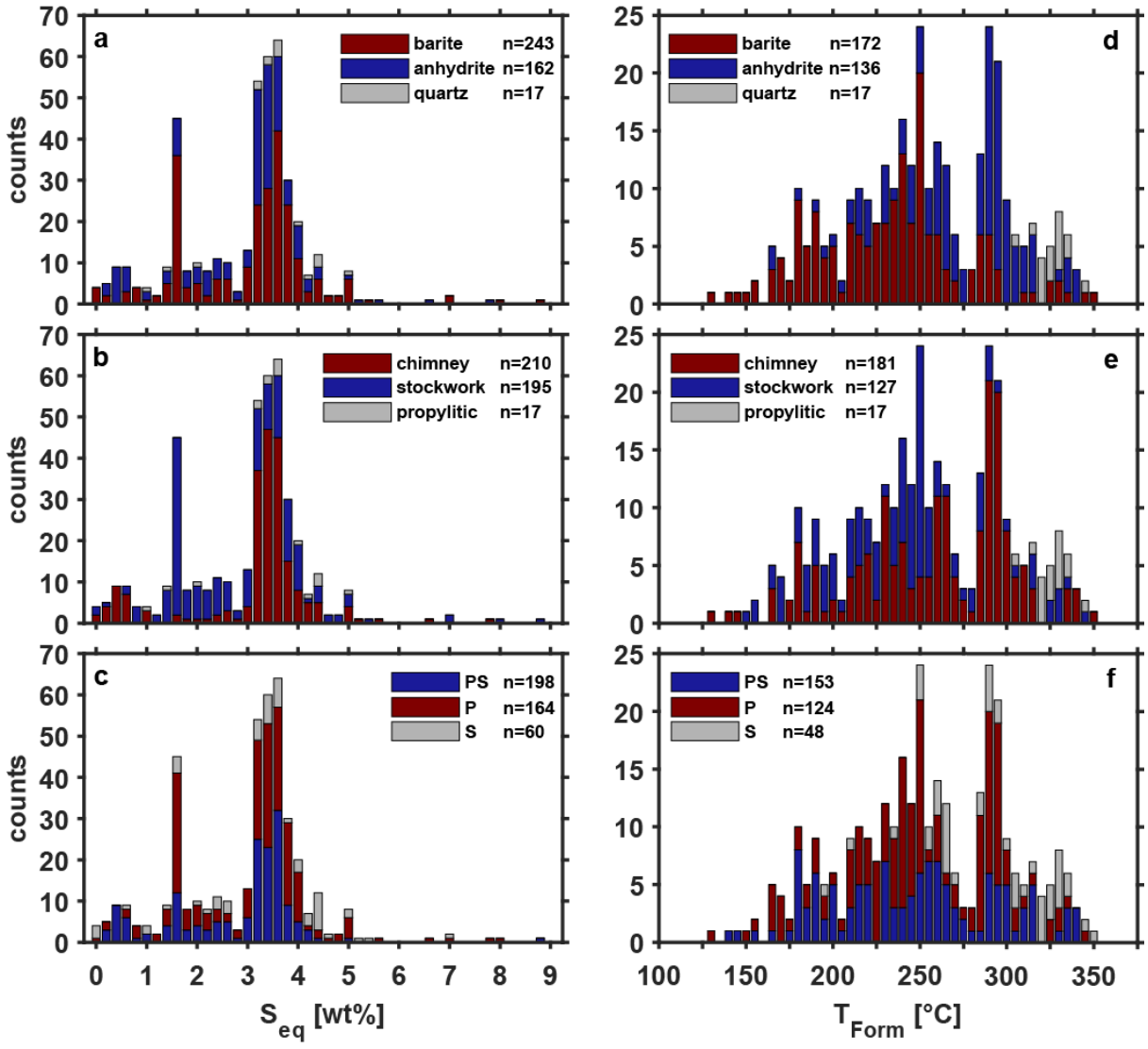

Figure 6.3: Histograms of fluid inclusion data. (Top: color-coded host phases. Center: color-coded host rock types. Bottom: color-coded petrographic classification (P: Primary, PS: Pseudosecondary, S: Secondary)).

6.3.4 Temperature and salinity variations with depth

We examined, how formation temperatures and salinities vary as a function of water depth (Figure 6.4). The fluid inclusion formation temperatures are compared against the position of the boiling curve of seawater (Figure 6.4A). The mean formation temperatures of all samples are lower than the boiling temperature of seawater. However, a subset of samples shows maximum formation temperatures that lie very close to (± 5 °C) the boiling curve of seawater.

These high formation temperatures occur in five of thirteen samples investigated (samples 061-17S, 064-10S, 064-9R, 067-14R, 081-6R; cf. Table 6.2).

Salinity data (Figure 6.4B) are similar to seawater on average, but show variable ranges for individual samples. Strong salinity variations occur in all but three samples, suggesting that phase separation has affected the compositions of fluids trapped in most inclusions. Only samples 081-1S, 1039-CH2, 1041-CH1 show very small standard deviations (< 0.6 wt.% NaCl), which may indicate that the trapped fluids represent seawater-derived fluids unmodified by phase separation. Also, in those three samples the maximum formation temperatures are considerably lower than the temperature of the boiling curve, which corroborates the idea that phase separation did not occur.

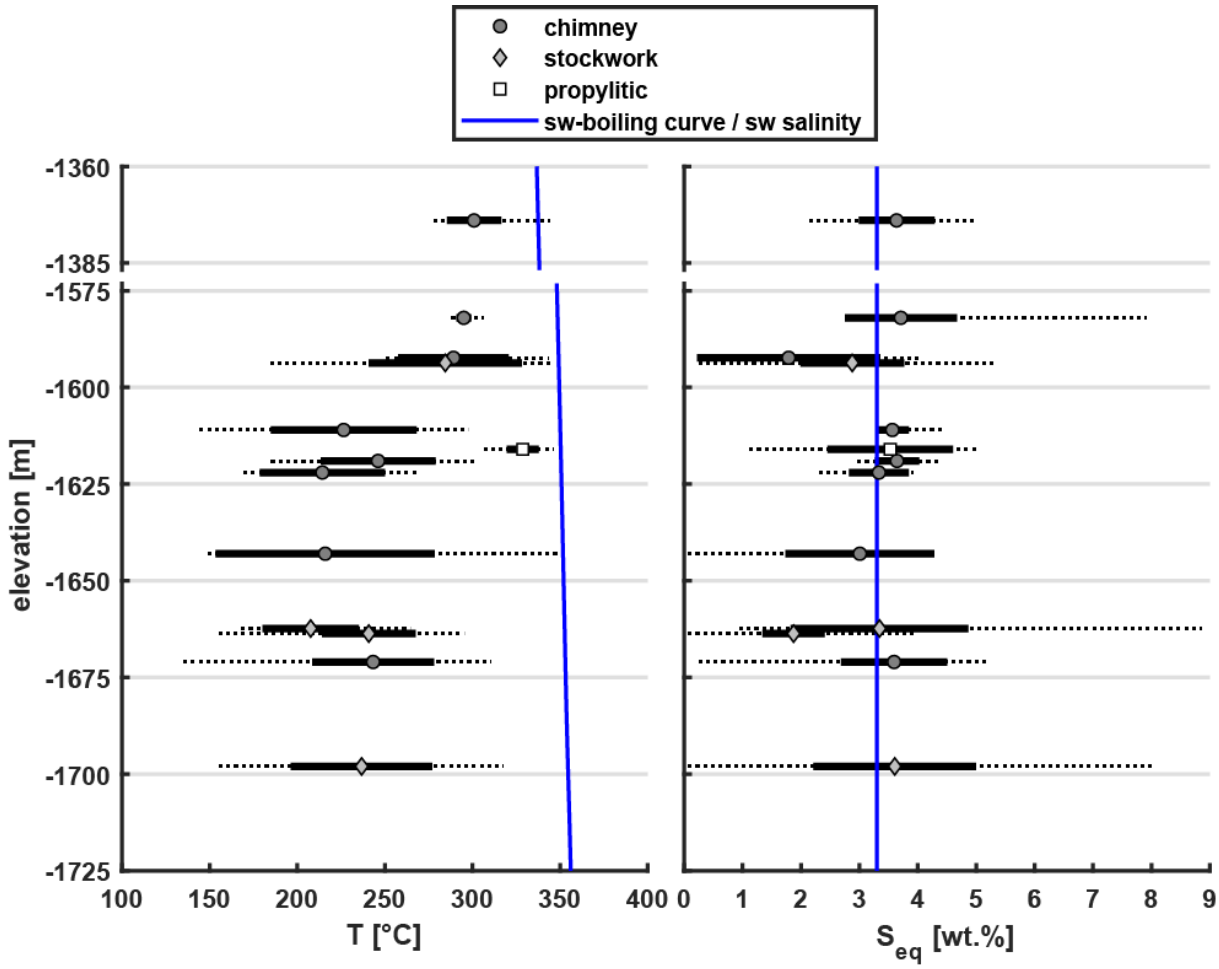

Figure 6.4: Variation of fluid inclusion data with elevation. (A) Formation temperatures compared to the boiling curve of seawater (calculated after Driesner & Heinrich (2007) and assuming a seawater density of 1030 kg m^{-3}). B) Salinities compared to seawater salinity. Note samples with identical elevation were slightly shifted to make the data visible (-1593 and -1663). Also note the break in scale in the y-axis.

6.3.5 $^{87}Sr/^{86}Sr$ composition of mineral separates and bulk samples

The $^{87}Sr/^{86}Sr$ of eleven mineral separates and bulk rock samples range from near hydrothermal end-member values established for the NW Caldera vent sites (0.70437 ± 0.00015, n = 10; Diehl et al., in prep., Chapter 4) to near seawater values (0.709183 ± 8 n = 1; Diehl et al., in prep., Chapter 5). The least radiogenic sample is an anhydrite separate from sample 085-6R1 with an $^{87}Sr/^{86}Sr$ of 0.704852 ± 14. The most radiogenic sample is a barite separate from sample 064-9R with an $^{87}Sr/^{86}Sr$ of 0.709040 ± 7. Anhydrite separates from chimneys are more radiogenic than those from stockwork samples (Table 6.4). Bulk compositions of sample 064-9R range from 0.707551 ± 5 to 0.708572 ± 5, which could be due to highly variable mixing proportions of hydrothermal end-member fluid and seawater (cf. Humphris & Bach, 2005; Craddock & Bach, 2010). Alternatively, the bulk samples may represent variable proportions of anhydrite and barite that have distinctly different isotopic compositions.

Table 6.4: $^{87}Sr/^{86}Sr$ values of mineral separates used for fluid inclusion studies and bulk rocks from stockwork samples. Note: The asterisk indicates bulk rock data presented in Diehl et al. (in prep., Chapter 4).

Sample name	Sample type	Inclusion separates		Bulk rocks*
		barite	anhydrite	
064-9R	Stockwork	0.709040 ± 7		
064-9R	Stockwork		0.705260 ± 10	
064-9R	Stockwork			0.708572 ± 5
064-9R	Stockwork			0.707551 ± 5
067-14R	Chimney		0.706807 ± 8	
081-6R	Propylitic			0.706130 ± 6
085-6R1	Stockwork		0.704852 ± 14	
085-6R1	Stockwork			0.706894 ± 6
085-6R1	Stockwork			0.706848 ± 8
085-8R	Stockwork			0.706365 ± 6
1038-13-R8	Chimney		0.705921 ± 5	

6.3.6 Isenthalpic-isobaric mixing models

The data presented above provide strong evidence for the importance of both phase separation and subsequent fluid mixing. We used isenthalpic-isobaric mixing models to examine possible mixing trends for generating the observed variability in formation temperature and salinity of fluid inclusions, as well as Sr isotope variations of the host phases. In these models, we determined the positions of phase separated end-member fluids and their corresponding mixing trends in T-X planes, where X is either salinity or Sr isotope composition. To address the effect

of pressure, these computations were conducted for several sub- and supercritical conditions. Isobaric T-X sections of phase relations in P-T-X space were computed following Driesner and Heinrich (2007) for a range of pressures (Table 6.5).

Using this approach, our model results predict the consequences of phase separation processes in different pressure/temperature environments in terms of salinity and formation temperature variations along isenthalpic-isobaric mixing paths between phase-separated hydrothermal end-member fluids and seawater.

We examined mixing paths with hydrothermal end-member fluids produced by shallow near-seafloor phase separation at 170 bar (*Model 1a* and *1b*). Further we examined sub-seafloor mixing processes in greater depths corresponding to pressures of 250 bar (still subcritical; *Model 2a* and *2b*), 300 bar (barely supercritical, *Model 3*) and 350 bar (supercritical, *Model 4*). In the subcritical realm, we assumed different vapor-liquid ratios (*Models a* and *b*) to generate model trends that bracket the observed variability well. We computed mixing paths between those end-members with cold seawater (5 °C) as well as seawater heated to as much as 300 °C in all four models.

Model 1a in Figure 6.5A shows isenthalpic mixtures at a pressure of 170 bar with an end-member temperature of 354.8 °C. The vapor-brine phases are created when a fluid with seawater salinity fractionates into 28 wt.% vapor ($S_{Em,vapor}$ = 0.00025 wt.% NaCl) and 72 wt.% brine ($S_{Em,brine}$ = 4.6 wt.% NaCl) and boiling of a rising fluid terminates under equilibrium conditions at 170 bar. This scenario (i.e. *Model 1a*) may explain the vast majority of fluid inclusion data except for two groups of inclusions: first, inclusions with relatively high salinities (S_{eq} > 4.5 wt.% NaCl) and low formation temperatures; second, inclusions with very low salinities and low formation temperatures. *Model 1b* also shows mixing lines between shallow end-members, in which boiling had terminated at 170 bar (Figure 6.5B). The corresponding phases have proportions of 60 wt.% vapor and 40 wt.% brine with salinities of $S_{Em,vapor}$ = 0.00008 wt.% NaCl and $S_{Em,brine}$ = 8.25 wt.% NaCl, respectively (Table 6.5). In contrast to *Model 1a*, this model scenario can account for the most saline inclusions that can be produced by mixing between this brine and seawater. Note that between the two models, the vapor salinity does not change significantly as the vapor branch in the T-X section is insensitive to the amount of gas fractionation. Subcritical phase separation of seawater-derived fluids at low pressures (< 250 bar) generally form a vapor phase that contains virtually no salt. This fact makes the vapor end-member more or less invariant with respect to salinity, whereas the salinity of the corresponding brine end-member is a function of how much gas has fractionated from the original fluid.

Table 6.5: Characteristics of co-existing hydrothermal end-member vapor-brine pairs used in isenthalpic mixing models. Temperature, pressure and salinities ($S_{Em,Vapor}$, $S_{Em,Brine}$ in wt.% NaCl) were derived from the L+V surface of the H_2O-NaCl system (Driesner & Heinrich 2007). F_{Vapor} and F_{Brine} (mass fractions in the corresponding vapor and brine pairs) were calculated by the lever rule and by assuming a source fluid with seawater salinity. The Sr concentrations (mmol/kg) of the vapor-brine pairs were calculated by assuming a Sr partitioning behavior identical to that of salt and using a seawater Sr concentration of 0.09 mmol/kg. $^{87}Sr/^{86}Sr$ ratio of the hydrothermal end-member was derived from ten hydrothermal fluid samples calculated to Mg = 0 (0.70437 ± 15).

MixingModel	T_{Em}	P	$^{87}Sr/^{86}Sr_{Em}$	F_{Vapor}	$S_{Em,Vapor}$	$Sr_{Em,Vapor}$	F_{Brine}	$S_{Em,Brine}$	$Sr_{Em,Brine}$
1a	354.80	170	0.70440	0.28	0.009	0.00025	0.72	4.60	0.12545
1b	356.64	170	0.70440	0.60	0.003	0.00008	0.40	8.25	0.22500
2a	389.50	250	0.70440	0.35	0.174	0.00473	0.65	5.00	0.13636
2b	391.88	250	0.70440	0.61	0.153	0.00416	0.39	8.25	0.22500
3	409.25	300	0.70440	0.52	0.800	0.02182	0.48	6.00	0.16364
4	429.20	350	0.70440	0.73	1.660	0.04527	0.27	10.00	0.27273

Figure 6.6 shows how formation temperatures and salinities co-vary with the $^{87}Sr/^{86}Sr$ ratios for the mixed fluids in *Models 1a* and *1b*. The mixing models can successfully account for the variation of formation temperatures with respect to Sr isotope ratios (Figure 6.6A), but they fail to explain the co-variation of salinity and $^{87}Sr/^{86}Sr$ (Figure 6.6B). In particular, *Model 1* cannot account for this co-variation in inclusions with lower-than-seawater salinities. Extremely low salinities in vapor end-members are expected to be accompanied by extremely low Sr concentrations (as the partitioning behavior is assumed to be equal). Vapor end-member hydrothermal fluids mixing with seawater will therefore exhibit seawater-like isotopic signatures even with small seawater fractions in the mix. Hence, if the host phases grew due to mixing of seawater with a vapor produced by boiling, they should exhibit $^{87}Sr/^{86}Sr$ values close to seawater composition.

Models 2a and *2b* (Figure 6.7-6.8) for mixing of seawater with end-member pairs produced by phase separation of rising fluids that terminated at 250 bar give results similar to *Models 1a* and *1b* for seafloor pressure conditions. The vapor salinity is still extremely low and hence the mixing path of the vapor and seawater is insensitive to the extent of vapor-brine fractionation. Likewise, the $^{87}Sr/^{86}Sr$ compositions of the mixing lines according to salinities look similar to *Models 1a* and *1b*. We hence suggest that the pressure of boiling does not impose a strong control on the composition of vapor-seawater mixtures.

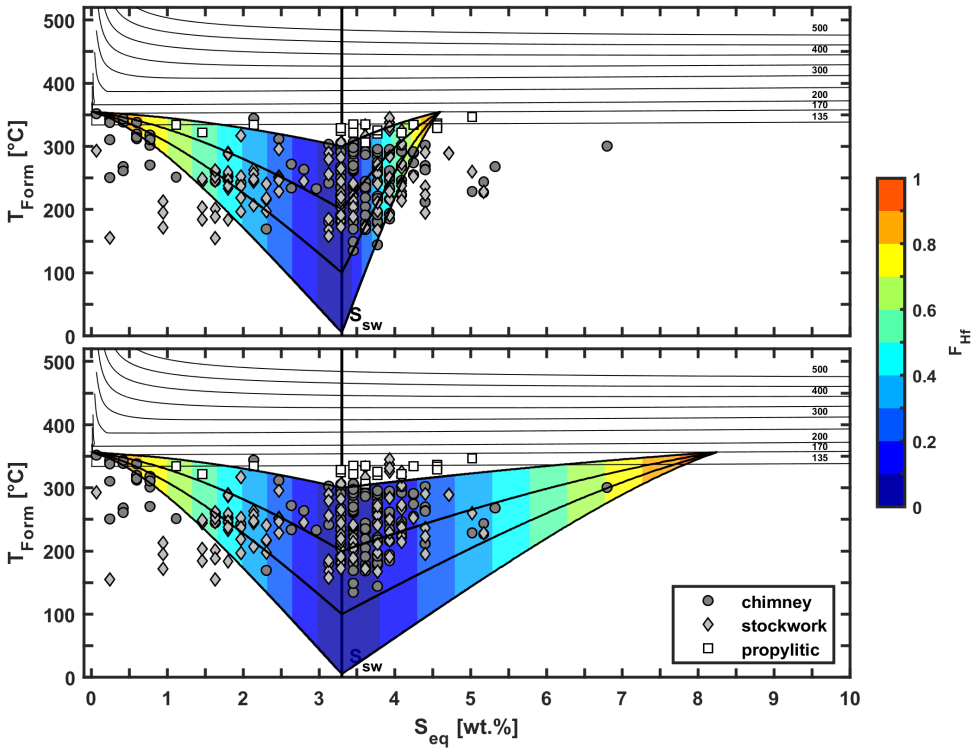

Figure 6.5: Salinity-temperature relation for isenthalpic mixing paths of mixtures between phase-separated hydrothermal fluids and cold to heated seawater at 170 bar (mixing *Models 1a* (top) and *1b* (bottom)). The thick black curves denote mixing paths with 5, 100, 200 and 300 °C. The vertical line denotes seawater salinity. The color code gives the mass fraction of the hydrothermal fluid F_{Hf} in the mix. Thin black curves represent isobaric V+L curves (coexisting phase separated fluids).

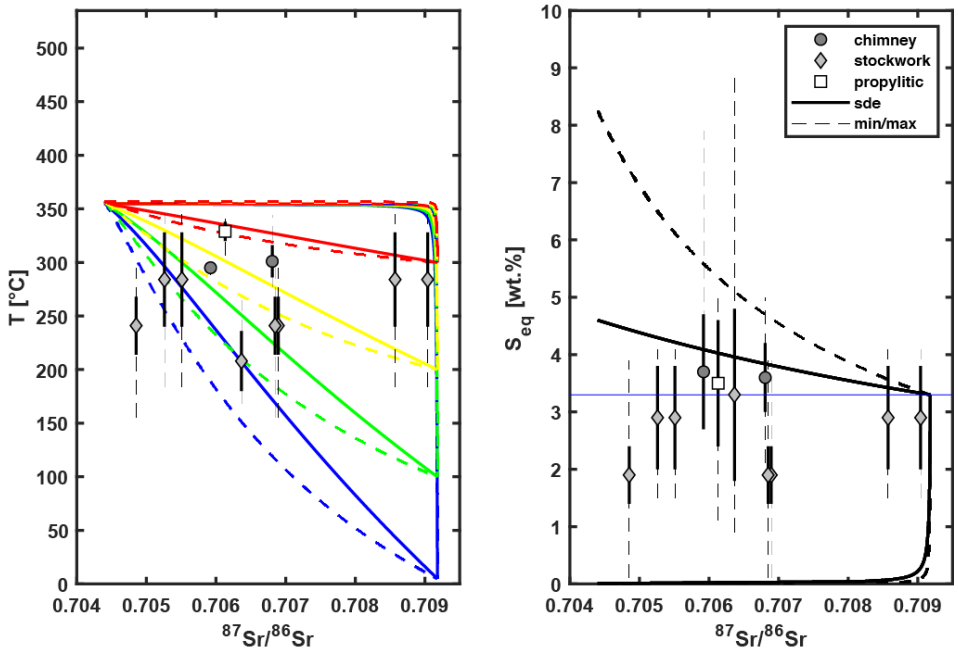

Figure 6.6: Relationship between $^{87}Sr/^{86}Sr$ and temperature (left) and salinity (right) for mixing *Models 1a* (solid lines) and *1b* (dashed lines). Colors represent mixing lines between the phase-separated end-member and cold to heated seawater (blue: 5°C; green: 100°C; yellow: 200°C; red: 300 °C). Symbols represent fluid inclusion mean values, vertical lines represent standard deviations and ranges. For temperatures, pressures, salinities, Sr concentrations and isotope ratios of the phase-separated end-member fluids see Table 6.5.

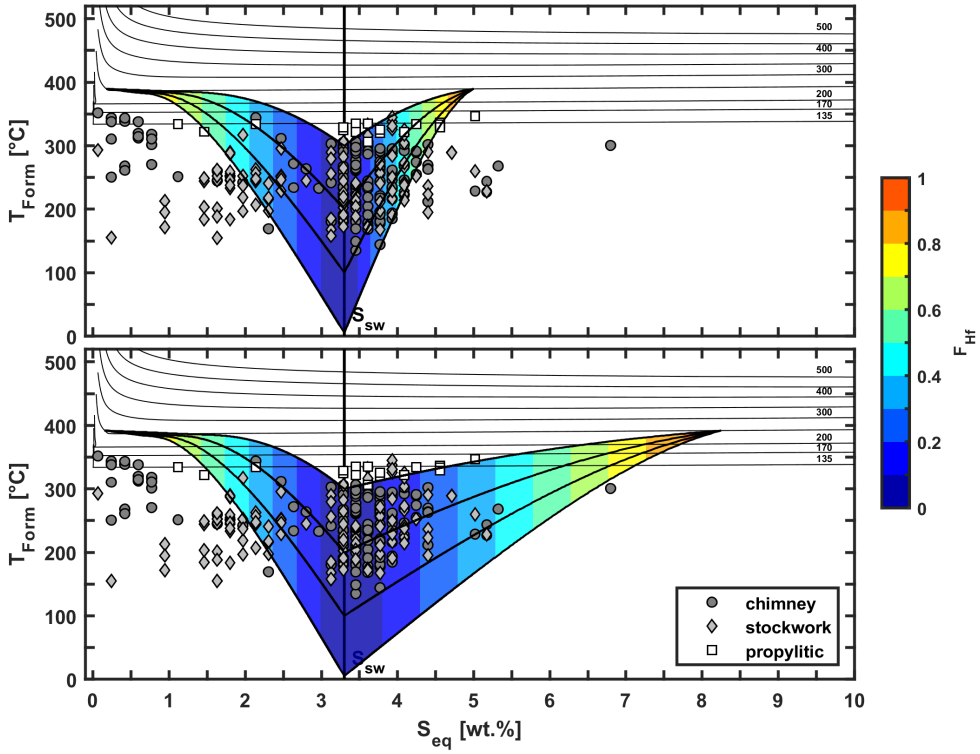

Figure 6.7: Salinity-temperature relation for isenthalpic mixing paths of mixtures between phase-separated hydrothermal fluids and cold to heated seawater at 170 bar (mixing *Models 2a* (top) and *2b* (bottom)). The thick black curves denote mixing paths with 5, 100, 200 and 300 °C. The vertical line denotes seawater salinity. The color code gives the mass fraction of the hydrothermal fluid F_{Hf} in the mix. Thin black curves represent isobaric V+L curves (coexisting phase separated fluids).

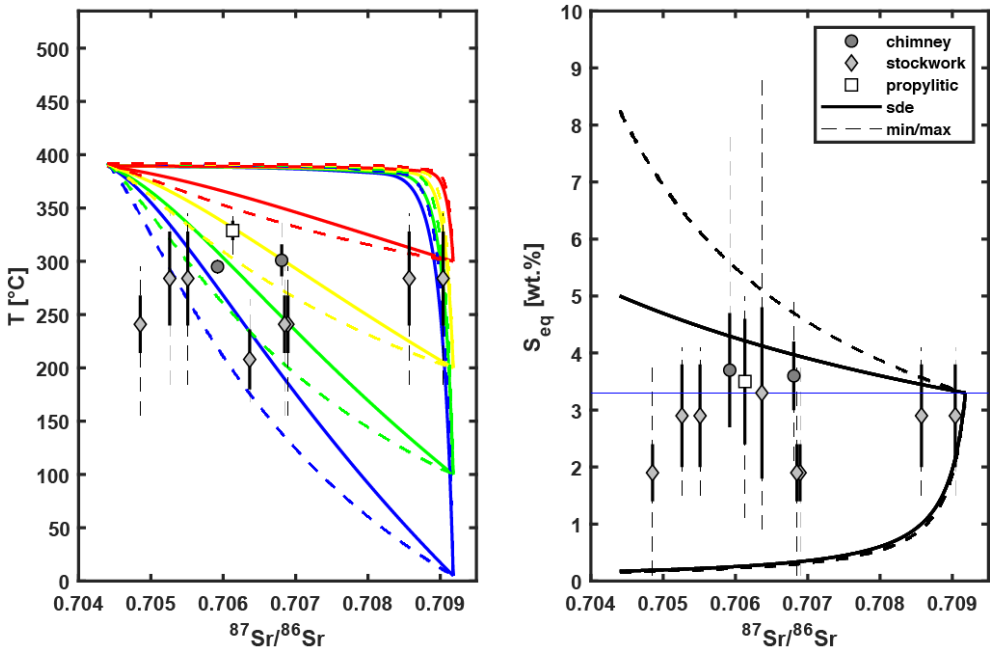

Figure 6.8: Relationship between $^{87}Sr/^{86}Sr$ and temperature (left) and salinity (right) for mixing *Models 2a* (solid lines) and *2b* (dashed lines). Colors represent mixing lines between the phase-separated end-member and cold to heated seawater (blue: 5°C; green: 100°C; yellow: 200°C; red: 300°C). Symbols represent fluid inclusion mean values, vertical lines represent standard deviations and ranges. For temperatures, pressures, salinities, Sr concentrations and isotope ratios of the phase-separated end-member fluids see Table 6.5.

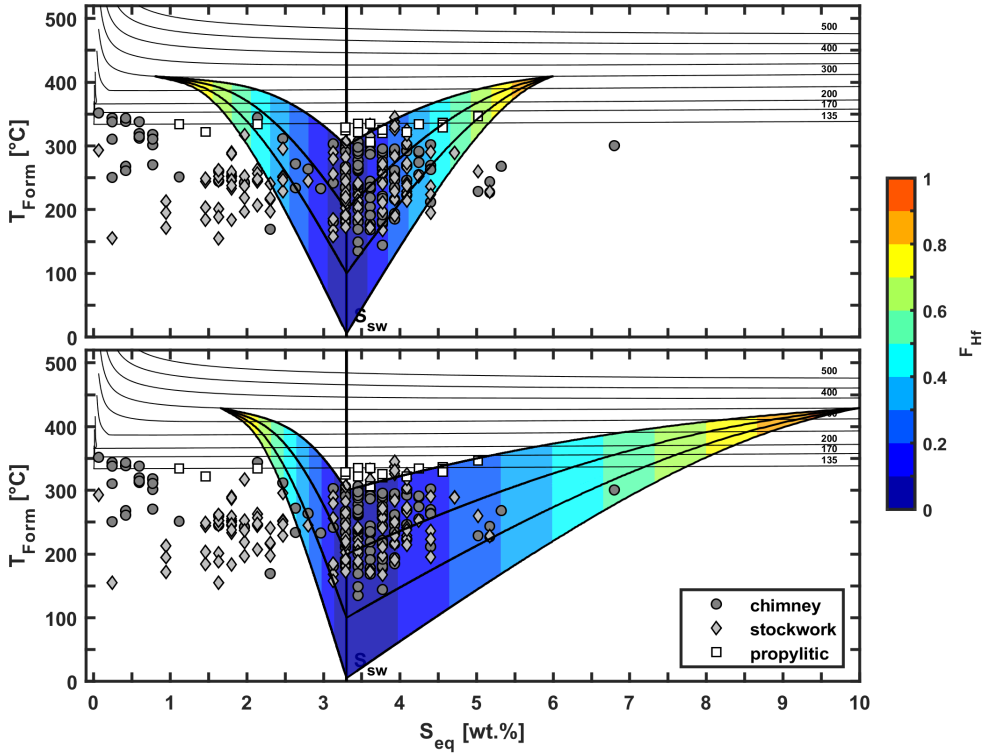

Figure 6.9: Salinity-temperature relation for isenthalpic mixing paths of mixtures between phase-separated hydrothermal fluids and cold to heated seawater at 300 bar (mixing *Model 3* (top)) and 350 bar (mixing *Model 4* (bottom)). The thick black curves denote mixing paths with 5, 100, 200 and 300 °C. The vertical line denotes seawater salinity. The color code gives the mass fraction of the hydrothermal fluid F_{Hf} in the mix. Thin black curves represent isobaric V+L curves (coexisting phase separated fluids).

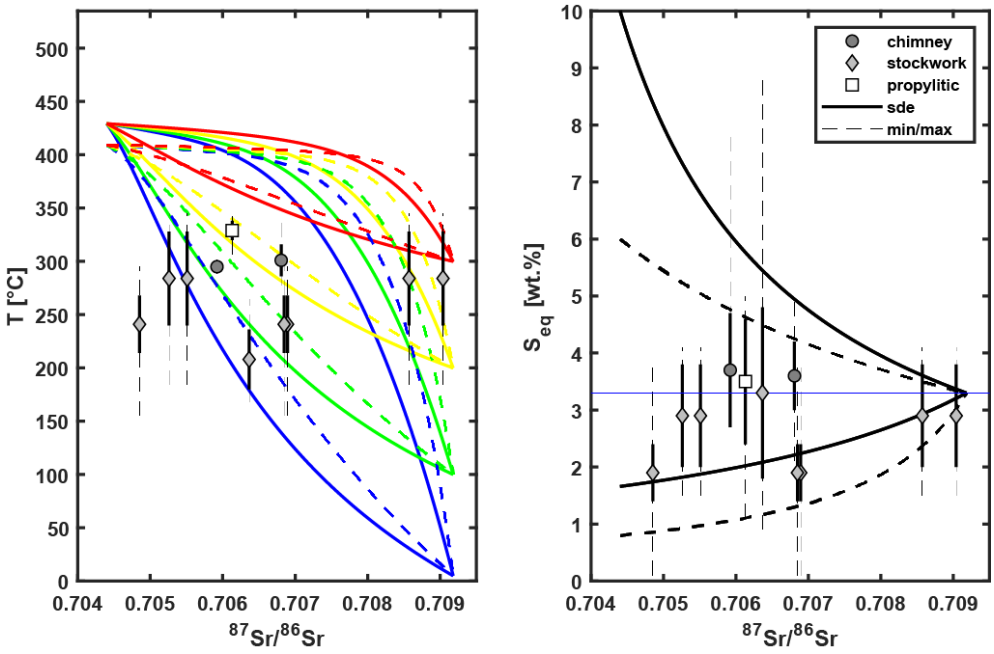

Figure 6.10: Relationship between $^{87}Sr/^{86}Sr$ and temperature (left) and salinity (right) for mixing *Models 3* (dashed lines) and *4* (solid lines). Colors represent mixing lines between the phase-separated end-member and cold to heated seawater (blue: 5°C; green: 100°C; yellow: 200°C; red: 300°C). Symbols represent fluid inclusion mean values, vertical lines represent standard deviations and ranges. For temperatures, pressures, salinities, Sr concentrations and isotope ratios of the phase-separated end-member fluids see Table 6.5.

Models 3 and *4* predict T-X variations in mixtures of seawater with hydrothermal fluids affected by supercritical phase separation (Figures 6.9-6.10). *Model 3* uses end-member fluids produced by phase separation at 300 bar, which were computed as 52 wt.% low-salinity fluid ($S_{Em,vapor}$ = 0.8 wt.% NaCl) and 48 wt.% brine ($S_{Em,brine}$ = 6 wt.% NaCl). *Model 4* has phase separation terminated at 350 bar, which would give phase proportions (and compositions) of 73 wt.% low-salinity fluid ($S_{Em,vapor}$ = 1.66 wt.% NaCl) and 27 wt.% brine ($S_{Em,brine}$ = 10 wt.% NaCl). Those mixing model scenarios can only account for a fraction of the salinities and formation temperatures of the fluid inclusions (Figure 6.9). The inclusions with higher-than-seawater salinities are matched well by the model trends, whereas most of the inclusions with lower salinities cannot be fitted by the mixing trends, unless significant conductive cooling of the end-member vapor prior to mixing is assumed. Both *Models 3* and *4* provide good fits for the co-variation of $^{87}Sr/^{86}Sr$ and formation temperature (Figure 6.10). Due to the fact that the vapor-like fluid has much higher salinities than the subcritical vapors, both these models provide a good fit for the variation of low saline inclusions with respect to $^{87}Sr/^{86}Sr$ signatures of their host minerals. In this regard, the results of model calculations invoking supercritical phase separation are more in line with the observed data, which may indicate that supercritical phase separation may indeed be recorded by our fluid inclusions.

6.4 Discussion

6.4.1 Evidence for phase separation and subseafloor mixing from microthermometry

The vast majority of fluid inclusions in mineralization products from the Brothers NW Caldera Wall hydrothermal vent field show salinities between 0.1 and 4.5 wt.% NaCl; higher salinities (up to 15 wt.% NaCl) also occur, but are rare. Three distinct groups of salinities can be found: A first group with salinities < 0.7 wt.% NaCl is hosted by anhydrite in chimneys. The second group has salinities of 1.5 to 1.7 wt.% NaCl and is dominantly hosted in barite from stockwork rocks. The third group is most prominent, has 3.2 to 4.5 wt.% NaCl and occurs predominantly in barite and anhydrite from chimneys.

Formation temperatures range between 135 and 352 °C with three pronounced modes: The first mode between 230-270 °C is found in inclusions from chimneys and stockwork rocks hosted in barite and anhydrite. The second mode occurs between 290 and 310 °C and is dominated by inclusions in anhydrite from chimneys. Fluid inclusions in a less pronounced third mode (320- 350 °C) occur in all mineralization types and host phases but are dominated by quartz-hosted inclusion from the propylitic altered rock.

Salinities of secondary inclusions are evenly distributed over the entire salinity range but formation temperatures are predominantly found at the high end of the spectrum (250-350 °C).

In five of thirteen samples maximum formation temperatures are close to the boiling curve of seawater and indicate boiling has occurred in these samples. High salinity variations in ten of thirteen samples suggest that phase separation was a dominant mechanism influencing fluids from which crystals have grown in almost all samples.

An increasing variability of fluid inclusion salinities with increasing formation temperatures was found. This provides further evidence that inclusions have grown from end-member hydrothermal fluids created by phase separation processes that subsequently mixed with seawater.

6.4.2 Mixing model constraints on phase separation

Isobaric-isenthalpic models of mixing between vapor-brine end-member pairs and cold or heated seawater can explain virtually the whole spectrum of the fluid inclusion data but the co-variation of temperatures and salinities cannot be explained by one single set of mixing models. Low-salinity fluid inclusions with low formation temperatures are most plausibly explained if they represent vapor end-member fluids that have conductively cooled during or prior to mixing with seawater. Mixing models of sub-critically phase-separated fluids indicated that mixing of a vapor with seawater heated to 100-200 °C may have played a role during the formation of most fluid inclusions with lower-than-seawater salinities. Some fluid inclusions with salinities just below seawater and high formation temperatures would require 300 °C warm seawater as mixing agent for the sub-critically phase-separated fluids. But it is unexpected to have this extensive heating of entrained seawater only few 10s of mbsf.

Sr isotope mass-balance constraints indicate that sulfate crystallized from a fluid that was produced by mixing of a vapor end-member and seawater (forming lower-than-seawater fluid inclusions) should inherit seawater $^{87}Sr/^{86}Sr$ compositions with only small seawater fractions. In fact, those sulfate crystals are relatively radiogenic in Sr isotope composition. These data cannot be fully explained by shallow and subcritical boiling and point to supercritical phase separation (cf. Section 6.3.6). Indeed, mixing models based on the assumption that phase separation of rising fluids must have terminated at greater depth (300-350 bar), indicate that the corresponding end-member pair of a low-saline fluid and a brine formed during supercritical conditions can account for both salinity and formation temperature of the most saline inclusions between 4.5 and 8 wt.% NaCl as well as for the inclusions with high formation temperatures and salinities just below seawater. Furthermore, when those low-salinity end-member fluids mix with seawater they may produce low salinity fluid inclusions in sulfate crystals with intermediate $^{87}Sr/^{86}Sr$ signatures.

In summary, the observed spread of fluid inclusion salinities and results of mixing models as well as Sr isotopic composition of host phases of inclusions are best explained if both sub- and supercritical phase separation are invoked.

6.4.3 Seawater entrainment and sulfate precipitation

$^{87}Sr/^{86}Sr$ ratios of sulfate separates range from near hydrothermal end-member values (0.70485) to near seawater values (0.70904). They represent data for small sample sizes, of only a few crystals per sample. The data indicates that individual crystals grew in very different mixing regimes from near-hydrothermal end-member conditions to seawater-dominated conditions. Bulk rock samples fall in a more restricted range of $^{87}Sr/^{86}Sr$ between 0.70551 and 0.70857. This variability of relatively large-size (tens of grams) bulk samples shows that variability also exists on larger scales. The data demonstrates that seawater entrainment during sulfate deposition within chimney walls and in the stockwork immediately underneath the vent fields is common and varied. The salinities of fluid inclusions in anhydrite and barite (ranging from 0.1 to 8 wt.%) are consistent with phase separation, but the clustering around seawater-salinity indicates widespread mixing between phase separated fluids and seawater.

Growth of sulfate crystals in mixing regimes with variable seawater contributions has been demonstrated before for deep-sea hydrothermal systems in oceanic spreading centers (Humphris & Bach, 2005; Craddock & Bach, 2010; Jamieson et al., 2016) and it affects not only $^{87}Sr/^{86}Sr$, but also sulfur isotopes and REE distributions. The results of this study suggest that sulfates are useful recorders of fluid compositions and temperatures in hydrothermal systems also in island arcs.

6.4.4 Extent and depth of phase separations at the NW Caldera Wall vent field

Formation temperatures for a subset of fluid inclusion samples (five of thirteen) indicate that boiling had likely occurred. Boiling is even more evident in the range of fluid inclusion salinities between 0 and 4.5 wt.%. Specifically, salinity variations in ten of thirteen samples indicate the presence of phase-separation-processes during the formation of fluids from which sulfate minerals had grown. One possibility to explain why salinities more faithfully record phase separation is re-equilibration upon cooling. Due to differences in the down-temperature volume changes between inclusion and host, the original formation temperatures could potentially be offset to lower values.

Another, perhaps more likely possibility is that fluid inclusions with high salinity variations and low formation temperatures represent mixing of hot upwelling fluids and cold entrained seawater prior to crystal growth. Such mixing processes would terminate boiling in the

subsurface due to efficient cooling. Any kind of cooling – by entrainment of small portions of seawater in the sub-surface or by conduction – can easily lower formation temperatures and at the same time preserve salinity variability.

Our results augment earlier findings of de Ronde et al. (2003), who investigated 82 barite-hosted fluid inclusions from two samples of the NW Caldera Wall vent site. The authors reported a mean salinity of 3.2 ± 0.3 wt.% NaCl and a mean formation temperature of 256 ± 27 °C, which are similar to the results of this study (3.1 ± 1.3 wt.% NaCl; 257 ± 47 °C; cf. Table 6.3). But the variability in both salinity and formation temperature of fluid inclusions indicated by de Ronde et al. (2003) is much more restricted than in our study. Three of thirteen samples examined in the course of our study also gave a narrow range of formation temperatures and salinities that are similar to the results of de Ronde et al. (2003). The authors suggested, based on their results from two samples, that the fluid inclusions do not record phase separation at the NW Caldera site. Our data, representing a much larger sample size, show that the majority of inclusions actually is affected by phase separation processes. Phase separation has been identified as common process based on vent fluid compositional variability (de Ronde et al., 2011; Kleint et al., submitted to GCA; Diehl et al., in prep., Chapter 5). Consistent with this notion, Gruen et al. (2014) presented results of numerical fluid flow simulations for Brothers volcano and find that seafloor phase-separation should take place below the NW Caldera Wall. The salinities of fluid inclusions can be matched against constraints from the vent fluid compositions (Kleint et al., submitted to GCA; Diehl et al., in prep., Chapter 5). The vent fluid zero-Mg end-members give maximum salinities of 4.5 wt.% NaCl, which is considerably lower than the highest salinities of fluid inclusions. This zero-Mg vent fluid end-member salinity corresponds to a vapor fraction of ~30 wt.% during boiling (cf. Table 6.5).

Despite salinity-based evidence for boiling, vent fluid temperatures measured during both expeditions to the NW Caldera Wall (SO253 and TN350) are notably below (> 15-20 °C) the boiling curve of seawater. To reconcile this apparent conundrum, we suggest that boiling is a common feature in the NW Caldera Wall hydrothermal system, but the amount of cooling en route to the seafloor is variable in space and time. The range of formation temperatures of fluid inclusions provides a record of this variability and indicates that boiling near or at the seafloor has occurred sporadically in the recent past.

6.5 Summary and Conclusions

Formation temperatures and salinity variations in fluid inclusions of hydrothermal precipitates from Brothers NW Caldera Wall vent field provide strong evidence for common phase separation in hydrothermal fluids that from chimneys and mineralized stockwork zones.

Temperature-salinity variations in the majority of samples suggest that sulfate minerals in stockwork zones and chimneys have grown during mixing of phase-separated fluids with seawater. Although, no evidence for boiling at the seafloor was observed during two vent fluid sampling campaigns, formation temperatures in some sulfate samples show that venting of boiling fluids may have occurred before.

Inclusion temperatures and salinities as well as $^{87}Sr/^{86}Sr$ values of most hydrothermal precipitates have been combined with results of isenthalpic mixing models. The results indicate that fluid end-members most likely formed during boiling just below the seafloor (at pressures around 170 bar; i.e. above the caldera floor) and then mixed with cold seawater or moderately heated seawater-derived fluids before venting. A small subset of fluid inclusions is hosted in crystals with relative unradiogenic $^{87}Sr/^{86}Sr$ values (< 0.7070) and show high formation temperatures (280-350 °C) in combination with salinities that are just slightly lower than seawater. These inclusions cannot be explained by mixing of seawater with a vapor produced by boiling. They are more likely a consequence of supercritical phase separation that occurred at greater pressures (300-350 bar), corresponding to > 1000 m depth below the caldera floor. These depths are similar to the vertical extent of the low magnetization zone identified by Caratori-Tontini et al. (2012b).

The results of this study highlight that shallow phase separation and mixing with entrained seawater occur extensively in the subseafloor of the NW Caldera Wall hydrothermal vent field. Since sulfate and sulfide mineralization are in close relation to each other, these findings can directly be transferred to the deposition of polymetallic sulfides. Phase separation processes heavily influence the transport and deposition of metals in seafloor mineralization systems. In addition, evidence for supercritical phase separation suggests that a fraction of the metals in the mineralized stockwork zone and the overlying seafloor polymetallic massive sulfide body may originate from greater depths and are transported over considerable vertical distances.

Acknowledgements

We acknowledge the science teams, crews and captains of the RV Sonne and RV Thompson for their work offshore. Thanks to the teams of ROV QUEST and ROV Jason II for their efforts to recover unique rock specimen that made this work possible. The research cruise TN350 was supported by the U.S. National Science Foundation awards OCE-1558356 to Susan Humphris and OCE-1558795 to Anna-Louise Reysenbach. The Bundesministerium für Bildung und Forschung (BMBF) enabled cruise SO253 and this work with grant no. 03G0253B. AD was also partly supported by the MARUM Center for Marine Environmental Science. Special thanks also to Andreas Klügel for instructions in the use of the microthermometry stage and to Friedrich Lucassen for his support during lab work and TIMS analysis.

References

Atkinson, Jr., A. B. (2002). A Model for the PTX Properties of H_2O-NaCl. Virginia Tech. doi: http://hdl.handle.net/10919/34376.

Baker, E. T., Walker, S. L., Embley, R. W., and de Ronde, C. E. (2012). High-Resolution Hydrothermal Mapping of Brothers Caldera, Kermadec Arc. Economic Geology. doi: 10.2113/econgeo.107.8.1583.

Bauer, O. and Engel, O. (1998). PROST Version 4.1. Technische Universität Hamburg- Harburg Arbeitsbereich 6-08 Technische Thermodynamik Denickestrasse 15 D-21073 Hamburg Germany.

Bieseler, B., Diehl, A., Jöns, N., Lucassen, F., and Bach, W. (2018). Constraints on Cooling of the Lower Ocean Crust from Epidote Veins in the Wadi Gideah Section, Oman Ophiolite. Geochemistry, Geophysics, Geosystems. doi: 10.1029/2018GC007679.

Bodnar, R. (2003). Reequilibration of Fluid Inclusions. In Samson, I., Anderson, A., and Marshall, D. e., editors, Fluid Inclusions: Analysis and Interpretation, volume Short Course 32, pages 213–230. Mineral. Assoc. Canada.

Bodnar, R., Lecumberri-Sanchez, P., Moncada, D., and Steele-MacInnis, M. (2014). Fluid Inclusions in Hydrothermal Ore Deposits. In Holland, H. and Turekian, K. e., editors, Treatise on Geochemistry, Second Edition, volume 13, pages 119–142. Oxford: Elsevier.

Bodnar, R. J. and Vityk, M. (1994). Interpretation of microthermometric data for H_2O- NaCl fluid inclusions. Fluid Inclusions in Minerals: Methods and Applications. doi: https://ci.nii.ac.jp/naid/10003717232/en/.

Caratori Tontini, F., Davy, B., de Ronde, C., Embley, R., Leybourne, M., and Tivey, M. A. (2012a). Crustal Magnetization of Brothers Volcano, New Zealand, Measured by Autonomous Underwater Vehicles: Geophysical Expression of a Submarine Hydrothermal System. Economic Geology. doi: 10.2113/econgeo.107.8.1571.

Caratori Tontini, F., de Ronde, C. E. J., Yoerger, D., Kinsey, J., and Tivey, M. (2012b). 3-D focused inversion of near-seafloor magnetic data with application to the Brothers volcano hydrothermal system, Southern Pacific Ocean, New Zealand. Journal of Geophysical Research: Solid Earth. doi: 10.1029/2012JB009349.

Craddock, P. R. and Bach, W. (2010). Insights to magmatic-hydrothermal processes in the Manus back-arc basin as recorded by anhydrite. Geochimica et Cosmochimica Acta. doi: https://doi.org/10.1016/j.gca.2010.07.004.

de Ronde, C. E., Faure, K., Bray, C. J., Chappell, D. A., and Wright, I. C. (2003). Hydrothermal fluids associated with seafloor mineralization at two southern Kermadec arc volcanoes, offshore New Zealand. Mineralium Deposita. doi: 10.1007/s00126-002- 0305-4.

de Ronde, C. E. and Stucker, V. K. (2015). Chapter 47 - Seafloor Hydrothermal Venting at Volcanic Arcs and Backarcs. In Sigurdsson, H., editor, The Encyclopedia of Volcanoes (Second Edition), pages 823 – 849. Academic Press, Amsterdam, Second Edition. doi: https://doi.org/10.1016/B978-0-12-385938-9.00047-X.

de Ronde, C. E. J., Hannington, M. D., Stoffers, P., Wright, I. C., Ditchburn, R. G., Reyes, A. G., Baker, E. T., Massoth, G. J., Lupton, J. E., Walker, S. L., Greene, R. R., Soong, C. W. R., Ishibashi, J., Lebon, G. T., Bray, C. J., and Resing, J. A. (2005). Evolution of a Submarine Magmatic-Hydrothermal System: Brothers Volcano, Southern Kermadec Arc, New Zealand. Economic Geology. doi: 10.2113/gsecongeo.100.6.1097.

de Ronde, C. E. J., Massoth, G. J., Butterfield, D. A., Christenson, B. W., Ishibashi, J., Ditchburn, R. G., Hannington, M. D., Brathwaite, R. L., Lupton, J. E., Kamenetsky, V. S., Graham, I. J., Zellmer, G. F., Dziak, R. P., Embley, R. W., Dekov, V. M., Munnik, F., Lahr, J., Evans, L. J., and Takai, K. (2011). Submarine hydrothermal activity and gold-rich mineralization at Brothers Volcano, Kermadec Arc, New Zealand. Mineralium Deposita. doi: 10.1007/s00126-011-0345-8.

Deniel, C. and Pin, C. (2001). Single-stage method for the simultaneous isolation of lead and strontium from silicate samples for isotopic measurements. Analytica Chimica Acta. doi: https://doi.org/10.1016/S0003-2670(00)01185-5.

Driesner, T. (2007). The system H_2O-NaCl. Part II: Correlations for molar volume, enthalpy, and isobaric heat capacity from 0 to 1000-C, 1 to 5000bar, and 0 to 1 XNaCl. Geochimica et Cosmochimica Acta. doi: https://doi.org/10.1016/j.gca.2007.05.026.

Driesner, T. and Heinrich, C. A. (2007). The system H_2O-NaCl. Part I: Correlation formulae for phase relations in temperature-pressure-composition space from 0 to 1000°C, 0 to 5000bar, and 0 to 1 XNaCl. Geochimica et Cosmochimica Acta. doi: https://doi.org/10.1016/j.gca.2006.01.033.

Dziak, R. P., Haxel, J. H., Matsumoto, H., Lau, T. K., Merle, S. G., de Ronde, C. E. J., Embley, R. W., and Mellinger, D. K. (2008). Observations of regional seismicity and local harmonic tremor at Brothers volcano, south Kermadec arc, using an ocean bottom hydrophone array. Journal of Geophysical Research: Solid Earth. doi: 10.1029/2007JB005533.

Embley, R. W., de Ronde, C. E. J., Merle, S. G., Davy, B., and Tontini, F. C. (2012). Detailed Morphology and Structure of an Active Submarine Arc Caldera: Brothers Volcano, Kermadec Arc. Economic Geology. doi: 10.2113/econgeo.107.8.1557.

GEBCO (2014). Intergovernmental Oceanographic Commission, IHO, and BODC. Centenary edition of the GEBCO digital Atlas, published on CD-ROM on behalf of the Intergovernmental Oceanographic Commission and the International Hydrographic Organization as part of the General Bathymetric Chart of the Oceans, British Oceanographic Data Centre, Liverpool, U. K.

Gruen, G., Weis, P., Driesner, T., de Ronde, C. E. J., and Heinrich, C. A. (2012). Fluid-Flow Patterns at Brothers Volcano, Southern Kermadec Arc: Insights from Geologically Constrained Numerical Simulations. Economic Geology. doi: 10.2113/econ- geo.107.8.1595.

Gruen, G., Weis, P., Driesner, T., Heinrich, C. A., and de Ronde, C. E. (2014). Hydrodynamic modeling of magmatic-hydrothermal activity at submarine arc volcanoes, with implications for ore formation. Earth and Planetary Science Letters. doi: https://doi.org/10.1016/j.epsl.2014.07.041.

Haar, L., Gallagher, J. S., and Kell, G. S. (1984). NBS/NRC Steam Tables. Hemisphere Publishing Corporation. NBS/NRC Wasserdampftafeln, Springer Verlag, 1988.

Haase, K. M., Stroncik, N., Garbe-Schönberg, D., and Stoffers, P. (2006). Formation of island arc dacite magmas by extreme crystal fractionation: An example from Brothers Seamount, Kermadec island arc (SW Pacific). Journal of Volcanology and Geothermal Research. doi: https://doi.org/10.1016/j.jvolgeores.2005.10.010.

Haase, K. M., Worthington, T. J., Stoffers, P., Garbe-Schönberg, D., and Wright, I. (2002). Mantle dynamics, element recycling, and magma genesis beneath the Kermadec Arc-Havre Trough. Geochemistry, Geophysics, Geosystems. doi: 10.1029/2002GC000335.

Haase, K. M., Stroncik, N., Garbe-Schönberg, D., and Stoffers, P. (2006). Formation of island arc dacite magmas by extreme crystal fractionation: An example from Brothers Seamount, Kermadec island arc (SW Pacific). Journal of Volcanology and Geothermal Research. doi: https://doi.org/10.1016/j.jvolgeores.2005.10.010.

Hansteen, T. H. and Klügel, A. (2008). Fluid Inclusion Thermobarometry as a Tracer for Magmatic Processes. Reviews in Mineralogy and Geochemistry. doi: 10.2138/rmg.2008.69.5.

Humphris, S. E. and Bach, W. (2005). On the Sr isotope and REE compositions of anhydrites from the TAG seafloor hydrothermal system. Geochimica et Cosmochimica Acta.
doi: https://doi.org/10.1016/j.gca.2004.10.004.

Jamieson, J. W., Hannington, M. D., Tivey, M. K., Hansteen, T., Williamson, N. M.- B., Stewart, M., Fietzke, J., Butterfield, D., Frische, M., Allen, L., Cousens, B., and Langer, J. (2016). Precipitation and growth of barite within hydrothermal vent deposits from the Endeavour Segment, Juan de Fuca Ridge. Geochimica et Cosmochimica Acta. doi: https://doi.org/10.1016/j.gca.2015.10.021.

Jochum, K. P., Nohl, U., Herwig, K., Lammel, E., Stoll, B., and Hofmann, A. W. (2005). Georem: A new geochemical database for reference materials and isotopic standards. Geostandards and Geoanalytical Research, 29(3):333–338.

Keith, M., Haase, K. M., Klemd, R., Smith, D. J., Schwarz-Schampera, U., and Bach, W. (2018). Constraints on the source of Cu in a submarine magmatic-hydrothermal system, Brothers volcano, Kermadec island arc. Contributions to Mineralogy and Petrology. doi: 10.1007/s00410-018-1470-5.

Lécuyer, C., Dubois, M., Marignac, C., Gruau, G., Fouquet, Y., and Ramboz, C. (1999). Phase separation and fluid mixing in subseafloor back arc hydrothermal systems: A microthermometric and oxygen isotope study of fluid inclusions in the barite-sulfide chimneys of the Lau Basin. Journal of Geophysical Research: Solid Earth. doi: 10.1029/1999JB900121.

Longpré, M.-A., Klügel, A., Diehl, A., and Stix, J. (2014). Mixing in mantle magma reservoirs prior to and during the 2011 - 2012 eruption at El Hierro, Canary Islands. Geology. doi: 10.1130/G35165.1.

Vanko, D. A. and Bach, W. (2005). Heating and freezing experiments on aqueous fluid inclusions in anhydrite: Recognition and effects of stretching and the low-temperature formation of gypsum. Chemical Geology. New Results in Fluid and Silicate Melt Inclusion Research (ECROFI XVII).

Vanko, D. A., Bach, W., Roberts, S., Yeats, C. J., and Scott, S. D. (2004). Fluid inclusion evidence for subsurface phase separation and variable fluid mixing regimes beneath the deep-sea PACMANUS hydrothermal field, Manus Basin back arc rift, Papua New Guinea. Journal of Geophysical Research: Solid Earth. doi: 10.1029/2003JB002579.

Wright, I., de Ronde, C., Faure, K., and Gamble, J. (1998). Discovery of hydrothermal sulfide mineralization from southern Kermadec arc volcanoes (SW Pacific). Earth and Planetary Science Letters. doi: https://doi.org/10.1016/S0012-821X(98)00225-8.

Wright, I. and Gamble, J. (1999). Southern Kermadec submarine caldera arc volcanoes (SW Pacific): caldera formation by effusive and pyroclastic eruption. Marine Geology.
doi: https://doi.org/10.1016/S0025-3227(99)00040-7.

Appendix

Appendix 6.A1: Fluid inclusion raw data. Trail #: Marks indiv. trails or groups of incluions; Host: Host crystal; Shape: shape of inclusion (el: elongated, euh: euhedral, rnd: round); L/V: volume fraction of the liquid (%). Reeq: decrepitation features (decr: decrepitated, imm; immature incluision, none: no visible features); Petro: petrography of inclusion (PS: pseudosecondary, S: secondary, P: primary); $Tm_{(initial)}$ beginning of melting; $Tm_{(final)}$ end of the melting interval; Thom: homogenization temperature; Mode: Mode of homogenization (L: homogenization into a liquid phase, V: homogenization into a vapor phase, crit: critical homogenization).

Sample	Piece #	Inc. #	Trail #	Host	Shape	Size(S)	Size(L)	L/V	Reeq.	Petro	$Tm_{(initial)}$	$Tm_{(final)}$	Thom	Mode
061-1S-1	A	1	1	barite	el.	1	4	10	none	PS	NaN	-2.2	NaN	NaN
061-1S-1	A	2	1	barite	el.	1	3	10	none	PS	NaN	NaN	188.0	L
061-1S-1	A	3	1	barite	euh.	2	2	20	none	PS	NaN	-2.1	223.0	L
061-1S-1	A	4	1	barite	euh.	2	4	10	decr.	PS	NaN	NaN	191.5	L
061-1S-1	A	5	2	barite	irr.	5	5	40	none	PS	NaN	-2.0	NaN	NaN
061-1S-1	A	6	2	barite	el.	2	5	20	none	PS	-6.9	-2.4	236.0	L
061-1S-1	A	7	2	barite	irr.	3	4	10	decr.	PS	NaN	-2.2	232.5	L
061-1S-1	A	8	2	barite	irr.	2	4	10	decr.	PS	NaN	-2.2	234.0	L
061-1S-1	A	9	2	barite	rnd.	2	2	10	none	PS	NaN	-2.3	223.0	L
061-1S-1	A	10	2	barite	rnd.	2	2	10	none	PS	NaN	-2.3	223.0	L
061-1S-1	A	11	2	barite	irr.	15	20	10	none	PS	NaN	-1.9	281.5	L
061-1S-1	A	12	2	barite	irr.	7	7	20	decr.	PS	-4.1	-1.9	225.5	L
061-1S-1	A	13	2	barite	irr.	4	15	30	none	PS	NaN	-2.2	280.0	L
061-1S-1	A	14	2	barite	euh.	3	4	10	none	PS	-2.7	-2.2	275.0	L
061-1S-1	A	15	2	barite	rnd.	1	1	10	none	PS	-19.2	-14.0	222.0	L
061-1S-1	A	16	2	barite	euh.	2	3	10	decr.	PS	NaN	-2.3	282.5	L
061-1S-1	A	17	2	barite	rnd.	1	2	20	decr.	PS	NaN	-2.3	235.5	L
061-1S-1	A	18	2	barite	rnd.	1	2	10	none	PS	-2.6	-2.2	168.0	L
061-1S-1	A	19	3	barite	irr.	3	4	10	decr.	PS	NaN	-2.3	242.5	L
061-1S-1	A	20	3	barite	euh.	3	4	20	none	PS	NaN	-2.0	250.5	L
061-1S-1	A	21	3	barite	irr.	3	4	10	decr.	PS	-2.5	-1.1	232.0	L
061-1S-1	A	22	3	barite	euh.	3	4	10	none	PS	-7.1	-2.3	206.0	L
061-1S-1	A	23	3	barite	el.	1	5	10	decr.	PS	NaN	-3.1	217.0	L
061-1S-1	A	24	3	barite	irr.,el.	1	5	10	decr.	PS	NaN	-2.2	283.5	L
061-1S-1	B	1	4	barite	irr.	3	3	10	decr.	PS	NaN	-2.0	126.0	L
061-1S-1	B	2	4	barite	euh.	3	4	20	decr.	PS	NaN	-1.8	231.5	L
061-1S-1	B	3	4	barite	el.	2	6	10	none	PS	NaN	-3.1	233.5	L
061-1S-1	B	4	4	barite	euh.	2	3	20	decr.	PS	NaN	-2.1	228.0	L
061-1S-1	B	5	4	barite	rnd.	2	2	10	decr.	PS	NaN	-3.0	218.5	L
061-1S-1	B	6	4	barite	irr.	2	5	10	decr.	PS	NaN	-2.1	222.0	L

Appendix 6.A1: Fluid inclusion raw data. Trail #: Marks indiv. trails or groups of incluions; Host: Host crystal; Shape: shape of inclusion (el: elongated, euh: euhedral, rnd: round); L/V: volume fraction of the liquid (%). Reeq: decrepitation features (decr: decrepitated, imm; immature incluision, none: no visible features); Petro: petrography of inclusion (PS: pseudosecondary, S: secondary, P: primary); $Tm_{(initial)}$ beginning of melting; $Tm_{(final)}$ end of the melting interval; Thom: homogenization temperature; Mode: Mode of homogenization (L: homogenization into a liquid phase, V: homogenization into a vapor phase, crit: critical homogenization).

Sample	Piece #	Inc. #	Trail #	Host	Shape	Size(S)	Size(L)	L/V	Reeq.	Petro	$Tm_{(initial)}$	$Tm_{(final)}$	Thom	Mode
061-1S-1	B	7	5	barite	euh.	3	5	20	imm.,decr.	PS	-2.1	-0.9	234.5	L
061-1S-1	B	8	5	barite	euh.	2	3	40	decr.	PS	-2.5	-1.9	NaN	NaN
061-1S-1	B	9	5	barite	rnd.	1	1	10	none	PS	NaN	-2.2	211.0	L
061-1S-1	B	10	5	barite	rnd.	1	1	10	none	PS	NaN	-2.2	205.0	L
061-1S-1	B	11	5	barite	el.	1	4	10	imm.	PS	NaN	-0.1	301.5	L
061-1S-1	B	12	5	barite	euh.	1	2	10	none	PS	NaN	-2.1	234.0	L
061-1S-2	A	1	1	barite	rnd.	4	8	30	decr.	P	-3.6	-2.3	329.0	V
061-17S-1	A	1	1	barite	euh.	11	23	20	none	P	NaN	-2.0	NaN	NaN
061-17S-1	A	2	1	barite	rnd.	11	23	20	none	P	NaN	-2.0	173.0	L
061-17S-1	A	3	1	barite	euh.	11	30	20	none	P	NaN	-1.8	171.0	L
061-17S-1	A	4	2	barite	euh.	15	23	20	decr.	P	NaN	-2.0	190.5	L
061-17S-1	A	5	2	barite	euh.	4	5	20	none	P	NaN	-2.2	173.0	L
061-17S-1	A	6	2	barite	euh.	5	8	20	none	P	NaN	-2.1	169.0	L
061-17S-1	A	7	2	barite	euh.,el.	12	40	20	none	P	NaN	-2.0	171.0	L
061-17S-1	B	1	3	barite	euh.	NaN	NaN	NaN	decr.	S	NaN	-1.4	NaN	NaN
061-17S-1	B	2	3	barite	el.	NaN	NaN	NaN	decr.	S	-3.0	-0.6	NaN	NaN
061-17S-1	B	3	3	barite	el.	NaN	NaN	NaN	decr.	S	NaN	-0.4	NaN	NaN
061-17S-1	B	4	3	barite	rnd.,el.	NaN	NaN	NaN	decr.	S	NaN	-2.0	NaN	NaN
061-17S-1	B	5	3	barite	irr.,el.	NaN	NaN	NaN	decr.	S	NaN	NaN	NaN	NaN
061-17S-1	B	6	3	barite	irr..el.	NaN	NaN	NaN	decr.	S	NaN	NaN	441.0	L
061-17S-1	B	7	3	barite	rnd.	NaN	NaN	NaN	decr.	S	NaN	-2.0	286.0	L
061-17S-1	B	8	3	barite	rnd.	1	2	NaN	none	S	NaN	-2.5	280.0	L
061-17S-1	B	9	3	barite	rnd.	1	2	NaN	none	S	NaN	-2.5	282.0	L
061-17S-1	B	10	3	barite	rnd.	2	3	NaN	none	S	NaN	NaN	380.0	V
061-17S-1	B	11	3	barite	rnd.	2	5	NaN	none	S	NaN	NaN	NaN	NaN
061-17S-1	C	1	4	barite	euh.	110	120	10	none	P	NaN	-2.2	NaN	V
061-17S-1	C	2	4	barite	euh.	35	45	10	none	P	NaN	-2.2	171.0	L
061-17S-1	C	3	4	barite	euh.	35	55	10	decr.	P	NaN	-2.0	140.0	L
061-17S-1	C	4	4	barite	euh.	20	28	10	decr.	P	NaN	-2.1	183.0	L
061-17S-1	C	5	4	barite	rnd.	3	12	10	none	P	NaN	-2.1	159.0	L

Appendix 6.A1: Fluid inclusion raw data. Trail #: Marks indiv. trails or groups of incluions; Host: Host crystal; Shape: shape of inclusion (el: elongated, euh: euhedral, rnd: round); L/V: volume fraction of the liquid (%). Reeq: decrepitation features (decr: decrepitated, imm; immature incluision, none: no visible features); Petro: petrography of inclusion (PS: pseudosecondary, S: secondary, P: primary); $Tm_{(initial)}$ beginning of melting; $Tm_{(final)}$ end of the melting interval; Thom: homogenization temperature; Mode: Mode of homogenization (L: homogenization into a liquid phase, V: homogenization into a vapor phase, crit: critical homogenization).

Sample	Piece #	Inc. #	Trail #	Host	Shape	Size(S)	Size(L)	L/V	Reeq.	Petro	$Tm_{(initial)}$	$Tm_{(final)}$	Thom	Mode
061-17S-1	C	6	4	barite	euh.	20	25	10	none	P	NaN	-2.2	NaN	NaN
061-17S-1	C	7	4	barite	euh.	5	9	10	none	P	NaN	NaN	NaN	NaN
061-17S-1	C	8	4	barite	euh.	12	15	10	none	P	NaN	NaN	NaN	NaN
061-17S-1	D	1	5	barite	irr.	5	35	10	decr.	P	NaN	3.3	NaN	NaN
061-17S-1	D	2	5	barite	irr.	3	9		none	P	NaN	3.3	NaN	NaN
061-17S-1	D	3	5	barite	irr.	10	40		none	P	NaN	-2.1	NaN	NaN
061-17S-1	D	4	5	barite	euh.	3	5		none	P	NaN	-2.3	NaN	NaN
061-17S-1	D	5	5	barite	irr.	NaN	NaN		none	P	-15.1	-15.0	NaN	NaN
061-17S-1	D	6	5	barite	irr.	NaN	NaN		decr.	P	-8.3	-5.4	NaN	NaN
064-9R	A	1	1	barite	euh.	4	8	50	none	PS	NaN	-2.4	319.0	L
064-9R	A	2	1	barite	euh.	3	8	30	none	PS	NaN	-2.3	325.0	L
064-9R	A	3	1	barite	euh.	5	6	50	none	PS	NaN	-2.1	328.0	L
064-9R	A	4	1	barite	euh.	5	8	30	none	PS	NaN	-2.3	320.0	L
064-9R	A	5	1	barite	euh.	2	4	30	none	PS	NaN	-2.3	334.0	L
064-9R	A	6	1	barite	euh.,el.	2	12	10	none	PS	NaN	-2.3	NaN	L
064-9R	A	7	1	barite	euh.,el.	8	25	40	none	PS	NaN	-2.3	343.0	L
064-9R	A	8	1	barite	euh.,el.	10	40	40	none	PS	NaN	-2.4	NaN	NaN
064-9R	A	9	1	barite	euh.,el.	5	25	20	decr.	PS	NaN	-1.4	219.0	L
064-9R	B	1	2	anhydrite	euh.	2	2	40	none	PS	NaN	-2.4	296.0	L
064-9R	B	2	2	anhydrite	euh.	3	4	40	none	PS	NaN	-1.7	NaN	NaN
064-9R	B	3	2	anhydrite	euh.	2	3	60	none	PS	NaN	-1.3	231.0	L
064-9R	B	4	2	anhydrite	euh.	1	1	80	none	PS	NaN	-1.9	NaN	NaN
064-9R	B	5	2	anhydrite	euh.	2	2	60	none	PS	NaN	-1.8	281.0	L
064-9R	B	6	2	anhydrite	euh.	2	2	40	none	PS	NaN	-1.8	270.0	L
064-9R	B	7	2	anhydrite	euh.	2	3	40	none	PS	NaN	-1.9	298.0	L
064-9R	B	8	2	anhydrite	euh.	2	2	NaN	none	PS	NaN	NaN	NaN	NaN
064-9R	B	9	2	anhydrite	euh.	2	2	80	none	PS	-2.4	-1.1	NaN	NaN
064-9R	B	10	2	anhydrite	euh.	2	3	20	none	PS	-2.4	-1.2	237.0	L
064-9R	B	11	2	anhydrite	euh.	2	2	60	none	PS	NaN	-1.3	NaN	NaN
064-9R	B	12	3	anhydrite	euh.	9	10	30	none	P	NaN	-2.1	309.0	L

Appendix 6.A1: Fluid inclusion raw data. Trail #: Marks indiv. trails or groups of incluions; Host: Host crystal; Shape: shape of inclusion (el: elongated, euh: euhedral, rnd: round); L/V: volume fraction of the liquid (%). Reeq: decrepitation features (decr: decrepitated, imm; immature incluision, none: no visible features); Petro: petrography of inclusion (PS: pseudosecondary, S: secondary, P: primary); $Tm_{(initial)}$ beginning of melting; $Tm_{(final)}$ end of the melting interval; Thom: homogenization temperature; Mode: Mode of homogenization (L: homogenization into a liquid phase, V: homogenization into a vapor phase, crit: critical homogenization).

Sample	Piece #	Inc. #	Trail #	Host	Shape	Size(S)	Size(L)	L/V	Reeq.	Petro	$Tm_{(initial)}$	$Tm_{(final)}$	Thom	Mode
064-9R	B	13	4	anhydrite	euh.	4	8	20	none	P	NaN	-1.3	206.0	L
064-9R	B	14	5	anhydrite	euh.	6	6	30	none	P	NaN	-2.3	326.0	L
064-9R	C	1	6	anhydrite	euh.,irr.	15	30	20	none	P	NaN	-0.8	234.5	L
064-9R	C	2	6	anhydrite	euh.,irr.	6	20	30	decr.	P	NaN	-0.9	236.0	L
064-9R	C	3	6	anhydrite	euh.,el.	6	20	30	none	P	NaN	-1.0	278.0	L
064-9R	C	4	6	anhydrite	euh.	5	14	20	decr.	P	NaN	-1.0	281.0	L
064-9R	C	5	6	anhydrite	euh.	6	6	30	none	P	NaN	-1.1	310.0	L
064-9R	C	6	6	anhydrite	euh.	12	25	40	decr.	P	NaN	-0.8	239.0	L
064-9R	C	7	6	anhydrite	euh.,irr.	10	10	20	decr.	P	NaN	-0.8	175.0	L
064-9R	C	8	7	anhydrite	euh.,el.	15	60	40	none	P	NaN	-2.1	NaN	NaN
064-9R	D	1	8	anhydrite	euh.	7	10	30	none	P	NaN	-1.3	NaN	NaN
064-9R	D	2	8	anhydrite	euh.	15	60	60	none	P	NaN	-0.9	NaN	NaN
064-9R	D	3	8	anhydrite	euh.	8	15	60	none	P	NaN	-1.5	NaN	NaN
064-9R	D	4	8	anhydrite	irr.	5	8	30	decr.	P	NaN	-1.5	NaN	NaN
064-9R	D	5	8	anhydrite	irr.	12	20	40	none	P	NaN	-1.4	NaN	NaN
064-9R	D	6	8	anhydrite	euh.	7	20	30	none	P	NaN	-2.0	NaN	NaN
064-9R	D	7	8	anhydrite	irr.	5	15	30	none	P	NaN	-2.1	NaN	NaN
064-9R	D	8	8	anhydrite	irr.	5	8	30	none	P	NaN	-1.4	NaN	NaN
064-9R	E	1	9	barite	euh.	8	20	30	none	P	NaN	-2.2	NaN	NaN
064-9R	E	2	9	barite	euh.	8	10	20	none	P	NaN	-1.8	246.5	L
064-9R	E	3	9	barite	euh.	4	5	30	none	P	NaN	-0.9	NaN	NaN
064-9R	E	4	9	barite	euh.	5	7	50	decr.	P	NaN	-1.9	273.0	L
064-9R	E	5	9	barite	euh.	2	3	40	none	P	NaN	-2.3	NaN	NaN
064-9R	E	6	9	barite	euh.	2	6	60	decr.	P	NaN	-1.2	NaN	NaN
064-10S	A	1	1	anhydrite	euh.	7	8	20	none	P	NaN	-0.1	241.0	L
064-10S	A	2	1	anhydrite	euh.,el.	4	7	20	none	P	NaN	-0.9	250.5	L
064-10S	A	3	1	anhydrite	euh.	5	5	20	none	P	NaN	-0.2	NaN	NaN
064-10S	A	4	1	anhydrite	euh.	2	3	20	decr.	P	NaN	-0.2	258.5	L
064-10S	A	5	1	anhydrite	euh.	2	4	20	decr.	P	NaN	-0.6	241.5	L
064-10S	A	6	1	anhydrite	irr.	14	22	20	none	P	NaN	-0.4	293.0	L

Appendix 6.A1: Fluid inclusion raw data. Trail #: Marks indiv. trails or groups of incluions; Host: Host crystal; Shape: shape of inclusion (el: elongated, euh: euhedral, rnd: round); L/V: volume fraction of the liquid (%). Reeq: decrepitation features (decr: decrepitated, imm; immature incluision, none: no visible features); Petro: petrography of inclusion (PS: pseudosecondary, S: secondary, P: primary); $Tm_{(initial)}$ beginning of melting; $Tm_{(final)}$ end of the melting interval; Thom: homogenization temperature; Mode: Mode of homogenization (L: homogenization into a liquid phase, V: homogenization into a vapor phase, crit: critical homogenization).

Sample	Piece #	Inc. #	Trail #	Host	Shape	Size(S)	Size(L)	L/V	Reeq.	Petro	$Tm_{(initial)}$	$Tm_{(final)}$	Thom	Mode
064-10S	A	7	2	anhydrite	euh.	2	4	30	none	P	NaN	-0.2	334.5	L
064-10S	A	8	2	anhydrite	euh.	2	2	20	none	P	NaN	-0.4	261.0	L
064-10S	A	9	2	anhydrite	euh.	1	1	30	none	P	NaN	-0.3	312.5	L
064-10S	A	10	2	anhydrite	el.	1	10	30	none	P	NaN	-0.3	334.0	L
064-10S	A	11	2	anhydrite	el.	1	9	50	decr.	P	NaN	-0.1	341.5	L
064-10S	A	12	3	anhydrite	euh.	4	8	30	none	P	NaN	-0.2	251.5	L
064-10S	A	13	3	anhydrite	euh.	3	10	20	none	P	NaN	-0.3	304.5	L
064-10S	A	14	3	anhydrite	euh.,el.	2	12	20	none	P	NaN	-0.4	310.0	L
064-10S	A	15	3	anhydrite	euh.	2	4	20	none	P	NaN	-0.6	NaN	NaN
064-10S	A	16	3	anhydrite	euh.	4	10	30	none	P	NaN	-0.4	NaN	NaN
064-10S	A	17	3	anhydrite	euh.	4	5	20	decr.	P	NaN	-0.4	311.0	L
064-10S	A	18	4	anhydrite	euh.	2	3	20	none	P	NaN	-0.4	303.0	L
064-10S	A	19	4	anhydrite	euh.	3	4	30	none	P	NaN	-0.3	307.0	L
064-10S	A	20	4	anhydrite	euh.	2	7	30	none	P	NaN	-0.1	334.0	L
064-10S	A	21	4	anhydrite	euh.	1	3	30	none	P	NaN	-0.2	341.0	L
064-10S	B	1	1	anhydrite	rnd.	4	4	20	none	S	-4.9	-3.2	258.5	L
064-10S	B	2	1	anhydrite	euh.	2	2	30	none	S	NaN	-2.6	260.0	L
064-10S	B	3	1	anhydrite	euh.	2	5	30	none	S	NaN	-1.5	262.5	L
064-10S	B	4	1	anhydrite	euh.	2	2	20	none	S	NaN	-2.2	257.0	L
064-10S	B	5	1	anhydrite	irr.	3	10	30	decr.	S	NaN	-1.4	304.0	L
064-10S	B	6	1	anhydrite	euh.	3	5	20	decr.	S	NaN	-1.9	257.5	L
064-10S	B	7	1	anhydrite	euh.	3	8	30	decr.	S	NaN	-2.2	258.5	L
064-10S	B	8	1	anhydrite	euh.	2	3	20	none	S	NaN	-2.4	258.5	L
064-10S	B	9	1	anhydrite	rnd.	1	1	20	none	S	NaN	-2.6	254.0	L
064-10S	B	10	1	anhydrite	rnd.	1	1	20	none	S	NaN	-2.0	253.0	L
064-10S	B	11	1	anhydrite	rnd.	1	1	20	none	S	NaN	-1.9	250.0	L
064-10S	B	12	1	anhydrite	euh.	3	4	20	none	S	NaN	-1.6	254.0	L
064-10S	B	13	1	anhydrite	euh.	3	10	20	decr.	S	NaN	NaN	256.5	L
064-10S	B	14	1	anhydrite	euh.	2	3	20	none	S	NaN	NaN	258.0	L
064-10S	B	15	1	anhydrite	euh.	3	5	20	none	P	NaN	-2.0	255.0	L

Appendix 6.A1: Fluid inclusion raw data. Trail #: Marks indiv. trails or groups of incluions; Host: Host crystal; Shape: shape of inclusion (el: elongated, euh: euhedral, rnd: round); L/V: volume fraction of the liquid (%). Reeq: decrepitation features (decr: decrepitated, imm; immature incluision, none: no visible features); Petro: petrography of inclusion (PS: pseudosecondary, S: secondary, P: primary); $Tm_{(initial)}$ beginning of melting; $Tm_{(final)}$ end of the melting interval; Thom: homogenization temperature; Mode: Mode of homogenization (L: homogenization into a liquid phase, V: homogenization into a vapor phase, crit: critical homogenization).

Sample	Piece #	Inc. #	Trail #	Host	Shape	Size(S)	Size(L)	L/V	Reeq.	Petro	$Tm_{(initial)}$	$Tm_{(final)}$	Thom	Mode
064-10S	B	16	1	anhydrite	euh.	2	2	20	none	S	NaN	NaN	255.0	L
067-14R	A	1	1	anhydrite	rnd.	3	3	20	none	P	NaN	-2.0	299.0	L
067-14R	A	2	2	anhydrite	irr.	8	10	30	none	P	NaN	-2.0	300.5	L
067-14R	A	3	3	anhydrite	el.,rnd.	4	20	30	none	S	6.1	-2.1	300.0	L
067-14R	A	4	3	anhydrite	el.	2	4	30	none	S	5.2	NaN	297.5	L
067-14R	A	5	3	anhydrite	el.	1	20	60	none	S	NaN	-2.6	296.0	L
067-14R	A	6	3	anhydrite	el.	1	25	30	none	S	NaN	-2.4	287.0	L
067-14R	A	7	3	anhydrite	el.	4	20	20	none	S	NaN	NaN	298.0	L
067-14R	A	8	2	anhydrite	irr.,el.	4	30	20	none	S	NaN	-1.9	300.0	L
067-14R	A	9	3	anhydrite	el.,euh.	3	10	20	none	S	NaN	NaN	302.5	L
067-14R	B	1	4	anhydrite	el.,rnd.	5	18	60	none	P	NaN	-1.9	NaN	NaN
067-14R	B	2	5	anhydrite	el.,rnd.	20	95	20	none	P	NaN	-1.8	297.0	L
067-14R	B	3	6	anhydrite	irr.,euh.	20	45	20	none	P	NaN	-1.2	346.2	L
067-14R	C	1	7	anhydrite	el,.euh.	4	15	30	none	P	NaN	-2.3	286.0	L
067-14R	C	2	7	anhydrite	euh.	3	5	30	none	P	NaN	-2.4	285.5	L
067-14R	D	1	8	anhydrite	euh.,irr.	15	30	30	none	P	NaN	-2.0	270.0	L
067-14R	D	2	8	anhydrite	euh.	55	60	50	none	P	NaN	-3.0	NaN	NaN
067-14R	D	3	8	anhydrite	el.,euh.	4	25	20	none	P	NaN	-2.0	286.0	L
067-14R	E	1	9	anhydrite	euh.,el.	4	15	30	none	P	NaN	-2.2	284.5	L
081-1S	A	1	1	barite	euh.	1	2	10		P		-1.9	NaN	NaN
081-1S	A	2	2	barite	irr.	14	20	20		P		-1.9	NaN	NaN
081-1S	A	3	3	barite	euh.	2	4	40		P		NaN	NaN	NaN
081-1S	A	4	4	barite	euh.	2	4	10		P		-2.6	253.0	L
081-1S	A	5	4	barite	euh.,el.	2	7	10		P		-2.0	214.0	L
081-1S	A	6	4	barite	irr.	2	4	NaN		P	-6.9	-2.1	195.0	L
081-1S	A	7	4	barite	irr.	3	5	10	decr.	P		-2.2	186.5	L
081-1S	A	8	5	barite	euh.,el.	1	6	10		P		NaN	220.5	L
081-1S	A	9	6	barite	euh..el.	1	4	10		P		-2.3	175.5	L
081-1S	B	1	1	anhydrite	euh.,el.	2	12	20	decr.	P		-2.4	260.0	L
081-1S	B	2	1	anhydrite	euh.	2	3	20		P		-2.2	265.5	L

Appendix 6.A1: Fluid inclusion raw data. Trail #: Marks indiv. trails or groups of incluions; Host: Host crystal; Shape: shape of inclusion (el: elongated, euh: euhedral, rnd: round); L/V: volume fraction of the liquid (%). Reeq: decrepitation features (decr: decrepitated, imm; immature incluision, none: no visible features); Petro: petrography of inclusion (PS: pseudosecondary, S: secondary, P: primary); $Tm_{(initial)}$ beginning of melting; $Tm_{(final)}$ end of the melting interval; Thom: homogenization temperature; Mode: Mode of homogenization (L: homogenization into a liquid phase, V: homogenization into a vapor phase, crit: critical homogenization).

Sample	Piece #	Inc. #	Trail #	Host	Shape	Size(S)	Size(L)	L/V	Reeq.	Petro	$Tm_{(initial)}$	$Tm_{(final)}$	Thom	Mode
081-1S	B	3	2	anhydrite	euh.	5	7	20		P		-2.5	NaN	NaN
081-1S	B	4	2	anhydrite	euh.	3	5	20		P		-2.5	264.5	L
081-1S	B	5	2	anhydrite	irr.	5	10	20		P		-2.2	255.5	L
081-1S	B	6	2	anhydrite	euh.	5	11	20		P		-1.9	223.5	L
081-1S	B	7	2	anhydrite	euh.	4	9	20	decr.	P		-2.3	250.0	L
081-1S	B	8	2	anhydrite	euh.	2	3	20		P		-1.9	213.0	L
081-1S	B	9	2	anhydrite	euh.,el.	2	6	20		P		-2.4	260.5	L
081-1S	B	10	2	anhydrite	euh.,el.	1	5	20		P		-2.2	205.5	L
081-1S	B	11	3	anhydrite	euh.	1	1	30		P		-2.1	222.5	L
081-1S	B	12	3	anhydrite	euh.	0.5	0.5	20		P		-2.1	209.0	L
081-1S	B	13	3	anhydrite	euh.	2	5	20		P		-1.9	254.0	L
081-1S	B	14	3	anhydrite	euh.	4	4	20		P		-2.5	245.0	L
081-1S	B	15	3	anhydrite	euh.	2	4	20		P		-2.3	252.0	L
081-1S	B	16	3	anhydrite	euh.	2	4	20		P		-2.2	208.0	L
081-1S	B	17	3	anhydrite	euh.	2	5	20		P		-1.9	210.5	L
081-1S	B	18	4	anhydrite	euh.	3	15	20		P		-1.9	225.0	L
081-1S	B	19	4	anhydrite	euh.	1	5	20		P		-1.9	211.5	L
081-1S	B	20	4	anhydrite	euh.	1	2	20		P		-1.9	282.0	L
081-1S	B	21	4	anhydrite	euh.	1	3	20		P		-2.4	213.0	L
081-1S	B	22	4	anhydrite	euh.	2	2	30		P		-2.1	294.0	L
081-1S	B	23	4	anhydrite	euh.	1	2	20		P		-1.9	290.0	L
081-1S	B	24	4	anhydrite	euh.	1	2	20		P		-2.0	288.0	L
081-1S	B	25	4	anhydrite	euh..el.	1	3	20		P		-2.4	293.0	L
081-1S	B	26	4	anhydrite	euh.	12	3	20		P		-2.0	223.0	L
081-1S	B	27	4	anhydrite	euh.	1	4	20		P		-1.9	201.0	L
081-1S	B	28	4	anhydrite	euh.,el.	3	40	20		P		-1.7	223.0	L
081-1S	B	29	4	anhydrite	euh.,el.	2	18	20		P		1.8	278.0	L
081-1S	B	30	4	anhydrite	euh.,el.	3	12	20		P		-1.8	NaN	NaN
081-6R	A	1	1	Qz?	rnd.	3	5	30	decr.	S	NaN	-2.1	298.0	L
081-6R	A	2	1	Qz?	euh.	2	5	20	decr.	S	NaN	-1.9	318.0	L

Appendix 6.A1: Fluid inclusion raw data. Trail #: Marks indiv. trails or groups of incluions; Host: Host crystal; Shape: shape of inclusion (el: elongated, euh: euhedral, rnd: round); L/V: volume fraction of the liquid (%). Reeq: decrepitation features (decr: decrepitated, imm; immature incluision, none: no visible features); Petro: petrography of inclusion (PS: pseudosecondary, S: secondary, P: primary); $Tm_{(initial)}$ beginning of melting; $Tm_{(final)}$ end of the melting interval; Thom: homogenization temperature; Mode: Mode of homogenization (L: homogenization into a liquid phase, V: homogenization into a vapor phase, crit: critical homogenization).

Sample	Piece #	Inc. #	Trail #	Host	Shape	Size(S)	Size(L)	L/V	Reeq.	Petro	$Tm_{(initial)}$	$Tm_{(final)}$	Thom	Mode
081-6R	A	3	1	Qz?	irr.	5	5	40	decr.	S	NaN	-2.1	330.0	L
081-6R	A	4	2	Qz?	rnd.	2	3	20	none	S	NaN	-1.9	323.0	L
081-6R	A	5	2	Qz?	irr.	4	15	40	decr.	S	NaN	-2.2	313.0	L
081-6R	A	6	2	Qz?	euh.	4	6	20	none	S	NaN	-2.4	315.0	V
081-6R	A	7	1	Qz?	euh.	4	5	NaN	none	S	NaN	NaN	NaN	NaN
081-6R	B	1	1	Qz	irr.	3	15	60	decr.	S	NaN	-3.0	344.5	L
081-6R	B	2	1	Qz	irr.	5	5	80	decr.	S	NaN	-0.6	329.0	L
081-6R	B	3	1	Qz	irr.	4	8	60	decr.	S	NaN	-2.7	332.0	L
081-6R	B	4	1	Qz	el.	2	7	20	decr.	S	NaN	-2.7	328.5	L
081-6R	B	5	1	Qz	irr.	3	6	20	decr.	S	NaN	-2.7	323.0	L
081-6R	B	6	1	Qz	irr.	6	8	60	decr.	S	NaN	-1.2	329.0	L
081-6R	B	7	1	Qz	irr.	8	8	40	decr.	S	NaN	-2.5	329.5	L
081-6R	B	8	1	Qz	irr.	8	15	40	decr.	S	NaN	-0.8	315.0	L
081-6R	B	9	1	Qz	euh.	2	6	20	decr.	S	NaN	-2.0	330.5	L
081-6R	C	1	1	Qz?	euh.	2	8	10		P	NaN	NaN	NaN	NaN
081-6R	C	2	2	Qz?	el.	3	10	30	decr.	S	NaN	-2.2	319.0	L
081-6R	C	3	2	Qz?	euh.	2	8	20	decr.	S	NaN	-2.0	315.0	L
081-6R	C	4	3	Qz?	euh.	4	4	30	decr.	P	NaN	NaN	NaN	NaN
085-6R1	A	1	1	barite	rnd.	2	2	20	none	PS	NaN	-1.0	241.0	L
085-6R1	A	2	1	barite	rnd.	2	3	20	none	PS	NaN	-1.0	239.0	L
085-6R1	A	3	1	barite	rnd.	2	3	20	none	PS	NaN	-1.0	234.5	L
085-6R1	A	4	1	barite	rnd.	1	2	20	none	PS	NaN	-0.9	242.0	L
085-6R1	A	5	1	barite	rnd.	1	2	20	none	PS	NaN	-1.1	242.0	L
085-6R1	A	6	1	barite	rnd.	1	2	20	none	PS	NaN	-1.0	241.0	L
085-6R1	A	7	1	barite	rnd.	1	2	20	none	PS	NaN	-1.0	242.5	L
085-6R1	A	8	1	barite	rnd.	1	2	20	none	PS	NaN	-1.0	242.5	L
085-6R1	A	9	1	barite	rnd.	2	3	20	none	PS	NaN	-1.0	223.0	L
085-6R1	A	10	1	barite	rnd.	2	3	20	none	PS	NaN	-1.0	242.0	L
085-6R1	A	11	1	barite	euh.	3	5	20	none	PS	NaN	-1.8	NaN	NaN
085-6R1	A	12	1	barite	euh.	8	10	40	none	PS	NaN	-0.8	NaN	NaN

Appendix 6.A1: Fluid inclusion raw data. Trail #: Marks indiv. trails or groups of incluions; Host: Host crystal; Shape: shape of inclusion.

Sample	Piece #	Inc. #	Trail #	Host	Shape	Size(S)	Size(L)	L/V	Reeq.	Petro	$Tm_{(initial)}$	$Tm_{(final)}$	Thom	Mode
085-6R1	A	13	1	barite	euh.	2	6	20	decr.	PS	NaN	-1.1	208.5	L
085-6R1	A	14	1	barite	euh.	5	8	60	none	PS	NaN	-1.7	NaN	NaN
085-6R1	A	15	1	barite	euh.	8	25	10	decr.	PS	NaN	-0.8	193.5	L
085-6R1	A	16	1	barite	rnd.	2	2	20	none	PS	NaN	-1.0	242.0	L
085-6R1	A	17	1	barite	rnd.	5	5	80	none	PS	NaN	-1.0	NaN	NaN
085-6R1	A	18	1	barite	euh.	10	12	NaN	decr.	PS	NaN	-1.0	NaN	NaN
085-6R1	A	19	1	barite	euh.,el.	4	15	NaN	none	PS	NaN	-1.3	207.5	L
085-6R1	A	20	1	barite	euh.	8	20	20	none	PS	NaN	-0.9	NaN	NaN
085-6R1	A	21	1	barite	euh.	10	15	20	none	PS	NaN	-0.9	NaN	NaN
085-6R1	A	22	1	barite	euh.	6	9	40	none	PS	NaN	-2.3	NaN	NaN
085-6R1	A	23	1	barite	irr.	6	7	20	none	PS	NaN	-0.7	NaN	NaN
085-6R1	A	24	1	barite	rnd.	4	5	NaN	none	PS	NaN	-0.8	NaN	NaN
085-6R1	A	25	1	barite	euh,	4	12	10	none	PS	NaN	-0.4	NaN	NaN
085-6R1	A	26	1	barite	rnd.	5	12	30	none	PS	NaN	-1.4	NaN	NaN
085-6R1	A	27	1	barite	rnd.	4	4	NaN	none	PS	NaN	NaN	NaN	NaN
085-6R1	A	28	1	barite	rnd.	5	6	NaN	none	PS	NaN	NaN	NaN	NaN
085-6R1	A	29	1	barite	euh.	5	7	20	none	PS	NaN	-1.2	NaN	NaN
085-6R1	A	30	1	barite	euh.	3	3	20	none	PS	NaN	0.0	NaN	NaN
085-6R1	A	31	1	barite	rnd.,el.	1	4	20	none	PS	NaN	-1.0	242.5	L
085-6R1	A	32	1	barite	rnd.,el.	1	5	20	none	PS	NaN	-1.0	234.5	L
085-6R1	A	33	1	barite	rnd.	3	8	20	none	PS	NaN	-1.0	242.5	L
085-6R1	A	34	1	barite	rnd.,el.	1	3	20	none	PS	NaN	-0.9	242.0	L
085-6R1	A	35	1	barite	rnd.,el.	1	6	20	decr.	PS	NaN	-1.0	174.0	L
085-6R1	A	36	1	barite	irr.	4	8	20	none	PS	NaN	-1.1	NaN	NaN
085-6R1	A	37	1	barite	euh.	10	18	20	none	PS	NaN	-0.4	NaN	NaN
085-6R1	A	38	1	barite	rnd.	1	3	20	none	PS	NaN	-1.0	242.5	L
085-6R1	A	39	1	barite	irr.	6	16	20	none	PS	NaN	-1.0	235.5	L
085-6R1	A	40	1	barite	rnd.	1	2	20	none	PS	NaN	-1.2	252.5	L
085-6R1	A	41	1	barite	rnd.	1	3	20	decr.	PS	NaN	-0.9	145.5	L
085-6R1	A	42	1	barite	euh.	4	5	10	none	PS	NaN	-0.8	NaN	NaN
085-6R1	A	43	2	barite	rnd.	2	2	20	none	S	NaN	-1.0	NaN	NaN
085-6R1	A	44	2	barite	rnd.,el.	1	4	20	none	S	NaN	-1.3	187.5	L

Appendix 6.A1: Fluid inclusion raw data. Trail #: Marks indiv. trails or groups of incluions; Host: Host crystal; Shape: shape of inclusion (el: elongated, euh: euhedral, rnd: round); L/V: volume fraction of the liquid (%). Reeq: decrepitation features (decr: decrepitated, imm; immature incluision, none: no visible features); Petro: petrography of inclusion (PS: pseudosecondary, S: secondary, P: primary); $Tm_{(initial)}$ beginning of melting; $Tm_{(final)}$ end of the melting interval; Thom: homogenization temperature; Mode: Mode of homogenization (L: homogenization into a liquid phase, V: homogenization into a vapor phase, crit: critical homogenization).

Sample	Piece #	Inc. #	Trail #	Host	Shape	Size(S)	Size(L)	L/V	Reeq.	Petro	$Tm_{(initial)}$	$Tm_{(final)}$	Thom	Mode
085-6R1	A	45	2	barite	rnd.	2	2	20	none	S	NaN	NaN	241.5	L
085-6R1	A	46	2	barite	rnd.	2	2	20	none	S	NaN	-1.0	241.0	L
085-6R1	A	47	2	barite	rnd.	2	3	20	none	S	NaN	-1.0	242.0	L
085-6R1	A	48	2	barite	rnd.	2	3	20	none	S	NaN	-1.4	242.0	L
085-6R1	A	49	3	barite	euh.,el.	10	65	50	none	P	NaN	-0.8	NaN	NaN
085-6R1	A	50	3	barite	euh.	11	14	20	none	P	NaN	-0.9	242.0	L
085-6R1	A	51	3	barite	euh.	5	8	20	none	P	NaN	-1.0	242.0	L
085-6R1	A	52	1	barite	euh.	20	30	20	none	PS	NaN	-1.0	278.5	L
085-6R1	A	53	1	barite	rnd.,el.	2	8	20	decr.	PS	NaN	-1.4	286.0	L
085-6R1	B	1	1	anhydrite	rnd.	3	5	20	none	P	-2.2	-1.1	187.0	L
085-6R1	B	2	2	anhydrite	irr.,el.	7	43	20	decr.	P		-1.0	245.5	L
085-6R1	B	3	2	anhydrite	euh.	5	7	20	none	P		-1.0	248.5	L
085-6R1	B	4	3	anhydrite	euh.	5	6	10	none	P		-1.2	197.0	L
085-6R1	B	5	3	anhydrite	euh.	5	7	10	none	P		-1.4	240.5	L
085-6R1	B	6	3	anhydrite	euh.	7	7	10	decr.	P		-1.3	NaN	L
085-6R1	B	7	3	anhydrite	rnd.,el.	2	5	20	none	P		-0.9	191.0	L
085-6R1	B	8	3	anhydrite	rnd.,el.	2	6	20	decr.	P		-1.2	234.0	L
085-6R1	B	9	3	anhydrite	rnd.	4	7	20	none	P		-1.1	227.0	L
085-6R1	B	10	3	anhydrite	el.	1	4	10	none	P		NaN	NaN	NaN
085-6R1	B	11	3	anhydrite	el.	2	5	10	none	P		-1.4	236.0	L
085-6R1	B	12	4	anhydrite	irr.,el.	3	15	20	none	PS		-1.0	236.5	L
085-8R	A	1	1	barite	rnd.,el.	2	5	30	none	S	NaN	-1.5	NaN	NaN
085-8R	A	2	1	barite	rnd..el.	2	6	10	none	S	-6.4	-2.3	NaN	NaN
085-8R	A	3	2	barite	rnd.	1	2	20	none	PS	NaN	-2.2	188.0	L
085-8R	A	4	2	barite	rnd.	1	2	20	decr.	PS	NaN	-1.0	227.5	L
085-8R	A	5	2	barite	rnd.	1	2	20	decr.	PS	NaN	-2.2	NaN	NaN
085-8R	A	6	2	barite	rnd.	1	1	20	none	PS	NaN	-0.5	203.0	L
085-8R	A	7	2	barite	rnd.	1	1	20	none	PS	NaN	NaN	NaN	NaN
085-8R	A	8	2	barite	irr.,el.	1	7	20	decr.	PS	NaN	-2.3	206.5	L
085-8R	A	9	2	barite	rnd.	1	2	20	none	PS	NaN	NaN	255.5	L

Appendix 6.A1: Fluid inclusion raw data. Trail #: Marks indiv. trails or groups of incluions; Host: Host crystal; Shape: shape of inclusion (el: elongated, euh: euhedral, rnd: round); L/V: volume fraction of the liquid (%). Reeq: decrepitation features (decr: decrepitated, imm; immature incluision, none: no visible features); Petro: petrography of inclusion (PS: pseudosecondary, S: secondary, P: primary); $Tm_{(initial)}$ beginning of melting; $Tm_{(final)}$ end of the melting interval; Thom: homogenization temperature; Mode: Mode of homogenization (L: homogenization into a liquid phase, V: homogenization into a vapor phase, crit: critical homogenization).

Sample	Piece #	Inc. #	Trail #	Host	Shape	Size(S)	Size(L)	L/V	Reeq.	Petro	$Tm_{(initial)}$	$Tm_{(final)}$	Thom	Mode
085-8R	A	10	2	barite	rnd.	1	2	20	none	PS	NaN	-0.9	251.5	L
085-8R	A	11	3	barite	rnd.	2	2	20	none	PS	NaN	-3.1	218.0	L
085-8R	A	12	3	barite	rnd.	1	2	20	none	PS	NaN	-2.4	218.5	L
085-8R	A	13	3	barite	euh.	2	4	20	none	PS	NaN	NaN	235.0	L
085-8R	A	14	3	barite	rnd.	1	2	20	none	PS	NaN	-2.4	213.5	L
085-8R	A	15	3	barite	euh.	1	2	20	decr.	PS	NaN	NaN	233.0	L
085-8R	A	16	3	barite	euh.	2	3	20	decr.	PS	NaN	NaN	232.0	L
085-8R	A	17	3	barite	euh.	3	4	20	decr.	PS	NaN	-1.9	216.0	L
085-8R	A	18	3	barite	euh.	3	4	20	none	PS	NaN	-1.2	246.5	L
085-8R	A	19	3	barite	euh.	4	5	20	none	PS	NaN	-1.9	254.5	L
085-8R	A	20	3	barite	rnd.	1	2	20	none	PS	NaN	-2.6	185.5	L
085-8R	A	21	3	barite	rnd.	2	2	20	none	PS	NaN	-1.8	158.5	L
085-8R	A	22	3	barite	irr.,rnd.	1	2	20	none	PS	NaN	-0.5	162.0	L
085-8R	A	23	3	barite	rnd.	1	2	100	none	PS	NaN	-3.1	NaN	NaN
085-8R	A	24	3	barite	rnd.	1	1	20	none	PS	NaN	-2.9	NaN	NaN
085-8R	A	25	3	barite	rnd.	1	1	20	none	PS	NaN	-2.3	181.0	L
085-8R	A	26	3	barite	rnd.	2	2	20	none	PS	NaN	-2.1	164.5	L
085-8R	A	27	3	barite	irr.	2	3	20	decr.	PS	NaN	-0.9	178.5	L
085-8R	A	28	3	barite	rnd.	2	2	80	none	PS	NaN	-0.5	185.0	L
085-8R	B	1	1	barite	euh.	5	14	10	decr.	P	NaN	-2.0	178.5	L
085-8R	B	2	1	barite	euh.	5	10	20	decr.	P	NaN	-1.9	184.0	L
085-8R	B	3	1	barite	irr.	5	5	20	none	P	NaN	-2.2	201.0	L
085-8R	B	4	1	barite	irr.	2	5	20	none	P	NaN	-0.9	NaN	L
085-8R	B	5	1	barite	euh.	2	4	10	none	P	NaN	-1.9	172.0	L
085-8R	B	6	1	barite	irr.	3	9	10	none	P	NaN	-1.9	NaN	L
085-8R	B	7	1	barite	irr.	5	10	100	decr.	P	NaN	-5.7	NaN	L
085-8R	B	8	1	barite	irr.,el.	1	9	10	none	P	NaN	-1.9	192.5	L
085-8R	B	9	1	barite	euh.	2	3	20	none	P	NaN	-1.9	181.0	L
085-8R	B	10	1	barite	euh.	4	5	10	none	P	NaN	-1.8	175.5	L
J2-1038-13-R8	A	1	1	anhydrite	euh.	3	7	30	none	PS	NaN	-2.0	294.5	L

Appendix 6.A1: Fluid inclusion raw data. Trail #: Marks indiv. trails or groups of incluions; Host: Host crystal; Shape: shape of inclusion (el: elongated, euh: euhedral, rnd: round); L/V: volume fraction of the liquid (%). Reeq: decrepitation features (decr: decrepitated, imm; immature incluision, none: no visible features); Petro: petrography of inclusion (PS: pseudosecondary, S: secondary, P: primary); $Tm_{(initial)}$ beginning of melting; $Tm_{(final)}$ end of the melting interval; Thom: homogenization temperature; Mode: Mode of homogenization (L: homogenization into a liquid phase, V: homogenization into a vapor phase, crit: critical homogenization).

Sample	Piece #	Inc. #	Trail #	Host	Shape	Size(S)	Size(L)	L/V	Reeq.	Petro	$Tm_{(initial)}$	$Tm_{(final)}$	Thom	Mode
J2-1038-13-R8	A	2	1	anhydrite	el.	1	11	80	none	PS	NaN	NaN	NaN	NaN
J2-1038-13-R8	A	3	1	anhydrite	euh.	2	5	30	none	PS	NaN	-2.0	281.0	L
J2-1038-13-R8	A	4	1	anhydrite	euh.	1	3	30	none	PS	NaN	-2.3	279.0	L
J2-1038-13-R8	A	5	1	anhydrite	euh.	10	35	40	decr.	PS	NaN	NaN	NaN	NaN
J2-1038-13-R8	A	6	1	anhydrite	el.	4	21	60	none	PS	NaN	-5.0	NaN	NaN
J2-1038-13-R8	A	7	1	anhydrite	euh.	4	7	40	none	PS	NaN	-3.5	NaN	NaN
J2-1038-13-R8	A	8	1	anhydrite	euh.	3	5	30	none	PS	NaN	-2.3	286.5	L
J2-1038-13-R8	A	9	1	anhydrite	euh.	5	9	30	none	PS	NaN	-2.0	290.0	L
J2-1038-13-R8	A	10	1	anhydrite	euh.	4	6	30	none	PS	NaN	-2.0	289.0	L
J2-1038-13-R8	A	11	1	anhydrite	euh.	5	6	20	none	PS	NaN	-2.0	289.0	L
J2-1038-13-R8	B	1	1	anhydrite	rnd.	5	28	30	decr.	PS	NaN	-1.9	284.0	L
J2-1038-13-R8	B	2	1	anhydrite	rnd.	4	8	30	none	PS	NaN	-2.0	287.0	L
J2-1038-13-R8	B	3	1	anhydrite	rnd.	3	10	30	decr.	PS	NaN	-1.9	283.5	L
J2-1038-13-R8	B	4	1	anhydrite	rnd.	4	6	30	none	PS	NaN	-1.9	287.0	L
J2-1038-13-R8	B	5	1	anhydrite	euh.	3	4	30	decr.	PS	NaN	-1.9	288.0	L
J2-1038-13-R8	B	6	1	anhydrite	rnd.	3	7	20	none	PS	NaN	-2.1	291.5	L
J2-1038-13-R8	B	7	2	anhydrite	euh.	4	15	20	none	PS	NaN	-2.0	289.0	L
J2-1038-13-R8	B	8	2	anhydrite	euh.	2	3	30	none	PS	NaN	-2.0	280.0	L
J2-1038-13-R8	B	9	2	anhydrite	rnd.	1	4	20	none	PS	NaN	-2.0	280.0	L
J2-1038-13-R8	B	10	2	anhydrite	euh.	2	2	30	none	PS	NaN	-2.1	283.5	L
J2-1038-13-R8	B	11	3	anhydrite	rnd.,el.	6	30	10	none	PS	NaN	-1.9	290.0	L
J2-1038-13-R8	B	12	3	anhydrite	rnd.,el.	5	18	30	none	PS	NaN	-2.0	286.0	L
J2-1038-13-R8	B	13	3	anhydrite	irr.,rnd.	5	10	80	none	PS	NaN	-4.2	292.5	L
J2-1038-13-R8	B	14	3	anhydrite	euh.	2	6	30	none	PS	NaN	-2.0	284.0	L
J2-1038-13-R8	B	15	3	anhydrite	euh.	3	5	30	none	PS	NaN	-1.9	289.5	L
J2-1038-13-R8	B	16	3	anhydrite	euh.	2	3	60	none	PS	NaN	-2.0	285.5	L
J2-1038-13-R8	B	17	3	anhydrite	irr.,rnd.	5	10	60	none	PS	NaN	-1.9	NaN	NaN
J2-1038-13-R8	B	18	3	anhydrite	euh.	3	4	30	none	PS	NaN	-2.0	298.5	L
J2-1038-13-R8	B	19	3	anhydrite	euh.	2	3	30	none	PS	NaN	-2.0	287.0	L

Appendix 6.A1: Fluid inclusion raw data. Trail #: Marks indiv. trails or groups of incluions; Host: Host crystal; Shape: shape of inclusion (el: elongated, euh: euhedral, rnd: round); L/V: volume fraction of the liquid (%). Reeq: decrepitation features (decr: decrepitated, imm; immature incluision, none: no visible features); Petro: petrography of inclusion (PS: pseudosecondary, S: secondary, P: primary); $Tm_{(initial)}$ beginning of melting; $Tm_{(final)}$ end of the melting interval; Thom: homogenization temperature; Mode: Mode of homogenization (L: homogenization into a liquid phase, V: homogenization into a vapor phase, crit: critical homogenization).

Sample	Piece #	Inc. #	Trail #	Host	Shape	Size(S)	Size(L)	L/V	Reeq.	Petro	$Tm_{(initial)}$	$Tm_{(final)}$	Thom	Mode
J2-1038-13-R8	B	21	3	anhydrite	el.	2	12	20	none	PS	NaN	-1.9	284.0	L
J2-1038-13-R8	B	22	3	anhydrite	irr.	6	18	30	none	PS	NaN	-1.9	291.5	L
J2-1038-13-R8	C	1	1	anhydrite	euh.	4	7	20	none	P	NaN	-2.0	288.0	L
J2-1038-13-R8	C	2	1	anhydrite	euh.	3	3	30	none	P	NaN	-1.9	287.5	L
J2-1038-13-R8	C	3	1	anhydrite	euh.	2	3	30	decr.	P	NaN	-2.2	287.0	L
J2-1038-13-R8	C	4	2	anhydrite	euh.	5	6	30	decr.	PS	NaN	-2.0	279.0	L
J2-1038-13-R8	C	5	2	anhydrite	euh.	2	5	30	none	PS	NaN	-1.9	282.0	L
J2-1038-13-R8	C	6	2	anhydrite	euh.	2	5	30	decr.	PS	NaN	-2.0	284.5	L
J2-1038-13-R8	C	7	2	anhydrite	euh.	2	2	30	none	PS	NaN	-2.0	283.0	L
J2-1038-13-R8	C	8	2	anhydrite	euh.	1	2	30	none	PS	NaN	-2.1	282.5	L
J2-1039-14-CH2	A	1	1	barite	euh.,irr.	12	20	20	none	P	NaN	-1.9	NaN	NaN
J2-1039-14-CH2	A	2	1	barite	euh.,irr.	5	8	20	none	P	NaN	-2.0	NaN	NaN
J2-1039-14-CH2	A	3	2	barite	euh.,irr.	8	25	20	none	P	NaN	-1.9	249.5	L
J2-1039-14-CH2	A	4	3	barite	euh.,irr.	20	30	20	none	P	NaN	-2.0	229.0	L
J2-1039-14-CH2	A	5	3	barite	euh.,irr.	6	13	20	none	P	NaN	-2.2	NaN	NaN
J2-1039-14-CH2	A	6	3	barite	euh.,irr.	3	6	20	none	P	-2.4	-1.9	258.0	L
J2-1039-14-CH2	A	7	4	barite	euh.	2	5	10	none	P	NaN	-2.1	181.5	L
J2-1039-14-CH2	A	8	4	barite	euh.	4	5	10	none	P	NaN	-2.3	184.5	L
J2-1039-14-CH2	A	9	4	barite	euh.,el.	2	9	10	decr.	P	NaN	-1.9	240.0	L
J2-1039-14-CH2	A	10	4	barite	euh.	2	2	30	decr.	S	NaN	-2.0	289.0	L
J2-1039-14-CH2	A	11	4	barite	el.	1	5	10	decr.	S	-3.6	-2.6	202.0	L
J2-1039-14-CH2	A	12	4	barite	euh.	4	5	20	none	P	NaN	NaN	185.0	V
J2-1039-14-CH2	B	1	1	barite	euh.,el.	4	12	20	decr.	P	-2.4	-2.2	253.0	L
J2-1039-14-CH2	B	2	2	barite	euh.,irr.	15	20	20	none	P	NaN	-2.0	201.5	L
J2-1039-14-CH2	B	3	3	barite	euh.,irr.	8	15	20	none	P	NaN	-2.2	247.0	L
J2-1039-14-CH2	B	4	3	barite	euh.	2	4	60	decr.	P	-2.7	-2.2	182.5	L
J2-1039-14-CH2	B	5	3	barite	euh.	4	7	60	none	P	-2.6	-2.2	135.5	L
J2-1039-14-CH2	B	6	4	barite	euh.,irr.	12	50	20	none	PS	NaN	-2.0	197.0	L
J2-1039-14-CH2	B	7	4	barite	euh.	4	4	20	decr.	PS	NaN	-2.1	277.5	L
J2-1039-14-CH2	B	8	4	barite	euh.	4	6	60	decr.	PS	NaN	-2.0	228.0	L

Appendix 6.A1: Fluid inclusion raw data. Trail #: Marks indiv. trails or groups of incluions; Host: Host crystal; Shape: shape of inclusion (el: elongated, euh: euhedral, rnd: round); L/V: volume fraction of the liquid (%). Reeq: decrepitation features (decr: decrepitated, imm; immature incluision, none: no visible features); Petro: petrography of inclusion (PS: pseudosecondary, S: secondary, P: primary); $Tm_{(initial)}$ beginning of melting; $Tm_{(final)}$ end of the melting interval; Thom: homogenization temperature; Mode: Mode of homogenization (L: homogenization into a liquid phase, V: homogenization into a vapor phase, crit: critical homogenization).

Sample	Piece #	Inc. #	Trail #	Host	Shape	Size(S)	Size(L)	L/V	Reeq.	Petro	$Tm_{(initial)}$	$Tm_{(final)}$	Thom	Mode
J2-1039-14-CH2	B	9	4	barite	euh.,irr.	20	30	20	none	PS	NaN	-1.9	178.0	L
J2-1039-14-CH2	B	10	4	barite	euh.,irr.	15	40	20	none	PS	NaN	-1.9	171.0	L
J2-1039-17-R1	A	1	1	barite	irr.	4	7	20	decr.	S	NaN	-2.0	NaN	NaN
J2-1039-17-R1	A	2	1	barite	irr.	4	6	60	decr.	S	NaN	-1.0	NaN	NaN
J2-1039-17-R1	A	3	1	barite	irr.	3	3	10	decr.	S	NaN	0.0	283.0	L
J2-1039-17-R1	A	4	2	barite	euh.	1	3	20	decr.	PS	NaN	-2.8	279.5	L
J2-1039-17-R1	A	5	2	barite	irr.,el.	1	4	30	decr.	PS	NaN	-1.2	237.0	L
J2-1039-17-R1	A	6	2	barite	irr.,el.	1	6	20	decr.	PS	NaN	-2.4	231.0	L
J2-1039-17-R1	A	7	2	barite	el.	3	18	10	decr.	PS	-3.6	-2.0	211.0	L
J2-1039-17-R1	A	8	2	barite	euh.	5	10	30	decr.	PS	-7.6	-5.1	NaN	NaN
J2-1039-17-R1	A	9	2	barite	el.	2	18	30	decr.	PS	-3.7	-2.4	204.0	L
J2-1039-17-R1	A	10	2	barite	euh.	3	5	NaN	decr.	PS	NaN	-4.4	NaN	NaN
J2-1039-17-R1	A	11	2	barite	euh.	4	6	20	none	PS	NaN	-0.7	NaN	NaN
J2-1039-17-R1	A	12	2	barite	euh.	10	11	60	decr.	PS	NaN	-2.9	NaN	NaN
J2-1039-17-R1	A	13	3	barite	irr.	3	8	70	decr.	S	NaN	-4.4	NaN	NaN
J2-1039-17-R1	A	14	4	barite	euh.	2	4	10	none	P	NaN	-2.2	246.5	L
J2-1039-17-R1	A	15	3	barite	euh.	2	3	20	decr.	S	-6.0	-3.0	249.5	L
J2-1039-17-R1	A	16	3	barite	irr.,el.	2	3	20	decr.	S	NaN	-2.8	279.0	L
J2-1039-17-R1	A	17	3	barite	el.	1	5	20	none	S	NaN	-2.6	226.0	L
J2-1039-17-R1	A	18	3	barite	euh.	1	3	20	none	S	NaN	-2.6	280.5	L
J2-1039-17-R1	A	19	3	barite	euh.	2	4	40	decr.	S	NaN	-3.3	NaN	NaN
J2-1039-17-R1	B	1	1	barite	euh.	6	23	10	none	P	NaN	-0.5	NaN	NaN
J2-1039-17-R1	B	2	2	barite	irr.	4	8	10	none	PS	NaN	-2.3	239.5	L
J2-1039-17-R1	B	3	2	barite	irr.	3	5	10	none	PS	NaN	-2.3	218.5	L
J2-1039-17-R1	B	4	2	barite	euh.	3	8	10	decr.	PS	NaN	-2.4	227.0	L
J2-1039-17-R1	B	5	2	barite	euh.	4	16	10	decr.	PS	NaN	-2.3	274.0	L
J2-1039-17-R1	B	6	2	barite	rnd.	3	5	10	none	PS	-1.6	-1.5	NaN	NaN
J2-1039-17-R1	B	7	2	barite	rnd.	2	4	10	none	PS	NaN	-2.6	213.0	L
J2-1039-17-R1	B	8	2	barite	rnd.	2	4	10	none	PS	NaN	-1.9	163.0	L
J2-1039-17-R1	B	9	2	barite	irr.	2	8	20	decr.	PS	NaN	-2.2	261.0	V

Appendix 6.A1: Fluid inclusion raw data. Trail #: Marks indiv. trails or groups of incluions; Host: Host crystal; Shape: shape of inclusion (el: elongated, euh: euhedral, rnd: round); L/V: volume fraction of the liquid (%). Reeq: decrepitation features (decr: decrepitated, imm; immature incluision, none: no visible features); Petro: petrography of inclusion (PS: pseudosecondary, S: secondary, P: primary); $Tm_{(initial)}$ beginning of melting; $Tm_{(final)}$ end of the melting interval; Thom: homogenization temperature; Mode: Mode of homogenization (L: homogenization into a liquid phase, V: homogenization into a vapor phase, crit: critical homogenization).

Sample	Piece #	Inc. #	Trail #	Host	Shape	Size(S)	Size(L)	L/V	Reeq.	Petro	$Tm_{(initial)}$	$Tm_{(final)}$	Thom	Mode
J2-1039-17-R1	B	10	2	barite	irr.	4	8	20	decr.	PS	NaN	-2.3	NaN	NaN
J2-1039-17-R1	C	1	1	barite	euh.	14	20	20	none	PS	NaN	-1.9	204.0	L
J2-1039-17-R1	C	2	1	barite	euh.	8	15	20	none	PS	NaN	-1.0	NaN	NaN
J2-1039-17-R1	C	3	1	barite	irr.	5	20	20	none	PS	NaN	-1.6	234.5	L
J2-1039-17-R1	C	4	1	barite	euh.	4	6	20	none	PS	NaN	NaN	NaN	NaN
J2-1039-17-R1	C	5	1	barite	irr.	7	12	20	decr.	PS	NaN	-1.8	NaN	NaN
J2-1039-17-R1	C	6	1	barite	euh.	4	6	60	none	PS	-4.7	-1.9	234.0	L
J2-1039-17-R1	C	7	1	barite	euh.	4	4	NaN	none	PS	NaN	NaN	NaN	NaN
J2-1039-17-R1	C	8	2	barite	irr.	5	40	10	none	PS	NaN	-1.8	NaN	NaN
J2-1039-17-R1	C	9	1	barite	euh.	5	7	30	none	PS	NaN	NaN	NaN	NaN
J2-1039-17-R1	C	10	3	barite	euh.	2	4	10	none	P	NaN	-1.9	209.0	L
J2-1039-17-R1	C	11	1	barite	euh.	4	7	20	none	PS	NaN	-2.0	229.0	L
J2-1039-17-R1	C	12	1	barite	irr.	6	6	20	decr.	PS	NaN	-2.0	231.0	L
J2-1039-17-R1	D	1	1	barite	el.	5	95	10	decr.	P	NaN	-1.6	NaN	NaN
J2-1039-17-R1	D	2	2	barite	euh.	6	8	20	decr.	PS	NaN	NaN	NaN	NaN
J2-1039-17-R1	D	3	2	barite	euh.	4	8	20	decr.	PS	NaN	NaN	NaN	NaN
J2-1039-17-R1	D	4	3	barite	rnd.	6	17	10	decr.	PS	-6.8	-0.1	145.5	L
J2-1039-17-R1	D	5	3	barite	euh.	12	42	20	none	PS	NaN	-2.1	NaN	NaN
J2-1039-17-R1	D	6	3	barite	rnd.	7	14	30	none	PS	NaN	-2.0	204.0	L
J2-1039-17-R1	D	7	4	barite	euh.	7	30	10	decr.	P	NaN	-2.2	230.0	L
J2-1039-17-R1	D	8	4	barite	euh.	15	70	10	decr.	P	NaN	-2.0	194.0	L
J2-1039-17-R1	D	9	4	barite	euh.	5	18	20	decr.	P	NaN	-2.0	178.5	L
J2-1039-17-R1	D	10	4	barite	euh.	2	4	10	none	P	NaN	NaN	200.5	L
J2-1039-17-R1	D	11	4	barite	euh.	3	5	10	none	P	NaN	NaN	214.5	L
J2-1039-17-R1	E	1	1	barite	euh.	7	22	20	decr.	P	NaN	-1.5	NaN	NaN
J2-1039-17-R1	E	2	2	barite	euh.	6	12	20	none	P	NaN	-1.8	148.5	L
J2-1039-17-R1	E	3	3	barite	irr.	20	35	20	none	P	NaN	-1.9	NaN	NaN
J2-1039-17-R1	E	4	3	barite	irr.	3	9	60	none	P	NaN	-1.4	NaN	NaN
J2-1039-17-R1	E	5	3	barite	irr.	4	20	60	none	P	NaN	NaN	NaN	NaN
J2-1039-17-R1	E	6	3	barite	euh.	8	17	30	none	P	NaN	-2.0	NaN	NaN

Appendix 6.A1: Fluid inclusion raw data. Trail #: Marks indiv. trails or groups of incluions; Host: Host crystal; Shape: shape of inclusion (el: elongated, euh: euhedral, rnd: round); L/V: volume fraction of the liquid (%). Reeq: decrepitation features (decr: decrepitated, imm; immature incluision, none: no visible features); Petro: petrography of inclusion (PS: pseudosecondary, S: secondary, P: primary); $Tm_{(initial)}$ beginning of melting; $Tm_{(final)}$ end of the melting interval; Thom: homogenization temperature; Mode: Mode of homogenization (L: homogenization into a liquid phase, V: homogenization into a vapor phase, crit: critical homogenization).

Sample	Piece #	Inc. #	Trail #	Host	Shape	Size(S)	Size(L)	L/V	Reeq.	Petro	$Tm_{(initial)}$	$Tm_{(final)}$	Thom	Mode
J2-1039-17-R1	E	7	4	barite	euh.	3	7	60	decr.	PS	NaN	NaN	NaN	NaN
J2-1039-17-R1	E	8	4	barite	euh.	4	5	60	decr.	PS	NaN	-2.0	NaN	NaN
J2-1039-17-R1	E	9	4	barite	euh.	3	5	20	decr.	PS	NaN	-2.1	162.0	L
J2-1039-17-R1	E	10	4	barite	euh.	2	3	30	none	PS	NaN	-2.4	309.5	L
J2-1039-17-R1	E	11	4	barite	euh.	1	3	10	none	PS	NaN	-2.2	158.0	L
J2-1039-17-R1	E	12	4	barite	euh.	1	1	10	none	PS	NaN	-2.5	242.0	L
J2-1039-17-R1	E	13	4	barite	euh.	1	2	10	none	PS	NaN	-2.4	256.0	L
J2-1039-17-R1	E	14	4	barite	euh.	1	1	10	none	PS	NaN	-2.4	262.5	L
J2-1041-31-CH1	A	1	1	barite	euh.	4	6	20	none	P	-2.0	-1.5	224.0	L
J2-1041-31-CH1	A	2	1	barite	euh.	5	8	20	none	P	NaN	-2.1	225.5	L
J2-1041-31-CH1	A	3	1	barite	euh.	10	16	20	decr.	P	NaN	-2.3	NaN	NaN
J2-1041-31-CH1	A	4	1	barite	euh.	12	15	20	decr.	P	NaN	-2.3	225.0	L
J2-1041-31-CH1	A	5	1	barite	irr.	4	15	10	decr.	P	NaN	NaN	NaN	NaN
J2-1041-31-CH1	A	6	1	barite	irr.	5	18	10	decr.	P	NaN	-2.0	260.0	L
J2-1041-31-CH1	B	1	1	anhydrite	euh.,el.	6	30	10	none	PS	NaN	-1.3	160.0	L
J2-1041-31-CH1	B	2	1	anhydrite	euh.,el.	3	12	10	none	PS	NaN	-2.0	160.0	L
J2-1041-31-CH1	B	3	1	anhydrite	euh.,el.	4	4	20	none	PS	NaN	-1.9	181.5	L
J2-1041-31-CH1	B	4	1	anhydrite	euh.	5	12	20	none	PS	NaN	-1.9	201.0	L
J2-1041-31-CH1	B	5	1	anhydrite	euh.	3	3	30	none	PS	NaN	-2.0	NaN	NaN

7 Conclusions

This work provides new insights into the chemical composition of hydrothermal fluids circulating in the shallow crust of intraoceanic arcs. The analysis of a comprehensive sample collection of different rock types and vent fluids recovered during two seagoing expeditions sheds new light on the importance of various subsurface processes. In the following section the overall findings are listed. In this context, it is useful to break the boundaries of the self-contained chapters and look at individual processes from a different perspective.

Bulk chemical data for massive sulfide mineralization help to estimate where valuable sulfide deposits may form in the ocean. Our chemical and mineralogical analyses demonstrate that at Brothers Caldera high-grade polymetallic sulfides do form. This finding is already well established (Wright et al.,1998, de Ronde et al., 2005, Berkenbosch et al., 2012, 2015). Sulfide accumulations are particular rich in Cu. Cu deposits represent one main target for deep sea mining prospects. In overall, our investigations further suggest that accumulations are restricted to chimney structures and their debris. On the other hand, all samples from the stockwork zone beneath the North West Caldera Wall vent field appeared to be barren and do not contain significant amounts of Cu or Zn. If these samples were representative, it would mean that Brothers NW Caldera Wall is likely not the best target for deep sea mining prospects. However, this evaluation bases on only four samples of stockwork rocks and cannot ascertain this. During other research expedition enargite veins cutting the basement are reported at the NW Caldera wall (de Ronde et al., 2005) and suggests polymetallic sulfide deposits also to form in the deeper subsurface. In any case the North West Caldera Wall is a superb place to study processes of ore formation:

The reaction path models in this study suggest that subsurface mineral alteration and the formation of sulfide deposits in seawater-dominated hydrothermal systems is controlled by the extent of fluid-mineral reactions rather than temperature fluctuations or the compositional difference of rocks from individual volcanos. When fluids equilibrated with low water-to-rock ratios in the subsurface (w/r = 10) and subsequently mix with seawater they are predicted to precipitate Zn-rich mineralization. When fluids equilibrated with high water to rock ratio (w/r = 100) they are predicted to form Cu-rich sulfide deposits. These finding suggest that hydrothermal fluids below the Brothers NW Caldera Wall undergo varying degrees of alteration, with some fluids equilibrating more extensive with rocks than others do. The finding that chimneys contain both Zn and Cu mineralization suggests that the fluid circulation pattern temporally and spatially evolve. This finding may point to variable magmatic input leading to

varying degree of alteration which has already been pointed out in different studies (e.g. de Ronde et al., 2006; Gruen et al. 2012, 2014). On the other hand, this finding shows that the Cu-dominated mineralization is rather an outcome of a mature vent field with a basement that has extensively altered. This finding is supported by the pronounced magnetic anomaly found underneath the vent field (Caratori Tontini et al., 2012a, 2012b) and by age dating (^{226}Ra/Ba) that suggests chimneys to be up to 1200 years old (de Ronde et al., 2005).
For the generally Zn-rich mineralization in the vent field of Haungaroa my findings suggest the vent field to be rather immature but the occurrence of chalcopyrite and tennantite suggests that the circulation has proceeded for some time and pervasively altered rocks existing in some flow paths of the system.

Another outcome of this work is the likely presence of phase separations in the seawater-dominated vents at Brothers NW Caldera wall vent field. My extensive fluid inclusion study demonstrates that phase separation occurs during stockwork mineralization as well as during the formation of chimneys. The record of fluid inclusions demonstrates that a significant proportion of the vent fluids that have circulated at the vent field have been influenced by boiling in the shallow subsurface during crystal growth. This impression is underlined by vent fluid compositions, which show that the vent fluids were affected by boiling at the time of the two expeditions with RV Sonne (December/January 2016/2017) and RV Thompson (March 2018). During these expeditions no direct physical evidence for boiling was detected (eg. pulsing fluids exiting chimneys or measured temperatures that comply with the boiling curve at the corresponding pressure). This suggests that boiling has terminated somewhere below the seafloor before the ascending fluids reach the seafloor. The fluid inclusion record provides additional evidence here: Formation temperatures close to the boiling curve and salinities of nearly zero suggest that boiling fluids have definitely exited chimneys at times. Further I have conducted a, to my knowledge, new approach using formation temperatures and salinities in fluid inclusions and combined these data with ^{87}Sr/^{86}Sr isotope composition in the host crystals to evaluate state-of-the-art mixing models that account for all the three parameters. This approach bears down the problem that salinity and temperature data alone cannot clearly identify if fluid inclusions have formed during mixing of seawater with a shallow-subcritically phase separated fluid, or if deep-supercritical phase separation has generated the source fluid. The use of ^{87}Sr/^{86}Sr in the host crystals was a key parameter in addressing this question and lead to the conclusion that some fluid inclusions were likely formed from a mixture of a source fluid that had undergone supercritical phase separation with seawater. This fact has direct implication for the possible transport of metals from near the magmatic source to the seafloor, since supercritically phase separated fluids have an enhanced metal transport capacity. These

findings clearly demonstrate the overall importance of phase separation and attests previous findings of phase separations predicted in hydrodynamic models (Gruen et al. 2012, 2014) and of previous vent fluid investigations (de Ronde et al., 2003, Kleint et al., submitted to GCA). My reaction path models demonstrated the impact of SO_2 degassing on alteration pattern during subsurface fluid-mineral reactions and how effectively sulfur disproportionation reactions lead to enhanced metal leaching. With contribution of SO_2 under low water-to-rock ratios the reaction path models demonstrate how metals and alkalis and even fluid-immobile elements like Al are manifold enriched in the hydrothermal fluids interacting with basement rocks. Thereby the host rock is altered to an advanced argillic assemblage of quartz and alunite. The mixing path models predict that native sulfur, alunite and sphalerite precipitate among some sulfate minerals when these metal-rich fluids mix with seawater. During our expedition we did not find any kind of sulfide precipitation in close vicinity to vents of acid-sulfate type fluids. Instead all vent sites were covered with precipitation of native sulfur. This suggest that precipitation of sulfides does not occur when acid-sulfate type fluids emanate although the phases were thermodynamically stable. This ultimately means that the metal rich acid-sulfate fluids carry their dissolved-load of metals and alkalis directly into the ocean and that these vents have a strong impact on the chemistry of the water masses near these vents. These vents might hence produce metal-rich plumes, which is of special interest when vents are seated very shallow and plumes reach the photic zone. In the introduction of this work the relationship of hydrothermal circulation to the global heat budget and the corresponding element fluxes between the lithosphere and the ocean was presented. These calculations do not account for acid sulfate-type vents and their individual chemical character. The chemical-fluxes between the lithosphere and the ocean for these vents, related to their chemical impact, must be manifold higher than they are for black smoker type vents. If we want to better quantify the chemical budget of the ocean-lithosphere interface we ultimately have to consider these types of vent in our calculations. Especially, due to the fact that species like SO_4 or dissolved Mg, which are usually nearly completely removed in mid-ocean ridge hydrothermal fluids may here be highly enriched compared to seawater.

The analyses of volatiles in hydrothermal fluids show the variable character of magmatic degassing in island arcs. My estimation of the source composition of magmatic gases demonstrated that in the South Kermadec Arc degassing may occur CO_2 dominated as well as SO_2 dominated. A CO_2:SO_2 ratio of 24:1 at Haungaroas generally very CO_2-rich vent fluids suggests more or less degassing of pure CO_2, additionally enriched due to phase separation, with only small proportions of sulfur gas. Compared to this at Macauley Caldera the ratio CO_2:SO_2 amounts to 4:7. Here the volatile species exiting the magmatic system clearly seems

to be SO_2. The Brothers Cone sites behave similar to this and the average ratio of the mentioned gases add up to a ratio 1:1. However, in single fluid samples the ratio of the gases vary from 1:2 to 2:1, a considerable scatter. Our finding for Brothers Cone sites suggests that magma degassing of the two species occurs decoupled and varies on temporal and spatial scales. The overall finding is that degassing in the South Kermadec is very individual for the different volcanoes.

For the North West Caldera site, I found that the concentrations of dissolved gases are to large extents controlled by phase separation. Anti-correlation of Cl and most volatiles demonstrates that boiling of vent fluids in the sub-surface affect fluid chemistry. Moreover, I found that CO_2, the most abundant dissolved gas in the North West caldera wall, is even more eligible to plot along with other dissolved gases to uncover phase separation processes. For the North West Caldera wall vent field some samples do markedly fall out of the trend for phase separation. These samples either contain relatively high CO_2 and/or high SO_4 concentrations. I assume that these samples have been affected by magmatic degassing, similar to the Cone Sites. The difference is that the gas input here is subtle and does not majorly affect the phase relations of the hydrothermal fluids. This suggests that the classification of hydrothermal fluids in magmatic-volatile and seawater-dominated types has to be handled with care since a clear distinction is not always possible.

8 Outlook

In the frame of this work I presented new data sets of chemical compositions of volcanic rocks, intensively altered rocks and massive sulfide mineralization. After successful publication these data will be uploaded to global chemical databases (e.g. PANGAEA, PETDB) and provide other scientist the opportunity to extend global dataset and evaluate rock data in a broader context. Major element compositions of unaltered volcanics allow inferences about crustal thicknesses, depth of crustal magma reservoirs, assimilation processes and extent of differentiation (Stern, 2002; Best, 2003). Hence, these data will provide a piece of the puzzle for over regional evaluations of volcanic processes in the Kermadec arc and volcanic arcs in general. Especially $^{87}Sr/^{86}Sr$ data are valuable in geochemical analyses that assess deep lithospheric processes, like the element recycling in subduction zones. An understanding of these processes enables scientist not only to trace these recycling processes, but eventually even to investigate plate tectonic processes. In the Kermadec arc the alongside variation of geochemical tracers (e.g. $^{87}Sr/^{86}Sr$) in volcanic rocks demonstrates how the Hikurangi plateau has rotated/retreated southwards from its former position (Timm et al., 2014). Such insights

into regional tectonic processes in a larger framework impacts models for the global tectonic cycle and finally improve plate movement reconstructions.

For the assessment of volcaogenic-sulfide deposits I was not able to reproduce the formation of one mineralization type. Some chimneys are particularly Fe-rich and comprise of assemblages of pyrrhotite and pyrite. In this assessment I wanted to investigate the coupling between rock alteration in the subsurface and the potential of sulfide mineralization and used model-fluids created during approaches of subsurface reactions. Another attempt would be to use actual vent fluid compositions and test the influence of varying concentrations of dissolved gases on the formation of sulfides during mixing with seawater. Fouquet et al. (2018) mention abundant pyrrhotite mineralization in sulfide precipitates from the Kulo Lasi Caldera. Here vent fluids contain milli-molar concentrations of H_2. This concentration is 10-100-fold enriched compared to Brothers NW Caldera wall vent fluids and likely responsible for formation of pyrrhotite. These models could help to find out if H_2 also at the Brothers NW Caldera wall vent field have been considerably higher in the past.

The newly developed fluid inclusion approach using $^{87}Sr/^{86}Sr$ of fluid inclusion host crystals together with salinities and formation temperatures of their corresponding fluid inclusions to be inserted in mixing models is a promising method to identify phase separation processes in various geologic environments. This approach may be used to asses phase separation processes in other hydrothermal vent systems and provide information about the penetration depth of fluids in the subsurface. For this purpose, the calculation of adiabatic cooling of ascending fluids has to be taken into account to correct extrapolate salinities and temperatures of the unmixed source fluid. Especially the comparison to geophysical evidences that constrain hydrothermal circulation depths (e.g. depth of magnetic anomalies, microseismicity due to fluid circulation) or chemical tracer for maximum fluid circulation depths (pressure-dependent Si solubility in end-member hydrothermal fluids) are promising in evaluating the lower boundary of hydrothermal circulation.

Acknowledgements

I would like to thank Prof. Dr. Wolfgang for the chance to carry out my PhD thesis in the realms of the working group Petrology of the Ocean crust. His constant advice and supply with new approaches to my research topics forwarded my research whilst his linguistic jokes kept me amused also in hard times. I thank him for the opportunity to spend a significant amount of my PhD time on various seagoing expeditions (PS101, SO253, TN350, SO263).

I thank the current and former members of the working group Petrology of the ocean crust (Andreas, Andreas, Bastian, Christian, Elmar, Karen, Lucy, Niki, Nils, Michael, Patrick, Stefan, Tony, Wolf, Wolfgang) for always being good-tempered and creating a pleasant and enjoyable time during working times and coffee breaks at the Department of Geosciences.

I want to thank PD Dr. Andreas Klügel for his doctrines on fluid inclusions prior to the thesis that enabled me to conduct my fluid inclusion study on the Brothers volcano.

Further, thanks go out to Dr. Friedrich Lucassen who guided me through the laboratory work and the measurements of Sr isotopes that comprise an important part of the thesis.

I also thank our cooperation partners from Oldenburg (Bernhard Schnetger and René Neuholz) with who we conducted the XRF analyses of Kermadec Rocks.

Further I acknowledge our partners from the Jacobs University (Prof. Dr. Andrea Koschinski, Dr. Charlotte Kleint, Annika Moje) for their cooperational work on the fluid chemistry of Kermadec hydrothermal fluids.

Thanks to my family that gave me financial support during my studies and enabled me to start my PhD thesis after a successful study of the geosciences.

Special thanks to Anna, my beloved girlfriend, who helped me to put this work in a proper layout and managed our household when I was on the run all day to get this job done.

References

Alt, J. C. (1995). Subseafloor processes in mid-ocean ridge hydrothermal systems. In Seafloor hydrothermal systems: physical, chemical, biological, and geological interactions. American Geophysical Union.

Baker, E. T. (2017). Exploring the ocean for hydrothermal venting: New techniques, new discoveries, new insights. Ore Geology Reviews, 86:55 – 69. doi: https://doi.org/10.1016/j.oregeorev.2017.02.006.

Baker, E. T., Edmonds, H. N., Michael, P. J., Bach, W., Dick, H. J. B., Snow, J. E., Walker, S. L., Banerjee, N. R., and Langmuir, C. H. (2004). Hydrothermal venting in magma deserts: The ultraslow-spreading Gakkel and Southwest Indian Ridges. Geochemistry, Geophysics, Geosystems, 5(8). doi: 10.1029/2004GC000712.

Baker, E. T., Embley, R. W., Walker, S. L., Resing, J. A., Lupton, J. E., Nakamura, K., de Ronde, C. E. J., and Massoth, G. J. (2008). Hydrothermal activity and volcano distribution along the Mariana arc. Journal of Geophysical Research: Solid Earth, 113(B8). doi: 10.1029/2007JB005423.

Berkenbosch, H. A., de Ronde, C., Gemmell, J. B., McNeill, A. W., and Goemann, K. (2012). Mineralogy and Formation of Black Smoker Chimneys from Brothers Submarine Volcano, Kermadec Arc. Economic Geology, 107(8):1613. doi: 10.2113/econ- geo.107.8.1613.

Berkenbosch, H. A., de Ronde, C. E. J., Paul, B. T., and Gemmell, J. B. (2015). Characteristics of Cu isotopes from chalcopyrite-rich black smoker chimneys at Brothers volcano, Kermadec arc, and Niuatahi volcano, Lau basin. Mineralium Deposita, 50(7):811–824. doi: 10.1007/s00126-014-0571-y.

Best, M. G. (2003). Igneous and Metamorphic Petrology. Blackwell Science Ltd, Second edition.

Bird, P. (2003). An updated digital model of plate boundaries. Geochemistry, Geophysics, Geosystems, 4(3). doi: 10.1029/2001GC000252.

Bischoff, J. and Rosenbauer, R. (1985). An empirical equation of state for hydrothermal seawater (3.2 percent NaCl). American Journal of Science.

Bodnar, R. (2003). Reequilibration of Fluid Inclusions. In Samson, I., Anderson, A., and Marshall, D. e., editors, Fluid Inclusions: Analysis and Interpretation, volume Short Course 32, pages 213–230. Mineral. Assoc. Canada.

Bodnar, R. J. and Vityk, M. O. (1994). Interpretation of microthermometric data for H_2O-NaCl fluid inclusions. Fluid Inclusions in Minerals: Methods and Applications. doi: https://ci.nii.ac.jp/naid/10003717232/en/.

Butterfield, D. A., Nakamura, K., Takano, B., Lilley, M. D., Lupton, J. E., Resing, J. A., and Roe, K. K. (2011). High SO_2 flux, sulfur accumulation, and gas fractionation at an erupting submarine volcano. Geology, 39(9):803. doi: 10.1130/G31901.1.

Caratori Tontini, F., Davy, B., de Ronde, C. E. J., Embley, R. W., Leybourne, M., and Tivey, M. A. (2012a). Crustal Magnetization of Brothers Volcano, New Zealand, Measured by Autonomous Underwater Vehicles: Geophysical Expression of a Submarine Hydrothermal System. Economic Geology. doi: 10.2113/econgeo.107.8.1571.

Caratori Tontini, F., de Ronde, C. E. J., Yoerger, D., Kinsey, J., and Tivey, M. (2012b). 3-D focused inversion of near-seafloor magnetic data with application to the Brothers volcano hydrothermal system, Southern Pacific Ocean, New Zealand. Journal of Geophysical Research: Solid Earth. doi: 10.1029/2012JB009349.

Corliss, J. B., Dymond, J., Gordon, L. I., Edmond, J. M., von Herzen, R. P., Ballard, R. D., Green, K., Williams, D., Bainbridge, A., Crane, K., and van Andel, T. H. (1979). Submarine thermal springs on the Galapagos rift. Science, 203(4385):1073– 1083. doi: 10.1126/science.203.4385.1073.

de Ronde, C. E., Faure, K., Bray, C. J., Chappell, D. A., and Wright, I. C. (2003). Hydrothermal fluids associated with seafloor mineralization at two southern Kermadec arc volcanoes, offshore New Zealand. Mineralium Deposita. doi: 10.1007/s00126-002- 0305-4.

de Ronde, C. E. J., Baker, E. T., Massoth, G. J., Lupton, J. E., Wright, I. C., Sparks, R. J., Bannister, S. C., Reyners, M. E., Walker, S. L., Greene, R. R., Ishibashi, J., Faure, K., Resing, J. A., and Lebon, G. T. (2007). Submarine hydrothermal activity along the mid-kermadec arc, new zealand: Large-scale effects on venting. Geochemistry, Geophysics, Geosystems, 8(7). doi: 10.1029/2006GC001495.

de Ronde, C. E. J., Hannington, M. D., Stoffers, P., Wright, I. C., Ditchburn, R. G., Reyes, A. G., Baker, E. T., Massoth, G. J., Lupton, J. E., Walker, S. L., Greene, R. R., Soong, C. W. R., Ishibashi, J., Lebon, G. T., Bray, C. J., and Resing, J. A. (2005). Evolution of a Submarine Magmatic-Hydrothermal System: Brothers Volcano, Southern Kermadec Arc, New Zealand. Economic Geology.
doi: 10.2113/gsecongeo.100.6.1097.

de Ronde, C. E. J., Massoth, G. J., Butterfield, D. A., Christenson, B. W., Ishibashi, J., Ditchburn, R. G., Hannington, M. D., Brathwaite, R. L., Lupton, J. E., Kamenetsky, V. S., Graham, I. J., Zellmer, G. F., Dziak, R. P., Embley, R. W., Dekov, V. M., Munnik, F., Lahr, J., Evans, L. J., and Takai, K. (2011). Submarine hydrothermal ac- tivity and gold-rich mineralization at Brothers Volcano, Kermadec Arc, New Zealand. Mineralium Deposita. doi: 10.1007/s00126-011-0345-8.

de Ronde, C. E. J. and Stucker, V. K. (2015). Chapter 47 - Seafloor Hydrothermal Venting at Volcanic Arcs and Backarcs. In Sigurdsson, H., editor, The Encyclopedia of Volcanoes (Second Edition), pages 823 – 849. Academic Press, Amsterdam, Second edition.
doi: https://doi.org/10.1016/B978-0-12-385938-9.00047-X.

DeMets, C., Gordon, R. G., and Argus, D. F. (2010). Geologically current plate motions. Geophysical Journal International, 181(1):1–80. doi: 10.1111/j.1365- 246X.2009.04491.x.

DeMets, C., Gordon, R. G., Argus, D. F., and Stein, S. (1994). Effect of recent revisions to the geomagnetic reversal time scale on estimates of current plate motions. Geophysical Research Letters, 21(20):2191–2194. doi: 10.1029/94GL02118.

Deniel, C. and Pin, C. (2001). Single-stage method for the simultaneous isolation of lead and strontium from silicate samples for isotopic measurements. Analytica Chimica Acta.
doi: https://doi.org/10.1016/S0003-2670(00)01185-5.

Elderfield, H. and Schultz, A. (1996). Mid-ocean ridge hydrothermal fluxes and the chemical composition of the ocean. Annual Review of Earth and Planetary Sciences, 24(1):191–224.
doi: 10.1146/annurev.earth.24.1.191.

Flanagan, F. and Gottfried, D. (1980). USGS rock standards; III, Manganese-nodule reference samples USGS-Nod-A-1 and USGS-Nod-P-1. USGS Publications Warehouse. doi: 10.3133/pp1155.

Fouquet, Y., Pelleter, E., Konn, C., Chazot, G., Dupré, S., Alix, A., Chéron, S., Donval, J. P., Guyader, V., Etoubleau, J., Charlou, J. L., Labanieh, S., and Scalabrin, C. (2018). Volcanic and hydrothermal processes in submarine calderas: The Kulo Lasi example (SW Pacific). Ore Geology Reviews, 99:314 – 343. doi: https://doi.org/10.1016/j.oregeorev.2018.06.006.

Gamo, T., Okamura, K., Charlou, J., Urabe, T., Auzende, J., Ishibashi, J., Shitashima, K., and Chiba, H. (1997). Acidic and sulfate-rich hydrothermal fluids from the Manus back-arc basin, Papua New Guinea. Geology, 25(2):139. doi: 10.1130/0091- 7613(1997)025<0139:AASRHF>2.3.CO;2.

German, C. and Von Damm, K. (2003). 6.07 - Hydrothermal Processes. In Holland, H. D. and Turekian, K. K., editors, Treatise on Geochemistry. doi: https://doi.org/10.1016/B0-08-043751-6/06109-0.

Graham, I. J., Reyes, A. G., Wright, I. C., Peckett, K. M., Smith, I. E. M., and Arculus, R. J. (2008). Structure and petrology of newly discovered volcanic centers in the northern Kermadec southern Tofua arc, South Pacific Ocean. Journal of Geophysical Research: Solid Earth, 113(B8). doi: 10.1029/2007JB005453.

Gruen, G., Weis, P., Driesner, T., de Ronde, C. E. J., and Heinrich, C. A. (2012). Fluid-Flow Patterns at Brothers Volcano, Southern Kermadec Arc: Insights from Geologically Constrained Numerical Simulations. Economic Geology. doi: 10.2113/econ- geo.107.8.1595.

Gruen, G., Weis, P., Driesner, T., Heinrich, C. A., and de Ronde, C. E. J. (2014). Hydrodynamic modeling of magmatic-hydrothermal activity at submarine arc volcanoes, with implications for ore formation. Earth and Planetary Science Letters. doi: https://doi.org/10.1016/j.epsl.2014.07.041.

Haase, K. M., Stroncik, N., Garbe-Schönberg, D., and Stoffers, P. (2006). Formation of island arc dacite magmas by extreme crystal fractionation: An example from Brothers Seamount, Kermadec island arc (SW Pacific). Journal of Volcanology and Geothermal Research. doi: https://doi.org/10.1016/j.jvolgeores.2005.10.010.

Haase, K. M., Worthington, T. J., Stoffers, P., Garbe-Schönberg, D., and Wright, I. (2002). Mantle dynamics, element recycling, and magma genesis beneath the Kermadec Arc-Havre Trough. Geochemistry, Geophysics, Geosystems. doi: 10.1029/2002GC000335.

Hansteen, T. H. and Klügel, A. (2008). Fluid Inclusion Thermobarometry as a Tracer for Magmatic Processes. Reviews in Mineralogy and Geochemistry. doi: 10.2138/rmg.2008.69.5.

Hawkes, J. A., Connelly, D. P., Rijkenberg, M. J. A., and Achterberg, E. P. (2014). The importance of shallow hydrothermal island arc systems in ocean biogeochemistry. Geophysical Research Letters. doi: 10.1002/2013GL058817.

Hedenquist, J. W. and Lowenstern, J. B. (1994). The role of magmas in the formation of hydrothermal ore deposits. Nature, 370. doi: https://doi.org/10.1038/370519a0.

Hedenquist, J. W., Simmons, S. F., Giggenbach, W. F., and Eldridge, C. S. (1993). White Island, New Zealand, volcanic-hydrothermal system represents the geochemical environment of high-sulfidation Cu and Au ore deposition. Geology, 21(8):731. doi: https://doi.org/10.1130/0091-7613(1993)021<0731:WINZVH>2.3.CO;2.

Jicha, B. R. and Jagoutz, O. (2015). Magma Production Rates for Intraoceanic Arcs. Elements, 11(2):105. doi: 10.2113/gselements.11.2.105.

Jochum, K. P., Nohl, U., Herwig, K., Lammel, E., Stoll, B., and Hofmann, A. W. (2005). Georem: A new geochemical database for reference materials and isotopic standards. Geostandards and Geoanalytical Research, 29(3):333–338.

Keith, M., Haase, K. M., Klemd, R., Smith, D. J., Schwarz-Schampera, U., and Bach, W. (2018). Constraints on the source of Cu in a submarine magmatic-hydrothermal system, Brothers volcano, Kermadec island arc. Contributions to Mineralogy and Petrology. doi: 10.1007/s00410-018-1470-5.

Palgan, D. (2017). Volcano-tectonic controls of hydrothermalism on a hot spot-influenced mid-ocean ridge: insights from Iceland and Reykjanes ridge. Dissertation.

Plank, T. and Langmuir, C. H. (1993). Tracing trace elements from sediment input to volcanic output at subduction zones. Nature. doi: https://doi.org/10.1038/362739a0.

Reeves, E. P., Seewald, J. S., Saccocia, P., Bach, W., Craddock, P. R., Shanks, W. C., Sylva, S. P., Walsh, E., Pichler, T., and Rosner, M. (2011). Geochemistry of hydrothermal fluids from the PACMANUS, Northeast Pual and Vienna Woods hydrothermal fields, Manus Basin, Papua New Guinea. Geochimica et Cosmochimica Acta, 75(4):1088 – 1123.
doi: https://doi.org/10.1016/j.gca.2010.11.008.

Resing, J. A., Lebon, G., Baker, E. T., Lupton, J. E., Embley, R. W., Massoth, G. J., Chadwick, Jr., W. W., and de Ronde, C. E. J. (2007). Venting of Acid-Sulfate Fluids in a High-Sulfidation Setting at NW Rota-1 Submarine Volcano on the Mariana Arc. Economic Geology.
doi: 10.2113/gsecongeo.102.6.1047.

Resing, J. A., Sedwick, P. N., German, C. R., Jenkins, W. J., Moffett, J. W., Sohst, B. M., and Tagliabue, A. (2015). Basin-scale transport of hydrothermal dissolved metals across the south Pacific Ocean. Nature. doi: https://doi.org/10.1038/nature14577.

Schreier, J. E. and Van Dover, C. L. (2018). Hydrothermal Vent Ecology. In Reference Module in Earth Systems and Environmental Sciences. Elsevier.
doi: https://doi.org/10.1016/B978-0-12-409548-9.11365-X.

Seewald, J., Reeves, E., Bach, W., Saccocia, P., Craddock, P., Shanks, W., Sylva, S., Pichler, T., Rosner, M., and Walsh, E. (2015). Submarine venting of magmatic volatiles in the Eastern Manus Basin, Papua New Guinea. Geochimica et Cosmochimica Acta, 163:178 – 199.
doi: https://doi.org/10.1016/j.gca.2015.04.023.

Seewald, J. S., Doherty, K. W., Hammar, T. R., and Liberatore, S. P. (2002). A new gas-tight isobaric sampler for hydrothermal fluids. Deep Sea Research Part I: Oceanographic Research Papers, 49(1):189 – 196. doi: https://doi.org/10.1016/S0967- 0637(01)00046-2.

Smith, I. E., Stewart, R. B., Price, R. C., and Worthington, T. J. (2010). Are arc-type rocks the products of magma crystallisation? Observations from a simple oceanic arc volcano: Raoul Island, Kermadec Arc, SW Pacific. Journal of Volcanology and Geothermal Research, 190(1):219 – 234.
doi: https://doi.org/10.1016/j.jvolgeores.2009.05.006.

Smith, I. E., Worthington, T. J., Price, R. C., Stewart, R. B., and Maas, R. (2006). Petrogenesis of dacite in an oceanic subduction environment: Raoul Island, Kermadec arc. Journal of Volcanology and Geothermal Research, 156(3):252 – 265. doi: https://doi.org/10.1016/j.jvolgeores.2006.03.003.

Spinelli, G. A. and Harris, R. N. (2011). Effects of the legacy of axial cooling on partitioning of hydrothermal heat extraction from oceanic lithosphere. Journal of Geophysical Research: Solid Earth, 116(B9). doi: 10.1029/2011JB008248.

Teagle, D. A. H., Alt, J. C., and Halliday, A. N. (1998). Tracing the chemical evolution of fluids during hydrothermal recharge: Constraints from anhydrite recovered in ODP Hole 504B. Earth and Planetary Science Letters, 155(3):167 – 182. doi: https://doi.org/10.1016/S0012-821X(97)00209-4.

Timm, C., Davy, B., Haase, K., Hoernle, K. A., Graham, I. J., de Ronde, C. E. J., Woodhead, J., Bassett, D., Hauff, F., Mortimer, N., Seebeck, H. C., Wysoczanski, R. J., Caratori-Tontini, F., and Gamble, J. A. (2014). Subduction of the oceanic Hikurangi Plateau and its impact on the Kermadec arc. Nature Communications.
doi: https://doi.org/10.1038/ncomms5923.

Tunnicliffe, V. and Fowler, M. R. (1996). Influence of sea-floor spreading on the global hydrothermal vent fauna. Nature. https://doi.org/10.1038/379531a0.

Von Damm, K. (1985). Chemistry of submarine hydrothermal solutions at 21 N, East Pacific Rise. Geochimica et Cosmochimica Acta. doi: https://doi.org/10.1016/0016- 7037(85)90222-4.

White, S. M., Crisp, J. A., and Spera, F. J. (2006). Long-term volumetric eruption rates and magma budgets. Geochemistry, Geophysics, Geosystems, 7(3). doi: 10.1029/2005GC001002.

Wright, I., Stoffers, P., Hannington, M., de Ronde, C., Herzig, P., Smith, I., and Browne, P. (2002). Towed-camera investigations of shallow-intermediate water-depth submarine stratovolcanoes of the southern Kermadec arc, New Zealand. Marine Geology, 185(3):207 – 218. doi: https://doi.org/10.1016/S0025-3227(01)00285-7.

Wright, I., Worthington, T., and Gamble, J. (2006). New multibeam mapping and geochemistry of the 30° - 35°S sector, and overview, of southern Kermadec arc volcanism. Journal of Volcanology and Geothermal Research, 149(3):263 – 296. doi: https://doi.org/10.1016/j.jvolgeores.2005.03.021.

Wright, I. C., de Ronde, C. E. J., Faure, K., and Gamble, J. A. (1998). Discovery of hydrothermal sulfide mineralization from southern Kermadec arc volcanoes (SW Pacific). Earth and Planetary Science Letters.
doi: https://doi.org/10.1016/S0012- 821X(98)00225-8.

Wysoczanski, R., Wright, I., Gamble, J., E.H. Hauri, E., Luhr, J., Eggins, S., and Handler, M. (2006). Volatile contents of Kermadec Arc-Havre Trough pillow glasses: Fingerprinting slab-derived aqueous fluids in the mantle sources of arc and back- arc lavas. Journal of Volcanology and Geothermal Research, 152(1):51 – 73.
doi: https://doi.org/10.1016/j.jvolgeores.2005.04.021.

Yang, K. and Scott, S. D. (1996). Possible contribution of a metal-rich magmatic fluid to a sea-floor hydrothermal system. Nature. doi: https://doi.org/10.1038/383420a0.